Title
Development and Microfabrication of Next Generation Biosensors for Nucleic Acids and Neurotransmitters

Author
Cao, Yan

Publication Date
2023

Peer reviewed|Thesis/dissertation

UNIVERSITY OF CALIFORNIA

Los Angeles

Development and Microfabrication of Next Generation Biosensors for Nucleic Acids and Neurotransmitters

A dissertation submitted in partial satisfaction of the requirement for the degree of Doctor of Philosophy in Chemical Engineering

by

Yan Cao

2023

ABSTRACT OF THE DISSERTATION

Development and Microfabrication of Next Generation
Biosensors for Nucleic Acids and Neurotransmitters

by

Yan Cao
Doctor of Philosophy in Chemical Engineering
University of California, Los Angeles, 2023
Professor Harold G. Monbouquette, Chair

Nucleic acid-based detection can be applied broadly to detect pathogens in, for example, clinical samples, livestock, food and water. The recent COVID-19 pandemic once again emphasized the importance of point-of-care (POC) diagnosis, which is rapid, inexpensive and reliable, to defend against public health threats. Currently, nucleic acid amplification tests (NAATs) rely on polymerase chain reaction (PCR) and other amplification methods that makes them more complex, less portable, dependent on perishable reagents and less suitable as POC tests. With the goal to develop portable, rapid and inexpensive diagnostic devices, we have been working on the further evolution of the previously reported nanopore-based, nucleic acid detection platform developed at UCLA. The detection scheme utilizes charge neutral peptide nucleic acid (PNA)

probes conjugated to carboxyl-functionalized microbeads for sequence-specific nucleic acid (NA) detection. The hybridization event with target NA introduces negative charge to the PNA-bead complex which results in electrophoretic mobility. The negatively charged PNA-bead complex after target NA hybridization is directed by an electric field to a nanopore of smaller diameter in a micron-thick glass membrane where it blocks at least partially the ionic current flow thereby providing a sustained current drop which serves as the detection signal. In order to demonstrate the potential broad application for detection of pathogens in clinical samples, both *Neisseria gonorrhoeae* and *Chlamydia trachomatis* spiked in human urine were detected at 10-100 CFU/mL against a background of representative bacterial flora. High sensitivities and specificities of ~95% were demonstrated and no false positives were observed with the representative bacterial flora which served as a control. An improvement of overall detection time was achieved by integrating the nanopore detector, which consists of a glass chip with an etched membrane and nanopore, with the lateral flow assay (LFA) format. The extracted NA sample flows along an LFA membrane by surface-tension driven capillary flow and hybridizes with a preloaded deposit of neutral PNA-beads. Driven by an external electric field, the negatively charged bead with hybridized NA successfully blocks the smaller nanopore integrated on the LFA chip and generates a detection signal. Therefore, the overall detection time is reduced significantly without the need for complex pumps or valves. Detection of 10 aM *E. coli* 16S rRNA against 10 fM *P. putida* 16S rRNA within 15 minutes was demonstrated successfully using the nanopore integrated into the LFA format. Further demonstrations with complex clinical samples and integration with simpler NA extraction schemes may lead to broad application for disease diagnosis at the POC.

The study of neurological disorders and the deciphering of complex behaviors rely on the ability to monitor neuronal processes including inter-neuronal chemical signaling. Compared to

extensively developed electrophysiological recordings, the detection of neurotransmitter release events in near-real time is far less advanced and remains limited in application. Neuroprobes with high spatiotemporal resolution would enable establishment of the relationships between neurotransmitter release events and subsequent behaviors. Our lab previously has reported glutamate (Glut) microbiosensors that can selectively detect glutamate against a background of electroactive interferents including dopamine (DA) and ascorbic acid (AA). In order to achieve better sensitivity and spatiotemporal resolution, further development could be achieved by optimizing the enzyme deposition technique and the thicknesses of the deposited enzyme layer and permselective polymer coatings. Microcontact printing (μCP) has been adopted as a direct method to deposit arrays of proteins on silicon or glass substrates without compromising the activity of the proteins. By incorporating a specially designed polymer with choline oxide to create a μCP "ink" led to improved choline sensor performance including a sensitivity of 639 ± 96 nA μM^{-1} cm^{-2} (pH 7.4; n = 4). Guided by simulations performed with a detailed mathematical model, choline sensors were constructed with exhibited sensitivity and response time of 660 ± 40 nA μM^{-1} cm^{-2} at 37 °C and 0.36 ± 0.05 s respectively. With assistance of microcontact printing to selectively transfer different enzymes onto specific microelectrodes in an array on 100-um-width microprobes, a demonstration of an implantable multifunctional neural microprobe for simultaneous multi-analyte sensing and chemical delivery has been achieved.

The dissertation of Yan Cao is approved.

Yi Tang

Dante A. Simonetti

Jacob J. Schmidt

Harold G. Monbouquette, Committee Chair

University of California, Los Angeles

2022

TABLE OF CONTENTS

Table of Contents

LIST OF FIGURES

LIST OF TABLES

ACKNOWLEDGEMENTS

I would like to first express my deepest gratitude to my Ph.D. advisor, Professor Harold G. Monbouquette for his guidance and continuous support in enlightening me to be a better researcher and a thoughtful person. Thanks to the open-minded discussions we had together, I'm motivated and immersed in critical thinking, systematic problem solving, consideration of others and encouragement. I have learned how to better organize my research project, execute experimental plans, and identify and resolve problems. I will always cherish his guidance, enthusiasm and dedication and I will be forever grateful for everything I learned which lays the basis of my future development.

I would also like to thank my committee members, Professor Yi Tang, Professor Dante Simonetti, and Professor Jacob J. Schmidt for their time, input, and valuable suggestions. In addition, I would like to acknowledge funding support from NIH. I would also like to thank my fantastic collaborators on my projects, including Professor Jacob J. Schmidt who always provided insightful suggestions, Professor Omai B. Garner and Dr. Sukantha Chandrasekaran from UCLA Pathology and Laboratory Medicine and Dr. Zhenrong Zheng on the nucleic acid detection project, and Professor Nigel Maidment, Professor Pei-yu Chiou, Dr. I-wen Huang, Dr. Mackenzie Clay, Dr. Ming Zhao, Dr. Bo Wang, Dr. Ximiao Wen, and Dr. Pei-Shan Chung on the electroenzymatic sensors projects, and Professor Anne Andrews, Professor Paul Weiss, Dr. Chuanzhen Zhao, Dr. Tianxing Man, Dr. Wenfei Liu on the aptamer-based FET sensors projects.

I also appreciate my fabulous lab mates, Dr. Allison M. Yorita, Dr. Bonhye Koo, Dr. I-wen (Brenda) Huang, Dr. Mac Clay, Dr. Bo Wang, Dr. Lili Feng, Dr. Zhenrong Zheng and Dmitriy Ruckodanov. Dr. Koo and Dr. Yorita first mentored me when I was an undergraduate student and

enlightened me with critical thinking and techniques in starting the nucleic acid detection project, and Dr. Huang shared experience and tips with me on nanofabrication and provided insightful suggestions on research directions. Dr. Clay gave me insight on mathematical simulations and problem solving. Dr. Wang and Dr. Feng encouraged and motivated me on the design and execution of experimental plans. Dr. Zheng has been a reliable and talented partner who I worked closely with on the nucleic acid detection project, and without his critical thinking and creative suggestions, we are not able to overcome many challenges. I also want to thank Dima as the best lab partner, and I always cherish the time we served as teaching assistants together.

Last but not least, I would like to express my deepest appreciation to my family for being my biggest pillar of support during my graduate school career. Their unconditional support and encouragement have kept my passion during the intense academic years. The endless love from Mom and Dad has accompanied me to overcome many challenges in my life. I would never be able to go this far without them.

VITA

2012-2016	*B.S., Chemical and Biomolecular Engineering* University of California, Los Angeles Los Angeles, CA
2018-2023	*Graduate Student Researcher, Department of Chemical and Biomolecular Engineering* University of California, Los Angeles Los Angeles, CA
2018-2023	*Teaching Assistant, Department of Chemical and Biomolecular Engineering* University of California, Los Angeles Los Angeles, CA

PUBLICATIONS AND PRESENTATIONS

Zhenrong Zheng, **Yan Cao***, Sukantha Chandrasekaran, Jacob J. Schmidt, Omai Garner, and Harold G. Monbouquette, "An amplification-free, 16S rRNA test for *Neisseria gonorrhoeae* in urine," *Sensors & Diagnostics, 2022, DOI: 10.1039/D2SD00128D*

Yan Cao*, Zhenrong Zheng, Jacob J. Schmidt, and Harold G. Monbouquette, "Amplification-free detection of 16S rRNA using a glass chip detector integrated into the lateral flow assay format," *In preparation*

Yan Cao and Harold G. Monbouquette, "Amplification-free, sequence-specific 16S rRNA detection for *Chlamydia trachomatis* in urine", *In preparation*

Yan Cao*, Zhenrong Zheng, and Harold G. Monbouquette, "Nucleic acid amplification-free detection of DNA and RNA at ultralow concentration*," Curr Opin Biotechnol*, 2021. **71**: p. 145-150.

Zhao Ming, **Yan Cao***, I-Wen Huang, and Harold G. Monbouquette, "Improved Microcontact Printing of Choline Oxidase using a Polycation-Functionalized Zwitterionic Polymer as Enzyme Immobilization Matrix", *In preparation*

Bo Wang, Ximiao Wen, **Yan Cao**, Shan Huang, Hoa A. Lam, Tingyi "Leo" Liu, Pei-Shan Chung, Harold G. Monbouquette, Pei-Yu Chiou, and Nigel T. Maidment, "An implantable multifunctional neural microprobe for simultaneous multi-analyte sensing and chemical delivery", *Lab on a Chip 20.8 (2020): 1390-1397.*

I-wen Huang, Mackenzie Clay, **Yan Cao,** Jingjing Nie, Yuwan Guo, and Harold G. Monbouquette, "Electroenzymatic choline sensing at near the theoretical performance limit." *Analyst 146.3 (2021): 1040-1047.*

Chuanzhen Zhao, Kevin M. Chung, I-wen Huang, Hongyan Yang, Nako Nakatsuka, Wenfei Liu, **Yan Cao**, Tianxing Man, Paul S. Weiss, Harold G. Monbouquette, and Anne M. Andrews, "Implantable aptamer–field-effect transistor neuroprobes for in vivo neurotransmitter monitoring." *Science Advances 7.48 (2021): eabj7422.*

Chuanzhen Zhao, Tianxing Man, **Yan Cao**, Paul S. Weiss, Harold G. Monbouquette, and Anne M. Andrews, "Flexible and Implantable Polyimide Aptamer-Field-Effect Transistor Biosensors." *ACS sensors 7.12 (2022): 3644-3653.*

Yan Cao*, Zhenrong Zheng, and Harold G. Monbouquette, "Amplification-free, rapid, nucleic acid detection based on a nanopore detector integrated into the lateral flow assay format" *ACS Spring 2022,* Division of Analytical Chemistry, San Diego, CA, 2022 (Oral Presentation)

* co-first author

Chapter 1: Introduction

1.1 Sequence-specific nucleic acid detection

1.1.1 Motivation

Nucleic acid-based, sequence-specific detection of pathogens has a wide range of applications including pathogen diagnosis, detecting food and water contamination, guiding proper treatment to reduce antibiotic resistance and screening to reduce transfusion transmitted infections (TTIs) in the blood donation recipients.[1] The recent COVID-19 pandemic once again emphasized the importance and apparent demand for inexpensive, sensitive, and convenient disease diagnostics. In order to better fight against public health crises, ideal diagnostic tests should be rapid, inexpensive and easy to operate and interpret.[2] Traditional clinical diagnosis requires standard laboratory facilities and professional specialists, and generally includes transportation to the lab, culturing, batching, testing, which usually requires up to a few days. Previous study has indicated that a significant portion of the patient population will not wait in a clinic for more than 20 mins for a test result[3, 4], therefore, the need for a rapid but reliable pathogen detection schemes that do not require a standard laboratory environment and that can meet requirements at the point-of-care (POC) becomes evident. Furthermore, if a diagnostic device is intended for widespread use, or made available to developing countries, it should be inexpensive and easy to operate, especially if tests are to be repeated at high frequency for everyone, such as during a pandemic.

1.1.2 Current nucleic acid-based detection schemes

Marketed POC immunoassays are a class of frontline diagnostics for detecting several pathogens and pathophysiological conditions. However, immunoassays often have marginal sensitivities and specificities leading to false negatives and positives.[5] Nucleic acid amplification tests (NAATs) with ultralow limits of detection (LODs) and both sensitivity and specificity in the 90-99% range could be more preferable, considering the combination of low detection limit, high sensitivity and high specificity.[6] Polymerase chain reaction (PCR) is the core method used by most NAATs to amplify the copy number of the target disease-specific nucleic acid (NA) in a sample. However, the process is inherently complex entailing the need to isolate and purify nucleic acid from a sample, to control temperature cycling during the enzyme-catalyzed amplification process, and to provide expensive reagents including polymerase, primers and nucleotides. Optical component also may be required to detect amplicons labeled with dyes.

Many studies have been pursued to develop inexpensive but rapid and accurate amplification-free, nucleic acid-based diagnostic techniques. Enabled generally by the advent of nanotechnology, numerous detection methods based on both optical and electrical measurements have been conceived over recent years. Over the past few years, many reports including ours, have demonstrated high accuracy in detecting pathogens in clinical samples or mock clinical samples, with NA at ultralow concentration in the single digit attomole range.[7-13]

A great number of optical methods have been reported to visualize the presence of a target NA sequence by conjugation with nanoparticles/nanorods. Common strategies including Förster resonance energy transfer (FRET), the bio-barcode method, quantum dot fluorescence, surface enhanced raman spectroscopy (SERS), surface plasmon resonance (SPR), and darkfield microscopy. A few optical methods exhibit outstanding LODs in the single-digit zeptomole range,

but the current limitation includes the lack of detection in complex samples obtained in the clinic, potentially lengthy multiple hybridization processes and common reliance on expensive spectroscopy instrumentation.

Electrochemical or electronic approaches for detection of NAs of specific sequence at ultralow concentration evolved later than optical schemes and all within about the last 10 years. The common detection schemes include mass spectrometry, constant potential amperometry, voltammetry, electrochemical impedance spectroscopy, field effect transistors, and piezoelectric plate sensors. The electrochemical methods displayed good potential to be integrated with simple electronics with low power requirements, however a large portion of them currently still have a lengthy assay time.

1.1.3 Nanopore based, amplification-free sequence specific detection scheme

Nanopore-based NA sensing systems are based on a resistive-pulse sensing mechanism following on the work of Coulter, where the conductance of an electrolyte-filled pore or channel is monitored as analyte species traverse or block it. Our form of nanopore-based detection relies on an electromechanical signal transduction mechanism that also enables detection of NA at ~1 aM.[7] Uncharged PNA capture probes are conjugated to ~800-nm-diameter polystyrene spheres that are designed to be very nearly charge neutral overall such that they do not exhibit electrophoretic movement in the presence of an electric field. However, the substantial negative charge acquired upon capture of a target NA sequence makes the hybridized conjugate mobile. Electrophoresis of the bead-PNA conjugate with hybridized target NA to the mouth of a smaller diameter glass pore causes a significant decrease in pore conductance, thereby resulting in a strong, sustained drop in measured ionic current. Nonspecifically bound NA is removed from the bead conjugate by the strong electric field at the pore mouth resulting in no sustained signal. Further,

the opposing electroosmotic flow through the glass pore sweeps PNA-bead conjugates without hybridized target away from the pore mouth. With this technology, pathogens such as *Neisseria gonorrhoeae* and *Chlamydia trachomatis* were detected in 10-100 CFU/mL range in sterilized pooled human urine and exhibited sensitivity and specificity of ≥95%.[14] However, since the procedure used involved multiple centrifugations and transfers via pipets, the overall assay time could be significantly reduced by integrating with the lateral flow assay format.

1.2 Electrochemical sensing of neurotransmitters

1.2.1 Motivation

A deep understanding of information processing in the brain is critical for neuroscience studies and rational development of effective treatments for complex neurological disorders including Huntington's disease, Alzheimer's disease, Parkinson's disease, ALS, and Jakob-Creutzfeldt disease.[15] Even though the signaling inside the brain is very complex, they can be classified as electrical and chemical signals. The electrical signals are generated by the firing of action potentials, which propagates electrical signals along a neuron. Neurotransmitters serve as chemical messengers to deliver chemical signals from one neuron to the next. In the past, numerous successful research studies have been performed with a focus on electrical signaling monitored through electrophysiological recordings.[16, 17] On the other hand, study of chemical signaling, which plays an important role in mood and behavior, is less developed and scientists still have very little data about the specific relationship between neurotransmitters and human neurological states.[18, 19]

Choline is a product of the hydrolysis of the neurotransmitter, acetylcholine, which acts as a messenger functioning in memory storage and body movement such as muscle contractions.[20]

Glutamate is an excitatory neurotransmitter and is associated with memory formation and learning. Known disorders associated with abnormal glutamate signaling includes Huntington's disease, Alzheimer's disease, Parkinson's disease, ALS, and Jakob-Creutzfeldt disease.[21, 22] Serotonin is a small-molecule neurotransmitter that carries messages between nerve cells in the brain and throughout the body, and it plays a key role in mood, sleep, digestion, nausea, wound healing, bone health, blood clotting and sexual desire.[18] Fabricating sensors with enhanced enzyme transfer and immobilization skills and with novel detection mechanisms could further elucidate the roles of the above-mentioned neurotransmitters in neural disorders and diseases.

1.2.2 Current sensing mechanisms for neurotransmitter detection

Currently, sensors focus on detecting the neurotransmitter that leaks into the extracellular space after release into the synapse during chemical signaling. Microdialysis with high performance liquid chromatography (HPLC) is one of the most popular traditional detection schemes. It generally has a very high sensitivity and can detect a broad range of species.[23, 24] However, long analysis times and relatively large probe sizes (>100 μm in width) result in limited temporal and spatial resolution. Fluorescence imaging with high sensitivity and high temporal and spatial resolution also exhibits good potential.[25, 26] However, limited light penetration in the brain as well as requirements for genetic encoding are the limitations. Besides, to achieve super high single neuron resolution, expensive two-photon microscopy is required.

Electrochemical sensing of neurotransmitters emerged as a viable and rapid way to monitor neurotransmitters with high temporal and spatial resolution. Fast scan cyclic voltammetry is one of the proven successful electrochemical detection methods that has advantages of high sensitivity, high temporal and spatial resolution and being label free.[27] However, it is limited by application to only a small number of electroactive species and by difficulty in multiplexing. Constant

potential amperometry is a promising method where the electrode is held at a constant potential and the oxidization of electro-oxidizable molecules can be measured by current change. It has advantages including high spatial and temporal resolution, being label free and providing a real time view of species detection. The major limitation is the inability to differentiate between different electrooxidizable species, however it could be overcome by coating selective layers on the electrodes.[20] Field-effect-transistors (FETs) conjugated with aptamers also displays great potential in integrated neural activity recordings at high spatiotemporal resolution, and it is not limited to electroactive species.

1.2.3 Further improvements of constant potential amperometry sensors and FET neurotransmitter detection

To better understand complex behaviors, the need for simultaneous electrochemical recording of multiple analytes is evident. In order to detect multiple neurotransmitters while retaining high spatial resolution, methods for depositing enzymes selectively on specific microelectrode in an array on a microprobe are required. Microcontract printing of protein, which entails the transfer of layers of protein in specific patterns to substrates using an elastomeric stamp, was developed and reported in previous studies.[28] It could be useful to create multianalyte sensing microprobes by targeted deposition of each of multiple enzymes onto distinct, selected sites of a microelectrode array. However, it is limited by insufficient enzyme transfer and inadequate spatial resolution of the deposit. One possible optimization approach is to include specially designed polymers in the protein solution that serves as the "ink" in order to increase viscosity while maintaining high adhesion to the microelectrode surface, thereby achieving more efficient enzyme immobilization and better sensor performance.

Traditionally, in order to achieve simultaneous electrochemical recording of multiple neurotransmitters, multiple electrode implants are required for each analyte as well as a counter electrode, a reference electrode (RE), and potentially, microinjectors for chemical delivery.[29] Such an approach requires prolonged surgical implantation procedures and results in significant damage to the brain. Moreover, the relative distance between separated chemical delivery devices, sensing electrodes, and the RE can be hard to control, hampering experimental reproducibility and introducing variability in baseline noise. Therefore, the development of a multifunctional probe that integrates these individual components into a single implantable device is highly desirable.

Current implantable devices enable electrophysiological recordings simultaneously from large numbers of interconnected neurons at millisecond temporal and cellular-scale spatial resolution. However, techniques for neurochemical recording have yet to achieve such high spatiotemporal resolution due to slow sensor kinetics exacerbated by the need for selectivity against the complex background of brain extracellular fluid.[20] In order to facilitate the understanding of brain function and neural disorders, a neurochemical recording sensor with enhanced spatiotemporal resolution as well as optimized sensitivity and response time is in great demand.

Field effect transistors conjugated with aptamer emerged recently as a novel neurotransmitter sensing scheme exhibiting great potential. Detection of neurotransmitters such as serotonin in physiological environments both *in vitro* (such as cultured brain tissue) and *in vivo* should be demonstrated for further development of this rising detection scheme. Also, for implantable sensors, to improve *in vivo* monitoring by reducing tissue damage and immunological responses, it would be ideal to develop thin and flexible (vs. stiff) sensors on organic substrates such as polyimide.

1.3 References

1. Dean, C. L.; Wade, J.; Roback, J. D. J Clin Microbiol 2018, 56, (7).
2. Cao, Y.; Zheng, Z.; Monbouquette, H. G. Curr Opin Biotechnol 2021, 71, 145-150.
3. Atkinson, L. M.; Vijeratnam, D.; Mani, R.; Patel, R. Int J STD AIDS 2016, 27, (8), 650-5.
4. Hsieh, Y. H.; Hogan, M. T.; Barnes, M.; Jett-Goheen, M.; Huppert, J.; Rompalo, A. M.; Gaydos, C. A. PLoS One 2010, 5, (11), e14144.
5. Sturgeon, C. M.; Viljoen, A. Ann Clin Biochem 2011, 48, (Pt 5), 418-32.
6. Lui, C.; Cady, N. C.; Batt, C. A. Sensors (Basel) 2009, 9, (5), 3713-44.
7. Koo, B.; Yorita, A. M.; Schmidt, J. J.; Monbouquette, H. G. Lab Chip 2018, 18, (15), 2291-2299.
8. Ho, H. A.; Dore, K.; Boissinot, M.; Bergeron, M. G.; Tanguay, R. M.; Boudreau, D.; Leclerc, M. J Am Chem Soc 2005, 127, (36), 12673-6.
9. Liu, Y. J.; Yao, D. J.; Chang, H. Y.; Liu, C. M.; Chen, C. Biosens Bioelectron 2008, 24, (4), 558-565.
10. Liyanage, T.; Masterson, A. N.; Oyem, H. H.; Kaimakliotis, H.; Nguyen, H.; Sardar, R. Anal Chem 2019, 91, (3), 1894-1903.
11. Yang, B.; Gu, K.; Sun, X.; Huang, H.; Ding, Y.; Wang, F.; Zhou, G.; Huang, L. L. Chem Commun (Camb) 2010, 46, (43), 8288-90.
12. Wu, W.; Kirimli, C. E.; Shih, W. H.; Shih, W. Y. Biosens Bioelectron 2013, 43, 391-9.
13. Spain, E.; McArdle, H.; Keyes, T. E.; Forster, R. J. Analyst 2013, 138, (15), 4340-4.
14. Zheng, Z.; Cao, Y.; Chandrasekaran, S.; Schmidt, J. J.; Garner, O. B.; Monbouquette, H. G. Sens Diagn 2023, 2, (1), 163-167.

15. Teleanu, R. I.; Niculescu, A. G.; Roza, E.; Vladacenco, O.; Grumezescu, A. M.; Teleanu, D. M. Int J Mol Sci 2022, 23, (11).

16. Jones, I. L.; Livi, P.; Lewandowska, M. K.; Fiscella, M.; Roscic, B.; Hierlemann, A. Anal Bioanal Chem 2011, 399, (7), 2313-29.

17. Liu, Q.; Ye, W.; Xiao, L.; Du, L.; Hu, N.; Wang, P. Biosens Bioelectron 2010, 25, (10), 2212-7.

18. Lovinger, D. M. Alcohol Health Res World 1997, 21, (2), 114-20.

19. Zhao, C.; Cheung, K. M.; Huang, I. W.; Yang, H.; Nakatsuka, N.; Liu, W.; Cao, Y.; Man, T.; Weiss, P. S.; Monbouquette, H. G.; Andrews, A. M. Sci Adv 2021, 7, (48), eabj7422.

20. Huang, I. W.; Clay, M.; Cao, Y.; Nie, J. J.; Guo, Y. W.; Monbouquette, H. G. Analyst 2021, 146, (3), 1040-1047.

21. Carvajal, F. J.; Mattison, H. A.; Cerpa, W. Neural Plast 2016, 2016, 2701526.

22. Ribeiro, F. M.; Paquet, M.; Cregan, S. P.; Ferguson, S. S. CNS Neurol Disord Drug Targets 2010, 9, (5), 574-95.

23. Ungerstedt, U.; Hallstrom, A. Life Sci 1987, 41, (7), 861-4.

24. Watson, C. J.; Venton, B. J.; Kennedy, R. T. Anal Chem 2006, 78, (5), 1391-9.

25. Liang, R.; Broussard, G. J.; Tian, L. ACS Chem Neurosci 2015, 6, (1), 84-93.

26. Muller, A.; Joseph, V.; Slesinger, P. A.; Kleinfeld, D. Nat Methods 2014, 11, (12), 1245-52.

27. Heien, M. L.; Johnson, M. A.; Wightman, R. M. Anal Chem 2004, 76, (19), 5697-704.

28. Wang, B.; Koo, B.; Huang, L. W.; Monbouquette, H. G. Analyst 2018, 143, (20), 5008-5013.

29. Wang, B.; Wen, X.; Cao, Y.; Huang, S.; Lam, H. A.; Liu, T. L.; Chung, P. S.; Monbouquette, H. G.; Chiou, P. Y.; Maidment, N. T. Lab Chip 2020, 20, (8), 1390-1397.

Chapter 2: Nucleic Acid Amplification-free Detection of DNA and RNA at Ultralow Concentration

Chapter 2 is a manuscript published with the following citation:

Cao, Y., Z. Zheng, and H.G. Monbouquette, Nucleic acid amplification-free detection of DNA and RNA at ultralow concentration. Current Opinion in Biotechnology, 2021. 71: p. 145-150.

ABSTRACT

The broad spectrum of approaches for nucleic acid amplification-free detection of DNA and RNA at single-digit attomolar (10^{-18} M) concentration and lower is reviewed. These low concentrations correspond roughly to the most clinically desirable detection range for pathogen-specific nucleic acid as well as the detection limits of commercially available, nucleic acid amplification tests based primarily on polymerase chain reaction (PCR). The need for more rapid and inexpensive, yet still highly accurate tests, has become evident during the pandemic. It is expected that publication of reports describing improved tests will accelerate soon, and this review covers the wide variety of detection methods based on both optical and electrical measurements that have been conceived over recent years, enabled generally by the advent of nanotechnology.

2.1 Introduction

The ongoing COVID-19 pandemic and the realization that this public health crisis likely will not be the last of its kind has made the need glaringly apparent for rapid, convenient, inexpensive, sensitive and reliable disease diagnostics. If a diagnostic device is intended for wide-spread use, it should accept a conveniently obtained clinical sample and be easy to operate and interpret, preferably in a point-of-care (POC) setting. Further, it must be rapid, as it has been

observed that a significant portion of the patient population will not wait in a clinic more than 20 min for a test result [1, 2]. Finally, ideal tests should be inexpensive, especially if tests are to be repeated at high frequency for each individual, such as during a pandemic; and if the technology is to be made available to developing countries where inefficient dis-ease diagnosis leads to 95% of deaths [3]. Currently, nucleic acid amplification tests (NAATs) appear to provide the best combination of low detection limit, high sensitivity and high specificity relative to conventional binding assays such as immunoassays [4, 5].

However, the most advanced NAATs currently US FDA approved, including those for POC clinical use (i.e. CLIA-waived), provide a complete result in 15 min or more, and the typical US Medicare/Medicaid program reimbursement rate is ~$40-50/test. Most NAATs rely on polymerase chain reaction (PCR) to amplify the copy number of the target, disease-specific nucleic acid (NA) in a sample. Although this approach can provide very low LODs in principle, the process is inherently complex entailing the need to isolate and purify NA from a sample so as to remove polymerase inhibitors; to control temperature cycling during the enzyme-catalyzed amplification process; to provide perishable reagents including polymerase, primers and nucleotides; and to integrate a means for labeled amplicon detection. Isothermal amplification approaches eliminate the need for temperature cycling, but all other requirements remain. As a result, many researchers have made an effort to conceive of alternate, amplification-free, NA-based pathogen detection schemes that may prove more promising.

This review focuses on discussion of published approaches for nucleic acid amplification-free detection of NA of specific sequence at the single-digit attomolar (~1-9 × 10^{-18} M) threshold or lower. The 1 aM level corresponds to ~1000 pathogens/mL based on chromosomal NA or ~1 viable bacterium/10 mL based on ribosomal RNA, since rRNA is present at ~10,000 copies per

viable bacterial cell. To put these numbers in perspective, the commercial, high throughput, clinical laboratory-based NAATs available for *N. gonorrhoeae* in urine have limits of detection (LODs) in the ~1-100 CFU/mL range. The SARS-CoV-2 virus, the causative agent of COVID-19, is present at as low as 104 virions/mL in throat samples taken from individuals several days post initial infection [6]. Since some NAATs have practical LODs for SARS-CoV-2 of $\geq 10^4$ copies/mL, this data may explain a significant portion of reported false negatives [7-10]. These data suggest that amplification-free methods should exhibit LODs in the low aM range or below to be competitive with NAATs and to be broadly useful for disease diagnosis. Recently, microRNAs have emerged as important disease markers and concentrations of these species in blood plasma also are very low (<pM) [11]. Clearly, the technical challenges are great.

2.2 Optical methods

A common theme throughout this review is the use of nanoparticles as key components of transduction mechanisms to convert a selective hybridization event into a detectable signal. This generalization applies well to those schemes based on optical detection methods with the exception of the approach described by Ho et al., which is one of the earliest reports of selective NA detection at the single-digit attomolar level or lower [12], and is based on Förster resonance energy transfer (FRET) from a cationic polythiophene to a fluorophore (Alexa Fluor 546). This approach provided the lowest limit of detection (LOD) among those discussed in this review at 3 zM (3×10^{-21} M) in as little as 5 min. More recently, the technique has been adapted to the micro-array format for multiplex detection [13]. At around the same time as this work described above, the Mirkin laboratory demonstrated the now well-known bio-bar- code-based DNA detection method utilizing oligonucleotide probe-modified gold nanoparticles (AuNPs), probe-functionalized magnetic beads

(MBs), and silver development for scanometric readout [14, 15, 16]. Also in an early study, Liu et al. appear to be the first to demonstrate the use of quantum dot (QD) fluorescence and magnetic beads (MBs) to achieve single-digit attomolar or lower detection of NAs [17]. More recently, two other groups have pursued a similar successful strategy [18, 19]. Although promising, the need for testing with clinical samples is a common issue among both the early work on optical technologies for amplification-free NA detection mentioned above and the more recent studies discussed below.

2.2.1 Surface enhanced Raman spectroscopy (SERS) and surface plasmon resonance (SPR)

Others have pursued alternative optical techniques using AuNPs as signal enhancers enabling application of SERS and SPR for NA detection [20, 21, 22]. Most recently, Liyanage et al. designed a scheme for label-free detection of tumor suppressor microRNAs at as low as 137 zM based on alteration of localized surface plasmon resonance when target microRNA binds to oligonucleotide probes on triangular AuNPs (AuTNPs) (Figure 2.1) [22]. Single base-pair mismatches also were shown to be discernable, and quantification of tumor suppressor microRNAs was demonstrated in diluted plasma samples. However, the reliance on spectroscopy instrumentation likely will limit such approaches to the clinical laboratory rather than POC use.

2.2.2 Darkfield microscopy

In yet another nanotechnology-based detection scheme described in this case by Li et al., target DNA is sandwiched between MBs conjugated with an oligonucleotide capture probe and gold nanorods (AuNRs) conjugated with a second capture probe complementary to a separate site on the target DNA [23]. The sandwich structures are isolated from unbound AuNRs in a magnetic field and the assemblies subsequently are dehybridized at 60 °C. The recovered AuNRs, each corresponding to a single DNA target, are electrostatically bound to a positively charged glass

surface modified with (3-aminopropyl)triethoxysilane. The deposited AuNRs, evident as red spots, are counted using darkfield microscopy and image recognition software. The technique was shown to be quantitative and the LOD for 63mer single-stranded DNA corresponding to the human papillomavirus (HPV) is 6.5 aM. However, lengthy hybridization steps and use of a laboratory microscope will need to be overcome, assuming detection using complex clinical samples is demonstrated successfully. Recent demonstrations of smartphone use for optical diagnostic applications may be helpful [24].

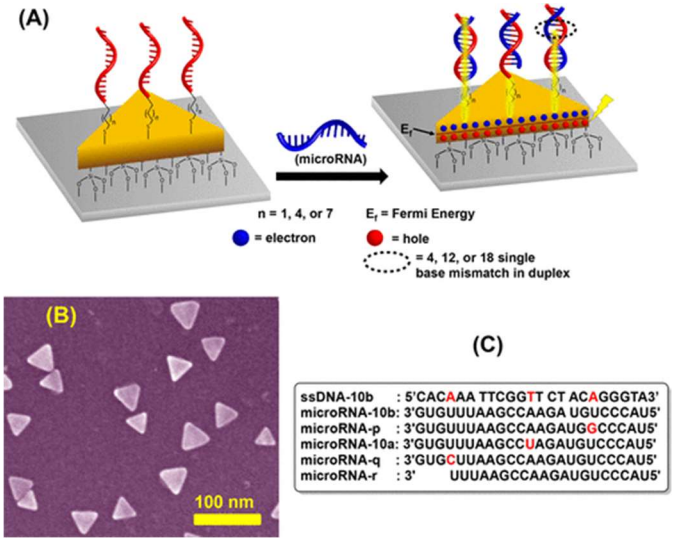

Figure 2.1. Detection of microRNA by surface plasmon resonance using triangular Au nanoparticles (see text) [22]

2.3 Electrochemical/Electronic methods

Electrochemical or electronic approaches for detection of NAs of specific sequence at ultralow concentration generally have been developed later than optical schemes and all within about the last 10 years, yet there is somewhat greater diversity of such technologies. Mass spectrometry (MS) clearly falls within this general category, although it may not be thought of

widely as a potentially inexpensive medical diagnostic technique. Advances in miniaturization suggest that perception may change [25, 26]. The work of Yang et al. serves to demonstrate one MS-based technique, based on a novel 'biomasscode' probe [27]. In yet another entirely different analytical approach demonstrating the diversity of electrochemical methods, a 1.6 aM DNA LOD was achieved using a piezoelectric plate sensor [28]. A response is evident in less than 10 min., however it is unclear how well the sensor will work with target in complex sample media. More recent reports of electrochemical or electronic methods are discussed below.

2.3.1 Constant potential amperometry

Perhaps the simplest electroanalytical technique is constant potential amperometry (CPA) where current is measured at a fixed potential. Spain et al. developed a CPA method with an estimated LOD of ~1 aM for detection of *Staphylococcus aureus* DNA based on usage of novel platinum nanoparticles (PtNPs) that have a portion of their surface area modified with an oligonucleotide capture probe and the remainder available for electrocatalyzed reduction of H_2O_2 for signal amplification (Figure 2.2) [29]. More recently an alternative, cata-lytic means to amplify a recognition event and to trans- duce it using CPA was demonstrated by Li et al. [30] using dual-thiolated, double-stranded hairpin DNA as capture probe immobilized on a gold electrode surface. Target recognition is amplified and transduced using streptavidin-labeled horseradish peroxidase (SA-HRP), and the LOD was estimated at 3 aM. This is a versatile approach that could be made more attractive if the relatively long assay time could be reduced significantly from ~1 hour.

2.3.2 Voltammetry

As a general class, voltametric techniques have been the most popular of electrochemical methods for detection of DNA and RNA at ultralow concentration. Of these volta- metric

approaches, cyclic voltammetry (CV) is the most widely known and among the most straightforward. In CV, potential at a working electrode is ramped linearly between reducing and oxidizing limits in a sawtooth wave, and the current is measured and plotted versus potential. For example, Kim et al. constructed a microfluidic-channel- based, electrochemical DNA biosensor that relies on CV as the detection method [31]. Square wave voltammetry (SWV) is a similar technique to CV in that potential is swept between potential limits while current is monitored. However, the potential is not swept linearly as in CV, rather the potential waveform may be regarded as a square wave superimposed onto an underlying staircase change in potential. Hu et al. employed electrochemically controlled reversible addition-fragmentation chain-transfer (eRAFT) polymerization to attach numerous electroactive ferrocenyl (Fc) tags that serve to amplify DNA capture events [32]. This is a promising quantitative method with a reported LOD of 4.1 aM that shows single-base selectivity. In differential pulse voltammetry (DPV), voltage pulses are superimposed on the background potential swept linearly or in stairstep mode. At least four publications have appeared describing the use of DPV to detect NAs at ultralow concentration [33–36]. In the most recent work, Widaningrum et al. constructed an electrochemical sensing strategy based on use of bio-barcode latex labels and detection of deposited Ag metal using DPV [34]. The technique is quantitative and an LOD of 560 zM was reported. EIS might be considered yet another related voltametric technique where a sinusoidal (AC) potential of varied frequency is imposed at the working electrode and the resulting current signal is monitored [37, 38, 39]. However, EIS is a relatively sophisticated technique with lengthy assay times (as with other voltammetric methods) that also could benefit from more testing with clinical samples.

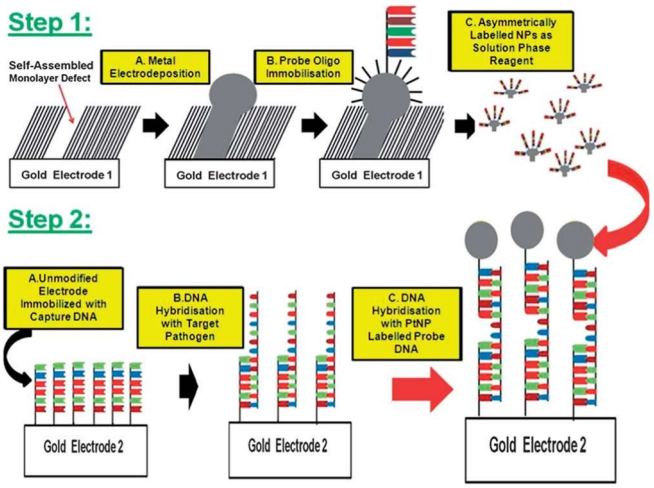

Figure 2.2. DNA detection by constant potential amperometry using Pt-labeled signal oligonucleotides and Pt-catalyzed, H_2O_2 electroreduction (see text) [29].

2.3.3 Field effect transistors (FETs)

The use of field effect transistors (FETs) as sensors constitutes an entirely different approach to electrochemical NA detection [40, 41]. A FET is a type of transistor where the electric field at a 'gate' controls the flow of current between 'source' and 'drain' electrodes. When configured as a sensor, the binding of an analyte at the gate results in a change in potential that gives rise to a measurable shift in the flow of current between the source and drain. Ramnani et al. demonstrated label-free and rapid detection of microRNA based on a carbon nanotube field-effect transistor (FET) functionalized with the Car-nation Italian ringspot virus (CIRV) p19 protein (Figure 2.3) [4]. The LOD was estimated at ~1 aM against a large background of nontarget RNA and quantitative detection in the range of 1 aM to 10 fM also was demonstrated. Although the total assay time is over 2 hours, this method is attractive for challenging, quantitative microRNA detection.

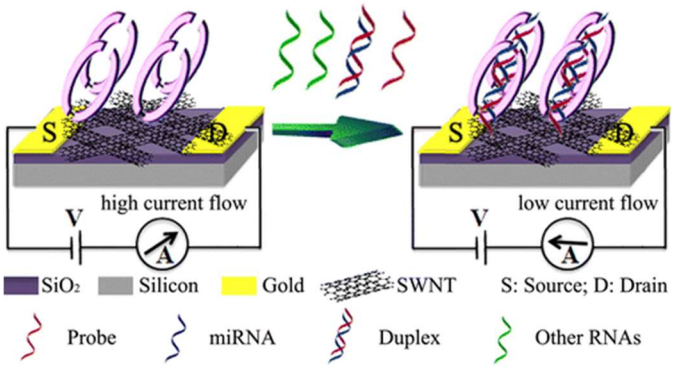

Figure 2.3. MicroRNA detection using carbon nanotube field effect transistors functionalized with the Carnation Italian ringspot virus p19 protein (see text)[41].

2.3.4 Nanopore sensors

Most nanopore-based NA sensing systems are based on a resistive-pulse sensing mechanism following on the work of Coulter [42], where the conductance of an electrolyte- filled pore or channel is monitored as analyte species traverse it. Rahman et al. pursued this general strategy while also taking advantage of optical trapping to enhance counting of target DNA species using nanopores [43]. The LOD was estimated at ~1 aM, and the DNA counting process is accomplished in just a few minutes, which is remarkable. However, the technique requires electronics capable of resolving millisecond-timescale, nA deflections in current. Rather than measure small, short-lived deflections in current as target species traverse a small diameter nanopore, the detection technique described by Koo et al. entails simple conductometric detection of much-larger-pore blockage events [44]. Uncharged PNA capture probes are conjugated to ~800-nm-diameter polystyrene beads that are designed to be very nearly charge neutral overall such that they do not exhibit electrophoretic movement in the presence of an electric field. However, the substantial negative charge acquired upon capture of a target NA sequence makes the hybridized conjugate mobile. Electrophoresis of the bead-PNA conjugate with hybridized target NA to the

mouth of a smaller diameter glass pore causes a significant decrease in pore conductance, thereby resulting in a strong, sustained drop in measured ionic current. *E. coli* rRNA was detected at 1 aM against a large background of *Pseudomonas putida* RNA. With a substantial decrease in overall assay time, this simple, potentially inexpensive, label-free technique may hold promise.

2.4 Conclusion and outlook

Commercially available nucleic acid (NA) amplification tests (NAATs) serve as the standard for both point-of-care (POC) and clinical laboratory-based disease diagnostics, yet the current assay time of ~15 min or more for the POC technology and the cost of these assays makes them nonideal. Mostly within the past 10 years, there has been a steady stream of reports describing NA amplification- free methods applicable to detection of pathogen-specific DNA or RNA at the most clinically desirable LODs of single-digit attomolar or lower. Such approaches hold promise for the development of faster, less expensive diagnostic systems. Without question, the emergence of nanotechnology has enabled conception of nearly all of the novel approaches with ultralow LODs published. However, very few of the methods described in this review have been tested sufficiently with clinical, or even mock clinical samples, that typically contain many species capable of interfering with an assay; and even fewer of the detection technologies have been integrated into complete diagnostic devices for which an overall assay time can be established. Lengthy reported hybridization times alone for many of these amplification-free schemes exceed the overall assay time for commercial POC NAATs, but there are published means to reduce hybridization steps to just a few minutes [45]. It should be expected that methods reliant on the fewest reagents and selective binding events as well as the simplest electrical or optical measurements such as constant potential amperometry, conductimetry, light scattering, and

fluorescence might have the greatest potential for eventual commercial success. Also, a number of developments have emerged in the recent literature that may eventually lead to additional schemes for ultralow, amplification-free NA detection including CRISPR technology [46, 47]. Based on the available evidence, it appears likely that during the next several years some new and exciting NA-based disease diagnostic technology will emerge commercially.

2.5 References

1. Atkinson LM, Vijeratnam D, Mani R, Patel R: *'The waiting game': are current chlamydia and gonorrhoea near-patient/point-of- care tests acceptable to service users and will they impact on treatment?* Int J STD AIDS 2016, 27:650-655.
2. Hsieh YH, Hogan MT, Barnes M, Jett-Goheen M, Huppert J, Rompalo AM, Gaydos CA, *Perceptions of an ideal point-of-care test for sexually transmitted infections--a qualitative study of focus group discussions with medical providers*. PLoS One, 2010. **5**:e14144.
3. Jayamohan H, Sant HJ, Gale BK, *Applications of microfluidics for molecular diagnostics*. Methods Mol. Biol (N. Y., NY, U. S.), 2013. **949**: p.305-334.
4. Cristillo AD, Bristow CC, Peeling R, Van Der Pol B, de Cortina SH, Dimov IK, Pai NP, Shin DJ, Chiu RYT, Klapperich C, et al., *Point-of-Care Sexually Transmitted Infection Diagnostics: Proceedings of the STAR Sexually Transmitted Infection-Clinical Trial Group Programmatic Meeting*. Sexually Transmitted Diseases, 2017. **44**: p. 211-218.
5. Lui C, Cady NC, Batt CA, *Nucleic Acid-based Detection of Bacterial Pathogens Using Integrated Microfluidic Platform Systems*. Sensors (Basel), 2009. **9**: p. 3713-3744.
6. Pan Y, Zhang D, Yang P, Poon LLM, Wang Q, *Viral load of SARS-CoV-2 in clinical samples.* The Lancet Infectious Diseases, 2020. **20**: p. 411-412.

7. Metsky HC, Freije CA, Kosoko-Thoroddsen T-SF, Sabeti PC, Myhrvold C, *CRISPR-based surveillance for COVID-19 using genomically-comprehensive machine learning design*. bioRxiv, 2020. p.1-11.

8. Wang M, Fu A, Hu B, Tong Y, Liu R, Gu J, Liu J, Jiang W, Shen G, Zhao W, et al., *Nanopore target sequencing for accurate and comprehensive detection of SARS-CoV-2 and other respiratory viruses*. medRxiv, 2020. p. 1-29.

9. Jung YJ, Park G-S, Moon JH, Ku K, Beak S-H, Kim S, Park EC, Park D, Lee J-H, Byeon CW, et al., *Comparative analysis of primer-probe sets for the laboratory confirmation of SARS-CoV-2*. bioRxiv, 2020. p. 1-13.

10. Lucia C, Federico P-B, Alejandra GC, *An ultrasensitive, rapid, and portable coronavirus SARS-CoV-2 sequence detection method based on CRISPR-Cas12*. bioRxiv, 2020. p. 1-10.

11. Jet T, Gines G, Rondelez Y, Taly V, *Advances in multiplexed techniques for the detection and quantification of microRNAs*. Chemical Society Reviews, 2021.

12. Ho HA, Dore K, Boissinot M, Bergeron MG, Tanguay RM, Boudreau D, Leclerc M, *Direct molecular detection of nucleic acids by fluorescence signal amplification.* Journal of the American Chemical Society, 2005. **127**: p. 12673-12676.

13. Najari A, Ho HA, Gravel J-F, Nobert P, Boudreau D, Leclerc M, **Reagentless** *Ultrasensitive Specific DNA Array Detection Based on Responsive Polymeric Biochips.* Analytical Chemistry, 2006. **78**: p. 7896-7899.

14. Nam JM, Stoeva SI, Mirkin CA, *Bio-bar-code-based DNA detection with PCR-like sensitivity*. Journal of the American Chemical Society, 2004. **126**: p. 5932-5933.

15. Taton TA, Mirkin CA, Letsinger RL, *Scanometric DNA Array Detection with Nanoparticle Probes*. Science, 2000. **289**: p. 1757.

16. Thaxton CS, Hill HD, Georganopoulou DG, Stoeva SI, Mirkin CA, A bio-bar-code assay based upon dithiothreitol-induced oligonucleotide release. Analytical Chemistry, 2005. **77**: p. 8174-8178.

17. Liu YJ, Yao DJ, Chang HY, Liu CM, Chen C, *Magnetic bead-based DNA detection with multi-layers quantum dots labeling for rapid detection of Escherichia coli O157:H7.* Biosensors & Bioelectronics, 2008. **24**: p. 558-565.

18. Kim GY, Son A, *Development and characterization of a magnetic bead-quantum dot nanoparticles based assay capable of Escherichia coli O157:H7 quantification*. Anal Chim Acta. 2010. **677**: p. 90-96.

19. Zhou J, Wang QX, Zhang CY, *Liposome-quantum dot complexes enable multiplexed detection of attomolar DNAs without target amplification.* J Am Chem Soc, 2013. **135**: p. 2056-2059.

20. D'Agata R, Breveglieri G, Zanoli LM, Borgatti M, Spoto G, Gambari R, *Direct detection of point mutations in nonamplified human genomic DNA*. Anal Chem, 2011. **83**: p. 8711-8717.

21. Hu J, Zheng PC, Jiang JH, Shen GL, Yu RQ, Liu GK, *Sub-attomolar HIV-1 DNA detection using surface-enhanced Raman spectroscopy*. Analyst, 2010. **135**: p. 1084-1089.

22. Liyanage T, Masterson AN, Oyem HH, Kaimakliotis H, Nguyen H, Sardar R, *Plasmoelectronic-Based Ultrasensitive Assay of Tumor Suppressor microRNAs Directly in Patient Plasma: Design of Highly Specific Early Cancer Diagnostic Technology*. Anal Chem, 2019. **91**: p. 1894-1903.

23. Li G, Zhu L, Wu Z, He Y, Tan H, Sun S, *Digital Concentration Readout of DNA by Absolute Quantification of Optically Countable Gold Nanorods*. Anal Chem, 2016. **88**: p. 10994-11000.

24. Contreras-Naranjo JC, Wei Q, Ozcan A, *Mobile Phone-Based Microscopy, Sensing, and Diagnostics*. *I*EEE Journal of Selected Topics in Quantum Electronics, 2016. **22**: p. 1-14.

25. Ma X, Ouyang Z, *Ambient ionization and miniature mass spectrometry system for chemical and biological analysis.* Trends Analyt Chem. 2016. **85**: p. 10-19.

26. Zhang W, Wang X, Xia Y, Ouyang Z, *Ambient Ionization and Miniature Mass Spectrometry Systems for Disease Diagnosis and Therapeutic Monitoring*. Theranostics, 2017. **7**: p. 2968-2981.

27. Yang B, Gu K, Sun X, Huang H, Ding Y, Wang F, Zhou G, Huang LL, *Simultaneous detection of attomolar pathogen DNAs by Bio-MassCode mass spectrometry*. Chem Commun (Camb), 2010. **46**: p. 8288-8290.

28. Wu W, Kirimli CE, Shih WH, Shih WY: *Real-time, in situ DNA hybridization detection with attomolar sensitivity without amplification using (pb(Mg1/3Nb2/3)O3)0.65-(PbTiO3)0.35 piezoelectric plate sensors.* Biosens Bioelectron 2013, **43**:391- 399 A piezoelectric plate sensor used to detect DNA at ultralow concentration.

29. Spain E, McArdle H, Keyes TE, Forster RJ, *Detection of sub-femtomolar DNA based on double potential electrodeposition of electrocatalytic platinum nanoparticles.* Analyst, 2013. **138**: p. 4340-4344.

30. Li C, Wu D, Hu X, Xiang Y, Shu Y, Li G, *One-Step Modification of Electrode Surface for Ultrasensitive and Highly Selective Detection of Nucleic Acids with Practical Applications.* Anal Chem, 2016. **88**: p. 7583-7590.

31. Kim YJ, Jones JE, Li H, Yampara-Iquise H, Zheng G, Carson CA, Cooperstock M, Sherman M, Yu Q, *Three-dimensional (3-D) microfluidic-channel-based DNA biosensor for ultra-sensitive electrochemical detection*. Journal of Electroanalytical Chemistry, 2013. **702**: p. 72-78.

32. Hu Q, Kong J, Han D, Niu L, Zhang X: *Electrochemical DNA biosensing via electrochemically controlled reversible addition-fragmentation chain transfer polymerization.* ACS Sens 2019, **4**:235-241.

33. Hu Q, Hu W, Kong J, Zhang X, *PNA-based DNA assay with attomolar detection limit based on polygalacturonic acid mediated in-situ deposition of metallic silver on a gold electrode.* Microchimica Acta, 2014. **182**: p. 427-434.

34. Widaningrum T, Widyastuti E, Pratiwi FW, Faidoh Fatimah AI, Rijiravanich P, Somasundrum M, Surareungchai W, *Sub-attomolar electrochemical measurement of DNA hybridization based on the detection of high coverage biobarcode latex labels at PNA-modified screen printed electrodes.* Talanta, 2017. **167**: p. 14-20.

35. Dong H, Zhu Z, Ju H, Yan F, *Triplex signal amplification for electrochemical DNA biosensing by coupling probe-gold nanoparticles-graphene modified electrode with enzyme functionalized carbon sphere as tracer.* Biosens Bioelectron, 2012. **33**: p. 228-232.

36. Gao W, Dong H, Lei J, Ji H, Ju H, *Signal amplification of streptavidin-horseradish peroxidase functionalized carbon nanotubes for amperometric detection of attomolar DNA*. Chem Commun (Camb), 2011. **47**: p. 5220-5222.

37. Benvidi A, Rajabzadeh N, Mazloum-Ardakani M, Heidari MM, Mulchandani A, *Simple and label-free electrochemical impedance Amelogenin gene hybridization biosensing based on reduced graphene oxide*, Biosens Bioelectron, 2014. **58**: p.145-152.

38. Sahoo P, Suresh S, Dhara S, Saini G, Rangarajan S, Tyagi AK, *Direct label free ultrasensitive impedimetric DNA biosensor using dendrimer functionalized GaN nanowires*. Biosens Bioelectron, 2013. **44**: p. 164-170.

39. Tripathy S, Krishna Vanjari SR, Singh V, Swaminathan S, Singh SG, *Electrospun manganese (III) oxide nanofiber based electrochemical DNA-nanobiosensor for zeptomolar detection of dengue consensus primer.* Biosens Bioelectron, 2017. **90**: p. 378-387.

40. Chen CP, Ganguly A, Lu CY, Chen TY, Kuo CC, Chen RS, Tu WH, Fischer WB, Chen KH, Chen LC, *Ultrasensitive in situ label-free DNA detection using a GaN nanowire-based extended-gate field-effect-transistor sensor*. Anal Chem, 2011. **83**: p. 1938-1943.

41. Ramnani P, Gao Y, Ozsoz M, Mulchandani A, *Electronic detection of microRNA at attomolar level with high specificity*. Anal Chem, 2013. **85**: p. 8061-8064.

42. DeBlois RW, Bean CP, *Counting and Sizing of Submicron Particles by the Resistive Pulse Technique*. Review of Scientific Instruments, 1970. **41**: p. 909-916.

43. Rahman M, Harrington M, Stott MA, Li Y, Sampad MJN, Yuzvinsky TD, Hawkins AR, Schmidt H, *Optical trapping assisted detection rate enhancement of single molecules on a nanopore optofluidic chip*. Optica, 2019. **6**.

44. Koo B, Yorita AM, Schmidt JJ, Monbouquette HG, *Amplification-free, sequence-specific 16S rRNA detection at 1 aM.* Lab Chip, 2018. **18**: p. 2291-2299.

45. Henry OYF, O'Sullivan CK, Rapid DNA hybridization in microfluidics. Trac-Trends in Analytical Chemistry, 2012. **33**: p. 9-22.

46. Gootenberg JS, Abudayyeh OO, Kellner MJ, Joung J, Collins JJ, Zhang F, *Multiplexed and portable nucleic acid detection platform with Cas13, Cas12a, and Csm6*. Science, 2018. **360**: p. 439.

47. Myhrvold C, Freije CA, Gootenberg JS, Abudayyeh OO, Metsky HC, Durbin AF, Kellner MJ, Tan AL, Paul LM, Parham LA, et al., Field-deployable viral diagnostics using CRISPR-Cas13. Science, 2018. **360**: p. 444.

Chapter 3: An Amplification-free, 16S rRNA Test for *Neisseria gonorrhoeae* in Urine

Chapter 3 is a manuscript published with the following citation:

Zheng, Z., Cao, Y., Chandrasekaran, S., Schmidt, J. J., Garner, O. B., & Monbouquette, H. G. (2023). An amplification-free, 16S rRNA test for Neisseria gonorrhoeae in urine. Sensors & Diagnostics.

ABSTRACT

An amplification-free, nanopore-based nucleic acid detection platform has been demonstrated for rapid, 16S rRNA sequence-specific detection of *Neisseria gonorrhoeae* at 10-100 CFU/mL in human urine against background bacterial flora at 1000 CFU/mL. Gonorrhea is a very common notifiable communicable disease, antibiotic resistant strains have emerged, and the rate of reported gonococcal infections continues to increase. Since rapid clinical identification of bacterial pathogens in clinical samples is needed to guide proper antibiotic treatment and to control disease spread, it is important to engineer rapid, sensitive, selective, and inexpensive point-of-care (POC) diagnostic devices for pathogens such as *N. gonorrhoeae*. Our detector technology is based on straightforward conductometric detection of sustained blockage of a glass nanopore. Charge neutral, complementary peptide nucleic acid probes are conjugated to polystyrene beads to capture *N. gonorrhoeae* 16S rRNA selectively. In the presence of an electric field applied externally through a glass nanopore, the PNA-microbead conjugates that acquire substantial negative charge upon target hybridization are driven to the smaller diameter nanopore. At least partial blockage of the nanopore results in a sustained drop in ionic current that can be measured easily with simple electronics. The ability to detect *N. gonorrhoeae* over the range of 10 to 100 CFU/mL spiked in human urine was demonstrated successfully with estimated sensitivity and specificity of ~98% and

~100%, respectively. No false positives were observed for the control group of representative background flora (*E. coli*, K. pneumoniae, and E. faecalis) at 1000 CFU/mL. Also, *N. gonorrhoeae* at 50 CFU/mL was successfully detected against 1000 CFU/mL of background flora in urine. These results suggest that this amplification-free technology may serve as the basis for rapid, inexpensive, low-power detection of pathogens in clinical samples at the POC.

3.1 Introduction

Gonorrhea is the second most common notifiable sexually transmitted infection in the US, and its prevalence has been increasing.[1] A total of 677,769 cases of gonorrhea were reported to the US Centers for Disease Control and Prevention (CDC) in 2020 out of an estimated 1.6M new infections that occur each year in the US.[1, 2] Since the historic low in 2009, reports of gonorrhea infection have increased 111%.[1] Alarmingly, strains of the gram-negative bacterium responsible for gonorrhea infections, *Neisseria gonorrhoeae*, have developed antibiotic resistance; and about half of all gonorrhea infections reported in 2020 were caused by an antibiotic resistant strain.[1] Only one recommended treatment remains: the cephalosporin, ceftriaxone.[2] Unfortunately, the infection often is asymptomatic in women, and if untreated, pelvic inflammatory disease leading to ectopic pregnancies and infertility can result.[3] Currently, the CDC recommends that all sexually active women under age 25, as well as sexually active gay or bisexual men, be tested each year.[3] In order to guide proper usage of antibiotics, to perform timely treatment, and to curtail disease spread, rapid, inexpensive point-of-care (POC) diagnostic tests are needed urgently.

The historical method for *N. gonorrhoeae* detection in a clinical sample has long entailed culturing; however, at least a day is required for results that must be generated by skilled technicians.[4] Microscopic examination of urethral smears also can be used to provide evidence of

infection, but the reliability of this diagnostic approach depends strongly on the quality of the specimen and the experience of the microscopist.[4] Currently, nucleic acid amplification tests (NAATs) are the preferred methods for gonorrhea diagnostic detection due to sensitivities >90% and very high specificities of ~99%.[5] However, most NAATs are conducted in the clinical laboratory where the turnaround time also is a day or longer, and these complex systems must be operated by trained personnel. POC NAATs have emerged on the market recently (i.e., Binx io, Visby Medical Sexual Health Test),[6, 7] but an external power source is required for these complex devices that entail nucleic acid (NA) isolation to high purity for removal of polymerase inhibitors; tight control of complex reaction steps involving expensive, perishable reagents (e.g., primers, polymerase, and nucleotides); optical or electrochemical means to detect amplicons; and assay times of ~15-30 minutes. An ideal NA-based POC diagnostic system would exhibit an assay time of ~5 minutes, would be battery powered and completely portable, would be inexpensive (~$20/test), and would provide competitive sensitivity and specificity of ≥95%.[8, 9]

The need for more optimal POC diagnostic tests has provided impetus for a number of studies focused on simpler, yet powerful, amplification-free, NA-based detection approaches. The "gold standard" limits of detection (LODs) of commercial clinical laboratory-based NAATs available for *N. gonorrhoeae* in urine in the ~1–100 CFU/mL range are reflective of clinical need and correspond to NA LODs at the single-digit aM (10-18 M) level.[10] Over the past 10 years or so, many reports, including ours, have appeared describing NA amplification-free systems exhibiting these very low LODs for NAs of specific sequence.[10, 11]

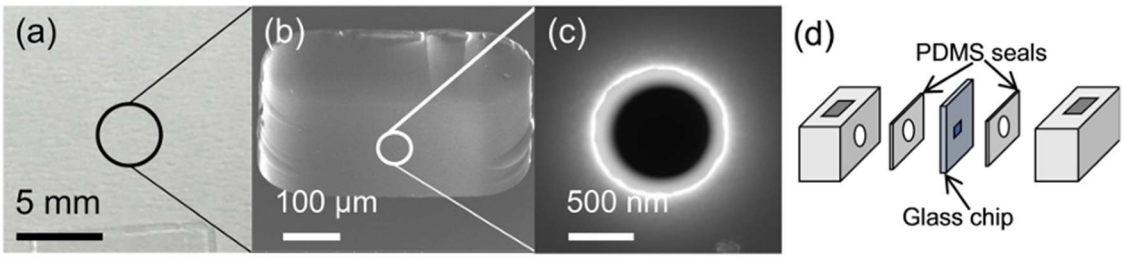

Figure 3.1. Glass chip detector assembly. (a) The 1 cm × 1 cm glass chip with ~1 µm-thick membrane and nanopore in the center. (b) Micrograph of the ~1 µm-thick membrane at the chip center. (c) Micrograph of the ~500 nm nanopore at the center of the glass membrane. (d) The glass chip sandwiched between PDMS seals and Teflon chambers (6 mm × 6 mm × 8 mm). The assembly was secured with four bolts (not shown). Figure 3.1(a)-(c) reproduced from Ref. 11 with permission from the Royal Society of Chemistry.

Our system utilized here relies on the use of peptide nucleic acid (PNA) capture probes.[12] PNA is an uncharged polyamide analog to DNA/RNA that we bind covalently to carboxylfunctionalized microbeads to form nearly charge neutral bead-probe conjugates. When the neutral PNA-microbead hybridizes target NA, it gains substantial negative charge thereby making it mobile in an electric field. If the negatively charged PNA-microbeads with hybridized target NA are directed to a glass nanopore of lesser diameter, they will at least partially block it, resulting in a sustained, easily measured drop in ionic current. In previous work, our group has successfully demonstrated the detection of *E. coli* rRNA at a concentration of 1 aM against a 10^6-fold background of *P. putida* RNA and *E. coli* at 10 CFU/mL against a 10^6-fold background of viable *P. putida*.[11] However, few NA amplification-free detection schemes, including ours, had been tested with clinical, or even mock clinical, specimens.[10]

3.2 Experimental

3.2.1 Materials

Carboxyl-functionalized, 820 nm-dia. polystyrene microspheres and Vivaspin® 2 mL ultrafiltration devices were purchased from Bangs Laboratories, Inc. (Fishers, IN). 1-Ethyl-3-(3-dimethylaminopropyl)carbodiimide hydrochloride (EDC) was obtained from ThermoFisher Scientific (Waltham, MA). 2-(NMorpholino) ethanesulfonic acid (MES), methoxypolyethylene glycol amine (mPEG-amine) and ethanolamine were purchased from Sigma-Aldrich (St. Louis, MO). Peptide nucleic acid (PNA) probes were synthesized by PNA Bio (Thousand Oaks, CA) and arrived as >95% HPLC-purified, lyophilized powders. *E. coli* (ATCC 25922), *P. putida* (ATCC 12633), spy broth and nutrient broth were purchased from American Type Culture Collection (Manassas, VA). Direct-zol RNA Miniprep kits and TRI Reagent were purchased from Zymo Research (Irvine, CA). Two mm-diameter, 4 mm-long Ag/AgCl pellet electrodes were purchased from A-M systems, Inc. (Carlsborg, WA). GE Healthcare Life Sciences Anotop 25 syringe filters (25 mmdiameter, 0.02 μm pore) were supplied by Genesee Scientific (San Diego, CA).

3.2.2 Methods

Detector assembly. Glass chips (1 cm × 1 cm) were micromachined from 4-in. borosilicate glass wafers (Plan Optik, Elsoff, Germany) as described earlier.[11] A ~0.25 mm^2, 1 μm-thick membrane was etched in the center of the chip and a ~500 nm nanopore was milled in the center of the membrane with a focused ion beam (FEI Nova 600 Nanolab DualBeam SEM/FIB). These glass chips were sandwiched between two, custom-machined Teflon chambers (each measuring 6 mm × 6 mm × 8 mm, 216 μL) with cast polydimethylsiloxane (PDMS) seals (Figure 3.1). A 4 mm-diameter hole drilled through the chamber walls facing the glass chip permitted buffer access

on either side of the chip. A Ag/AgCl pellet electrode was placed in each, buffer-filled chamber, and voltage was controlled and current monitored using a Versatile Multichannel Potentiostat (model VMP3) equipped with the 'p' low current option and N'Stat box driven by EC-LAB software (Bio-Logic USA, LLC, Knoxville, TN). This assembly constituted our detection system for target *N. gonorrhoeae* 16S rRNA hybridized to PNA probe conjugated to microspheres (see below).

Coupling PNA probe to microspheres. The complementary PNA probe sequence with PEG linker for detecting *N. gonorrhoeae* 16S rRNA consisted of NH_2-$(CH_2CH_2OCH_2CH_2OCH_2CO)_6$-TTG CCA ATA TCG GCG GCC.[13] In order to prepare microspheres to be conjugated with PNA, one μL of 820 nm-diameter carboxylic group-functionalized polystyrene microspheres, at a concentration of ~3.25 × 1011/mL, was suspended and washed three times in 100 mM MES buffer (pH 4.5). For each wash step, after centrifugation at 14,000 rpm for 15 minutes, the sedimented pellet microspheres were resuspended in fresh MES buffer. After the third wash, the microbeads were resuspended in 600 μL of MES buffer, and EDC (200 mM final concentration) was added to the suspension to serve as a crosslinker between the carboxyl groups on the polystyrene microbeads and the terminal primary amine groups appended on the PNA probes. This preparation was incubated for 15 minutes at 50 °C. Immediately afterward, 1.14 nmol of the PNA target probe was added followed by incubation for an additional two hours at 50 °C. Next, mPEG-amine was added to a final concentration of 100 mM followed by incubation for another hour at 50 °C. This latter conjugation step was added to inhibit microbead aggregation. Finally, ethanolamine was added to a final concentration of 138 mM and incubated for yet another hour at 50 °C. Ethanolamine was added to fully cap any remaining carboxyl groups, thereby ensuring that the PNA-conjugated microbeads were nearly charge neutral. After completion of

microbead surface modification, the beads were washed three times with 0.4 × SSC buffer (60 mM NaCl, 6 mM trisodium citrate, and 0.1% Triton X-100, pH 8). Each wash was conducted for 15 minutes at 14,000 rpm in microfuge tubes. One fourth of the final product was set aside for zeta potential measurements, while the rest of the PNA-beads were stored in hybridization buffer at room temperature (10 mM NaCl, 25 mM Tris-HCl, pH 7). The zeta potential was measured for modified microbeads suspended in the testing buffer (10 mM KCl, 5.5 mM HEPES, 0.01% Tween-80, pH 7) using a Malvern Zetasizer Nano ZS (Malvern Instruments Ltd, Worcestershire, England). A zeta potential in the negative single-digit mV range was taken as evidence of successful microbead surface modification.

RNA extraction. *N. gonorrhoeae* (ATCC 43069) frozen stock was subcultured onto chocolate agar. Agar plates were incubated at 35 °C with 5% CO2 for 16-18 hrs. The bacterium was cultured in ATCC 814 medium to a McFarland standard 0.5 corresponding to ~1.5 × 108 CFU/mL. The culture then was serially diluted in 0.85% saline to achieve the desired concentrations for spiking into sterilized pooled human urine (BioIVT, Westbury, NY). The background bacterial flora including *E. coli*, *K. pneumoniae*, and *E. faecalis* served as negative controls. The protocols for use of the Direct-zol RNA Miniprep kit and TRI Reagent (Zymo Research, Irvine, CA) were followed for total RNA extraction and purification. Each extraction began with 1 mL of human urine previously spiked with 10-100 CFU/mL of *N. gonorrhoeae*, 1000 CFU/mL of background flora, or 10-100 CFU/mL of *N. gonorrhoeae* and 1000 CFU/mL of background flora. Extracted total RNA was eluted into 100 µL of RNase-free purified water and used within ~1-2 hours.

Hybridization of RNA to PNA-bead conjugates. Hybridization was accomplished in Vivaspin® 2 mL ultrafiltration devices with 0.02-µm-diameter membranes. Bead-PNA conjugates in 600 µL

hybridization buffer (see above) were transferred to Vivaspin® devices and spun at 1000 rpm for 5 minutes to form a compact bed of the conjugates on the membrane surface. Subsequently, extracted RNA from *N. gonorrhoeae* spiked in human urine was added to the loaded Vivaspin® device and spun at 1000 rpm for 5 minutes to facilitate intimate contact and hybridization of target 16S rRNA with the previously deposited bead-PNA conjugates. Finally, after two rounds of washes with hybridization buffer in the Vivaspin®, hybridized beads were collected in hybridization buffer by reverse spinning the loaded Vivaspin® devices.

Sample detection. Prior to the injection of a sample, the initial current in the absence of beads and sample was measured to verify the integrity of the glass chips. Depending on the exact nanopore size, clean glass chips had typical initial currents of 35 nA to 100 nA. After undergoing the hybridization procedure, bead-PNA conjugates potentially bound with target *N. gonorrhoeae* 16S rRNA were injected into the detector chamber contacting the smooth backside (opposite the etched well) of the glass chip. After bead sample addition, a potential of 1.5 V was imposed, and the current was monitored for a sustained, ionic current drop that would signal detection of target 16S rRNA. After each detection signal (indicated by sustained ionic current drop of ~50 s) was observed, the polarity of the electronic field was reversed to -1.5 V to attempt to unblock the pore. After ~1 min of reversed polarity, the field was flipped back to 1.5 V to confirm baseline current recovery and detection signal reproducibility.

3.3 Results and discussion

Forty-four samples of *N. gonorrhoeae* spiked in human urine over the 10-100 CFU/mL concentration range (14 at 10 CFU/mL, 10 each at 50 and 100 CFU/mL, and 10 at 50 CFU/mL against representative bacterial flora at 1000 CFU/mL) were processed and tested as described

above. The bacterial flora control representative of microbes frequently present in human urine included *E. coli*, *K. pneumoniae*, and *E. faecalis*. Out of these 44 trials, only one false negative was observed at 50 CFU/mL. No positive detection results were recorded for any of 10 samples of the background flora alone at a concentration of 1000 CFU/mL in human urine, which served as a negative control. Sample data showing easily recognized, reproducible detection events as well as the lack of response to the negative control is presented as Figure 3.2, and the complete results are summarized in Table 3.1.

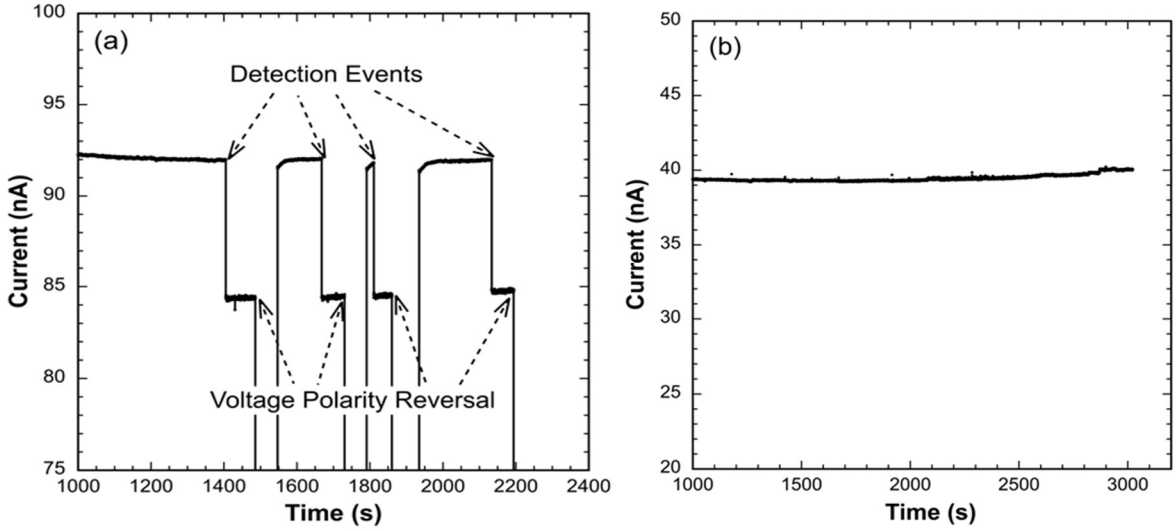

Figure 3.2. Detector current response to the presence of target *N. gonorrhoeae* 16S rRNA and the lack of response to RNA extracted from background bacterial flora alone. (a) Reproducible, sustained current signal step reductions in response to the presence of PNA-beads with hybridized target 16S rRNA extracted from *N. gonorrhoeae* at 10 CFU/mL in human urine. The applied voltage for detection events was 1.5 V. After a sustained current signal of ~50 s, the voltage polarity was reversed temporarily to -1.5 V to drive bead complexes away from the pore before demonstrating signal reversibility by reimposing a potential of 1.5 V. (b) No current signal in response to the presence of PNA-beads hybridized with RNA extracted from background bacterial flora spiked at 1000 CFU/mL in human urine (negative control).

Table 3.1. Summary of *N. gonorrhoeae* (NG) detection data over a concentration range of 10-100 CFU/mL in human urine

Sample	Agreement with expected result*
10 CFU NG/mL	14/14
50 CFU NG/mL	9/10
100 CFU NG/mL	10/10
50 CFU NG/mL & 1000 CFU flora**/mL	10/10
1000 CFU flora**/mL	10/10
Total agreement	53/54 (98.1%)

*(number of expected test results) / (number of tests)
**Background bacterial flora: *E. coli*, *K. pneumoniae*, and *E. faecalis*

The data presented in Table 3.1 provide the basis for preliminary estimates of sensitivity and specificity of 98% (95% CI: 88%-100%) and 100% (95% CI: 69%-100%), respectively, for detection of *N. gonorrhoeae* over the range of 10 to 100 CFU/mL when spiked in sterile, pooled human urine. Note that the first detection event for true positive cases, indicated by the first sustained ionic current drop, occurred from 500 seconds to 1500 seconds. The variation in time to signal arises from the random initial distance of beads with hybridized target from the glass chip in the detector assembly (Figure 3.1d). Absence of ionic current drop for over 3000 seconds constituted negative detection (likely an extreme waiting period based on many test runs), and only one false negative was observed at 50 CFU/mL. Since 50 CFU/mL is well above the detection limit of our device, we suspect that RNA instability may have played a role since samples were

lysed at the off-campus clinical laboratory and subsequently transported on campus for testing. Nevertheless, the preliminary sensitivity and specificity data presented here compare very well to the currently preferred NAATs, both those that are lab-based and those that are designed for the POC.[6, 7]

As an amplification-free test, this technology is considerably less complex than NAATs and avoids the need for perishable reagents (i.e., polymerase, primers, nucleotides). The current lab-based version of our amplification-free test with the glass nanopore detector requires ~10 minutes for RNA extraction, ~10 minutes for hybridization, and ~15 minutes for sample detection, which makes it competitive in overall assay time with many fully automated NAATs. However, the detection chamber in a microfluidic device under development is reduced ~10 × in characteristic dimension thereby reducing the transit time of bead-PNA conjugates with hybridized target to the glass nanopore detector. In the near future, we anticipate reporting on the time savings achieved with our glass chip detectors integrated into a microfluidic system.

3.4 Conclusions

A novel amplification-free rRNA test based on a nanopore glass detector was used successfully to assay for *N. gonorrhoeae* spiked in human urine with high sensitivity (~98%) and specificity (~100%). *N. gonorrhoeae* was detected successfully over the 10-100 CFU/mL range and against background bacterial flora at 1000 CFU/mL. These results suggest that this potentially rapid and inexpensive technology may one day prove advantageous for POC use. Indeed, with further improvement in overall assay time and integration of the glass nanopore detector with automated frontend sample processing, this simple, amplification-free detection technology may

lead to rapid, inexpensive, low-power and portable POC pathogen detection devices with minimal reagent requirements.

3.5 References

1. CDC, Sexually Transmitted Disease Surveillance 2020, https://www.cdc.gov/std/statistics/2020/overview.htm# Gonorrhea, (accessed July 19, 2022).
2. K. Schlanger and R. D. Kirkcaldy, Sex Transm Dis, 2021, 48, S91-S92.
3. CDC, Gonorrhea—CDC Detailed Fact Sheet, https://www.cdc.gov/std/gonorrhea/stdfact-gonorrheadetailed.htm, (accessed July 19, 2022).
4. L.-K. Ng and I. E. Martin, Canadian Journal of Infectious Diseases and Medical Microbiology, 2005, 16, 323082.
5. J. R. Papp, J. Schachter, C. A. Gaydos and B. Van Der Pol, Morbidity and Mortality Weekly Report, 2014, 63, 1-19.
6. S. R. Morris, C. C. Bristow, M. R. Wierzbicki, M. Sarno, L. Asbel, A. French, C. A. Gaydos, L. Hazan, L. Mena, P. Madhivanan, S. Philip, S. Schwartz, C. Brown, D. Styers, T. Waymer and J. D. Klausner, The Lancet Infectious Diseases, 2021, 21, 668-676.
7. B. Van Der Pol, S. N. Taylor, L. Mena, J. Lebed, C. J. McNeil, L. Crane, A. Ermel, A. Sukhija-Cohen and C. A. Gaydos, JAMA Netw Open, 2020, 3, e204819.
8. C. A. Gaydos, Y. C. Manabe and J. H. Melendez, Sex Transm Dis, 2021, 48, S71-S77.
9. L. M. Atkinson, D. Vijeratnam, R. Mani and R. Patel, Int J STD AIDS, 2016, 27, 650-655.
10. Y. Cao, Z. Zheng and H. G. Monbouquette, Curr Opin Biotechnol, 2021, 71, 145-150.
11. B. Koo, A. M. Yorita, J. J. Schmidt and H. G. Monbouquette, Lab Chip, 2018, 18, 2291-2299.

12. P. E. Nielsen, M. Egholm, R. H. Berg and O. Buchardt, Science, 1991, 254, 1497-1500.

13. L. Chui, T. Chiu, J. Kakulphimp and G. J. Tyrrell, Clin. Microbiol. Infect., 2008, 14, 473-479.

Chapter 4: Amplification-free Detection of 16S rRNA Using a Glass Chip Detector Integrated into the Lateral Flow Assay Format

ABSTRACT

A nucleic acid amplification-free platform integrated into the lateral flow assay (LFA) format has been demonstrated for rapid detection of 10 attomolar (aM) *Escherichia coli* 16S rRNA in 5 minutes total assay time. Rapid, inexpensive and user-friendly identification of bacterial pathogens in readily available clinical samples are in demand to enable point-of-care (POC) diagnosis and immediate administration of appropriate therapies, especially in regions with limited laboratory resources. Lateral flow assays (LFA), with metrics including low cost, ease of distribution and capillary force-driven sample flow, are ideal for POC usage and high frequency diagnostics. In order to address POC requirements better, an NA detection method integrated into the LFA format has been developed. The single-use component of the system is composed of a glass chip-based nanopore detector integrated with a lateral flow membrane strip, which is preloaded with polystyrene microbeads conjugated with peptide nucleic acid (PNA) probe complementary to the target pathogen 16S rRNA. A 100 μL lysed and filtered sample deposited on the test strip quickly flows along the LFA membrane due to capillary action, and target rRNA hybridizes with the complementary PNA probes conjugated to the preloaded microbeads. Driven by an externally applied electronic field, the PNA-microbeads with the negative charge added by the hybridized rRNA are directed to the smaller nanopore in the integrated glass chip and at least partially block it resulting in a sustained drop in ionic current. This easily measured, step change in current constitutes the signal indicating the presence of target nucleic acid. With this system, the detection of 10 aM *E. coli* 16S rRNA against 10 fM *P. putida* 16S rRNA has been successfully demonstrated. Finally, our LFA device readily detected *E. coli* at 10 CFU/mL against a one-

million-fold background of viable *P. putida*. With further improvements in sensitivity and reliability, this simple, rapid, and inexpensive amplification-free technology may be promising for widespread diagnostic usage in defense of public health.

4.1 Introduction

The urgent demand for low cost and sensitive nucleic acid (NA) tests that can meet the requirements for point-of-care (POC) usage was once again revealed by the COVID-19 pandemic and the public health issues that emerged during this global healthcare crisis. Persistent efforts have been made to pursue unique NA sequence identification technologies with rapid and comprehensive operating procedures to result in diagnostic devices for extensive utilization. [1] In the standard clinical laboratory environment, traditional culturing methods and nucleic acid amplification tests (NAATs) are the "gold standard", high sensitivity diagnostic methods for most infectious diseases; but both have turnaround times of a day or more, and proper patient treatment is therefore dependent on undependable follow-up visits. [2] Previous observations have indicated that a significant portion of patients will not wait in a clinic for more than 20 minutes for a test result, and the suggested turnaround time for POC testing should be ≤15 minutes. [3] To date, several NAATs have been developed for POC applications. [4] These PCR-dependent POC NAATs are highly sensitive and specific compared to traditional POC immunoassays, but the NA amplification step requires precise reaction control, expensive reagents such as primers and polymerases, and added time and expense. The overall assay time for most POC NAATs is ~30 minutes which is non-ideal. [5, 6] As a result, numerous efforts have been made to develop amplification-free NA detection methods with single-digit attomolar (10^{-18} M) detection limits to be competitive with NAATs. Optical methods are common among these amplification-free

methods with utilization of nanoparticles, such as gold nanoparticles, functionalized magnetic beads or quantum dot fluorescence, as the key element to transduce a selective hybridization event into an optical signal. [7, 8] Yet more evidence needs to be provided with clinical samples. Further, the requirement for advanced optical components, for example to analyze the quantum dot fluorescence increases complexity and cost. Electrochemical approaches, such as constant potential amperometry (CPA), cyclic voltammetry (CV) and field effect transistors (FETs), also provide ultralow concentration detection by transducing the hybridization event into an electric signal, yet additional labels and/or lengthy assay times are currently required for many of the schemes. [9-11]

Our group has developed a simple detection platform that does not involve NA amplification or additional labels. In our system, we utilize peptide nucleic acid (PNA), an uncharged polyamide analog to DNA/RNA, as a probe for sequence-specific detection of the unique 16S rRNA of target bacterial pathogens. [12] With PNA covalently bound to carboxyl-functionalized polystyrene microbeads, nearly charge neutral bead-probe conjugates created. When charge neutral PNA-microbeads hybridize target rRNA, substantial negative charge is acquired resulting in mobility in an electric field, which directs the PNA-microbead complex to a glass nanopore of smaller diameter. The presence of target rRNA is signaled by a sustained drop in ionic current generated by partial blockage of the nanopore with the PNA microbead complex with hybridized rRNA. In previous work, our group successfully demonstrated the detection of 16S rRNA of *E. coli* at a concentration of 100 zM and 50 CFU/mL of *N. gonorrhoeae* against a 1000 CFU/mL background of bacterial flora. However, an average one-hour detection time was reported from sample to result due to the macroscopic size of the experimental setup and the need for an external hybridization step. The lateral flow assay (LFA) format enables an inexpensive,

robust and user-friendly strategy with attractive characteristics such as capillary force-driven sample flow that avoids usage of complex microfluidic channels with pumps and valves. [13, 14] This technology has proven highly favorable and is the basis for the immunoassay-based pregnancy test strips. [15-17] In this article, we present a manageable approach for integrating our nanopore detector into inexpensive handheld POC devices. With the integration of our nanopore detection technology, the historical lack of sensitivity pitfall of the LFA immunoassay systems can be remedied with further potential advantages of affordability and simplified operation. The hybridization step is integrated by pre-depositing the PNA-beads downstream of the sample loading area in the LFA test strip. The glass nanopore-detector is integrated with the dry LFA strip. The total assay time, including sample lysis and filtration prior to loading on the LFA test strip is within 15 minutes with a limit of detection of 10 aM 16S rRNA.

4.2 Method and Materials

4.2.1 Reagents

Carboxyl-functionalized, 1 μm-dia. polystyrene microspheres were purchased from Bangs Laboratories, Inc. (Fishers, IN). (1-Ethyl-3-(3-dimethylaminopropyl) carbodiimide hydrochloride) (EDC) was obtained from ThermoFisher Scientific (Waltham, MA). 2-(N-Morpholino)ethanesulfonic acid (MES), methoxypolyethylene glycol amine (mPEG-amine), ethanolamine and 0.0025 mm-thick platinum foil were purchased from Sigma-Aldrich (St. Louis, MO). Peptide nucleic acid (PNA) probes were synthesized by PNA Bio (Thousand Oaks, CA) and arrived as >95% HPLC-purified, lyophilized powders. *E. coli* (ATCC 25922), *P. putida* (ATCC 12633), soy broth and nutrient broth were purchased from American Type Culture Collection (Manassas, VA). Direct-zol RNA miniprep kits were purchased from ZYMO Research

(Irvine, CA). Ag/AgCl pellet electrodes of 2 mm dia. were purchased from A-M systems, Inc. (Carlsborg, WA). GE Healthcare Life Sciences Anotop 25 syringe filters (25 mm-diameter, 0.02 μm pore) were supplied by Genesee Scientific (San Diego, CA). Fusion 5 membrane material and backing cards were purchased from Cytiva (Marlborough, MA).

4.2.2 Coupling PNA probe to microspheres

The target PNA probe for detecting *E. coli* 16S rRNA was NH_2-$(CH_2CH_2OCH_2CH_2OCH_2CO)_6$- CTC CTT CCC TCA TTT CA. [18] To prepare microspheres to be conjugated with PNA, 1 μL of 1 μm-diameter carboxylic group-functionalized polystyrene microspheres, at a stock concentration of 1.58×10^{11}/mL were suspended and washed three times in MES buffer (100 mM 2-(N-morpholino) ethanesulfonic acid, pH 4.5). For each wash step, after centrifugation at 14,000 rpm for 15 minutes, the sedimented pellet microspheres were resuspended in fresh MES buffer. After the third wash, the beads were resuspended in 600 μL MES buffer, and EDC (200mM final concentration) was added to the suspension to serve as a crosslinker between the carboxyl groups on the polystyrene microbeads and the terminal primary amine groups on the PNA probes. This preparation was incubated at 50 °C for 15 minutes. Next, 1.14 nmol of the PNA target probe was added followed by incubation for two hours at 50 °C, which resulted in a surface density of PNA probes of $10^{14}/cm^2$. [12] To inhibit bead aggregation, mPEG-amine was added to a final concentration of 100 mM and incubated at 50 °C for one hour. Finally, ethanolamine was added to a final concentration of 138 mM and incubated at 50 °C for another hour. Ethanolamine was added to fully cap any remaining carboxyl groups, ensuring the PNA conjugated beads are near charge neutral. After surface modification of the polystyrene microbeads, the beads were washed three times in 0.4 × SSC solution (60 mM NaCl, 6 mM trisodium citrate, and 0.1% Tween-20, pH 8). Each wash was done at 14,000 rpm for 15 minutes. One fourth of the final product was

taken for zeta potential measurement, and the rest of the beads were stored in the hybridization buffer at room temperature (10 mM NaCl, 25 mM Tris-HCl, and 0.1% Tween-20, pH 7). The zeta potential was measured with microbeads suspended in the hybridization buffer with a Malvern Zetasizer Nano ZS (Malvern Instruments Ltd, Worcestershire, England). A zeta potential in the negative single-digit mV range was taken as evidence of successful microbead surface modification.

4.2.3 Cell culturing and counting

E. coli ATCC 25922 was cultured in tryptic soy broth, and *P. putida* ATCC 12633 was cultured in ATCC nutrient broth. Both lysogeny broth (LB) and nutrient broth were sterilized at 120 °C for 20 minutes prior to use. To initiate the bacterial culture of *E. coli* and *P. putida*, lyophilized preparations were mixed into LB broth and nutrient broth, respectively, followed by incubation for two days. *E. coli* was cultured at 37 °C and 250 rpm, and *P. putida* was cultured at room temperature and 250 rpm. Aliquots of both cultures were stored at -80 °C to serve as inoculum for future cultures. To prepare a sample for RNA extraction (see below), a small portion of frozen *E. coli* and *P. putida* were taken and mixed into 3 mL of LB broth and nutrient broth, respectively. Both *E. coli* and *P. putida* were incubated overnight under the same conditions described above. Cultured bacterial cells were then serially diluted, plated and incubated overnight for colony counting.

4.2.4 RNA extraction

For the experiments to determine the limit of detection (LOD), total RNA from both *E. coli* and *P. putida* cultures were extracted separately. Prior to the extraction, 1 mL of bacterial culture was pelleted out by centrifugation. Next, 1 mL of TRI Reagent was added followed by an

incubation of 5 minutes. Cell lysate including TRI reagent was transferred into a Zymo-Spin™ IIICG Column for purification, and the final RNA product was eluted into 100 µL of RNase-free purified water and used within ~1-2 hours. The concentration of the total extracted RNA was measured using a Thermo Scientific Nanodrop 2000. An A260/A280 ratio above 1.8 suggested highly purified RNA. According to previous measurements, approximately 18.2% of the total RNA is 16S rRNA for *E. coli* and 25.7% of the total RNA is 16S rRNA for *P. putida*. [19] The estimated concentration varied from ~50 nM to ~200 nM for both cultures in different trials. To verify the detection of viable cells, 10 CFU/mL of *E. coli* was mixed with 10^6 CFU/mL of *P. putida* prior to the total RNA extraction. Next, 1 mL of the bacterial mixture was collected into 3 mL of TRI reagent followed by the same procedure described above. The concentration of viable cells was determined by serial dilution and colony counts on agar plates.

4.2.5 Lateral flow assay system assembly and sample detection

Glass chips (shown in Figure 4.1) were previously microfabricated from 4-in. borosilicate glass wafers. After a ~0.25 mm^2 1 µm-thick membrane was etched in the center of the chip with hydrofluoric acid, a ~500 nm pore was then bored in the center of the membrane with a focused ion beam (FEI Nova 600 Nanolab DualBeam SEM/FIB). [12] The LFA detection system is illustrated in Figure 4.2. First, a platinum foil electrode soldered with silicon wire was placed in the center of the backing card, and two pieces of Fusion 5 membrane (15 mm in length, 3 mm in width, and 0.37 mm in thickness) were placed on either side of the platinum electrode, leaving a gap of ~1 mm between them. Two PDMS strips of about the same thickness as the Fusion 5 membrane were aligned parallel with the membrane on the backing card to prevent leakage. Since the Fusion 5 membrane has a large pore size such that PNA-beads can move through it, PNA-beads were preloaded on the Fusion 5 membrane just upstream of the gap. [20] One thinner PDMS

O-ring (~100 μm in thickness) was attached to the smooth backside (opposite to the etched well) of the glass chip to protect the nanopore, and another thicker PDMS O-ring (~500 μm in thickness) was attached to the other side of the glass chip to serve as a reservoir for the top electrode. The glass chip with the smooth backside face down was then placed on top of the membrane assembly with the nanopore positioned directly above the gap. One Ag/AgCl pellet electrode was placed in the PDMS reservoir on the top side of the chip in a droplet of hybridization buffer (10 mM NaCl, 25 mM Tris-HCl, pH 7). Both electrodes were connected to a multichannel potentiostat. After setting up the LFA system, we first deposited 10 μL of extracted RNA sample near the previously deposited PNA beads and allowed the hybridization to occur. After 3 minutes of hybridization, 100 μL of extracted RNA sample was injected at the origin of upstream Fusion 5 membrane. As the RNA sample flowed over the PNA-beads by capillary action, the hybridized PNA beads were swept slowly into the gap below the glass chip and therefore entered the nanopore proximity. A voltage of 1.5 V was applied across the nanopore, and the current over time was recorded. Immediately after the first detection signal (indicated by ≥10 seconds of sustained ionic current drop) was observed, the polarity of the electronic field was reversed to -1.5 V to attempt to unblock the pore. After ~20 seconds of reversed polarity, the field was flipped back to 1.5 V to confirm baseline current recovery and detection signal reproducibility.

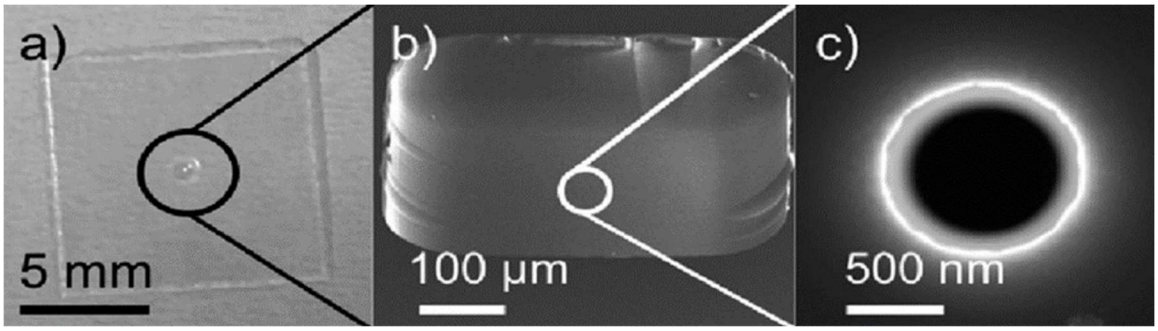

Figure 4.1. a) A microfabricated 1 cm × 1 cm glass chip. b) SEM image of ~0.25 mm^2, 1 µm-thick membrane in the center of glass chip created by wet etching. c) SEM image of ~500 nm diameter nanopore milled in the center of the etched membrane using a focused ion beam (FIB).[12]

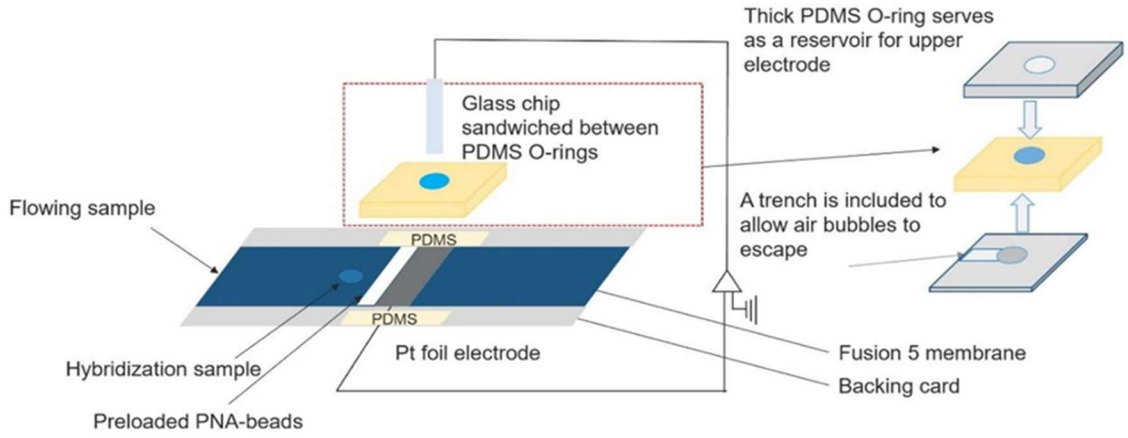

Figure 4.2. Schematic diagram of the lateral flow assay with integrated nanopore detector. Not to scale.

4.3 Results and Discussion

The experimental results obtained with our LFA format nanopore detector are summarized in Tables 4.1-4.2 and Figure 4.3. By hybridizing *E. coli* PNA-beads with target *E. coli* 16S rRNA, we successfully demonstrated rapid detection with rRNA samples ranging from 10 fM to 10 aM. Negative controls were performed by hybridizing *E. coli* PNA-beads with *P. putida* RNA, and no

false positives were observed during 1000 seconds (>15 mins) of observation. This indicated that the limit of detection (LOD) of the LFA detector is ~10 aM. In a more realistic simulation of pathogen rRNA detection, we conducted tests with samples generated by mixing *E. coli* RNA with a 1000-fold greater amount of *P. putida* RNA and compared these results with a control consisting of 1000-fold greater amount of *P. putida* RNA only. The results also confirmed rapid detection at 10 aM with no false negatives, which indicated that our LFA format nanopore detector can selectively detect target RNA against a higher concentration of off-target RNA.

Our LFA format nanopore detector also achieved great success in total assay time. By preloading and drying the PNA-beads in concentrated form on the lateral flow chip, a compact-bed structure was formed that enabled better interfacial contact between the PNA-beads and target rRNA as the sampled flowed over it. This arrangement assured better hybridization efficiency and avoided the time-consuming external sampling and centrifuging steps. This LFA process provided the added benefit of filtering out small, charged dust particles by the porous Fusion 5 LFA membrane. However, after the electric field is applied excess ions from the dried buffer in which the PNA-beads were suspended accumulate in the proximity of the nanopore and cause an initial current drift. In addition to increased hybridization efficiency, the detection time was shortened by reducing the travel distance from the PNA-bead deposition area on the LFA membrane to the nanopore. The first detection event, indicated by a sustained ionic current drop, occurred in ~100 seconds in most cases. One additional reversibility check was done by temporarily reversing the voltage polarity, which drove the PNA-beads with hybridized target RNA away from the pore. The detection signal was subsequently confirmed by resumption of the baseline operating voltage. Note that the reversibility check in some cases took a few hundred seconds to complete, and we hypothesize that PNA-beads with hybridized target RNA were swept into the downstream Fusion

5 membrane by the ongoing sample flow after reversing the voltage polarity, which inhibited movement of the hybridized PNA-beads conjugates back to proximity with the nanopore. This issue could be addressed by possibly decreasing the pore size of the downstream membrane, decreasing the reversed voltage time period and/or increasing the voltage. Including the three minutes of hybridization time, the total assay time for our LFA format detector is anywhere from 5 to 15 minutes, which is remarkable for this easily assembled POC prototype that does not rely on NA amplification.

Similar to previous work, transient drops in ionic current were observed in some tests, and we hypothesized this is due to the approach of PNA-beads with nonspecifically bound, negatively charged species to the nanopore where the weakly bound species were removed in the strong electric field and the PNA-beads subsequently were swept away by the opposing electroosmotic flow. [19, 12, 21, 22] At around neutral pH, silanol groups on the glass surfaces deprotonate giving rise to a layer of fixed negative charges. Cationic counterions form a second layer of mobile positive charges. The movement of these hydrated cations toward the cathode results in an electroosmotic flow that exerts a drag force on beads opposite in direction to the electrophoretic force. This active mechanism to avert false positives is a unique aspect of our nanopore detection system.

To better illustrate the potential clinical applicability of our LFA format detector, tests with 10 CFU/mL of *E. coli* against 10^6 CFU/mL of *P. putida* were also performed. The concentration of 10 CFU/mL was chosen to represent a clinically relevant low concentration and to ensure with high probability that at least one viable cell existed for the milliliter of sample processed. The results agreed with the tests conducted with extracted RNA. It was notable that our current LOD of 10 attomole was 10 times higher than our previous record with the Teflon chambers setup.[12]

Based on our observations, a portion of the beads dried on the Fusion 5 membrane were retained after flow through of sample. As the sample concentration decreased, less PNA-beads were bound to target RNA, and therefore the bead retention issue became a more significant factor affecting LOD. Since a viable bacterial cell typically contains ≥10,000 copies of 16S rRNA, 10 attomoles of 16S rRNA corresponds to less than 10 CFU/mL. [18, 23] Therefore, successful detection of 10 aM 16S RNA is still competitive in clinically relevant POC applications. In future work, we anticipate resolving the beads retention issue by freeze-drying the PNA-beads in the gap between the two Fusion 5 membranes.

Table 4.1. Summary of results where *E. coli* PNA-beads were hybridized separately with *E. coli* RNA (target) and *P. putida* RNA (negative control)

Target *E. coli*			Control *P. putida*		
Concentration		Drop/reversibility	Concentration		Drop/reversibility
10 fM	1	Yes/R	10 fM	1	No
	2	Yes/R		2	No**
	3	Yes/R		3	No
100 aM	1	Yes/R*			
	2	Yes/R			
	3	Yes/R			
10 aM	1	Yes/R*			
	2	Yes/R			
	3	Yes/R			

Yes/R* Reversibility check took approximately 100 - 300 seconds more than typical.
No** Transient drop was observed.

Table 4.2. Summary of results where *E. coli* PNA-beads were hybridized with mixed *E. coli* and *P. putida* RNA; and where *E. coli* PNA-beads were hybridized with RNA extracted from mixtures of cultures of *E. coli* and *P. putida.*

10 aM *E. coli* + 10 fM *P. putida*	10 CFU/mL *E. coli* + 10^6 CFU/mL *P. putida*

	Drop/reversibility		Drop/reversibility
1	Yes/R	1	Yes/R
2	Yes/R	2	Yes/R*
3	Yes/R*	3	Yes/R

Yes/R* Reversibility check took approximately 100 - 200 second more than typical.

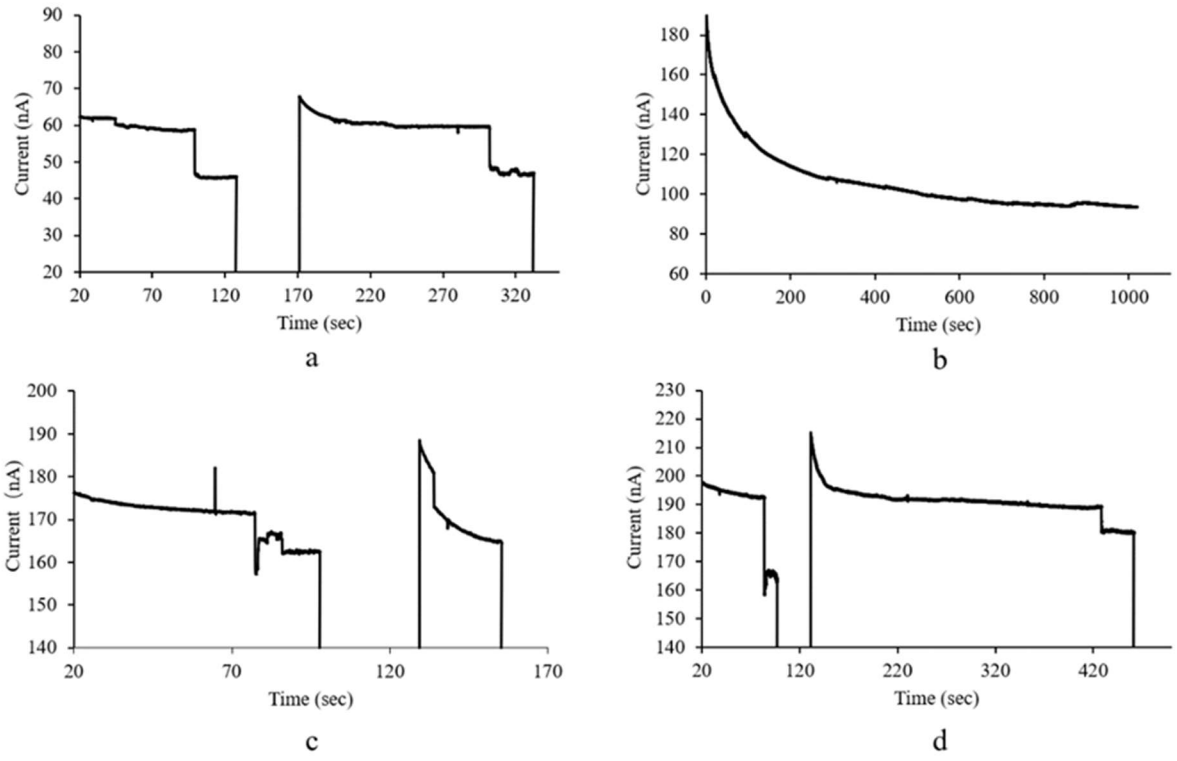

Figure 4.3. PNA-bead tests with the LFA format nanopore detector: a) Repeated, consistent current drops for *E. coli* PNA-beads hybridized with 10 aM of target *E. coli* 16S rRNA, b) No current drop for *E. coli* PNA-beads hybridized with 10 fM control *P. putida* 16S rRNA, c) Repeated, consistent current drops for *E. coli* PNA-beads hybridized with 10 aM of *E. coli* 16S rRNA against 10 fM control *P. putida* 16S rRNA, and d) Repeated, consistent current drops for *E. coli* PNA-beads hybridized with RNA extracted from a mixture of 10 CFU/mL of *E. coli* and 106 CFU/mL of *P. putida*.

4.4 Conclusion

A novel nanopore detector was successfully integrated with the LFA format. This LFA format nanopore detector was used successfully to detect *E. coli* 16S rRNA at 10 aM and *E. coli* in culture at 10 CFU/mL. No false positives were observed with 100 fM of *P. putida* RNA or with *P. putida* cells. This integrated diagnostic testing process was accomplished within 15 mins. These results suggest that this rapid and potentially inexpensive technology may one day prove advantageous for POC use. Indeed, with further integration of cell lysis and RNA extraction, this simple, amplification-free detection technology may lead to inexpensive, rapid POC pathogen detection devices with minimal reagent requirements.

4.5 Reference

1. Mao, X., et al., Disposable nucleic acid biosensors based on gold nanoparticle probes and lateral flow strip. Anal Chem, 2009. 81(4): p. 1660-8.
2. Cristillo, A.D., et al., Point-of-Care Sexually Transmitted Infection Diagnostics: 2. Proceedings of the STAR Sexually Transmitted Infection-Clinical Trial Group Programmatic Meeting. Sex Transm Dis, 2017. 44(4): p. 211-218.
3. Gaydos, C.A., Y.C. Manabe, and J.H. Melendez, A Narrative Review of Where We Are With Point-of-Care Sexually Transmitted Infection Testing in the United States. Sexually Transmitted Diseases, 2021. 48: p. S71-S77.
4. Niemz, A., T.M. Ferguson, and D.S. Boyle, Point-of-care nucleic acid testing for infectious diseases. Trends Biotechnol, 2011. 29(5): p. 240-50.

5. Atkinson, L.M., et al., 'The waiting game': are current chlamydia and gonorrhoea near-patient/point-of-care tests acceptable to service users and will they impact on treatment? Int J STD AIDS, 2016. 27(8): p. 650-5.
6. Hsieh, Y.H., et al., Perceptions of an ideal point-of-care test for sexually transmitted infections--a qualitative study of focus group discussions with medical providers. PLoS One, 2010. 5(11): p. e14144.
7. Ho, H.A., et al., Direct molecular detection of nucleic acids by fluorescence signal amplification. J Am Chem Soc, 2005. 127(36): p. 12673-6.
8. Nam, J.M., S.I. Stoeva, and C.A. Mirkin, Bio-bar-code-based DNA detection with PCR-like sensitivity. J Am Chem Soc, 2004. 126(19): p. 5932-3.
9. Benvidi, A., et al., Simple and label-free electrochemical impedance Amelogenin gene hybridization biosensing based on reduced graphene oxide. Biosensors & Bioelectronics, 2014. 58: p. 145-152.
10. Ramnani, P., et al., Electronic Detection of MicroRNA at Attomolar Level with High Specificity. Analytical Chemistry, 2013. 85(17): p. 8061-8064.
11. Cao, Y., Z. Zheng, and H.G. Monbouquette, Nucleic acid amplification-free detection of DNA and RNA at ultralow concentration. Curr Opin Biotechnol, 2021. 71: p. 145-150.
12. Koo, B., et al., Amplification-free, sequence-specific 16S rRNA detection at 1 aM. Lab Chip, 2018. 18(15): p. 2291-2299.
13. Henderson, W.A., et al., Simple lateral flow assays for microbial detection in stool. Anal Methods, 2018. 10(45): p. 5358-5363.
14. Tian, T., et al., Integrated paper-based microfluidic devices for point-of-care testing. Analytical Methods, 2018. 10(29): p. 3567-3581.

15. Bishop, J.D., et al., Sensitivity enhancement in lateral flow assays: a systems perspective. Lab Chip, 2019. 19(15): p. 2486-2499.
16. Huang, D., et al., Microfluidic Ruler-Readout and CRISPR Cas12a-Responded Hydrogel-Integrated Paper-Based Analytical Devices (muReaCH-PAD) for Visible Quantitative Point-of-Care Testing of Invasive Fungi. Anal Chem, 2021. 93(50): p. 16965-16973.
17. Fridley GE, H.C., Oza SB, Yager P, The evolution of nitrocellulose as a material for bioassays. MRS Bulletin, 2013. 38: p. 326–330.
18. Stender, H., et al., Rapid detection, identification, and enumeration of Escherichia coli cells in municipal water by chemiluminescent in situ hybridization. Appl Environ Microbiol, 2001. 67(1): p. 142-7.
19. Esfandiari, L., et al., PCR-Independent Detection of Bacterial Species-Specific 16S rRNA at 10 fM by a Pore-Blockage Sensor. Biosensors (Basel), 2016. 6(3).
20. Ruiz-Vega G, K.M., Pellitero MA, Baldrich E, del Campo FJ., Electrochemical Lateral Flow Devices: Towards Rapid Immunomagnetic Assays. ChemElectroChem, 2017. 4(4): p. 880-889.
21. Esfandiari, L., et al., Sequence-specific DNA detection at 10 fM by electromechanical signal transduction. Anal Chem, 2014. 86(19): p. 9638-43.
22. Esfandiari, L., H.G. Monbouquette, and J.J. Schmidt, Sequence-specific nucleic acid detection from binary pore conductance measurement. J Am Chem Soc, 2012. 134(38): p. 15880-6.
23. Janda, J.M. and S.L. Abbott, 16S rRNA gene sequencing for bacterial identification in the diagnostic laboratory: pluses, perils, and pitfalls. J Clin Microbiol, 2007. 45(9): p. 2761-4.

Chapter 5: Amplification-free, Sequence-specific 16S rRNA-Based Detection of *Chlamydia trachomatis* in Urine

ABSTRACT

A nucleic acid amplification-free, nanopore based technique has been demonstrated for sequence-specific detection of *Chlamydia trachomatis* at 10-100 CFU/mL in human urine with a limit of detection of 1 aM (10^{-18} M) for *C. trachomatis* 16S rRNA has been confirmed. *C. trachomatis* is the most common notifiable sexually communicable disease in the US, and infections are often asymptomatic in women. Untimely treatment can result in pelvic inflammatory disease leading to ectopic pregnancies and infertility. In order to curb disease spread and defend public health against potential healthcare crises, the need for rapid, sensitive and low-cost point-of-care devices for species-specific bacteria detection such as *C. trachomatis* is urgent. Our nanopore conductometric detection platform is based on sustained blockage of a glass nanopore to indicate the presence of target pathogen. Charge neutral, oligonucleotide probe-microbead conjugates are formed using peptide nucleic acid (PNA) capture probes complementary to target 16S rRNA which are conjugated to polystyrene microbeads. The sequence-specific binding of target 16S rRNA introduces substantial negative charge to the PNA-bead conjugate, and therefore, with externally applied electric field, the conjugates are driven to the glass nanopore of smaller diameter. At least partial blockage of the nanopore generates a sustained and readily observable step decrease in ionic current. Successful detection of *C. trachomatis* was demonstrated over the range of 10 to 100 CFU/mL spiked in human urine. No false positive signals were observed with *E. coli* control group spiked in human urine at 1000 CFU/mL. The limit of detection was estimated to be less than 1 aM *C. trachomatis* 16S rRNA. These results suggest that this amplification-free

platform may serve as the basis for rapid, inexpensive, portable detection of *C. trachomatis* in clinical urine samples at the POC.

5.1 Introduction

As the most common notifiable sexually communicable disease in the US, a total of 1,579,885 chlamydia cases were reported to the US Centers for Disease Control and Prevention (CDC) with a rate of 481.3 cases per 100,000 population.[1] Despite the reduction in new chlamydia infections in 2020, it is hypothesized that the decrease in infectious rate is mainly due to the deduction of screening coverage for patients with symptoms, since the in-person visits to health care clinics were reduced during the COVID-19 pandemic. This hypothesis is supported by the substantial decrease in the number of reported chlamydia cases since March and April 2020 when the initial shelter-in-place orders were placed, and such a shortfall persevered throughout the year. Moreover, the infection is commonly asymptomatic in women until complications such as pelvic inflammatory disease (PID), ectopic pregnancy, and tubal infertility emerge due to untimely treatment.[2, 3] The CDC currently recommends that sexually active women under 25 as well as older women with certain risk factors be tested every year.[4] In contemplation of executing timely treatment and to curtail disease spread, especially during the quarantine period caused by potential healthcare crisis now and in the future, the need for portable, inexpensive, and reliable diagnostic techniques for point-of-care (POC) tests is apparent.

Traditional diagnosis for most infectious diseases including chlamydia entails long culturing periods and laborious analysis relying on experienced specialists and therefore usually results in a turnaround time of more than a day.[5] Another class of frontline diagnostics for detecting several pathogens and pathophysiological conditions is the POC immunoassay. However,

immunoassays often have marginal sensitivities and specificities leading to false positives and negatives.[6] Considering the combination of low detection limit, high sensitivity and high specificity, nucleic acid amplification tests (NAATs) with exhibited ultralow LODs and both sensitivity and specificity in the 90-99% range would be more preferable but are less common at the POC.[7, 8] Polymerase chain reaction (PCR) is the core mechanism for most NAATs to amplify the copy number of the target disease-specific nucleic acid (NA) in a sample. Therefore, the inherent complexity of NAATs causes it to require demanding NA isolation, precise control of temperature cycling, perishable reagents including polymerase, primers and nucleotides. Optical components also are used frequently to detect dye-labeled amplicons. Even the most advanced NAATs with US FDA approval are no exception and total assay times for these complex devices is typically ~30 minutes. NAATs currently are reimbursed by US Medicare/Medicaid programs at ~$40-50/test.[9] Currently, most NA-based tests for *Chlamydia trachomatis* (CT, chlamydia) are conducted in clinical laboratories where the whole process including transporting samples to a lab, batching, testing, and returning results typically takes days.

Driven by the demand for more optimal POC diagnostic techniques, many efforts have been made to develop inexpensive, yet reliable, amplification-free, NA-based pathogen detection schemes. In order to be competitive with laboratory based NAATs, the amplification-free schemes should exhibit LODs at clinically relevant concentrations in the single digit aM (10^{-18} M) level and be broadly applicable.[9] Previously, numerous reports, including ours, have appeared describing NA amplification-free systems demonstrating these very low LODs for sequence specific NA-based detection.[10-14] Our potentially low-cost system circumvented the need for additional reagents and labels and only involved peptide nucleic acid (PNA) capture probes.[15] Uncharged PNA, a polyamide analog to DNA/RNA, was bound covalently to carboxyl functionalized microbeads to

form nearly charge neutral probe-bead conjugates. Target NA hybridization with the capture PNA probe-bead conjugates introduces substantial negative charge to the probe-bead complexes and thus enables them to be electrophoretically mobile. If this negatively charged bead complex with bound target are driven toward a smaller diameter pore, the beads will at least partially occlude the pore, which is signaled by a large, sustained reduction in ionic current. In previous work, such a device for electromechanical signal transduction was shown to give a highly selective, binary response signaling the presence or absence of the target NA and achieved estimated sensitivity and specificity of ~98% and ~100% for detection of *Neisseria gonorrhoeae* at 10-100 CFU/mL in human urine.[16] This work further demonstrates the potential broad application to disease diagnosis by detecting *Chlamydia trachomatis* spiked in human urine.

5.2 Experimental

5.2.1 Materials

Carboxyl-functionalized, 820 nm-dia. polystyrene microspheres and Vivaspin® 2 mL ultrafiltration devices were purchased from Bangs Laboratories, Inc. (Fishers, IN). 1-Ethyl-3-(3-dimethylaminopropyl) carbodiimide hydrochloride (EDC) was obtained from ThermoFisher Scientific (Waltham, MA). 2-(NMorpholino) ethanesulfonic acid (MES), methoxypolyethylene glycol amine (mPEG-amine) and ethanolamine were purchased from Sigma-Aldrich (St. Louis, MO). Peptide nucleic acid (PNA) probes were synthesized by PNA Bio (Thousand Oaks, CA) and arrived as >95% HPLC-purified, lyophilized powders. *E. coli* (ATCC 25922) and tryptic soy broth was purchased from American Type Culture Collection (Manassas, VA). Microbiologics™ inactivated *Chlamydia trachomatis* was purchased from Fisher Scientific (Hampton, NH). Direct-zol RNA Miniprep kits and TRI Reagent were purchased from Zymo Research (Irvine, CA). Two

mm-diameter, 4 mm-long Ag/AgCl pellet electrodes were purchased from A-M systems, Inc. (Carlsborg, WA). GE Healthcare Life Sciences Anotop 25 syringe filters (25 mmdiameter, 0.02 μm pore) were supplied by Genesee Scientific (San Diego, CA).

5.2.2 Methods

Detector assembly. Glass chips (1 cm × 1 cm) were micromachined from 4-in. borosilicate glass wafers (Plan Optik, Elsoff, Germany) as described in previous work.[10] In the center of the chip, a ~0.25 mm^2, 1 μm-thick membrane was etched and a ~500 nm nanopore was bored in the center of the thin membrane with a focused ion beam (FEI Nova 600 Nanolab DualBeam SEM/FIB).

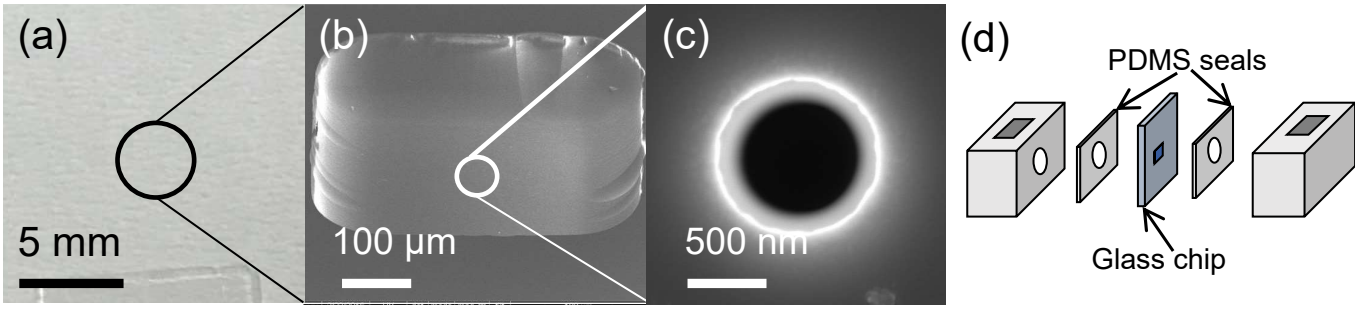

Figure 5.1. Glass chip detector assembly. (a) The 1 cm × 1 cm glass chip with ~1 μm-thick membrane and nanopore in the center. (b) Micrograph of the ~1 μm-thick membrane at the chip center. (c) Micrograph of the ~500 nm nanopore at the center of the glass membrane. (d) The glass chip sandwiched between PDMS seals and Teflon chambers (6 mm × 6 mm × 8 mm). The assembly was secured with four bolts (not shown).

These glass chips were sandwiched between two cast polydimethylsiloxane (PDMS) O-rings and custom-machined Teflon chambers (each measuring 6 mm × 6 mm × 8 mm, 216 μL) with 4 mm-diameter holes drilled into the side of each chamber creating an opening to the glass chip (Figure 6.1). A Ag/AgCl pellet electrode was placed in each, buffer-filled chamber, and

voltage was controlled and current monitored using a Versatile Multichannel Potentiostat (model VMP3) equipped with the 'p' low current option and N'Stat box interfaced to a computer running EC-LAB software (Bio-Logic USA, LLC, Knoxville, TN) for data collection. This assembly constituted our detection system for target *C. trachomatis* 16S rRNA hybridized to PNA probe conjugated to microspheres (see below).

Coupling PNA probe to microspheres. The complementary PNA probe sequence with PEG linker for detecting *C. trachomatis* 16S rRNA consisted of NH_2-$(CH_2CH_2OCH_2CH_2OCH_2CO)_6$- ATA TGT CCT TGC GGA AAA CG.[17] In order to prepare PNA-conjugated microspheres, one μL of 820 nm-diameter carboxylic group-functionalized polystyrene microspheres, at a concentration of ~3.25×10^{11}/mL, was suspended and washed three times in 100 mM MES buffer (pH 4.5). For each wash step, after centrifugation at 14,000 rpm for 15 minutes, the sedimented pellet microspheres were resuspended in fresh MES buffer. After the third wash, the microbeads were resuspended in 600 μL of MES buffer, and EDC (200 mM final concentration) was added to the suspension to serve as a crosslinker between the carboxyl groups on the polystyrene microbeads and the terminal primary amine groups appended on the PNA probes. This preparation was incubated for 15 minutes at 50 °C. Immediately afterward, 1.14 nmol of the PNA target probe was added followed by incubation for an additional two hours at 50 °C. Next, mPEG-amine was added to a final concentration of 100 mM followed by incubation for another hour at 50 °C. This latter conjugation step was added to inhibit microbead aggregation. Finally, ethanolamine was added to a final concentration of 138 mM and incubated for yet another hour at 50 °C. Ethanolamine was added to fully cap any remaining carboxyl groups, thereby ensuring that the PNA-conjugated microbeads were nearly charge neutral. After completion of microbead surface modification, the beads were washed three times with 0.4 × SSC buffer (60 mM

NaCl, 6 mM trisodium citrate, and 0.1% Tween-20, pH 8). Each wash was conducted for 15 minutes at 14,000 rpm in microfuge tubes. One fourth of the final product was set aside for zeta potential measurements, while the rest of the PNA-beads were stored in hybridization buffer at room temperature (10 mM NaCl, 25 mM Tris-HCl, pH 7). The zeta potential was measured for modified microbeads suspended in the testing buffer (10 mM KCl, 5.5 mM HEPES, 0.01% Tween-20, pH 7) using a Malvern Zetasizer Nano ZS (Malvern Instruments Ltd, Worcestershire, England). A zeta potential in the negative single-digit mV range was taken as evidence of successful microbead surface modification.

RNA extraction. Microbiologics™ inactivated *C. trachomatis* was purchased from Fisher Scientific (Hampton, NH). One inactivated pellet (~2×10^6 cells) was rehydrated with 1 mL 0.85% saline and rehydrated inactivated *C. trachomatis* then was serially diluted in 0.85% saline to achieve the desired concentrations for spiking into sterilized pooled human urine (BioIVT, Westbury, NY). After ATCC tryptic soy broth (15 g in 500 mL water) was made and sterilized at 121 °C for 20 minutes, *E. coli* ATCC 25922 was cultured by incubating at 37 °C at 250 rpm overnight. The cultured *E. coli* served as a negative control. The protocols for use of the Direct-zol RNA Miniprep kit and TRI Reagent (Zymo Research, Irvine, CA) were followed for total RNA extraction and purification. Each extraction began with 1 mL of human urine previously spiked with 10-100 CFU/mL of *C. trachomatis*, 1000 CFU/mL of *E. coli* control or 10-100 CFU/mL of *C. trachomatis* and 1000 CFU/mL of *E. coli* control. Extracted total RNA was eluted into 100 µL of RNase-free purified water and used within ~1-2 hours.

Hybridization of RNA to PNA-bead conjugates. Hybridization was fulfilled in Vivaspin® 2 mL ultrafiltration devices with 0.02- µm-diameter membranes. Bead-PNA conjugates in 600 µL hybridization buffer (see above) were transferred to Vivaspin® devices and spun at 2000

rpm for 5 minutes to form a compact bed of the conjugates on the membrane surface. Subsequently, extracted RNA from *C. trachomatis* spiked in human urine was added to the loaded Vivaspin® device and spun at 1000 rpm for 10 minutes to facilitate intimate contact and hybridization of target 16S rRNA with the previously deposited bead-PNA conjugates. Finally, hybridized beads were collected in hybridization buffer by reverse spinning the loaded Vivaspin® devices at 2500 rpm for 3 minutes.

Sample detection. Prior to the injection of a sample, the initial current in the absence of beads and sample was measured to verify the integrity of the glass chips. Depending on the exact nanopore size, clean glass chips had typical initial currents of 35 nA to 100 nA. After undergoing the hybridization procedure, bead-PNA conjugates potentially bound with target *C. trachomatis* 16S rRNA were injected into the detector chamber contacting the smooth backside (opposite the etched well) of the glass chip. After bead sample addition, a potential of 1.5 V was imposed, and the current was monitored for a sustained, ionic current drop that would signal detection of target 16S rRNA. After each detection signal (indicated by sustained ionic current drop of ~50 s) was observed, the polarity of the electronic field was reversed to -1.5 V to attempt to unblock the pore. After ~1 min of reversed polarity, the field was flipped back to 1.5 V to confirm baseline current recovery and detection signal reproducibility.

5.3 Results and discussion

Pore blocking experiments with samples consisting of *C. trachomatis* spiked in human urine over a 10-100 CFU/mL concentration range were processed and conducted as described above. The results are summarized in Table 5.1, with the detection limit (LOD) of the system investigated by serial dilution of the isolated *C. trachomatis* NA from 10 CFU/mL *C. trachomatis*

spiked in human urine. *E. coli* was chosen as the control group since it is one of the microbes frequently present in human urine.

Table 5.1. Summary of *C. trachomatis* (CT) detection data over a concentration range of 10-100 CFU/mL in human urine

Sample	Drop/reversible	Agree with expected result
100 CFU CT/mL	Expt.1 Yes/R Expt.2 Yes/R	Yes Yes
50 CFU CT/mL	Expt.1 Yes/R Expt.2 Yes/R Expt.3 Yes/N*	Yes Yes Yes Yes
10 CFU CT/mL	Expt.1 Yes/R Expt.2 Yes/R Expt.3 Yes/N*	Yes Yes Yes
1 attomolar CT NA	Expt.1 Yes/R Expt.2 Yes/R	Yes Yes
50 CFU CT/mL & 1000 CFU *E. coli* /mL	Expt.1 Yes/N*	Yes
100 CFU CT/mL & 1000 CFU *E. coli* /mL	Expt.1 Yes/R	Yes
1000 CFU *E. coli* /mL	Expt.1 No Expt.2 No Expt.3 No Expt.4 No	Yes Yes Yes Yes
Total agreement	16/16 (100%)	

N: open current did not return to the original level.

Sample data showing easily recognized, reproducible detection events as well as the lack of response to the negative control is presented as Figure 5.2. The applied voltage for detection events was 1.5 V. After a sustained current signal of ~30 s, the voltage polarity was reversed temporarily to -1.5 V to drive bead complexes away from the pore before demonstrating signal

reversibility by reimposing a potential of 1.5 V. After reimposing the potential, sustained current signal was reproduced and the process was repeated three times in total which corresponds to the three detection signals in Figure 5.2.

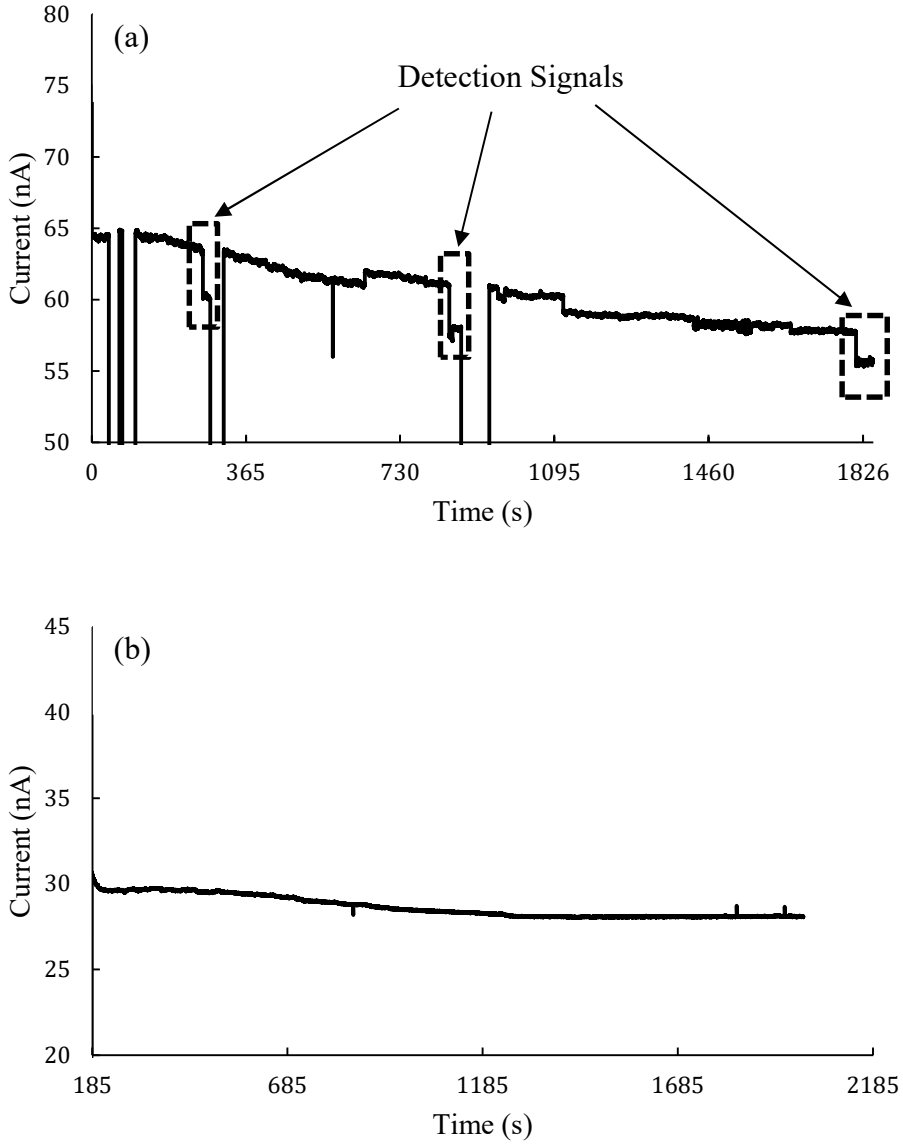

Figure 5.2. Integrated detector data response to the presence of target *C. trachomatis* 16S rRNA and the lack of response to RNA extracted from *E. coli* negative control alone. (a) PNA-beads hybridized with 16S rRNA extracted from 10 CFU/mL *C. trachomatis* spiked in human urine. Sustained and reproduceable current signal step reductions in response to the presence of target *C. trachomatis*. (b) No current signal in response to the presence of PNA-beads hybridized with RNA extracted from *E. coli* spiked at 1000 CFU/mL in human urine (negative control).

Detection of *C. trachomatis* spiked in human urine over 10-100 CFU/mL was successfully demonstrated with reproduceable results and within 1500s of detection time. The limit of detection is estimated to be less than the single-digit attomolar range which is competitive to both the nucleic acid amplification tests and other amplification-free detection schemes. Even though a LOD of 1 aM is not the lowest on record, 1 aM level corresponds to ~1 viable bacterium/10 mL based on ribosomal RNA, and therefore, it demonstrates a broad potential for disease diagnosis especially with clinical samples.[9, 18, 19] Note that the first detection event for true positive cases, indicated by the first sustained ionic current drop, occurred from 500 seconds to 1500 seconds. The variation in time to signal arises from the random initial distance of beads with hybridized target from the glass chip in the detector assembly. Absence of ionic current drop for over 2000 seconds constituted negative detection, since based on previous preliminary test runs with *C. trachomatis* PNA-beads with various concentrations of isolated *C. trachomatis* RNA, no true positive ionic current drop occurred after 1500 seconds. No positive detection results were recorded before 2000 seconds for of the *E. coli* negative control group alone at a concentration of 1000 CFU/mL in human urine. The one false negative result was observed for *E. coli* negative control group, which occurred after 2000 s which is much longer than the standard detection time. The hypothesis for this unexpected false positive is because of the accumulation of charged impurities inside the chamber either from air or from imperfect cleaning of the chambers potentially leading to false positives, especially for the long negative control tests.

This study further extends the detection of sexually transmitted pathogens to *C. trachomatis*, and further demonstrates the broad potential of the nanopore detection platform. Compared with currently widespread NAATs, this amplification-free test with considerably simpler procedure, avoidance of perishable reagents (i.e., polymerase, primers, nucleotides), but

robust and characterized by low LODs may hold promise for an inexpensive device for widespread POC use.

5.4 Conclusion

Successful demonstration of sequence specific detection of *C. trachomatis* in human urine was achieved with a low LOD of 1 attomolar using a NA amplification-free, label-free, sequence-specific NA detection scheme. A concentration range of 10-100 CFU/mL of *C. trachomatis* in human urine samples were assayed reproducibly with this novel amplification-free technique based on a nanopore glass detector. These results suggest that this potentially inexpensive, yet robust, technology may be suitable for broad POC use. The current assay time with all the intermediate processing steps such as multiple centrifugations and NA extraction could be further optimized by the integration of the glass nanopore detector with automated frontend sample processing. With a substantial decrease in overall assay time, there is potential to develop a sensing platform for rapid, inexpensive, and sensitive disease diagnostics in a POC setting.

5.5 References

1. CDC Sexually Transmitted Disease Surveillance 2020. https://www.cdc.gov/std/statistics/2020/overview.htm#Chlamydia (accessed February, 16, 2022),
2. Paavonen, J.; Lehtinen, M. *Hum Reprod Update* **1996,** 2, (6), 519-29.
3. Xia, Q.; Wang, T.; Xian, J.; Song, J.; Qiao, Y.; Mu, Z.; Liu, H.; Sun, Z. *Medicine (Baltimore)* **2020,** 99, (1), e18489.

4. CDC Chlamydia – CDC Basic Fact Sheet. https://www.cdc.gov/std/chlamydia/stdfact-chlamydia.htm
5. Chernesky, M. A. *Can J Infect Dis Med Microbiol* **2005,** 16, (1), 39-44.
6. Warade, J. *EJIFCC* **2017,** 28, (3), 224-232.
7. Cristillo, A. D.; Bristow, C. C.; Peeling, R.; Van Der Pol, B.; de Cortina, S. H.; Dimov, I. K.; Pai, N. P.; Jin Shin, D.; Chiu, R. Y.; Klapperich, C.; Madhivanan, P.; Morris, S. R.; Klausner, J. D. *Sex Transm Dis* **2017,** 44, (4), 211-218.
8. Lui, C.; Cady, N. C.; Batt, C. A. *Sensors (Basel)* **2009,** 9, (5), 3713-44.
9. Cao, Y.; Zheng, Z.; Monbouquette, H. G. *Curr Opin Biotechnol* **2021,** 71, 145-150.
10. Koo, B.; Yorita, A. M.; Schmidt, J. J.; Monbouquette, H. G. *Lab Chip* **2018,** 18, (15), 2291-2299.
11. Chen, C. P.; Ganguly, A.; Lu, C. Y.; Chen, T. Y.; Kuo, C. C.; Chen, R. S.; Tu, W. H.; Fischer, W. B.; Chen, K. H.; Chen, L. C. *Anal Chem* **2011,** 83, (6), 1938-43.
12. D'Agata, R.; Breveglieri, G.; Zanoli, L. M.; Borgatti, M.; Spoto, G.; Gambari, R. *Anal Chem* **2011,** 83, (22), 8711-7.
13. Dong, H.; Zhu, Z.; Ju, H.; Yan, F. *Biosens Bioelectron* **2012,** 33, (1), 228-32.
14. Yang, B.; Gu, K.; Sun, X.; Huang, H.; Ding, Y.; Wang, F.; Zhou, G.; Huang, L. L. *Chem Commun (Camb)* **2010,** 46, (43), 8288-90.
15. Nielsen, P. E.; Egholm, M.; Berg, R. H.; Buchardt, O. *Science* **1991,** 254, (5037), 1497-500.
16. Zheng, Z.; Cao, Y.; Chandrasekaran, S.; Schmidt, J. J.; Garner, O. B.; Monbouquette, H. G. *Sens Diagn* **2023,** 2, (1), 163-167.
17. Monstein, H. J.; Kihlstrom, E.; Tiveljung, A. *APMIS* **1996,** 104, (6), 451-8.
18. Janda, J. M.; Abbott, S. L. *J Clin Microbiol* **2007,** 45, (9), 2761-4.

19. Brehm-Stecher, B. F.; Hyldig-Nielsen, J. J.; Johnson, E. A. *Appl Environ Microbiol* **2005,** 71, (9), 5451-7.

Chapter 6: Improved Microcontact Printing of Choline Oxidase using a Polycation-Functionalized Zwitterionic Polymer as Enzyme Immobilization Matrix

ABSTRACT

Choline oxidase (ChOx) patterning on microelectrode arrays (MEA) and sensor performance have been greatly improved through the use of microcontact printing (μCP) combined with a polycation-functionalized zwitterionic polymer as enzyme immobilization matrix. μCP has emerged as an effective means to enable surface patterning with feature sizes in the millimeter to nanometer range, therefore, it could be useful to create multianalyte sensing microprobes by targeted deposition of each of multiple enzymes onto distinct, selected sites of a MEA. However, to date, the less than sufficient enzyme loading and inadequate spatial resolution achieved with current uCP approaches has limited both the sensitivity and the use of the resulting microsensors. These challenges are traced to problems with the formulation of the enzyme-containing aqueous solution (*i.e.*, the "ink") that is stamped. The current "inks" exhibit a poor balance between the ink-substrate interaction and intermolecular interaction within the ink. In this report, a specially designed polymer, poly(2-methacryloyloxyethyl phosphorylcholine)-*g*-poly(allylamine hydrochloride) (PMPC-*g*-PAH) is described, which serves as an alternative crosslinkable ink additive to conventional bovine serum albumin (BSA) for enzyme immobilization. During μCP, PMPC-*g*-PAH contributes a stronger intermolecular force while maintaining high adhesion to the microelectrode surface, which leads to a thicker immobilized ChOx deposited that is applied at higher spatial resolution, thereby leading to improved choline sensor performance including a sensitivity of 639 ± 96 nA μM^{-1} cm^{-2} (pH 7.4; n = 4). Such improvements in sensitivity lead to

smaller sensor probes that minimize tissue damage and make possible the creation of MEAs to monitor multiple neurochemicals simultaneously with high spatial resolution.

6.1 Introduction

The capability to monitor simultaneously multiple neurochemicals *in vivo* in near-real-time with high selectivity and spatial resolution has triggered interest from neuroscientists, as behaviors and physiological disorders are controlled by neuronal networks influenced by the complex interplay among various neurotransmitters.[1, 2] While conventional microdialysis enables the monitoring of multiple analytes simultaneously and has provided important insight into the regulation of neurotransmissions, this technique is constrained by its generally low temporal resolution in the range of minutes.[3-6] In contrast, electrochemical techniques based on implantable microprobes with an array of electroenzymatic sensing sites offers a means for multianalyte sensing at high temporal as well as spatial resolution and has developed rapidly into a robust analytical technique for neurotransmitters over the past few years.[7-11] Electroenzymatic sensors typically rely on specific oxidase enzymes to catalyze oxidations of the target analyte to produce hydrogen peroxide (H_2O_2) that is oxidized or reduced at an underlying electrode at moderate potential to give a current signal. Development of microelectrode array (MEA) microprobes for multiple neurotransmitter detection consequently requires a method to selectively deposit multiple different enzymes onto specific microelectrode sites of a MEA microprobe probe.

Enzyme deposition and immobilization on microelectrode surfaces is most commonly achieved by manually loading a mixture of enzyme, bovine serum albumin (BSA), and glutaraldehyde (GAH) as crosslinker on the electrode surface.[12] However, the manual approach becomes problematic when the MEA feature size is in the micrometer range. In previous work, we

demonstrated the use of microcontact printing (μCP) for creation of multianalyte sensing microprobes by patterning two different enzyme/BSA mixtures onto selected, distinct sites on a MEA and subsequent crosslinking with GAH vapor.[10] Although this accomplishment demonstrates the potential of MEAs for recordings of multiple neurochemicals simultaneously *in vivo* with high spatiotemporal resolution, the use of enzyme/BSA mixtures in aqueous solution as the "ink" has important disadvantages. Since the BSA protein behaves as a globular particle in solution that contributes little to the viscosity of the "ink", imprinted enzyme patterns tend to be so thin that low sensitivity results or problematic surface spreading and low spatial-resolution deposits occur when higher enzyme loading is attempted. For the application described in this work, excessive spreading of "ink" deposits is highly undesirable as it can lead to contamination of adjacent microelectrodes less than 100 μm away resulting in sensor crosstalk. As these problems are inherently related to ink properties, there has been a need for a new formulation that provides high adhesion to substrate, stronger intermolecular forces for higher viscosity and yet similar functionality as BSA to enable enzyme immobilization through covalent crosslinking.

While great strides have been made in modifying "ink" properties to achieve high resolution patterns, the focus has been on creating very thin layers of chemicals or proteins on substrates via covalent attachment.[13-15] In this report, we designed a novel graft polymer, poly(2-methacryloyloxyethyl phosphorylcholine)-*g*-poly(allylamine hydrochloride) (PMPC-*g*-PAH), which serves as an alternative enzyme immobilization matrix to BSA that enhances the capability and efficiency of enzyme transfer to microelectrode surfaces via μCP. The zwitterionic polyphosphorylcholine moieties of the graft polymer serve to enhance surface hydrophilicity, the free amine groups provide functional groups for crosslinking with GAH vapor, and the polymer itself increases solution viscosity so as to curtail undesirable "ink" spreading. The minimization of

ink surface spreading enables longer stamp alignment times, enhanced control of enzyme loading for better sensor performance, as well as potentially minimizing immune response that would improve long-term stability *in* vivo.[16]

6.2 Materials and Methods

6.2.1 Reagents

Nafion (5 wt% in lower aliphatic alcohols and 15-20% water), *m*-phenylenediamine (PD), bovine serum albumin (BSA) lyophilized powder, choline oxidase (ChOx) from *Alcaligenes* sp., choline chloride, L-ascorbic acid (AA), 3-hydroxytyramine (dopamine, DA), chitosan (from crab shells, minimum 85% deacetylated), glutaraldehyde (GAH) (25% in water), sodium phosphate dibasic, sodium chloride, HCl (36.5-38%), hydrogen peroxide (30 wt% aqueous solution), polyallylamine hydrochloride (PAH, MW 17,500), 2-methacryloyloxyethyl phosphorylcholine (MPC), dimethyl sulfoxide (DMSO), 4-cyano-4-(phenylcarbonothioylthio)pentanoic acid (CTA), and poly(*N*-(3-aminopropyl)methacrylamide) were purchased from Sigma-Aldrich (St. Louis, MO). 1-Ethyl-3-(-3-dimethylaminopropyl) carbodiimide hydrochloride (EDC), *N*-hydroxysuccinimide (NHS), 2,2'-azobis[2-(2-imidazolin-2-yl)propane] dihydrochloride (VA-044), and isopropyl alcohol (IPA) were purchased from Thermo Fisher Scientific (Waltham, MA). Solvents were used as received. Ag/AgCl glass-bodied reference electrodes with NaCl electrolyte (3M) and a 0.5-mm-diameter Pt wire auxiliary electrode were obtained from BASi (West Lafayette, IN). Sodium phosphate buffer (PBS, pH 7.4) used for sensor calibration was composed of 50 mM sodium phosphate dibasic and 100 mM sodium chloride. Four-inch silicon wafers (p-type boron doped; thickness 150 μm) were purchased from Silicon Valley Microelectronics (Santa Clara, CA).

SU-8 2075 and SU-8 developer were obtained from MicroChem (Westborough, MA). The Sylgard® 184 silicone elastomer kit was purchased from Dow Corning (Auburn, MI).

6.2.2 Instrumentation

Electrochemical preparations and *in vitro* calibrations were performed using a Versatile Multichannel Potentiostat (VMP3, Bio-Logic) equipped with the 'p' low-current option and low-current N stat box. A standard three-electrode system consisting of a separate Pt-wire as counter electrode, a separate Ag/AgCl reference electrode and modified Pt microelectrode sites on our MEA microprobe as the working electrodes was used in a Faraday cage. The film thicknesses on microelectrodes were measured using a SEM (Nova 600 SEM/FIB system).

6.2.3 Synthesis of PMPC conjugated PAH via RAFT polymerization (PMPC-g-PAH)

The PAH macroCTA was synthesized by conjugating the chain transfer agent (CTA) to the amino groups of PAH. Briefly, 3 mg of 4-cyano-4-(phenylcarbonothioylthio) pentanoic acid was dissolved in 400 µL DMSO. The DMSO solution was mixed with 10.5 mg EDC and 2.5 mg NHS in 50 µL MES buffer (pH 5.0), followed by incubation at 4 °C for 1 h. Next, 20 mg of PAH in 100 µL of MES buffer was added. The mixture was stirred at room temperature for 24 h. Afterwards, the reaction mixture was dialyzed against acetate buffer (pH 5.0) for 4 h to remove EDC, NHS, DMSO and unreacted CTA. The conjugation ratio was determined by UV-vis spectra. The final product was obtained by freeze-drying as a pink solid.

The PMPC-*g*-PAH graft polymer was synthesized via RAFT polymerization. First, 10 mg of PAH-CTA (CTA, 0.0054 mmol), 80 mg MPC (0.27 mmol), and 8.7 mg VA-044 (0.027 mmol) were dissolved in 500 µL of acetate buffer at pH 5.0 and added to a Schlenk flask. The mixture was deoxygenized through three, freeze-pump-thaw processes. Next, the flask was placed in a

water bath at 25 °C and stirred for 6 h. The polymerization was stopped by immersing the flask in liquid nitrogen. Finally, the reaction solution was dialyzed against DI water to remove the unreacted initiator and monomer. The final product was obtained by freeze drying. The successful synthesis of PMPC-*g*-PAH was verified from the H^1NMR spectrum (Figure 6.2), which showed PMPC bears about 50 MPC units per polymer chain and the average molecular weight was approximated at ~16.6K per polymer chain.

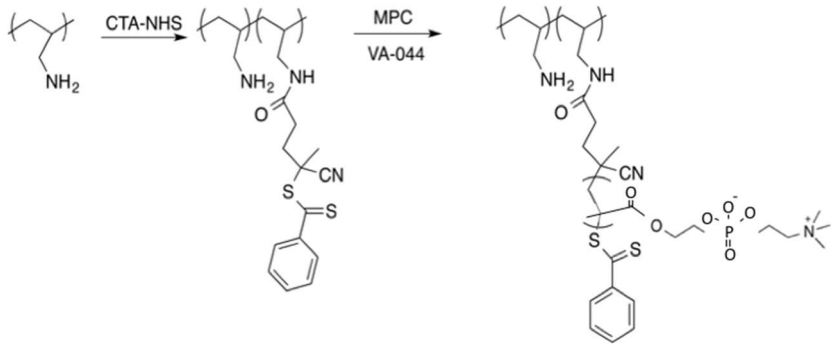

Figure 6.1. Synthesis route of PAH-*g*-PMPC polymer

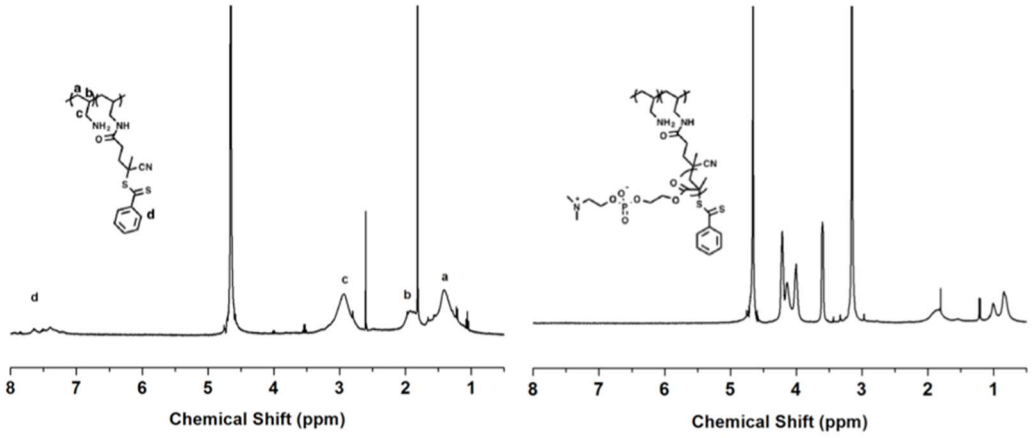

Figure 6.2. Proton NMR of PAH-CTA and PAH-*g*-PMPC

6.2.4 Fabrication of mold and PDMS stamps

SU-8 2075 was spin-coated at 2000 rpm for 30 seconds on a four-inch Si wafer to give a ~100 μm thick layer. Soft bakes were conducted at 65 °C for 5 min and then at 95 °C for 40 min followed by 27 s of UV exposure using Karl Suss with 8 mJ/cm^2 sec setting through a Chromium mask for stamp patterning (total exposure 216 mJ cm^2, wavelength of 365 nm). After UV exposure, the spin-coated SU-8 layer was baked once again at 65 °C for 5 min and then at 95 °C for 10 min. The mold pattern was developed in SU-8 developer for 20 min, followed by isopropanol cleaning and drying in air at room temperature.

Polydimethylsiloxane (PDMS) microstamps were fabricated using the Sylgard® 184 silicone elastomer kit. Six grams of monomer were mixed with 0.6 g of curing agent (10: 1; monomer: curing agent) and then centrifuged at 15,000 rpm for 5 min to remove air bubbles and degassed under vacuum. After pouring into the SU-8 mold, the PDMS was degassed under vacuum to remove any remaining air bubbles followed by curing at 60 °C for 4 h. The molded PDMS subsequently was detached from the SU-8 mold and cut into 1 cm × 1 cm pieces. The size of the microstamp surface (50 μm × 160 μm) was designed to be slightly larger than the size of a microelectrode to ensure complete coverage. The PDMS stamps were cleaned in 7.5% hydrogen peroxide with sonication before re-use.

6.2.5 Sensor preparation

The silicon-based microelectrode array (MEA) probes were manufactured from 4-in, 150-μm-thick Si wafers in-house using previously described microelectromechanical system (MEMS) techniques. The processes included the physical vapor deposition of Pt as electrode material, and the chemical vapor deposition of silicon oxide/nitride as insulation. Shaping was done by deep reactive ion etching from the front side. Each probe was 150 μm thick, 140 μm wide and 9 mm

long, with four platinum recording sites (40 μm × 150 μm) at the tip arranged in pairs separated by 40 μm (Fig. 3).

The choline sensor design is shown in Fig. 4. A polyphenylenediamine (PPD) film first was electrodeposited on the Pt microelectrodes from a 5 mM PD solution in phosphate-buffered saline (0.1 M PBS) by holding the voltage constant at 0.85 V vs. Ag/AgCl for 20 mins. Afterward, a Nafion layer was dip-coated from a 2% Nafion solution (diluted from stock with 4:1 isopropyl alcohol (IPA): water) and annealed at 115 °C for 20 min. Next, a 0.1% w/v aqueous solution for chitosan deposition was prepared by mixing chitosan into water and adjusting the pH to 3 using HCl (0.1 M) followed by stirring for over 48 h to ensure complete dissolution of chitosan flakes. Subsequently, the chitosan solution was filtered using a 0.2 μm syringe filter, and the pH was adjusted to 5 with NaOH solution (0.5 M). The MEA probe coated with PPD and Nafion than was immersed in the aqueous chitosan preparation, and a constant potential of −0.7 V vs. Ag/AgCl was applied at the Pt microelectrode surfaces for 1 min, and repeated twice more for 1 min each, to electrodeposit the chitosan film.[17, 18]

Subsequently, the enzyme "ink" was prepared by mixing 4 μL ChOx (0.5 U/μL) with either 1 μL PMPC-*g*-PAH polymer solution (20 mg/ml) or 2 μL BSA solution (60 mg/ml). A droplet (~3 μL) of the prepared enzyme "ink" was deposited on the PDMS microstamp and after ~20 mins incubation in air at room temperature, the inked stamp was aligned carefully to the target microelectrode surface under a microscope fitted with a custom-built, manually adjustable stage to position the stamp. Deposition on the desired microelectrode surface was performed by adjusting the stage to achieve gentle contact of the PDMS stamp coated with viscous enzyme "ink" with the electrode surface for a few seconds. A wet enzyme layer remained after removal of the

PDMS stamp as illustrated in Fig. 5.[10] Finally, the printed enzyme layer was exposed to vapor from a 5% GAH aqueous solution for 1 min to effect crosslinking.

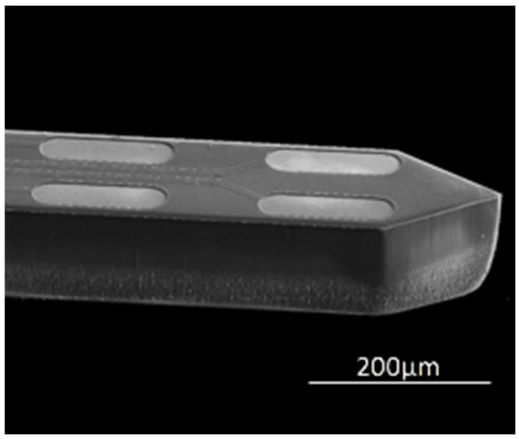

Figure 6.3. Scanning electron microscopy (SEM) image of the microelectrode array probe.

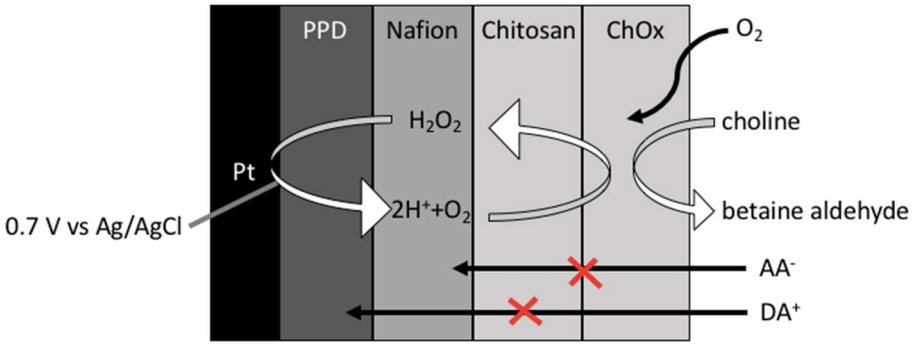

Figure 6.4. Schematic diagram showing the construction of the choline sensors (not to scale) as well as the sensing mechanism. The chitosan layer serves as an adhesive for the immobilized enzyme layer. Nafion acts primarily to reject negatively charged interfering species found in brain extracellular fluid such as ascorbic acid (AA^-), while the PPD layer acts primarily to reject dopamine (DA^+). ChOx catalyzes the oxidation of choline to produce H_2O_2, which is electrooxidized at the Pt electrode surface to give H^+, O_2 and the electrons that give rise to a current signal.

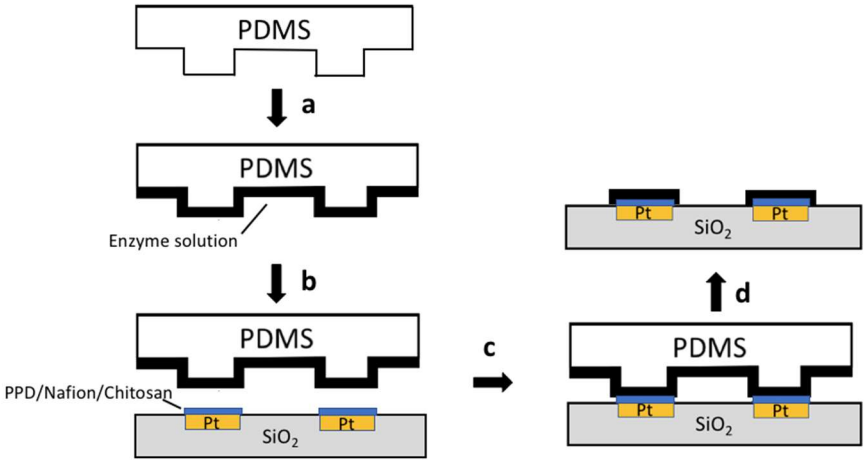

Figure 6.5. Diagram illustrating the enzyme μCP process. (a) The PDMS stamp is inked with enzyme "ink". (b) The inked stamp is aligned carefully to the target microelectrode surface(s) under a microscope fitted with a custom-built adjustable stage. (c) Gentle pressure is maintained for a few seconds. (d) The stamp is removed leaving an enzyme layer patterned on the targeted microelectrodes of the microprobe (d).

6.2.6 Sensor calibration

Constant potential amperometric measurements were conducted in stirred PBS buffer at 0.7 V vs. Ag/AgCl and at ambient temperature. The sensors were permitted to equilibrate in PBS buffer for approximately 30 mins before adding analytes. Solutions of AA, DA, Ch or H_2O_2 were added individually to the stirred buffer solution to give final concentrations of 250 μM AA, 10 μM DA, 20-60 μM Ch and 20 μM H_2O_2 to assess sensitivity and selectivity.

6.3 Results and discussion

6.3.1 Comparison of printed ChOx using two different inks

BSA-ChOx ink

Unlike many applications of μCP for deposition of monolayer-thick patterns of protein, the goal here was to deposit a ~5-um-thick film corresponding to may equivalent enzyme layers on a

well-defined microelectrode substrate in order to give optimal sensor performance. The printing of a thick pattern with micron-scale, lateral spatial resolution is challenging; as it requires a good combination of surface wettability of the ink and ink viscosity (Figure 6.6), since the chitosan film on the microelectrodes presents a hydrophilic surface for a water-based ink to wet and spread. If a conventional enzyme ink composed of ChOx and BSA in water is permitted to dry for 60 mins on the PDMS stamp before transfer in an effort to increase ink, viscosity and reduce spread, the resulting pattern was limited to the microelectrode surface but was too thin (in the few hundred nm range) and showed incomplete coverage. In contrast, if the ChOx/BSA ink is permitted to dry only 5 mins on the PDMS surface before stamping, this wet ink also was not preferred as it spread laterally, well beyond the edges of the microelectrode. Adequate spatial resolution was achieved after pre-drying the ink on the stamp for 15-20 mins, which presumably resulted in an ink state with sufficiently reduced water content. However, the deposit was only 2-μm-thick, which is less than half optimal. In our prior work, at least two stamping cycles were required to obtain a high-performance choline sensor. Also, subsequent unacceptable surface spreading was observed during the crosslinking step with humid GAH vapor (Figure 6.7). It was hypothesized that these problems were inherently related to the ink properties, as both BSA and ChOx behave as globular particles that provide relatively weak intermolecular forces within the ink resulting in ink viscosity that is too low to control spreading on a chitosan-coated microelectrode surface. Finally, the narrow drying time window during which nearly acceptable stamping can be achieved made manual alignment of the microstamp and the targeted microelectrode a challenging process. These issues prompted formulation of alternative ChOx-containing inks that could be used to deposit sufficiently thick enzyme layers with good spatial resolution that could be crosslinked effectively.

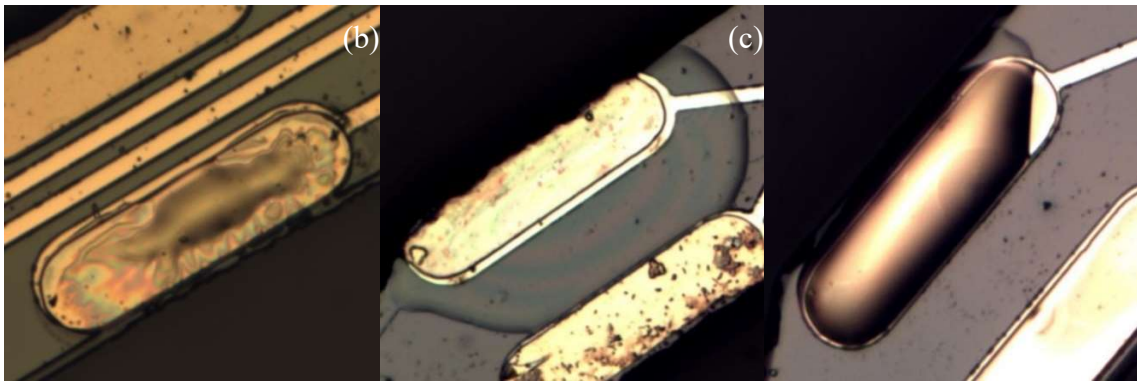

Figure 6.6. Distinct ChOx pattern on chitosan-coated substrate with various wettabilities after PDMS stamping of BSA-ChOx ink. (a) is a demonstration of insufficient enzyme transfer with ~35-45 mins of incubation time. The PDMS stamp was partially dried, and stamping nearly dry BSA-ChOx ink gave insufficient enzyme coverage pattern. (b) shows the stamping pattern with less than 10 mins of incubation time. The high mobility of molecules due to excessive wettability caused sever spreading problem. (c) shows a proper wettability with 15 to 20 mins of incubation time and a thick enzyme layer was transferred with an appropriate enzyme coverage pattern.

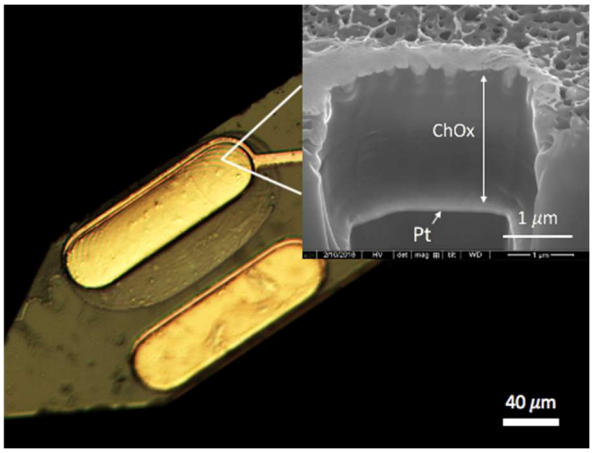

Figure 6.7. Optical microscope image of BSA-ChOx ink pattern stamped on the top microsensor in the micrograph after exposure to humid GAH vapor for crosslinking. The inset shows an SEM image of the ~2-µm-thick deposit cross-section.

PMPC-*g*-PAH-ChOx ink

It is known that the physical properties of the polymer incorporated in enzyme ink are particularly important in determining enzyme transfer efficiency during μCP. The key to enable high enzyme loading without surface spreading on a hydrophilic surface is to add a hydrophilic polymer with sufficiently strong intermolecular forces, due to for example, hydrogen bonding and van der Waals forces. Initially, experiments were conducted with poly(*N*-(3-aminopropyl)methacrylamide) (PAPM), a polymer of easily tuned length during free-radical polymerization that also provides free amine-groups for GAH crosslinking (data not shown). Although higher molecular weight PAPM provided better control of ink spreading, the preparation was too viscous to provide the flexibility needed to control the thickness of printed patterns. However, these initial PAPM trials provided valuable insight into the influence of polymer characteristics on enzyme μCP and led to the choice of commercially available PAH (MW = 17,500 g/mol) as a promising alternative for future work due to its well-defined structure, convenient chemistry for modifications, and low price.

To further enhance PAH-based ink hydrophilicity and to provide anti-fouling properties to printed enzyme patterns, zwitterionic MPC was conjugated to PAH to synthesize the polymer, PMPC-*g*-PAH. Zwitterionic polymers have been used widely as ultralow fouling coatings on biomedical devices due to their super hydrophilic nature that forms a surrounding shell of water molecules to inhibit protein adsorption.[19-21] In addition, it is known that enzymes keep their natural conformation in more hydrophilic environments, which the effect of PMPC-*g*-PAH on ChOx activity will be discussed later. The hydrophilicity of PMPC-*g*-PAH was assessed and confirmed by measuring the contact angle on hydrophobic PDMS stamp that showed a large angle of over 90° (Figure 6.8). PMPC-g-PAH showed clear promise as a key component of an enzyme ink formulation.

Subsequent tests were conducted to assess the performance of the PMPC-*g*-PAH-based ink for microcontact printing of ChOx onto microelectrodes. As shown in Figure 6.9, the thickness of the printed ChOx layer with PMPC-g-PAH-based ink was measured at ~4 μm without observable surface spreading after exposure to GAH/water vapor. This layer thickness was ~2-fold thicker than that obtained with the BSA-ChOx and close to the predicted optimal thickness for electroenzymatic choline sensors. Moreover, use of the PMPC-g-PAH-ChOx has greatly improved the μCP success rate by enabling a much longer stamp alignment time with gentle contact between stamp and microprobe. This could be attributed to the stronger hydrogen bonding of water to the zwitterionic PMPC side chains, which slow the water evaporation rate from the ink.

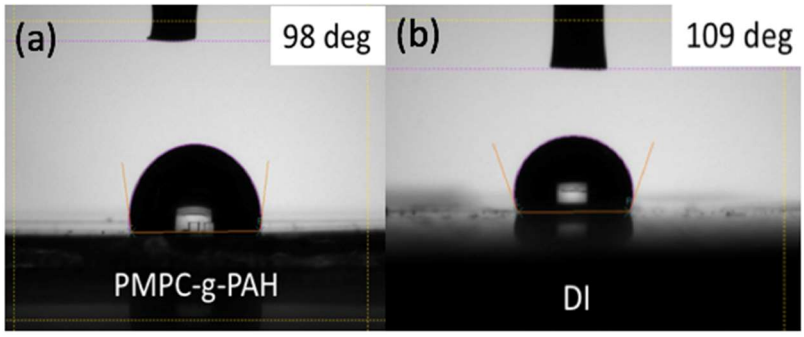

Figure 6.8. Contact angle measurements on PDMS for (a) PMPC-g-PAH and (b) DI water.

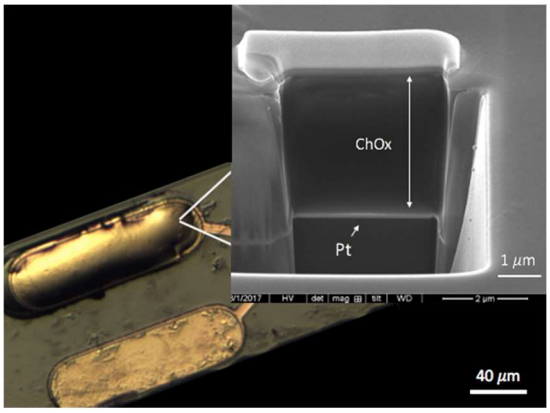

Figure 6.9. Optical microscope image of PMPC-g-PAH-ChOx ink stamped and GAH crosslinked on a microelectrode (top site). The inset shows the corresponding cross-sectional SEM image.

6.3.2 Stamped choline microsensor performance

To demonstrate that enzyme function was retained after μCP and crosslinking, all microsensors were tested with choline in solution at 0 to 60 μM at the constant operating potential of 0.7 V (vs. Ag/AgCl). The choline sensor selectivity was also tested against two common electrooxidizable interferents, ascorbic acid (AA) and dopamine (DA) at 250 μM and 10 μM respectively, which are found in brain extracellular fluid at 200-400 μM for AA and 6 nM to 2.5 μM for DA.[22, 23] As expected, the data showed an increase in sensitivity with increased thickness of the immobilized ChOx deposit up to a maximum of ~4 μm. Compared to our previous work where BSA-ChOx ink was used to create a very thin immobilized ChOx deposit (estimated at <1 μm) that resulted in a sensitivity of 286 ± 63 nA μM^{-1} cm^{-2}, a ~1.5-fold improvement in Ch sensitivity was achieved simply by creating a thicker BSA-ChOx deposit here of ~2 μm (with some compromise in spatial resolution) that resulted in a sensitivity of 444 ± 133 nA μM^{-1} cm^{-2} (n = 5) (Figure 6.10 (b)).[10] A further increase in ChOx loading corresponding to a high spatial resolution deposit of ~4 μm in thickness when PMPC-*g*-PAH used as enzyme matrix, led to another 1.5-fold improvement in sensitivity to 639 ± 96 nA μM^{-1} cm^{-2} (n = 4). As these improvements in sensitivity

were achieved without sacrificing background noise and selectivity, the limit of detection (at signal-to-noise ratio of 3) of printed PMPC-*g*-PAH-ChOx sensors relative to printed BSA-ChOx sensors were also improved, 0.31 ± 0.06 μM (n = 4) versus 0.45 ± 0.17 μM (n = 5), respectively (Figure 6.10 (c)). The high sensitivity obtained with PMPC-*g*-PAH-ChOx stamped microsensors exceeds that of most other published choline sensors, including those that employed manual, non-stamping enzyme deposition methods in their construction and is statistically the same as the highest recorded sensitivity that was achieved by manually spreading and crosslinking 12-15 layers of BSA-ChOx solution on a microelectrode in order to achieve a ~4-μm-thick deposit.[10, 24-28]

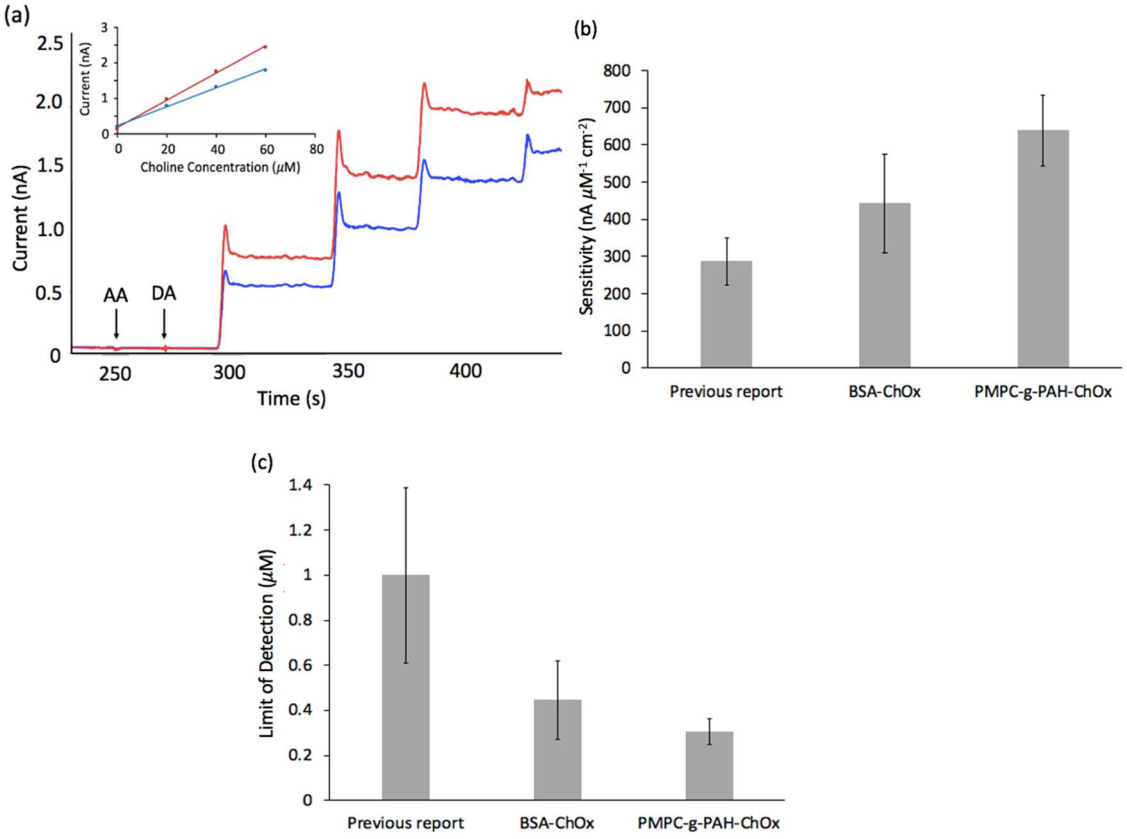

Figure 6.10. (a) Representative current response of stamped BSA-ChOx (blue trace) and stamped PMPC-g-PAH-ChOx (red trace) Ch sensors to interferents, 250 μM AA and 5 μM DA, followed by three 20 μM step increase in ChCl and a 20 μM increase in H_2O_2. (b) Choline sensitivity and (c) limit of detection. Error bars give 95% confident intervals.

6.3.3 Enzyme Affinity

The apparent Michaelis-Menten parameters, I_{max} and K_m^{app} (Eq. 1) were estimated for the choline biosensors to provide insight into factors affecting the sensitivity measurements presented above. Here, the concentration of co-substrate O_2 is assumed constant, and K_m^{app} is defined as the Ch concentration at half the corresponding I_{max}.

$$I = \frac{I_{max}[\mathrm{Ch}]}{K_m^{app} + [\mathrm{Ch}]} \tag{1}$$

As shown in Figure 6.11, a ~1.5-fold increase in I_{max} achieved with PMPC-g-PAH-ChOx stamped microsensors compared to those stamped with BSA-ChOx indicated greater enzyme activity and/or improved mass transfer characteristics of the PMPC-g-PAH-ChOx layer transferred onto the electrode surface. However, one would expect a greater $K_M{}^{app}$ value with the 2-fold thicker PMPC-*g*-PAH-ChOx layer, yet it was similar to that for the BSA-ChOx biosensor, 110 ± 18 μM (n = 4) versus 101 ± 27 μM (n = 5), respectively. Zwitterionic polymers such as PMPC have the unique property of retaining or improving binding affinity through enhanced protein-substrate hydrophobic interactions.[29] Unlike BSA (pI: 4.7) that provides a negatively charged matrix, the PMPC-g-PAH polymer is positively charged, thereby helping counterbalancing polyanionic ChOx to prevent enzymes from aggregation. This result consistent with other published experimental reports showing that pre-coating the Pt with polycation led to a large decrease in the $K_M{}^{app}$.[30] The positively charged PMPC-g-PAH polymer also may improve partitioning of negatively charged choline into the immobilized enzyme layer resulting in a locally higher concentration in the layer as opposed to the solution. In addition, glutamate effective diffusivity in the PMPC-g-PAH-ChOx layer may be improved, a possibility that would require further experimentation. Nevertheless,

these results demonstrate improved choline sensor performance using the GAH crosslinked PMPC-g-PAH matrix for the immobilized enzyme layer rather than the conventional immobilization medium based on crosslinked BSA.

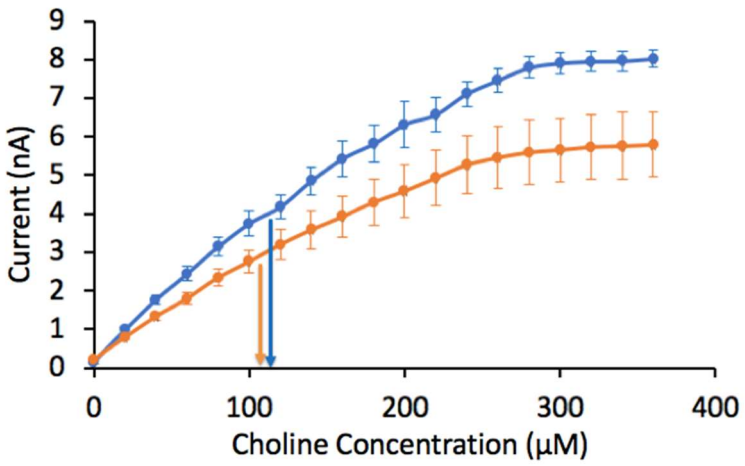

Figure 6.11. Plots of current, *I*, versus choline concentration obtained with sensors stamped with PMPC-g-PAH-ChOx (blue curve: $K_M{}^{app}$ = 110±18 µM, I_{max} = 7.9±0.6 nA, *n* = 4) and BSA-ChOx (orange curve: $K_M{}^{app}$ = 101±27 µM, I_{max} = 5.8±1.7 nA, *n* = 5) with error bars indicating 95% confident intervals.

6.4 Conclusion

Enzyme loading and pattern resolution on the microelectrode surface are two critical factors to allow creation of highly sensitive microprobe for multianalyte sensing. We demonstrated PMPC-*g*-PAH polymer as an effectively alternative enzyme immobilization matrix to BSA for enhancing µCP enzyme. Compared to sensors imprinted with ChOx-BSA, PMPC-*g*-PAH-ChOx printed sensors led to much thicker ChOx pattern in high resolution that showed high

sensitivity for Ch (639 ± 96 nA μM^{-1} cm^{-2} (n = 4)), fast response time within a second, and very low limit of detection (0.31 ± 0.06 μM (n = 4)). Furthermore, incorporation of PMPC-*g*-PAH greatly improved μCP success rate by allowing much longer alignment time. Therefore, μCP combined with PMPC-*g*-PAH as enzyme immobilization matrix is expected to contribute to neuroscience research by making possible the creation of thick enzyme layer in high resolution on selected microelectrode sites on a microprobe thereby enabling highly sensitive detection of multiple analytes in close proximity simultaneously. This high sensitivity will also allow greater flexibility in shrinking electrode surface size in the future to minimize tissue damage. Finally, the use of PMPC-*g*-PAH has potential to provide better stability for long-term experiment *in vivo,* as zwitterionic MPC has been widely reported to minimize immune response, which will require further investigation *in vivo*.[14, 16, 17]

6.5 References

1. E. D. Levin, in *Neurotransmitter Interactions and Cognitive Function*, ed. E. D. Levin, Birkhäuser Basel, Basel, 2006, DOI: 10.1007/978-3-7643-7772-4_1, pp. 1-3.
2. Y. Ou, A. M. Buchanan, C. E. Witt and P. Hashemi, *Anal Methods*, 2019, **11**, 2738-2755.
3. M. T. Bowser and R. T. Kennedy, *Electrophoresis*, 2001, **22**, 3668-3676.
4. M. L. Rogers, D. Feuerstein, C. L. Leong, M. Takagaki, X. Niu, R. Graf and M. G. Boutelle, *ACS Chem Neurosci*, 2013, **4**, 799-807.
5. E. C. Rutherford, F. Pomerleau, P. Huettl, I. Stromberg and G. A. Gerhardt, *J Neurochem*, 2007, **102**, 712-722.
6. H. Y. Yang, A. B. Thompson, B. J. McIntosh, S. C. Altieri and A. M. Andrews, *Acs Chemical Neuroscience*, 2013, **4**, 790-798.

7. J. J. Burmeister, F. Pomerleau, M. Palmer, B. K. Day, P. Huettl and G. A. Gerhardt, *J Neurosci Meth*, 2002, **119**, 163-171.

8. A. L. Collins, T. J. Aitken, I. W. Huang, C. Shieh, V. Y. Greenfield, H. G. Monbouquette, S. B. Ostlund and K. M. Wassum, *Biol Psychiat*, 2019, **86**, 388-396.

9. I. W. Huang, M. Clay, S. Q. Wang, Y. W. Guo, J. J. Nie and H. G. Monbouquette, *Analyst*, 2020, **145**, 2602-2611.

10. B. Wang, B. Koo, L.-w. Huang and H. G. Monbouquette, *Analyst (Cambridge, U. K.)*, 2018, **143**, 5008-5013.

11. K. M. Wassum, V. M. Tolosa, T. C. Tseng, H. G. Monbouquette and N. T. Maidment, *Ieee Sensor*, 2010, DOI: Doi 10.1109/Icsens.2010.5690944, 2351-2353.

12. C. H. Lei and J. Q. Deng, *Analytical Chemistry*, 1996, **68**, 3344-3349.

13. E. Blinka, K. Loeffler, Y. Hu, A. Gopal, K. Hoshino, K. Lin, X. Liu, M. Ferrari and J. X. Zhang, *Nanotechnology*, 2010, **21**, 415302.

14. M. Buhl, B. Vonhoren and B. J. Ravoo, *Bioconjug Chem*, 2015, **26**, 1017-1020.

15. A. Perl, D. N. Reinhoudt and J. Huskens, *Adv Mater*, 2009, **21**, 2257-2268.

16. M. Zhao, D. Xu, D. Wu, J. W. Whittaker, R. Terkeltaub and Y. Lu, *Nano Research*, 2018, **11**, 2682-2688.

17. L. Q. Wu, A. P. Gadre, H. M. Yi, M. J. Kastantin, G. W. Rubloff, W. E. Bentley, G. F. Payne and R. Ghodssi, *Langmuir*, 2002, **18**, 8620-8625.

18. T. T. C. Tseng, J. Yao and W. C. Chan, *Biochem Eng J*, 2013, **78**, 146-153.

19. X. Xie, J. C. Doloff, V. Yesilyurt, A. Sadraei, J. J. McGarrigle, M. Omami, O. Veiseh, S. Farah, D. Isa, S. Ghani, I. Joshi, A. Vegas, J. Li, W. Wang, A. Bader, H. H. Tam, J. Tao, H. J.

Chen, B. Yang, K. A. Williamson, J. Oberholzer, R. Langer and D. G. Anderson, *Nat Biomed Eng*, 2018, **2**, 894-906.

20. Dhanjai, X. Lu, L. Wu, J. Chen and Y. Lu, *Anal Chem*, 2020, **92**, 5830-5837.

21. E. Zhang and Z. Cao, *Nat Biomed Eng*, 2018, **2**, 881-882.

22. M. J. Neal, J. R. Cunningham and K. L. Matthews, *Investigative Ophthalmology & Visual Science*, 1999, **40**, 2983-2987.

23. C. A. Owesson-White, M. F. Roitman, L. A. Sombers, A. M. Belle, R. B. Keithley, J. L. Peele, R. M. Carelli and R. M. Wightman, *J Neurochem*, 2012, **121**, 252-262.

24. J. J. Burmeister, F. Pomerleau, P. Huettl, C. R. Gash, C. E. Wemer, J. P. Bruno and G. A. Gerhardt, *Biosensors & Bioelectronics*, 2008, **23**, 1382-1389.

25. A. H. Keihan, S. Sajjadi, N. Sheibani and A. A. Moosavi-Movahedi, *Sensors and Actuators B: Chemical*, 2014, **204**, 694-703.

26. H. Zhang, Y. Yin, P. Wu and C. Cai, *Biosens Bioelectron*, 2012, **31**, 244-250.

27. P. Rahimi, H. Ghourchian and S. Sajjadi, *Analyst*, 2012, **137**, 471-475.

28. A. Khan and S. Ab Ghani, *Biosens Bioelectron*, 2012, **31**, 433-438.

29. A. J. Keefe and S. Jiang, *Nat Chem*, 2011, **4**, 59-63.

30. C. P. McMahon, G. Rocchitta, P. A. Serra, S. M. Kirwan, J. P. Lowry and R. D. O'Neill, *Analyst*, 2006, **131**, 68-72.

Chapter 7: An Implantable Multifunctional Neural Microprobe for Simultaneous Multi-analyte Sensing and Chemical Delivery

Chapter 7 is a manuscript published with the following citation:

Wang, B., Wen, X., Cao, Y., Huang, S., Lam, H.A., Chung, P.S., Monbouquette, H.G., Chiou, P.Y. and Maidment, N.T., 2020. An implantable multifunctional neural microprobe for simultaneous multi-analyte sensing and chemical delivery. Lab on a Chip, 20(8), pp.1390-1397.

ABSTRACT

A multifunctional chemical neural probe fabrication process exploiting PDMS thin-film transfer to incorporate a microfluidic channel onto a silicon-based microelectrode array (MEA) platform, and enzyme microstamping to provide multi-analyte detection is described. The Si/PDMS hybrid chemtrode, modified with a nano-based on-probe IrOx reference electrode, was validated in brain phantoms and in rat brain.

7.1 Introduction

Implantable neural microprobes are widely used in neuroscience studies for chemical and electrophysiological recordings of neural activities in deep brain regions.[1–5] The probes are often used in conjunction with local chemical delivery systems to manipulate neural circuits. Conventionally, in order to achieve simultaneous electrochemical recording of multiple analytes (e.g., dopamine, glutamate, and acetylcholine), which work together to control complex behaviors, and chemical modulation, multiple implants are required, including (1) multiple electrochemical sensors for different analytes; (2) counter electrode (CE) and reference electrode (RE), or RE also acting as CE; and (3) an independent microinjector separated from or glued manually onto the shank of the sensing electrodes[6–8] for chemical delivery (Figure 7.1a, left). Such an approach requires prolonged surgical implantation procedures and results in significant damage to the brain.

Moreover, the relative distance between separated chemical delivery devices, sensing electrodes, and RE can be hard to control, hampering experimental reproducibility and introducing variability in baseline noise.[9] Therefore, the development of a multifunctional probe that integrates these individual components into a single implantable device is highly desirable (Figure 7.1a, right).

To this end, advances in MEMS technology have been harnessed to create silicon microelectrode array (MEA) microprobes with integrated microfluidic channels on the same shank using bulk or surface micromachining.[10] Compared to conventional approaches such as gluing glass pipettes to the probes, sophisticated microfluidic functions such as multi-channel delivery and on-probe mixing can be achieved with minimal increase in probe dimension.[11,12] In bulk micromachining, the channel is formed by etching the silicon substrate, which is sealed by either depositing materials isotropically, such as by plasma enhanced chemical vapor deposition (PECVD) of silicon dioxide,[13,14] or by wafer bonding.[11,15] In surface micromachining, the channel is formed by removal of sacrificial film deposited on top of the silicon substrate.[16,17] Such silicon-based chemtrodes are batch fabricated with high precision; however, the process for fabricating the microfluidic channels requires multiple additional MEMS fabrication steps such as wafer bonding, polishing, film deposition and etching, which is often complicated, costly and may not be readily accessible.

Here, we describe the development of a customized PDMS thin-film transfer process based on soft lithography that enables integration of microfluidic channels on silicon microprobes. In this highly flexible process, free-standing ultra-thin PDMS microfluidic channels can be fabricated in batch mode[5,18] with minimal increase in dimensions, or can be used to modify pre-fabricated MEAs since PDMS channels

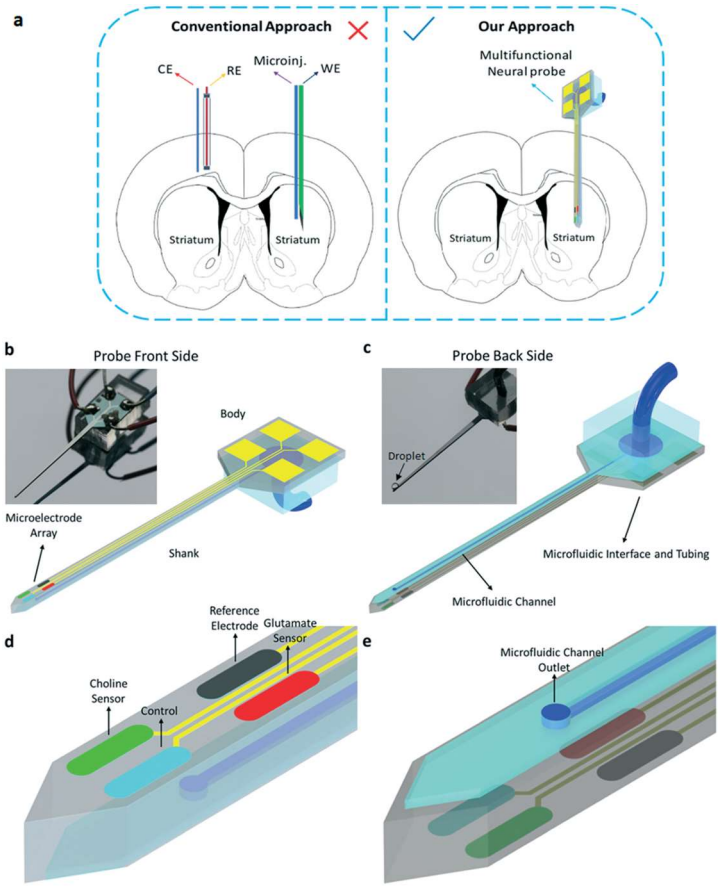

Figure 7.1. (a) Schematic diagram showing conventional chemical sensing and agent delivery system vs. our single multifunctional neural probe. (b–e) Conceptual diagram of the proposed multi-functional neural probe with chemical delivery and multi-sensing capabilities. (b) Front side of the microprobe; (c) back side of the microprobe; (d) chemtrode shank tip (front side) showing the functionalized microelectrode array; (e) microprobe shank tip (back side) showing the outlet of the microfluidic channel.

are transferred as the last step of the process. It is very convenient and cost-effective for building prototypes to iterate microfluidic channel design or to validate other functionalities on the probe (biosensing in this work) without designing and fabricating a new batch of MEAs each time. Second, we incorporated a platinum (Pt) nanoparticlemodified IrOx reference electrode, replacing the conventional unstable Ag/AgCl film, by electrodeposition on the microprobe as previously described.[3,5,9] Finally, we adapted our recently developed PDMS microstamping technique[19,20] to selectively transfer glutamate and choline oxidases onto individual electrodes of the MEA, thereby

demonstrating the potential for manipulation and detection of multiple nonelectroactive analytes, in this case of glutamate and of choline, a metabolite of acetylcholine, with a single implantable device. This results in a 3-in-1 multifunctional neural probe that integrates multi-analyte sensing, on-probe reference electrode and local chemical delivery.

7.2 Results and discussion

The fabrication procedure was optimized to be compatible with our existing silicon-based neural probe design (150 μm thick, 144 μm width, and 9 mm long).[3,21] Here, for proof of concept, a chemtrode is demonstrated (Figure 7.1b–e) incorporating a Pt microelectrode array (2 × 2) at the tip, which consists of a nano-based IrOx reference electrode, a glutamate sensing electrode, a choline sensing electrode, a control electrode, and a back-sided microfluidic channel. The fabrication process (Figure 7.2a) is described in the ESI† in detail and can be summarized as (1) integration of an ultra-thin, free-standing microfluidic channel via a customized PDMS thin-film transfer process (Figure 7.2a i and ii), (2) construction of a nano-based IrOx reference microelectrode via electrodeposition (Figure 7.2a iii and v); (3) deposition of enzyme mixture onto two closely juxtaposed permselective membrane-modified working electrodes for the detection of glutamate and choline via PDMS microstamping (Figure 7.2a). In our thin-film transfer process, it is important to keep the top surface of the mould flat. To this end, we fabricated the mould from a polished flat top silicon wafer. Through two steps of time-controlled DRIE etching, a silicon mould with two different depths is formed to enable the transfer of free-standing ultra-thin PDMS channels in one step (Figure 7.2b).

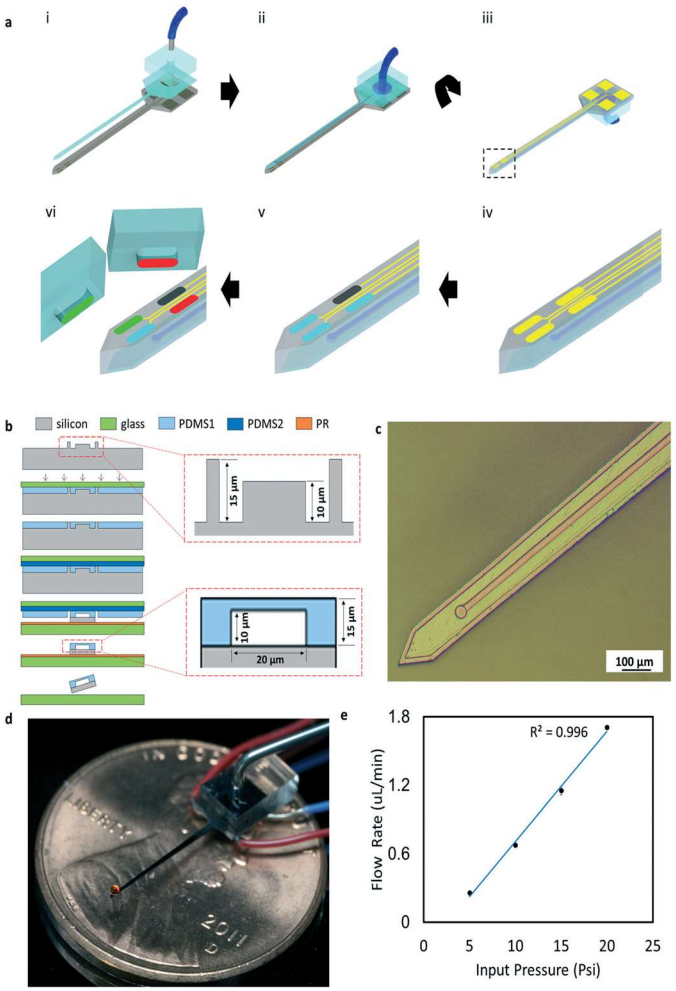

Figure 7.2. a) Multi-functional neural probe fabrication process. i) An exploded-view drawing of the microfluidic channel on the back of the microprobe; ii) back side of the microprobe; iii) front side of the microprobe; iv) microprobe shank tip showing Pt microelectrode array (yellow); v) reference electrode (black) and permselective membrane coating (light blue); vi) PDMS stamping to transfer two different enzymes to designated microelectrodes (red and green). b) Customized thin-film transfer process for microfluidic channel fabrication. c) Optical image showing the outlet of the microfluidic channel at the back of the probe tip. d) Optical image showing the delivery of dye solution to the outlet of the microfluidic channel at the back of the probe tip. e) Demonstration of a linear relationship between flow rate and pumping pressure (R2 = 0.996) and high repeatability of the measure (n = 3 per pressure point for a representative microprobe). Error bar: standard error.

Specifically, one layer of PDMS thin-film with channel, cured against the silicon mould with two different depths, was transferred directly to the back side of the probe SiO_2 surface by oxygen plasma bonding to form an enclosed channel, with the silicon probe itself as the channel

bottom surface and PDMS as the cover. To avoid probe fracture during the transfer process, silicon probes were temporarily fixed on a glass slide with photoresist (PR, AZ 5214/non-exposed SU-8), which was subsequently dissolved in acetone. Thanks to the rigid glass backing used to pick up the PDMS, the features are dimensionally stable. An alignment accuracy of <5 μm can be achieved using a contact mask aligner (Neutronix Quintel 7000). This produced a PDMS microfluidic channel, with a length of 9 mm, a total thickness of 15 μm, and a channel dimension of 10 × 20 μm (thickness × width) that enables precise chemical delivery at flow rates ranging from 0.25 to 1.75 μL min−1 with pumping pressure from 5 to 20 psi. The tested flow rates are similar to other chemtrodes.10 While higher flow rates could be achieved by increasing the pumping pressure up to 60 psi without PDMS delamination, such high rates increase the risk of tissue deformation and liquid backflow along the probe shank. A 40 μm-diameter fluid outlet (Figure 7.2c), formed in the same moulding process, was placed on top of the PDMS membrane such that fluid is ejected perpendicular to the probe surface instead of towards the probe tip to avoid channel occlusion22 during the probe insertion process. Local injection of chemical solution (Figure 7.2d) with nanoliter precision can be controlled by the pumping pressure and duration. Flow rates were measured in triplicate at 4 different pumping pressures (5–20 psi) to demonstrate the expected linear relationship between pressure and flow rate ($R^2 = 0.996$) and low variability across replicate measures (Figure 7.2e).

In this proof of concept design, the microfluidic channel is integrated onto the back side of the existing Si probe. The ejected chemicals diffuse from the fluid outlet to the sensors on the front, separated by the thickness of the probe (150 μm). The advantage of this approach is that the sensors are less impacted by dilution effects than they would otherwise be if the fluid outlet was on the front of the probe. Nevertheless, the current set-up may not be suitable for certain applications

where a more localized delivery in the immediate vicinity of the electrodes is desired. In such cases, fluidic outlets can be easily fabricated on the front by either (1) transferring PDMS channels to the probe front after allocating sufficient space for the fluidic interface; or (2) creating vias in the probe shank to connect the fluidic channels on the back. Further, more sophisticated PDMS structures, with multi-channels or multi-shanks, can be molded and transferred to the corresponding Si probes in one step.[5,18] Our prior work has demonstrated that PDMS channels with a spacing of 20 μm can be achieved providing stable, leak-free operation at 60 psi,[23] such that it should be possible to accommodate 3 microfluidic channels on the current platform. In addition, the thickness of the probe can be further reduced simply by starting with a thinner silicon substrate without changing the fabrication process – silicon probes with 50 μm thickness have been fabricated in our lab. We do not anticipate problems with probe fracture during the transfer process since the probes are temporarily fixed to a glass substrate using photoresist. Further, we do not expect the long-term stability of the probes to be impacted by addition of the ultra-thin (15 μm) PDMS channel due to its extremely low stiffness (1 MPa vs. 100 GPa, PDMS vs. Si).

To construct an on-probe reference electrode, one microelectrode of the MEA was first deposited with Pt nanoparticles (PtNP) to enhance the surface area using a previously described non-cytotoxic electrodeposition procedure,[3,24,25] followed by IrOx electrodeposition (0.0–0.6 V, 100 cycles). A typical cyclic voltammogram of IrOx electrodeposition on a PtNP/Pt microelectrode is shown in ESI† (Figure. S6). The IrOx film has been shown to be mechanically stable and biocompatible.26–29 Although the potential of IrOx film shows strong pH dependence, the small dynamic range of normal brain pH (7.15–7.4) makes this issue unimportant in most cases.30 Recently, we9 and others[30–32] validated that the open circuit potential of the IrOx film remained stable over a two-week period. Although electrophysiological recording and electrical

stimulation with the IrOx electrode were not performed in this study, the impedance of the nano-based IrOx electrodes, 4.48 ± 0.25 kΩ (n = 5) at 1 kHz, was found to be significantly lower than unmodified Pt microelectrodes (~20 kΩ at 1 kHz).5 After the deposition of the Nafion layer, the impedance of the IrOx electrode increased to 15.21 ± 1.18 kΩ (n = 5) at 1 kHz. Here, the performance of the IrOx, as a reference electrode (RE), was verified by amperometric detection of H_2O_2, which is the byproduct of the oxidase-based enzymatic reactions, at Pt microelectrodes (0.6 V vs. IrOx), employing H_2O_2 concentration step changes (0–80 μM; sensitivity: 2516.1 ± 20.1 μA mM^{-1} cm^{-2}; limit of detection: 0.13 ± 0.01 μM), showing high stability and repeatability (Figure 7.3a). The nano-based IrOx RE was further tested in the context of glucose sensors, where crosslinked enzyme layers were applied on top of permselective membrane (poly-mphenylenediamine (PPD) and Nafion)-modified Pt electrodes (see ESI† for details of permselective layer and enzyme deposition). The deposited PPD and Nafion layers acted as size and charge exclusion membranes, allowing hydrogen peroxide molecules to pass through to the Pt electrode surface but excluding common interferents (e.g., negativelycharged ascorbic acid (AA) and positively-charged dopamine (DA)) present in the brain extracellular fluid.[18,20,33] The performance of a representative glucose sensor in stirred phosphate-buffered saline (PBS) solution is shown in Figure 7.3b showing a linear concentration–response from 0–360 μM glucose and response time of ~2 s. Further data from multiple probes is provided in ESI† Figure S5 demonstrating a sensitivity of 52.2 ± 5.5 μA mM− 1 cm−2 and a calculated detection limit of 1.5 ± 0.8 μM (n = 6). Selectivity is demonstrated by the lack of response to the physiological interferents, AA and DA, at physiologically relevant concentrations34,35 (Figure 7.3c).

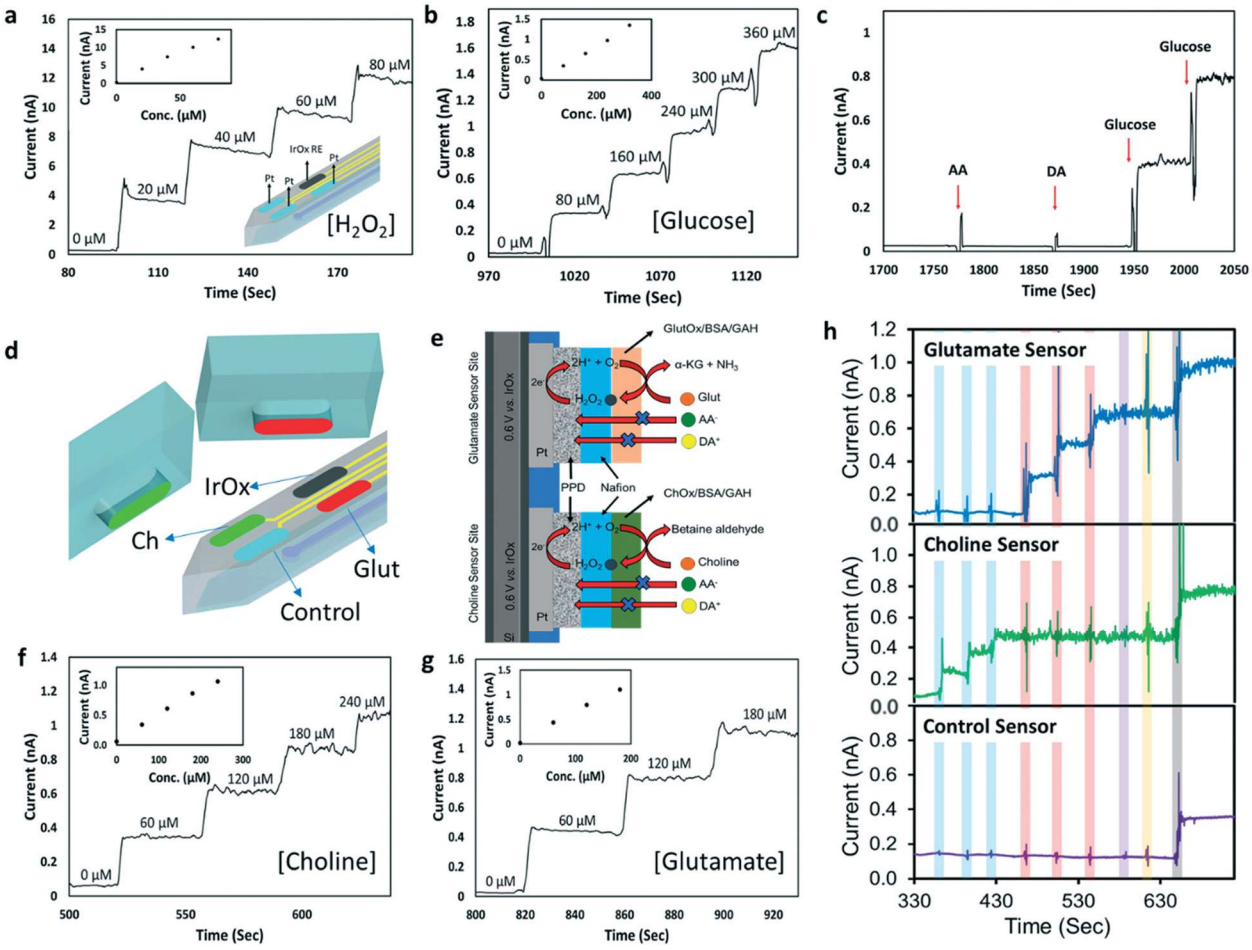

Figure 7.3. a) A representative current–time response of the microelectrode array to increasing concentrations of H_2O_2 with IrOx as an on-probe reference electrode (0.6 V vs. IrOx). Insert: plot of current vs. H_2O_2 concentration. b) A representative current–time response of the microelectrode array to increasing concentrations of glucose with IrOx as an on-probe reference electrode (0.6 V vs. IrOx). Insert: plot of current vs. glucose concentration. c) A representative current–time response to glucose and electroactive interferents. The sensor response at a constant potential of 0.6 V (vs. IrOx) was monitored upon sequential injections to give 250 μM AA, 5 μM DA, 160 μM glucose, and 320 μM glucose. d) Schematics of a microelectrode array showing the location of the IrOx reference electrode, control electrode, and enzyme-stamped glutamate and choline sensors. e) Schematic of the final dual glutamate/choline sensor configuration. f) A representative current–time response of a choline oxidasestamped electrode (of an MEA limited to such coated electrodes) to increasing concentrations of choline (0.6 V vs. IrOx). Insert: plot of current vs. choline concentration. g) A representative current–time response of a glutamate oxidase-stamped electrode (of an MEA limited to such coated electrodes) to increasing concentrations of glutamate (0.6 V vs. IrOx). Insert: plot of current vs. glutamate concentration. h) Combined sensing of glutamate and choline on a representative MEA at a constant potential of 0.6 V (vs. Ag/AgCl). The individual sensor responses of the MEA were monitored upon sequential injections to give stepwise final concentrations as follows: 60 μM choline, 120 μM choline,180 μM choline (blue), 180 μM choline/60 μM glutamate, 180 μM choline/120 μM glutamate, 180 μM choline/180 μM glutamate

(pink), 180 μM choline/180 μM glutamate/250 μM AA (purple), 180 μM choline/180 μM glutamate/250 μM AA/5 μM DA (yellow), and 180 μM choline/180 μM glutamate/250 μM AA/5 μM DA/20 μM H_2O_2 (grey).

To achieve simultaneous sensing of more than one nonelectroactive analyte, PDMS stamping[11,12] was adapted to selectively and sequentially transfer each of the two different enzyme/BSA mixtures – glutamate oxidase/BSA and choline oxidase/BSA – onto two distinct, juxtaposed microelectrodes (∼100 μm separation, Figure 7.3d) previously coated with permselective layers as described in ESI, followed by crosslinking via glutaraldehyde vapor (see ESI† for full details of the stamping procedure and Figure S1–S4). For dual sensing, one of the 4 microelectrodes remained free of enzyme and served as a control electrode, and another (top left) was converted to an on-probe reference electrode as described above. A schematic of the various permselective and enzyme layers of the constructed dual sensor and the sensing mechanism is shown in Figure 7.3e. The choline and glutamate sensors were first characterized in stirred PBS solution, separately (i.e. on probes with only one of the two enzymes applied, see ESI† for methods). Figure 7.3f and g show linear responses of representative electrodes to serial additions of choline and glutamate, respectively, each with a response time of ∼2 s. Sensitivities for choline and glutamate of 74.8 ± 4 μA mM^{-1} cm^{-2} (n = 4) and 84.7 ± 15 μA mM^{-1} cm^{-2} (n = 3), were obtained with calculated detection limits of 4.1 ± 1.4 μM and 3.8 ± 1.9 μM, respectively (ESI† Figure S5). Subsequently, the performance of the dual sensor platform was assessed and shown to display zero crosstalk among glutamate, choline and control sites at the concentrations tested, and to exclude interfering species (Figure 7.3h).

The integrated functions of electrochemical sensing and chemical delivery were initially tested in brain phantoms (0.6% w/v agarose in artificial cerebrospinal fluid, aCSF). Figure 7.4a shows the reproducibility of glucose detection following repeated local injection of a glucose

solution (800 μM in aCSF) at 20 psi for pumping durations of 2 s and 0.2 s. Selectivity of glutamate and choline detection by the dual sensor is shown in Figure 7.4b (see ESI for further methodological details).

Validation of the integrated microbiosensor/chemical delivery platform in vivo was conducted with microprobes acutely inserted into the dorsal striatum of the rat brain. Figure 7.4c shows glucose detection following repeated local injection of 4 mM glucose at 20 psi with increasing injection durations. The more transient nature of the signals compared to injections into brain phantoms is likely due to active uptake of glucose. Interestingly, the amplitude of the signal reached a plateau at an injection duration of 1.2 s, but the area under the curve continued to increase. This may be due to acute activation of glucose transport, a possibility supported by the overshooting below baseline after injection, but this requires further investigation. Preliminary validation of the glutamate/choline dual sensor is shown in Figure 7.4d demonstrating detection of both glutamate and choline following injections of a mixture of the two compounds. The need for higher concentrations of analytes when delivered to live brain tissue compared to static agar phantoms is likely due to the presence of both active cellular uptake mechanisms and diffusion into circulating blood in the former condition, reducing the concentration attained at the electrode surface. We observed the same phenomenon in our previous studies.[5] Post-calibration of the sensors upon removal from the brain demonstrated a less than 20% reduction in signal amplitude for the three analytes, compared with pre-calibration data. Such decreases are commonly reported for all types of implantable electrochemical sensors and is attributed to biofouling (e.g., protein aggregation on the sensor surface). The shelf life of the fabricated sensors is limited by the stability of both the on-probe IrOx reference electrode and enzymes on the electrode surfaces. For the IrOx reference electrode, we[9] previously

demonstrated that the performance was stable for at least 2 weeks and preferred to use them within a day or two of their preparation. Similarly, we have not tested the probes beyond two weeks in vivo. The long-term stability and biocompatibility of the sensors will be a subject for future investigation and may include incorporation of anti-fouling biopolymers such as 2-methacryloyloxethylphosporylcholine (MPC).[36–38]

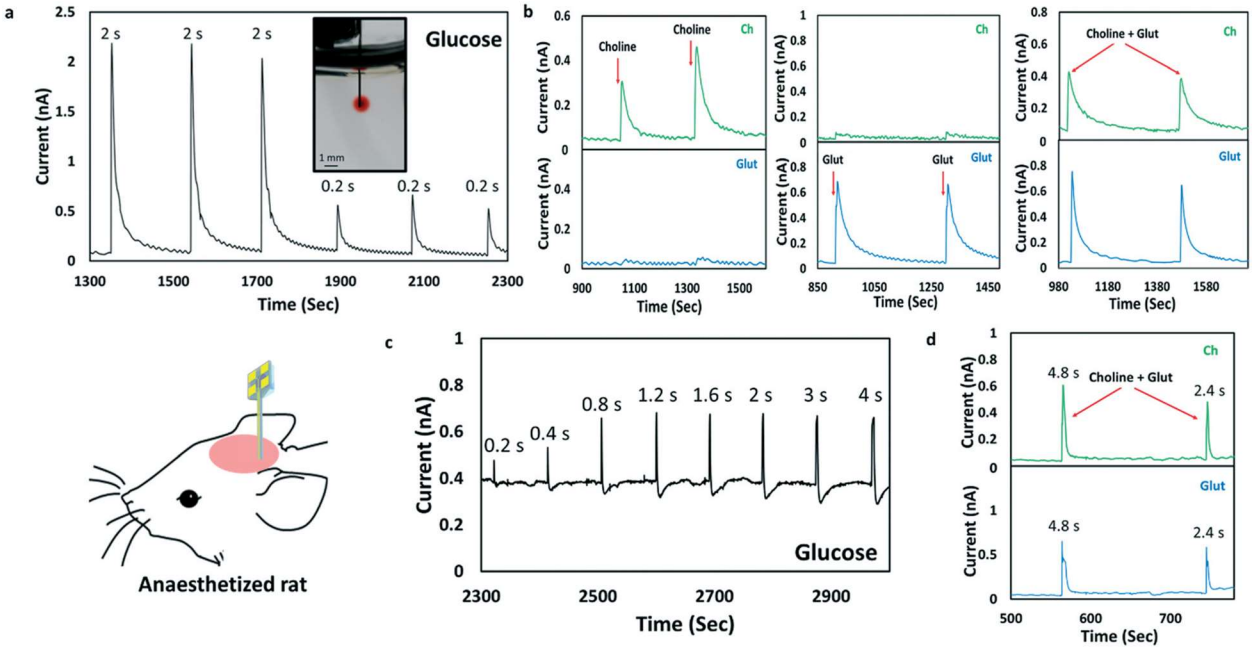

Figure 7.4. Sensor validation in brain phantoms and in vivo. a) In vitro testing of 800 µM glucose injection and detection in 0.6% agarose gel. The slow decrease in the glucose concentration is due to pure diffusion in this un-mixed medium. Pumping pressure: 20 psi. Insert: optical image demonstrating delivery of liquid (aqueous solution with red dye) into a brain phantom (0.6% agarose gel). b) Selectivity of glutamate (Glut) and choline (Ch) dual sensor. From left to right: local injection of choline or glutamate alone (800 µM in aCSF) and a choline/glutamate mixture (800 µM in aCSF). Pumping pressure: 10 psi. c) In vivo glucose (4 mM) injection and sensing in rat striatum. Injection pressure was kept at 20 psi with increasing injection duration. d) Dual detection of glutamate and choline in rat striatum following injection of a choline/glutamate mixture in aCSF (50 mM for each analyte). Pumping pressure 20 psi.

7.3 Conclusion

We present an approach to the fabrication of multifunctional neural microprobes using a novel PDMS thin-film transfer process to transfer microfluidic channels to silicon based neural probes. Incorporation of PDMS enzyme stamping and an integrated on-probe reference electrode permits simultaneous detection of multiple analytes together with local delivery of agents that can both validate biosensor function and manipulate neuronal activity. Although a single microfluidic channel was employed here, the approach can be readily scaled up with additional channels for multiple chemical delivery. The integration of these multiple functions on a single platform removes the need for implanting multiple probes, with the dual benefits of reducing brain damage and surgical complexity.

7.4 References

1. N. Obidin, F. Tasnim and C. Dagdeviren, Adv. Mater., 2019, 1901482.
2. J. P. Seymour, F. Wu, K. D. Wise and E. Yoon, Microsyst. Nanoeng., 2017, 3, 16066.
3. B. Wang, L. Feng, B. Koo and H. G. Monbouquette, Electroanalysis, 2019, 31, 1249–1253.
4. K. Wassum, V. Tolosa, J. Wang, E. Walker, H. Monbouquette and N. Maidment, Sensors, 2008, 8, 5023–5036.
5. X. M. Wen, B. Wang, S. Huang, T. Y. Liu, M. S. Lee, P. S. Chung, Y. T. Chow, I. W. Huang, H. G. Monbouquette, N. T. Maidment and P. Y. Chiou, Biosens. Bioelectron., 2019, 131, 37–45.
6. J. Zhou, L. Zhang and Y. Tian, Anal. Chem., 2016, 88, 2113–2118.
7. O. Frey, T. Holtzman, R. McNamara, D. Theobald, P. Van Der Wal, N. De Rooij, J. Dalley and M. Koudelka-Hep, Sens. Actuators, B, 2011, 154, 96–105.

8. E. Walker, J. Wang, N. Hamdi, H. G. Monbouquette and N. T. Maidment, Analyst, 2007, 132, 1107–1111.
9. V. M. Tolosa, K. M. Wassum, N. T. Maidment and H. G. Monbouquette, Biosens. Bioelectron., 2013, 42, 256–260.
10. J. Y. Sim, M. P. Haney, S. I. Park, J. G. McCall and J.-W. Jeong, Lab Chip, 2017, 17, 1406–1435.
11. H. Shin, H. J. Lee, U. Chae, H. Kim, J. Kim, N. Choi, J. Woo, Y. Cho, C. J. Lee and E.-S. Yoon, Lab Chip, 2015, 15, 3730–3737.
12. H. J. Lee, Y. Son, J. Kim, C. J. Lee, E.-S. Yoon and I.-J. Cho, Lab Chip, 2015, 15, 1590–1597.
13. J. Chen, K. D. Wise, J. F. Hetke and S. C. Bledsoe, IEEE Trans. Biomed. Eng., 1997, 44, 760–769.
14. S. T. Retterer, K. L. Smith, C. S. Bjornsson, K. B. Neeves, A. J. Spence, J. N. Turner, W. Shain and M. S. Isaacson, IEEE Trans. Biomed. Eng., 2004, 51, 2063–2073.
15. K. Seidl, S. Spieth, S. Herwik, J. Steigert, R. Zengerle, O. Paul and P. Ruther, J. Micromech. Microeng., 2010, 20, 105006.
16. L. Lin and A. P. Pisano, J. Microelectromech. Syst., 1999, 8, 78–84.
17. K. Neeves, C. Lo, C. Foley, W. Saltzman and W. Olbricht, J. Controlled Release, 2006, 111, 252–262.
18. T. L. Liu, X. Wen, Y.-C. Kung and P. Y. Chiou, 2017 IEEE 30th International Conference on Micro Electro Mechanical Systems (MEMS), pp. 663–666.
19. B. Wang, B. Koo, L. W. Huang and H. G. Monbouquette, Analyst, 2018, 143, 5008–5013.
20. B. Wang, B. Koo and H. G. Monbouquette, Electroanalysis, 2017, 29, 2300–2306.
21. T. T. C. Tseng and H. G. Monbouquette, J. Electroanal. Chem., 2012, 682, 141–146.

22. Z.-J. Chen, G. T. Gillies, W. C. Broaddus, S. S. Prabhu, H. Fillmore, R. M. Mitchell, F. D. Corwin and P. P. Fatouros, J. Neurosurg., 2004, 101, 314–322.

23. Y.-C. Kung, K.-W. Huang, Y.-J. Fan and P.-Y. Chiou, Lab Chip, 2015, 15, 1861–1868.

24. C. Boehler, T. Stieglitz and M. Asplund, Biomaterials, 2015, 67, 346–353.

25. B. Wang, X. Wen, P. Y. Chiou and N. T. Maidment, Electroanalysis, 2019, 31, 1641–1645.

26. K. Yamanaka, Jpn. J. Appl. Phys., 1989, 28, 632–637.

27. J. D. Weiland and D. J. Anderson, IEEE Trans. Biomed. Eng., 2000, 47, 911–918.

28. E. Slavcheva, R. Vitushinsky, W. Mokwa and U. Schnakenberg, J. Electrochem. Soc., 2004, 151, E226–E237.

29. S. A. Marzouk, S. Ufer, R. P. Buck, T. A. Johnson, L. A. Dunlap and W. E. Cascio, Anal. Chem., 1998, 70, 5054–5061.

30. R. K. Franklin, M. D. Johnson, K. Scottt, J. H. Shim, H. Nam, D. Kipket and R. B. Brown, IEEE Sens. J., 2005, 1400–1403.

31. R. K. Franklin, S. Joo, S. Negi, F. Solzbacher and R. B. Brown, IEEE Sens. J., 2009, 1086–1089.

32. H. Yang, S. K. Kang, C. A. Choi, H. Kim, D.-H. Shin, Y. S. Kim and Y. T. Kim, Lab Chip, 2004, 4, 42–46.

33. N. Wahono, S. Qin, P. Oomen, T. Cremers, M. de Vries and B. Westerink, Biosens. Bioelectron., 2012, 33, 260–266.

34. E. Eriksson, G. Engberg, O. Bing and H. Nissbrandt, Neuropsychopharmacology, 1999, 20, 287–296.

35. R. Spector, N. Engl. J. Med., 1977, 296, 1393–1398.

36. S. H. Ye, J. Watanabe, Y. Iwasaki and K. Ishihara, Biomaterials, 2003, 24, 4143–4152.

37. T. Goda, M. Tabata, M. Sanjoh, M. Uchimura, Y. Iwasaki and Y. Miyahara, Chem. Commun., 2013, 49, 8683–8685.

38. J. Sibarani, M. Takai and K. Ishihara, Colloids Surf., B, 2007, 54, 88–93.

Chapter 8: Electroenzymatic Choline Sensing at Near the Theoretical Performance Limit

Chapter 8 is a manuscript published with the following citation:

Huang, I.W., Clay, M., Cao, Y., Nie, J., Guo, Y. and Monbouquette, H.G., 2021. Electroenzymatic choline sensing at near the theoretical performance limit. *Analyst*, *146*(3), pp.1040-1047.

ABSTRACT

A high performance, electroenzymatic microsensor for choline based on choline oxidase (ChOx) immobilized on Pt coated with permselective polymer layers has been created that exhibits sensitivity approaching the theoretical performance limit. Sensor construction was guided by simulations performed with a detailed mathematical model. Implantable microsensors with an array of electroenzymatic sensing sites provide a means to record concentration changes of choline, an effective surrogate for acetylcholine due to its very rapid turnover in the brain, and other neurochemicals in vivo. However, electroenzymatic sensors generally have insufficient sensitivity and response time to monitor neurotransmitter signaling on the millisecond timescale with cellular-level spatial resolution. Model simulations suggested that choline sensor performance can be improved significantly by optimizing immobilized ChOx layer thickness and minimizing the thicknesses of permselective polymer coatings as well. Electroenzymatic choline sensors constructed with a ~5 μm-thick crosslinked ChOx layer atop 200 nm-thick permselective films (poly(mphenylenediamine) and Nafion) exhibited unprecedented sensitivity and response time of 660 ± 40 nA μM^{-1} cm^{-2} at 37 °C and 0.36 ± 0.05 s, respectively, while maintaining excellent selectivity. Such performance characteristics provide greater flexibility in the design of microelectrode array (MEA) probes with near cellular-scale sensing sites arranged in more dense arrays. Also, faster response times enable better resolution of transient acetylcholine signals and

better correlation of these events with electrophysiological recordings so as to advance study of brain function.

8.1 Introduction

A deep understanding of information processing in the brain is critical for rational development of effective treatments for complex neurological disorders including drug addiction. Brain processes are controlled by neuronal networks whose functioning is evidenced both by neurochemical signaling and electrophysiological events. Thus, there is great incentive to develop advanced technologies for neurochemical and electrophysiological recordings with similar spatiotemporal resolution in vivo so that this data may be correlated and used to unravel network functions. Current implantable devices enable electrophysiological recordings simultaneously from large numbers of interconnected neurons at millisecond temporal and cellular-scale spatial resolution.[1–5] However, techniques for neurochemical recording have yet to achieve such high spatiotemporal resolution due to slow sensor kinetics exacerbated by the need for selectivity against the complex background of brain extracellular fluid.[6–14] Historically, broadly applicable neurotransmitter detection in vivo has been accomplished using microdialysis probes coupled to analytical instrumentation (e.g., high performance liquid chromatography (HPLC)). However, the typical minute-to-minute temporal resolution and relatively large size of the probes has limited utility of this technique, although there have been recent impressive advances both in probe size and sampling rate.[15,16]

Micromachined microprobes supporting an array of microelectrode sensing sites have emerged as alternative tools to monitor concentration changes for a limited number of neurochemicals. These microsensors, once implanted in the brain, are in direct contact with

extracellular fluid, potentially providing a means for near-real time neurochemical sensing.[17–21] Sites on these microelectrode array (MEA) microprobes may be modified with permselective polymer films and immobilized redox enzymes to create selective electroenzymatic sensors. For example, the electroenzymatic choline (Ch) sensor studied in this work consists of a platinum (Pt) microelectrode coated first with permselective polyphenylenediamine (PPD) and Nafion films and then a layer of cross-linked choline oxidase (ChOx). ChOx catalyzes the 4-electron oxidation of Ch to glycine betaine in the presence of oxygen to give two equivalents of hydrogen peroxide (H2O2), which diffuse through the underlying polymer layers to the electrode surface where they are electrooxidized thereby generating a current signal indicating the presence of Ch.

$$\mathrm{Ch} + \mathrm{O_2} \xrightarrow{\mathrm{ChoX}} \text{betaine aldehyde} + \mathrm{H_2O_2} \quad (1)$$

$$\text{Betaine aldenyde} + \mathrm{O_2} + \mathrm{H_2O} \xrightarrow{\mathrm{ChoX}} \text{glycine betaine} + \mathrm{H_2O_2} \quad (2)$$

Electrooxidizable interfering species existing in brain extracellular fluid such as dopamine (DA) and ascorbic acid (AA), which are larger than H2O2 and charged, are blocked from the electrode surface by the PPD and negatively charged Nafion films through a combination of size exclusion and charge repulsion mechanisms. The high specificity of ChOx for Ch provides selectivity against non-electroactive species other than Ch.[22]

Choline is a useful surrogate for the important neurotransmitter, acetylcholine (ACh), which is turned over very rapidly to Ch and acetate in the brain.[23] Our group and others have demonstrated successfully the feasibility of such electroenzymatic Ch sensors with response times in the ~1 s range for the detection of Ch both in vitro and in vivo.[14,19,21,24] An alternative approach to achieve selective detection of Ach directly is to co-immobilize acetylcholinesterase and ChOx

on an electrode and to employ fast-scan cyclic voltammetry (FSCV) rather than constant potential amperometry. However, a FSCV sampling rate of 10 Hz (100 ms sampling interval) leads to an effective response time of ∼1 s as well (sampling at 10 Hz cannot resolve ∼100 ms events).[25,26] Such 1 s temporal response times still are not fast enough to detect rapid neurotransmitter signaling events that are thought to occur on the millisecond time scale. Furthermore, the previously published sensitivities are too low to create small microsensors with cellular-scale spatial resolution.

To address these challenges of spatiotemporal resolution, a mathematical model has been developed for devices of this type. Our previous glutamate (Glut) sensor modelling and experimental studies showed that performance can be improved dramatically by engineering the compositions and thicknesses of the immobilized enzyme and permselective film compositions.[27,28] To construct an electroenzymatic sensor, the protein catalyst most commonly is immobilized by loading a mixture of enzyme and BSA on the microelectrode surface and crosslinking with glutaraldehyde (GAH).[9,11,14,20,29–31] The resulting enzyme layer thicknesses typically have been in the 10 μm range to ensure adequate signal. Our simulation results suggested that such thick coatings cause elevated mass-transfer resistances leading to long response times.[28] If enzyme activity and accessibility could be preserved well during the immobilization process, the density of active enzyme in the layer could be increased so that layer thicknesses could be reduced with an actual enhancement in sensitivity. The systematic optimization of Glut sensors based on the guidance of our simulations led to a remarkable 6-fold improvement in sensitivity and a 10-fold reduction in response time to 80 ms.[28]

In this work, a model of electroenzymatic Ch sensors was developed and used to guide sensor optimization in the same manner as was done for Glut sensors previously.[28] Simulations of

Ch sensors similarly illustrated the importance of depositing enzyme layers with optimal thicknesses, dependent on the active enzyme concentration, in order to maximize H_2O_2 generation near the electrode surface. Such an approach shortens diffusion times and improves sensor response. Retention of enzyme activity was enhanced by exploring additional enzyme crosslinkers and changes to the enzyme immobilization conditions. The optimized, thinner immobilized ChOx layer resulted in sensors with higher sensitivities approaching theoretical limits, significantly faster response times, low detection limits, and excellent selectivity.

8.2 Experimental

8.2.1 Reagents

Nafion (5 wt% in lower aliphatic alcohols and water, 15–20% water), m-phenylenediamine (PD), bovine serum albumin (BSA) lyophilized powder, choline oxidase (ChOx, from Alcaligenes sp.), choline chloride (Ch), glutaraldehyde solution (25% in water, GAH), L-ascorbic acid (AA), 3-hydroxytyramine (dopamine, DA), sodium phosphate dibasic, sodium chloride, and hydrogen peroxide solution (30%) were purchased from Sigma-Aldrich (St Louis, MO). Sulfuric acid (30%), hydrochloric acid (36.5–38%), bis(sulfosuccinimidyl)suberate (BS3), sulfo-(ethylene glycol bis (sulfosuccinimidyl succinate)) (EGS), and (1-ethyl-3-(3-dimethylaminopropyl) carbodiimide hydrochloride) (EDC) were purchased from Thermo Fisher Scientific (Pittsburgh, PA). Ag/AgCl glassbodied reference electrodes with NaCl electrolyte (3 M) and a 0.5 mm-diameter Pt wire auxiliary electrode were obtained from BASi (West Lafayette, IN). Sodium phosphate buffer (PBS, pH 7.4) was composed of 50 mM sodium phosphate dibasic and 100 mM sodium chloride. Four-inch, 150 μm silicon wafers were purchased from Silicon Valley Microelectronics (Santa Clara, CA).

8.2.2 Instrumentation

Electrochemical preparation and calibration of the microsensors were performed using a Versatile Multichannel Potentiostat (model VMP3) equipped with the 'p' low current option and N'Stat box driven by EC-LAB software (Bio-Logic USA, LLC, Knoxville, TN) in a three-electrode configuration consisting of the sensing electrode, a Pt wire auxiliary electrode, and a Ag/AgCl reference electrode. The film thicknesses on microelectrodes were determined by milling pores on the deposited films using a focused ion beam (FIB) and measuring cross-section thicknesses using a scanning electron microscope (Nova 600 SEM/FIB System).

8.2.3 Sensor preparation

Figure 8.1 shows a scanning electron micrograph (SEM) and optical microscopy image of the microelectrode array (MEA) tip of a single probe used in this work. The probe shafts were 150 μm thick, 140 μm wide and 9 mm long with four 6000 μm2 (40 μm × 150 μm) Pt recording sites arranged in pairs at the tip. Microelectrode array probes were manufactured using microelectromechanical system (MEMS) fabrication techniques as described in our previous work.[11] Each microsensor was cleaned with 0.1 M H_2SO_4 solution by cycling the potential between −0.2 V and 1.5 V at a scan rate of 50 mV s^{-1} vs. Ag/AgCl, repeated at least 4 times. Afterward, a poly-phenylenediamine (PPD) film was electrodeposited from a 5 mM PD solution in phosphate-buffered saline (0.1 M PBS) by holding the voltage constant at 0.85 V vs. Ag/AgCl until the total transferred charge reached 7.6×10^{-7} coulombs. A Nafion layer then was applied by dip-coating a 2% Nafion solution (diluted from stock with 4 : 1 IPA : water) once, followed by annealing at 115 °C for 20 min. Next, enzyme immobilization was accomplished by manually swiping ∼1 μL of a ChOx and BSA mixture (at different ratios, see below) onto the microelectrode sites using a microliter syringe and exposing the deposit to different crosslinkers, also as described below.

Twelve to 15 coatings of enzyme solution typically give a ~4 μm thick ChOx layer on the electrode surface, depending on solution concentration and environmental conditions.

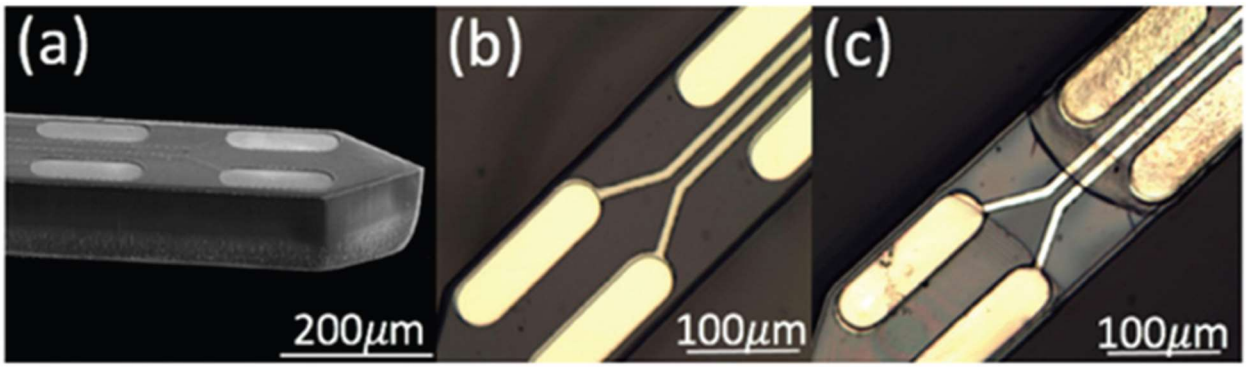

Figure 8.1. (a) SEM and (b) optical microscopy images of the bare microelectrode array (MEA) probe. (c) Optical microscopy image of the MEA probe after polymer and enzyme deposition.

In this work, four different crosslinkers, including three amine-to-amine crosslinkers with different spacer arm lengths (GAH, BS3, EGS) and one carboxyl-to-amine crosslinker (EDC), were used and compared. Each set of crosslinking conditions was optimized individually before making comparisons. A previously loaded ChOx/BSA mixture was exposed to 5% GAH vapor for 1 min at room temperature or to manually applied ~0.5 μL BS3 (100 mg ml^{-1} in PBS) or ~0.5 μL EGS (100 mg ml^{-1} in PBS). Alternatively, when EDC was used as crosslinker, EDC was mixed directly with ChOx and BSA to give a final EDC concentration of ~6.3 mg ml^{-1} in PBS prior to rapid application onto a microelectrode. After the crosslinking step, sensors were stored dry at 4 °C for 48 h prior to testing.

8.2.4 Electrochemical measurements

To determine the selectivity and sensitivity, a constant potential of 0.7 V vs. Ag/AgCl was applied to the microsensors in rapidly stirred PBS buffer solution at pH 7.4 and ~37 °C. Selectivity

was assessed relative to AA and DA, which are electroactive interferents commonly found in brain extracellular fluid (ECF). Their typical concentrations in ECF are in the range of a few hundred μM for AA and from nM to a few μM for DA.[32,33] In selectivity tests, the current signal from a probe immersed in stirred buffer was allowed to stabilize. Subsequently AA and DA were added separately to the beaker to reach final concentrations of 250 μM AA and 10 μM DA. Next, serial injections were made to give final concentrations of 20–100 μM Ch and 20 μM H_2O_2 to determine sensitivities to both species. The response time ($t_{0–90\%}$) of Ch sensors was estimated from the current response to a near step change in concentration created by analyte injection into rapidly stirred PBS buffer.

8.2.5 Mathematical model and simulations

Simulations of sensor performance were generated using an adaptation of our established model for electroenzymatic glutamate (Glut) sensors that was modified to include ChOx rather than glutamate oxidase in the immobilized enzyme coating.[28,34] In the model, a set of partial differential equations describe one-dimensional transport as well as consumption or generation rates of Ch, O_2, and H_2O_2 within and between separately modelled PPD, Nafion, and immobilized enzyme domains,

$$\varepsilon_i \frac{\partial C_i}{\partial t} = -\alpha_j D_i \frac{\partial^2 C_i}{\partial x^2} + r_{i,j} \quad (3)$$

In each equation for species i in coating j, C_i is the concentration within the pores of the coating, t is time, x is the distance from the Pt microelectrode surface, ε_j is the void fraction, αD is the effective diffusivity, and r is the reaction rate (if enzyme is present). In these equations, each

chemical species is allowed to diffuse freely within the void spaces of the coatings in which they are soluble, as defined by the transport parameters that were used in the Glut sensor model, assuming them to be unchanged; the Ch diffusion coefficient at 25 °C has been reported,[35] and the diffusivity at 37 °C (1.816×10^{-9} m^2 s^{-1}) was calculated according to the Stokes–Einstein equation. It is also assumed that the H_2O_2 electrooxidation kinetics on the Pt microelectrode sensing sites is also unchanged from that used previously.36 Enzymatic reaction rates reflect ChOx kinetics for the full oxidation of Ch to glycine betaine, recognizing that the betaine aldehyde intermediate does not leave the enzyme active site,

$$r_{ch} = \frac{k_{cat} c_e c_{Ch} c_{O_2}}{k_{m,O_2} c_{Ch} + k_{m,Ch} c_{Ch} + c_{Ch} c_{O_2}} = 2 r_{O_2} \quad (4)$$

Since the measured kinetic rates for ChOx isolated from Alcaligenes sp. are for air-saturated concentrations of O_2 (~206 μM) and do not account for oxygen dependence,[37] which is important to consider in modelling biosensors, O_2 kinetics terms were added and the published, apparent k_{cat} and $k_{m,Ch}$ were multiplied by a factor of $(1 + k_{m,O_2}/c_{O_2})$ to give the k_{cat} and $k_{m,Ch}$ in the rate equation above and to reflect the intrinsic, O_2- dependent rates (k_{m,O_2} was assumed to be 1 mM). The resulting enzymatic rate constants were found to be consistent with values found from ChOx isolated from *A. globiformis* at the temperature and pH used (k_{cat} = 95 s^{-1}; $k_{m,Ch}$ = 5.07 mM; $k_{m,O2}$ = 1 mM),[38] suggesting that ChOx isolated from either organism may show similar kinetic behavior. The enzyme concentration (mol L^{-1}) depends on the fraction of ChOx in the layer and the void fraction, and was calculated in the same way as in the Glut model based on a protein density of 1.41 g mL^{-1}: $c_e = [1000 \times 1.41 \times f_{ChOx} \times (1 - \varepsilon)]/MW_{ChOx}$, where f_{ChOx} is the mass fraction of protein in the immobilized enzyme layer that is ChOx. Numerical solutions were

obtained using COMSOL (COMSOL, Inc., Los Angeles), employing boundary conditions that simulate a step-change in Ch concentration from 0 to 20 μM at the microsensor surface at time, t = 0.

8.3 Results and discussion

8.3.1 Effect of enzyme loading and activity

In an effort to improve enzyme activity retention, the alternative homobifunctional crosslinkers BS3 and EGS (that like GAH also react with amine groups at neutral pH) were studied. We demonstrated earlier that Glut sensors made with enzyme crosslinked with BS3 showed great improvement in sensitivity compared to those crosslinked with GAH, probably due to the longer spacer arm of BS3, 11.4 Å vs. 5 Å.[28] In this work, in addition to BS3 and GAH, the crosslinker, EGS, with the longest spacer arm of 16.1 Å was used in order to explore further the effect crosslinker spacer arm length on resulting sensor performance. Before making a comparison among these three reagents, crosslinking conditions were investigated individually by varying crosslinker concentrations and vapor exposure times to find the best conditions for use of the reagent for Ch sensor fabrication. Representative EGS optimization data is illustrated in Figure 8.2 (b), which shows that above ~100 mg mL^{-1} EGS, there is no statistically meaningful improvement in sensor sensitivity.

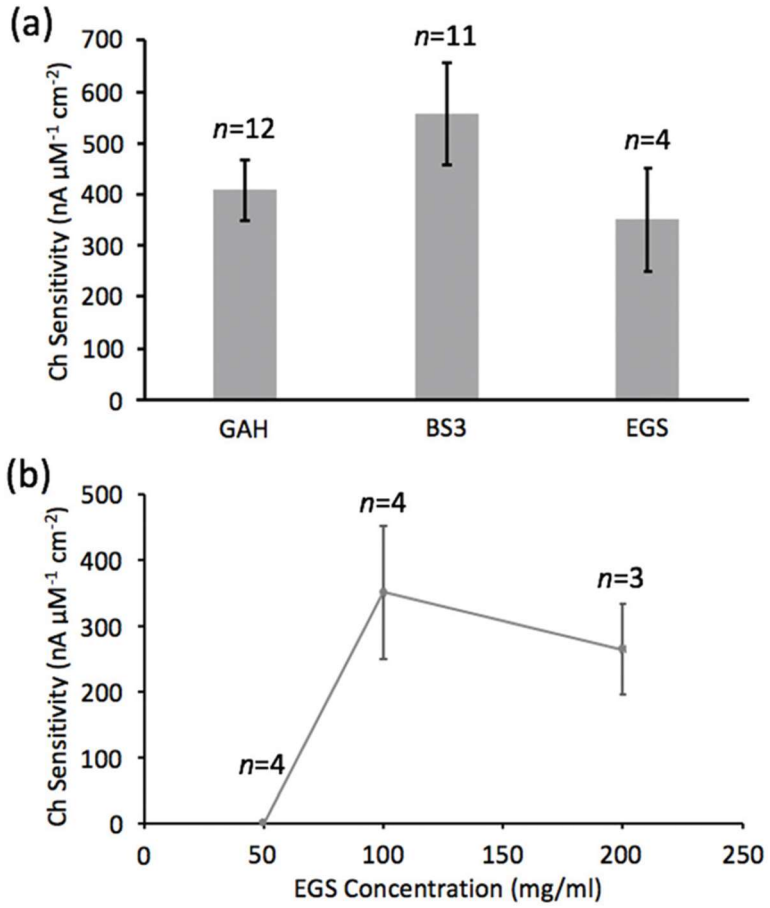

Figure 8.2. (a) Ch sensitivity comparison between GAH, BS3 and EGS crosslinked Ch sensors with error bars giving 95% confidence intervals. (b) Effect of EGS concentration on the Ch sensitivity. In all cases, the mass ratio of ChOx to BSA was 2 : 3 and the enzyme layer was ~3–4 μm thick.

After this optimization process, Ch sensors made with BS3-crosslinked ChOx showed the greatest sensitivity relative to those crosslinked with GAH or EGS, 557 ± 99 nA μM^{-1} cm^{-2} (n = 11), 409 ± 59 nA μM^{-1} cm^{-2} (n = 12) and 351 ± 101 nA μM^{-1} cm^{-2} (n = 4), respectively. This ~1.5-fold improvement in sensitivity of Ch sensors crosslinked with BS3 compared to those crosslinked via GAH agrees with our previous work on Glut sensor optimization.[28] However, it was interesting to observe the decrease in Ch sensitivity when the longest crosslinker, EGS, was used. We hypothesize that spacer arm length not only affects the accessibility of substrate to the

enzyme active site, but also the void fraction within the enzyme layer and the concentration of active enzyme entrapped in the BSA/ChOx network. The optimal crosslinker will immobilize ChOx as densely as possible without becoming a barrier to diffusion or restricting any enzyme conformational changes that may occur during catalysis. The moderate length of the BS3 spacer arm may be preferable, because such a length (11.4 Å) is long enough to reduce enzyme crowding and improve active site accessibility, but also short enough to maintain a stable, high enzyme concentration in the crosslinked BSA/ChOx network.

The effort to improve Ch sensor performance was carried further by conducting a study of the effect of deposited enzyme concentration on sensor performance, which can be performed straightforwardly by changing the relative proportion of ChOx and BSA without changing enzyme layer thickness of ~3–4 μm. The mass fraction of ChOx (f_{ChOx}) was varied from 0.2 to 0.8 for the sensors coated with PPD and Nafion and crosslinked with BS3. The experimental Ch sensitivity versus f_{ChOx} plot showed that Ch sensitivity tends to fall above f_{ChOx} = ~0.4 and drops to zero at high enzyme concentration corresponding to f_{ChOx} = 0.8 (Figure 8.3). It is noteworthy that this general trend also was observed for GAH- and EGS-crosslinked Ch sensors. For the thin enzyme layers explored here, a decrease in Ch sensitivity at low f_{ChOx} was expected due to insufficient active enzyme available to turnover Ch at the high rate needed for a strong current signal. However, high relative enzyme concentration (low BSA concentration) also was found not to be preferable. This result again matched our previously published data on Glut sensor optimization showing that there are insufficient lysine groups available for crosslinking of the protein layer at low relative concentrations of lysine-rich BSA (Figure 8.3).

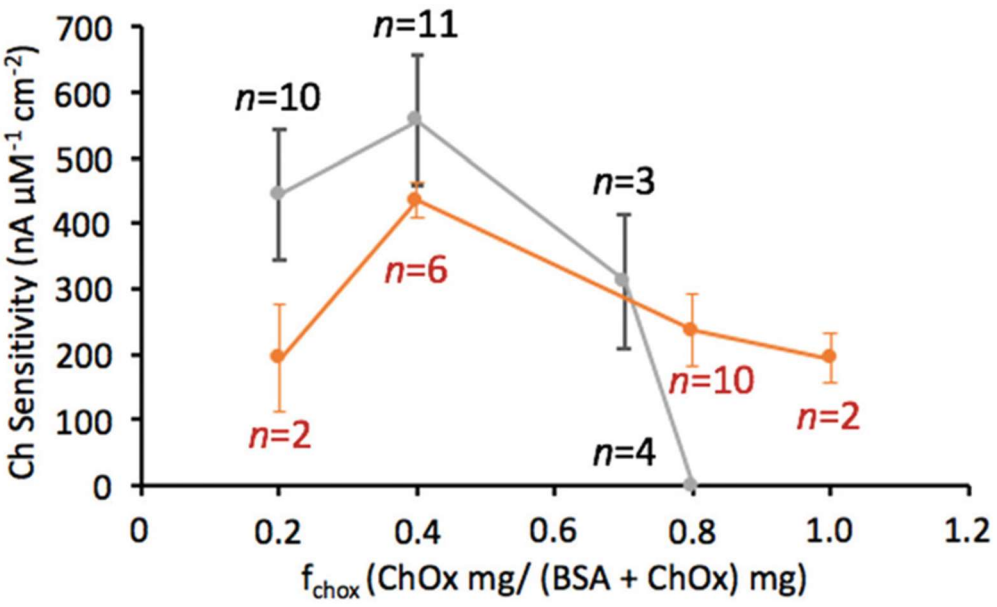

Figure 8.3. Effect of immobilized ChOx concentration on the Ch sensitivity of sensors crosslinked via BS3 (grey trace) and sensors crosslinked via EDC (orange trace). In all cases, the enzyme layer thickness was ~3–4 µm. Error bars represent 95% confidence intervals.

These consistent results prompted us to consider crosslinkers that react with carboxyl groups of which ChOx has an abundance on its surface. The heterobifunctional crosslinker, EDC, which crosslinks carboxyl and amine groups, was chosen due to its ready commercial availability. The mass fraction of ChOx was varied from $f_{ChOx} = 0.2$ to $f_{ChOx} = 1.0$ and the experimental results are shown as the orange trace in Figure 8.3. This amine-to-carboxyl crosslinker enabled the stable immobilization of ChOx in the absence of BSA ($f_{ChOx} = 1.0$). This data supports our unsurprising contention that the availability of crosslinkable functional groups on the enzyme surface plays an important role in stable enzyme immobilization at higher concentration. However, a decrease in Ch sensitivity at high enzyme concentration was still observed, which may be due to hindered accessibility of the enzyme active site and/or increased enzyme deactivation as more EDC, which has a very short spacer arm, reacts directly with ChOx instead of BSA. Overall, sensors crosslinked with EDC showed lower Ch sensitivity of 435 ± 27 nA $\mu M^{-1} cm^{-2}$ (n = 6) compared to those

crosslinked with BS3 at optimal values of f_{ChOx}. As a result, the BS3 crosslinked sensor with f_{ChOx} = 0.4 was chosen for future work due to its best sensitivity.

8.3.2 Optimized enzyme layer thickness

Figure 8.4 shows Ch sensitivity for varied thicknesses of the enzyme layer, using the optimal fChOx of 0.4 and best crosslinker (BS3). As expected, Ch sensitivity decreased sharply for enzyme layer thicknesses less than 3 μm due to insufficient deposited enzyme. Sensitivity reached a plateau as enzyme layer thickness increased beyond ~4 μm. Since response time is known to increase with layer thickness, a ChOx layer thickness of 4–6 μm was determined to be best to ensure both high Ch sensitivity and fast response time. The plateau in sensitivity for enzyme layers more than 3 μm thick may be due to the counterbalancing effects of greater enzyme availability and increasing mass-transfer limitation as the enzyme layer is thickened.

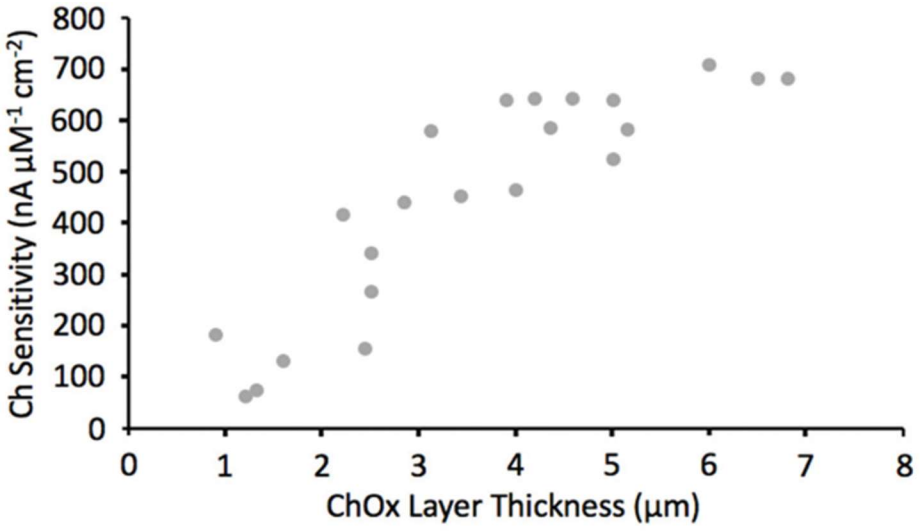

Figure 8.4. Sensitivity versus immobilized ChOx layer thickness. In all cases, f_{ChOx} = 0.4. All sensors were crosslinked with BS3. Each data point represents one trial.

8.3.3 Optimized sensor performance

The sensitivity of the best Ch sensor constructed was based on the slope of the linear range of calibration curves (0–100 μM Ch), and the detection limit was determined at a signal-tonoise ratio of 3. Ch sensors generated with optimal enzyme layer composition $f_{ChOx} = 0.4$, crosslinked with BS3, and with enzyme layer thickness in the 4–6 μm range showed high Ch sensitivity of 658 ± 40 nA $\mu M^{-1}cm^{-2}$ (n = 20), low detection limit of 0.34 ± 0.06 μM (n = 20), and excellent selectivity against two common interferents, AA and DA, tested at physiologically relevant concentrations (Figure 8.5). This detection limit is suitable for detecting Ch transients in the brain, which have been reported in the range of 0.5^{-2} μM in response to behavioural cues and up to ~6 μM following KCl injections.[39,40]

8.3.4 Response time

Response time is defined here as the time for the current signal to reach 90% of its steady-state value in response to a step change in Ch from zero to 60 μM in a stirred beaker. Compared to other sensors in the literature that reported response times of Ch sensors of ~1 s,[14,19] our improved sensor with thinner enzyme and permselective layers showed fast response time of 0.36 ± 0.05 s (n = 8) without compromising sensitivity and selectivity (Figure 8.6). The very rapid response of bare Pt to 10 μM H_2O_2 is also shown in Figure 8.6 as a benchmark, which is close to a step as expected. A comparison of the performance of reported Ch sensors illustrates the remarkably improved sensitivity and response time of the sensor reported here (Table 8.1).

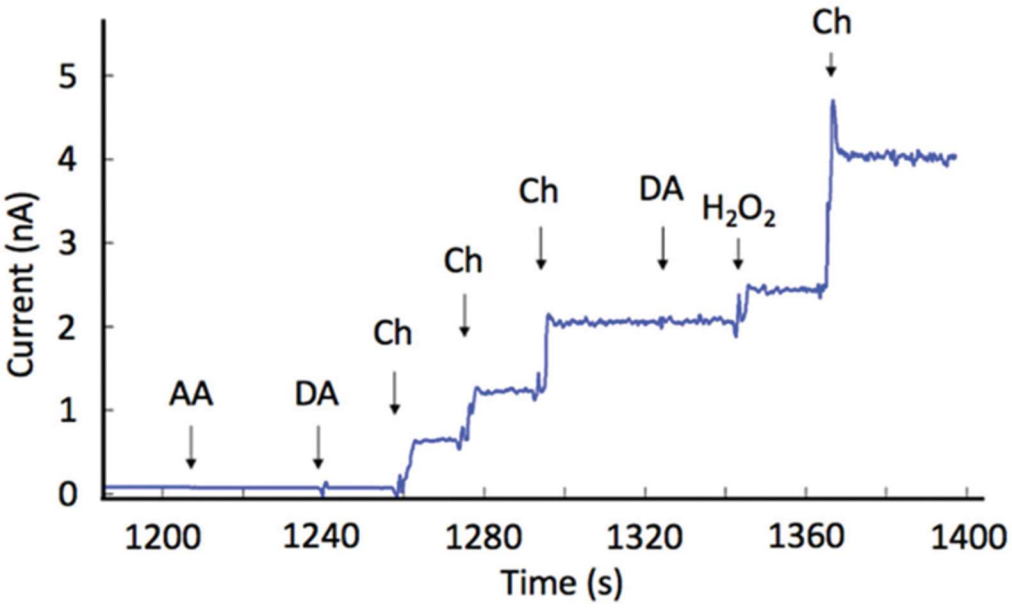

Figure 8.5. Representative current responses of optimized Ch sensors tested in batch with key interferents AA (250 μM), DA (5 μM), target Ch (final 20, 40, 60 μM in solution), interferent DA (final 15 μM in solution), H_2O_2 (20 μM) and Ch (final 100 μM in solution) in series.

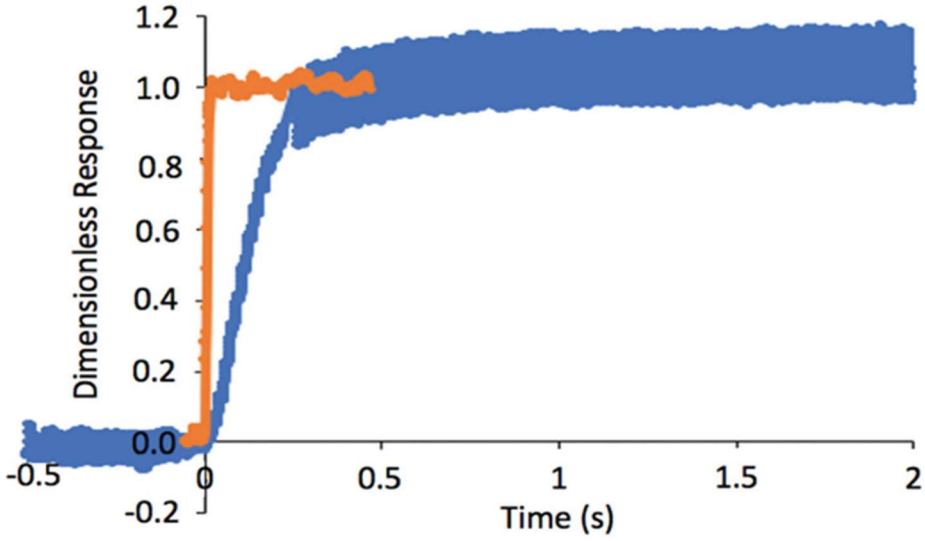

Figure 8.6. Representative optimized Ch sensor response to a step-change in Ch concentration from 0 to 60 μM (blue trace) and a step-change in H_2O_2 for a bare Pt sensor (orange trace) serving as a benchmark.

Table 8.1. Comparison of the performance characteristics of the Ch sensor of this work with other recently reported electroenzymatic Ch sensors.

Sensitivity (nA mM^{-1} cm^{-2})	Response time (s)	Limit of detection (mM)	Reference
654	0.35	0.34	This work
354	2	0.45	[41]
286	1.5	1.00	[14]
204	4	0.60	[42]
128	1.16	0.12	[19]
75	2	15.00	[43]

8.3.5 Stability

The stability of the Ch sensor in vitro was expressed as half-life, the amount of time required for the sensitivity to be reduced to one half of its original value, for sensors stored in PBS at 4 °C and tested periodically at 37 °C. The decay in sensitivity over time, nondimensionalized relative to the initial sensitivity, is shown in Figure 8.7. Results showed that Ch sensors crosslinked with BS3 (n = 4) had longer half-lives on average than those crosslinked conventionally with GAH (n = 4), which were ∼11 days and ∼8 days, respectively. After 2 weeks, the GAH-crosslinked Ch sensors exhibited less than 10% of initial sensitivity, whereas BS3-crosslinked Ch sensors retained 40% sensitivity over the same time period. The fast decrease in Ch sensitivity after 2 weeks for GAH-crosslinked sensors is likely due to the instability of the immobilized enzyme layer, which was readily observed under the microscope. We hypothesize that the smaller GAH is more likely

to form intramolecular bonds that do not contribute as well to a more stable three-dimensional network.[31]

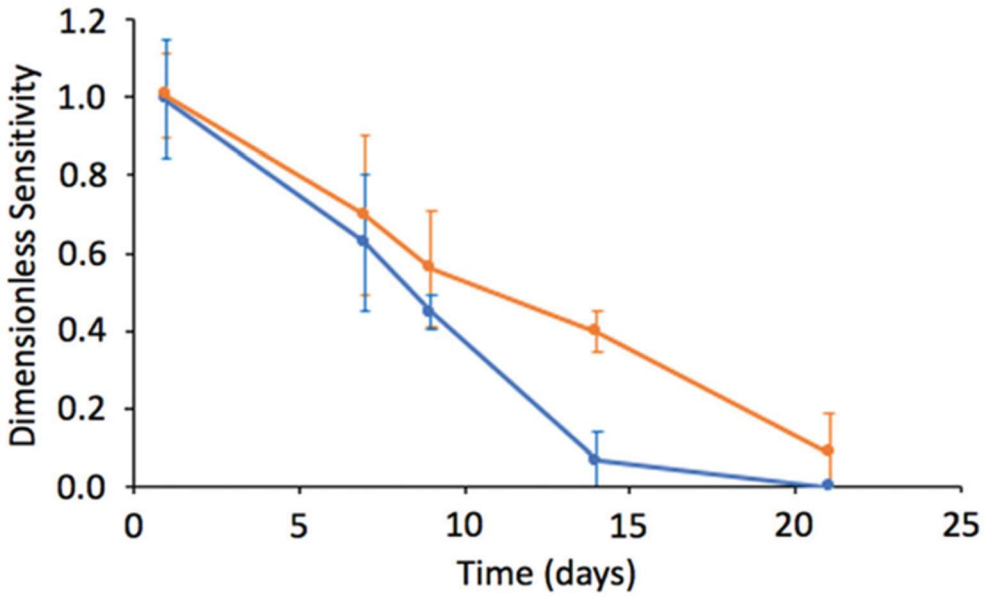

Figure 8.7. Stability of GAH-crosslinked (blue trace) and BS3-croslinked (orange trace) Ch sensors stored in PBS at 4 °C and tested periodically at 37 °C. Data shown with 95% confident intervals (n = 4 for both cases).

8.3.6 Simulations to determine theoretical performance limits

Simulations of optimized Ch sensors (Figure 8.8) predict the maximum theoretical sensitivities of sensors with the required permselective films, and the enzyme layer thicknesses and compositions that were tested experimentally. The fraction of active ChOx is expected to decrease upon immobilization and over time, prompting simulations to consider how sensitivity is affected when f_{ChOx} drops below 0.4. Experimental data suggest that f_{ChOx} is significantly reduced after immobilization, consistent with simulations and optimizations of Glut sensors.[28] In Ch sensors, experimental maximum sensitivities are consistent with a simulated f_{ChOx} of 0.2.

Comparison of experimental performance to theoretical predictions may suggest that sensors perform as though they have a thinner enzyme layer; this could be explained by considering the roughness of the immobilized enzyme layer's surface, which can result in a lower effective thickness.

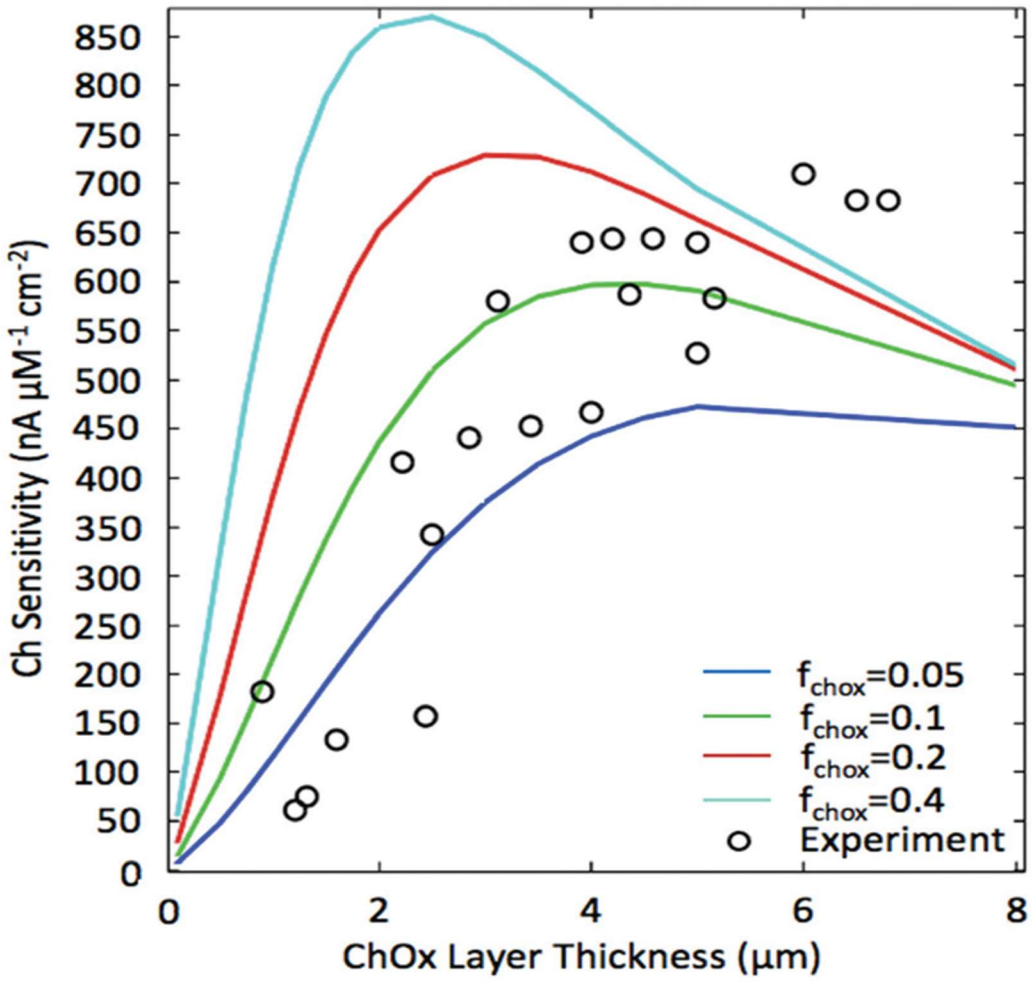

Figure 8.8. Simulated sensitivity over a range of ChOx layer thicknesses and fChOx within the layer. Experimental values included for reference.

Simulated response times increased linearly with increasing enzyme layer thicknesses as expected, but simulations also predict that response time could be as fast as 0.048 s for sensors

with an enzyme thickness of 5 μm rather than the 0.35 s found experimentally. Model modifications could be made to increase simulated response times without affecting sensitivity by incorporating in the model an accounting of Ch adsorption to protein surfaces. The likelihood of this type of interaction is supported by experimental data showing reduced response times for later additions of Ch (Figure 8.6), when more of the proposed Ch binding sites may already be filled. If this is true, it is likely that in vivo response times will approach the theoretical response times, which are significantly faster than those observed in vitro, although further work would be required before making definitive conclusions.

Oxygen dependence was investigated by simulating sensor response to varying O_2 and Ch concentrations. The linear range of the sensor was found to be determined linearly by the bulk concentration of O_2 for concentrations of Ch at least as high as 200 μM, where the concentration of O_2 must be >60% of the Ch concentration for >90% of the maximum sensor response or >150% of the Ch concentration for full sensor response. Since the concentration of O_2 in the brain is known to range from ~5 to 50 μM, it is plausible for Ch sensors to begin showing nonlinearity in vivo at Ch concentrations in the range of 10 to 100 μM, depending on O_2 availability.

8.4 Conclusions

A detailed mathematical model has been developed for an electroenzymatic Ch sensor to guide the optimization of sensor construction. Model simulations showed the importance of maximizing active enzyme concentration in the immobilized layer and predicted the optimal enzyme thickness to ensure both high sensitivity and fast response time. Therefore, an experimental optimization was conducted whereby enzyme activity retention is first improved

followed by an optimization of immobilized enzyme layer thickness. Such an approach resulted in a significantly improved Ch sensor with a 4–6 μm-thick crosslinked ChOx layer on a 200 nm-thick underlying permselective coating of PPD and Nafion, which shortened diffusion times and enhanced H_2O_2 generation near the electrode surface. This design modification led to unprecedent Ch sensitivity of 654 ± 40 nA μM^{-1} cm^{-2} (n = 20) and fast response time of 0.36 ± 0.05 s (n = 8) without compromising selectivity. The improved Ch sensors provide greater flexibility to fabricate more densely arrayed MEAs comprised of near-cellular-scale sensing sites. Such MEAs will facilitate better resolution of choline transients reflective of acetylcholine signals and better correlation of neurotransmitter signaling with electrophysiological activity.

8.5 References

1. J. Du, T. J. Blanche, R. R. Harrison, H. A. Lester and S. C. Masmanidis, PLoS One, 2011, 6, 26204.
2. G. Rios, E. V. Lubenov, D. Chi, M. L. Roukes and A. G. Siapas, Nano Lett., 2016, 16, 6857–6862.
3. J. J. Jun, N. A. Steinmetz, J. H. Siegle, D. J. Denman, M. Bauza, B. Barbarits, A. K. Lee, C. A. Anastassiou, A. Andrei, Ç. Aydın, M. Barbic, T. J. Blanche, V. Bonin, J. Couto, B. Dutta, S. L. Gratiy, D. A. Gutnisky, M. Häusser, B. Karsh, P. Ledochowitsch, C. Mora Lopez, C. Mitelut, S. Musa, M. Okun, M. Pachitariu, J. Putzeys, P. Dylan Rich, C. Rossant, W. Sun, K. Svoboda, M. Carandini, K. D. Harris, C. Koch, J. O'Keefe and T. D. Harris, Nature, 2017, 551, 232–236.
4. G. Hong and C. M. Lieber, Nat. Rev. Neurosci., 2019, 20, 330–345.

5. I. L. Jones, P. Livi and M. K. Lewandowska, Anal. Bioanal. Chem., 2011, 399, 2313–2329.
6. A. Jaquins-Gerstl and A. C. Michael, Analyst, 2015, 140, 3696.
7. H. Yang, A. B. Thompson, B. J. Mcintosh, S. C. Altieri and A. M. Andrews, ACS Chem. Neurosci., 2013, 4, 790–798.
8. Z. D. Sandlin, M. Shou, J. G. Shackman and R. T. Kennedy, Anal. Chem., 2005, 77, 7702–7708.
9. E. C. Rutherford, F. Pomerleau, P. Huettl, I. Strömberg and G. A. Gerhardt, J. Neurochem., 2007, 102, 712–722.
10. M. C. Parkin, S. E. Hopwood, D. A. Jones, P. Hashemi, H. Landolt, M. Fabricius, M. Lauritzen, M. G. Boutelle and A. J. Strong, J. Cereb. Blood Flow Metab., 2005, 25, 402–413.
11. K. M. Wassum, V. M. Tolosa, J. Wang, E. Walker, H. G. Monbouquette and N. T. Maidment, Sensors, 2008, 8, 5023–5036.
12. M. L. Rogers, D. Feuerstein, C. L. Leong, M. Takagaki, X. Niu, R. Graf and M. G. Boutelle, ACS Chem. Neurosci., 2013, 4, 799–807.
13. M. T. Bowser and R. T. Kennedy, Electrophoresis, 2001, 22, 3668–3676.
14. B. Wang, B. Koo, L. W. Huang and H. G. Monbouquette, Analyst, 2018, 143, 5008–5013.
15. M. Wang, N. D. Hershey, O. S. Mabrouk and R. T. Kennedy, Anal. Bioanal. Chem., 2011, 400, 2013–2023.
16. W. H. Lee, T. Ngernsutivorakul, O. S. Mabrouk, J. M. T. Wong, C. E. Dugan, S. S. Pappas, H. J. Yoon and R. T. Kennedy, Anal. Chem., 2016, 88, 1230–1237.
17. M. Malvaez, V. Y. Greenfield, A. S. Wang, A. M. Yorita, L. Feng, K. E. Linker, H. G. Monbouquette and K. M. Wassum, Sci. Rep., 2015, 5, 12511.

18. A. L. Collins, T. J. Aitken, I. Huang, C. Shieh, V. Y. Green, H. G. Monbouquette, S. B. Ostlund and K. M. Wassum, Biol. Psychiatry, 2019, 86, 388–396.
19. J. J. Burmeister, F. Pomerleau, P. Huettl, C. R. Gash, C. E. Werner, J. P. Bruno and G. A. Gerhardt, Biosens. Bioelectron., 2008, 23, 1382–1389.
20. A. Khan and S. A. Ghani, Biosens. Bioelectron., 2012, 31, 433–438.
21. D. Jerusalinsky, E. Kornisiuk, I. Izquierdo, J. A. Dani, D. Ji, F. M. Zhou, P. Kasa, Z. Rakonczay, K. Gulya, J. Lemiere, D. V. Gool, R. Dom, M. G. Garguilo, N. Huynh, A. Proctor, A. C. Michael, J. Cui, N. V. Kulagina, Q. Xin, R. M. Wightman, Z. Huang, R. Villarta-Snow, G. J. Lubrano, G. G. Guilbault, I. Karube, K. Yokoyama, E. Tamiya, J. L. Kawagoe, D. E. Niehaus, E. N. Navera, K. Sode, A. Guerrieri and F. Palmisano, Biosens. Bioelectron., 1997, 9, 1098–1106.
22. S. Ikuta, S. Imamura, H. Misaki and Y. Horiuti, J. Biochem., 1977, 82, 1741–1749.
23. M. G. Garguilo and A. C. Michael, J. Neurosci. Methods, 1996, 70, 73–82.
24. M. G. Garguilo, N. Huynh, A. Proctor and A. C. Michael, Anal. Chem., 1993, 65, 523–528.
25. R. Asri, B. O’Neill, J. C. Patel, K. A. Siletti and M. E. Rice, Analyst, 2016, 141, 6416–6421.
26. B. M. Kile, P. L. Walsh, Z. A. McElligott, E. S. Bucher, T. S. Guillot, A. Salahpour, M. G. Caron and R. M. Wightman, ACS Chem. Neurosci., 2012, 3, 285–292.
27. M. Clay and H. G. Monbouquette, ACS Chem. Neurosci., 2018, 9, 241–251.
28. I. Huang, M. Clay, S. Wang, Y. Guo, J. Nie and H. G. Monbouquette, Analyst, 2020, 145, 2602–2611.
29. J. J. Burmeister, F. Pomerleau, M. Palmer, B. K. Day, P. Huettl and G. A. Gerhardt, J. Neurosci. Methods, 2002, 119, 163–171.

30. J. J. Burmeister, F. Pomerleau, J. E. Quintero, P. Huettl, Y. Ai, J. Jakobsson, M. Lundblad, A. Heuer, J. T. Slevin and G. A. Gerhardt, Neuromethods, 2018, 130, 327–351.
31. I. Migneault, C. Dartiguenave, M. J. Bertrand and K. C. Waldron, BioTechniques, 2004, 37, 790–802.
32. B. Ghasemzedah, J. Cammack and R. N. Adams, Brain Res., 1991, 547, 150–154.
33. K. T. Kawagoe, P. A. Garris, D. J. Wiedemann and R. M. Wightman, Neuroscience, 1992, 51, 55–64.
34. F. Fan and G. Gadda, J. Am. Chem. Soc., 2005, 127, 2067–2074.
35. R. Fleming and L. J. Gosting, J. Phys. Chem., 1973, 77, 2371–2376.
36. S. B. Hall, E. A. Khudaish and A. L. Hart, Electrochim. Acta, 1997, 43, 579–588.
37. M. Ohta-fukuyama, Y. Miyake, S. Emi and T. Yamano, J. Biochem., 1980, 88, 197–203.
38. F. Fant and G. Gadda, J. Am. Chem. Soc., 2005, 127, 17954–17961.
39. J. P. Bruno, C. Gash, B. Martin, A. Zmarowski, F. Pomerleau, J. Burmeister, P. Huettl and G. A. Gerhardt, Eur. J. Neurosci., 2006, 24, 2749–2757.
40. V. Parikh, R. Kozak, V. Martinez and M. Sarter, Neuron, 2007, 56, 141–154.
41. A. H. Keihan, S. Sajjadi, N. Sheibani and A. A. Moosavi-Movahedi, Sens. Actuators, B, 2014, 204, 694–703.
42. H. S. Magar, M. E. Ghica, M. N. Abbas and C. M. A. Brett, Talanta, 2017, 167, 462–469.
43. H. Zhang, Y. Yin, P. Wu and C. Cai, Biosens. Bioelectron., 2012, 31, 244–250.

Chapter 9: Implantable Aptamer–field-effect Transistor Neuroprobes for in Vivo Neurotransmitter Monitoring

Chapter 9 is a manuscript published with the following citation:

Zhao, C., Cheung, K.M., Huang, I.W., Yang, H., Nakatsuka, N., Liu, W., Cao, Y., Man, T., Weiss, P.S., Monbouquette, H.G. and Andrews, A.M., 2021. Implantable aptamer–field-effect transistor neuroprobes for in vivo neurotransmitter monitoring. *Science Advances*, *7*(48), p.eabj7422.

ABSTRACT

While tools for monitoring in vivo electrophysiology have been extensively developed, neurochemical recording technologies remain limited. Nevertheless, chemical communication via neurotransmitters plays central roles in brain information processing. We developed implantable aptamer–field-effect transistor (FET) neuroprobes for monitoring neurotransmitters. Neuroprobes were fabricated using high-throughput microelectromechanical system (MEMS) technologies, where 150 probes with shanks of either 150- or 50-μm widths and thicknesses were fabricated on 4-inch Si wafers. Nanoscale FETs with ultrathin (~3 to 4 nm) In_2O_3 semiconductor films were prepared using sol-gel processing. The In_2O_3 surfaces were coupled with synthetic oligonucleotide receptors (aptamers) to recognize and to detect the neurotransmitter serotonin. Aptamer-FET neuroprobes enabled femtomolar serotonin detection limits in brain tissue with minimal biofouling. Stimulated serotonin release was detected in vivo. This study opens opportunities for integrated neural activity recordings at high spatiotemporal resolution by combining these aptamer-FET sensors with other types of Si-based implantable probes to advance our understanding of brain function.

9. 1 Introduction

Determining how information is encoded in brain function is at the heart of neuroscience. Discoveries in brain information processing lead to improved understanding of healthy brain function and the etiologies of neurological and neuropsychiatric disorders (1–6). Decoding neural function requires advanced technologies to make multiplexed measurements that approach the spatial scales and temporal dynamics of chemical neurotransmission. Implantable neural recording probes have emerged as powerful tools to monitor brain activity with high spatiotemporal resolution (7–9). Efforts in implantable electrode development have focused on monitoring electrical signals, which can be sorted and analyzed to decode spiking activity in single neurons (10, 11). With recent innovations in micro- and nanofabrication, materials science, surface functionalization, and electrical engineering, implantable neural devices have become more sophisticated so as to have increased densities of recording elements with reduced sizes (12–19). Recently, up to ~1000 electrophysiological recording units have been integrated into single neuroprobes of <100-μm width (16, 20).

We developed aptamer–field-effect transistor (FET) biosensors for electronic small-molecule detection under high ionic strength conditions (21–23). We used nanoscale In_2O_3 semiconducting films (3 to 4 nm) as an ultrasensitive platform for biosensing. Aptamers selected for specific target recognition were coupled to the semiconductor surfaces of FETs (23). Conformational changes of the negatively charged aptamer backbones occur upon target capture. The subsequent surface charge redistribution is detected by the voltage-gated semiconductor. This sensing mechanism is independent of the charge or electrochemical properties of the analytes themselves and thus represents a universal approach for monitoring small molecules (23).

We detected a number of different targets in complex physiological environments using aptamer FETs, including the neurotransmitters serotonin and dopamine, glucose, and the amino acid phenylalanine (21–24). Because of the high selectivity of the aptamers we use, aptamer-FET biosensors recognize their specific targets but not structurally similar molecules. We recently reported the real-time and simultaneous detection of serotonin and dopamine using aptamer-FET biosensor arrays, establishing a foundation for multiplexed monitoring of brain neurotransmitters and other targets (21). Here, we advance our approach by designing, fabricating, and testing implantable aptamer-FET neuroprobes to monitor the small-molecule neurotransmitter serotonin. We investigated device functionality in vitro, ex vivo, and in vivo (scheme shown in Figure 9.1). We designed Si-based neuroprobes with In_2O_3 FETs on the shank tips (Figure 9.1, A and B). Serotonin aptamers were functionalized on the In_2O_3 surfaces of the FETs to detect serotonin. We show that aptamer-FET neuroprobes can monitor serotonin flux in vivo in real time.

9.2 Results

A schematic illustration of the neuroprobe fabrication process is shown in Figure 9.2A. Here, microelectromechanical system (MEMS) technologies were used to produce neuroprobes in a high-throughput manner, where 150 probes were fabricated on each Si wafer. This fabrication process is compatible with conventional microfabrication processes, which is advantageous for integrating additional sensors and actuators previously fabricated on Si or other biomaterials (e.g., temperature, enzyme-based, photonic, and electrophysiology sensors, and optical and microfluidic actuators) (14, 16, 25–27). The MEMS fabrication approach enables the production of large numbers of devices needed for translation to neuroscience applications.

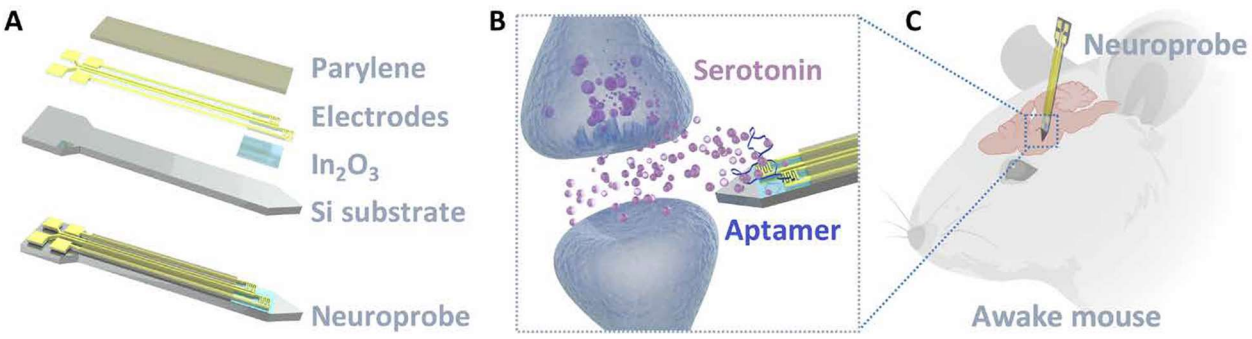

Figure 9.1. Schematic illustrations of the design and application of implantable aptamer-FET neuroprobes. (A) Layer-by-layer design of a neuroprobe with two FETs at the tip. Top to bottom: Parylene, Au electrodes, In_2O_3, the Si substrate, and a fully constructed neuroprobe. (B) Illustration showing released serotonin in the extracellular space monitored by an aptamer-FET neuroprobe (not to scale). (C) Illustration of a neuroprobe implanted in the brain of a mouse for in vivo neurotransmitter monitoring.

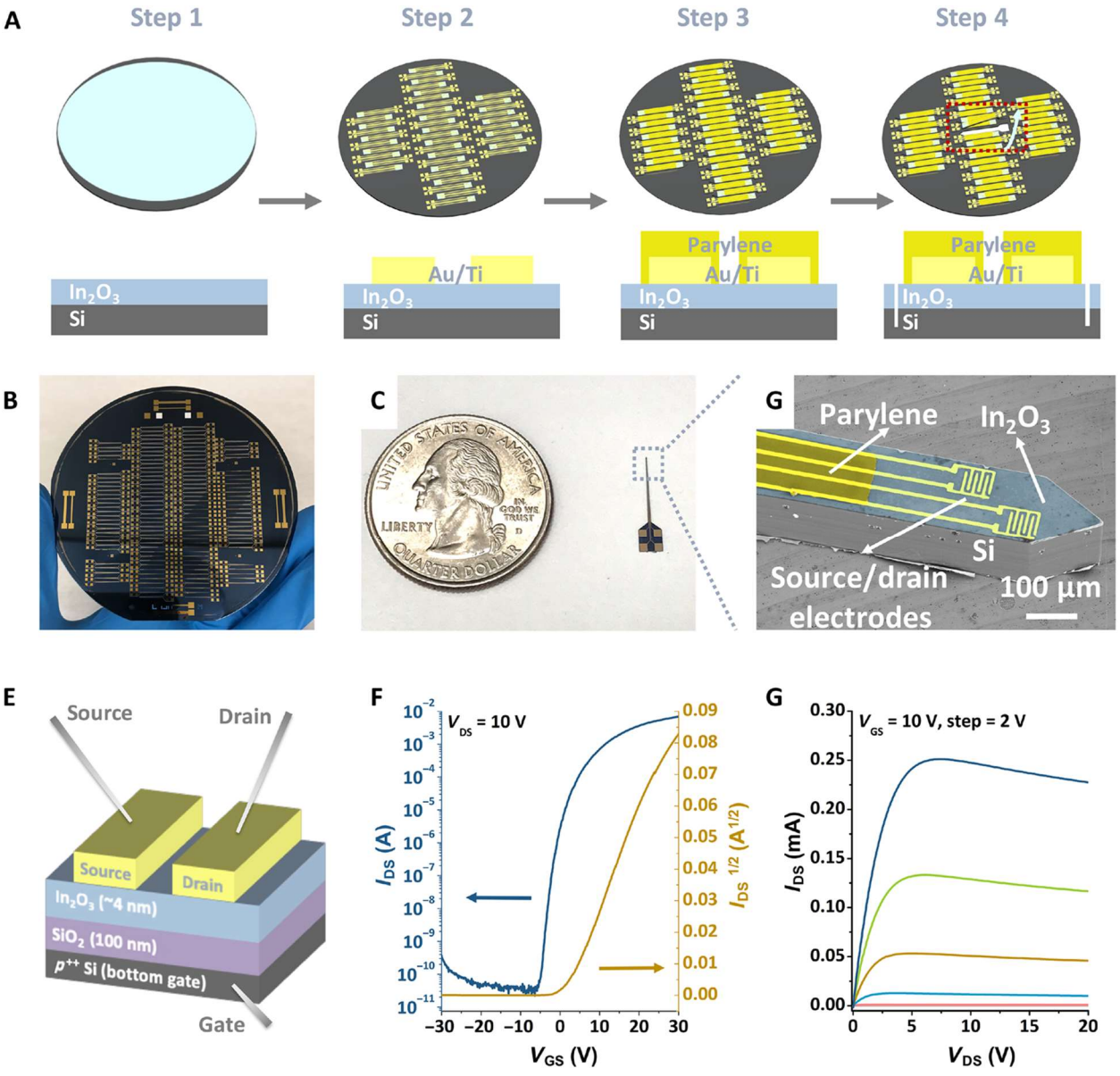

Figure 9.2. Neuroprobe fabrication and FET characterization. (A) Schematic illustration showing the neuroprobe fabrication process. (B) Photograph of a 4-inch Si wafer with 150 fabricated 150-µm neuroprobes after deep reactive-ion etching but before individual probe release. (C) Photograph showing a released 150-µm-wide by 150-µm-thick neuroprobe next to a U.S. quarter dollar coin to illustrate neuroprobe size. (D) Scanning electron microscope (SEM) image of the shank and tip of a 150-µm wide by 150-m-thick neuroprobe with two staggered FETs. False colors show the parylene layer, Au electrodes, In_2O_3, and the Si substrate. (E) Schematic illustration of the solid-state measurement setup (layers not to scale). (F and G) Representative transfer and output characteristics for 60 µm–by–80 µm FETs, respectively. Photo credit: Chuanzhen Zhao, UCLA.

Briefly, thin films of In_2O_3 were formed via sol-gel chemistry (28) by spin-coating an aqueous solution of indium (III) nitrate hydrate onto heavily doped 4-inch Si wafers (150-μm-thick p++ Si with 100-nm-thick SiO_2 on top) (step 1 in Figure 9.2A). We used In_2O_3 as the semiconductor because of the straightforward fabrication of thin (~3 to 4 nm) layers that impart high sensitivity associated with high surface-to-volume ratios and stable performance in electrolyte solutions compared with other metal oxides [e.g., indium-gallium-zinc oxide (IGZO) or ZnO] (29–31). The Au and Ti electrodes (30 and 10 nm thick, respectively) were then patterned on top of the In_2O_3 (step 2 in Figure 9.2A). In some cases, a thin layer of parylene (~1 μm) was coated on the probe surfaces to provide insulation of the interconnects (step 3 in Figure 9.2A). Parylene is a biocompatible and biostable material with excellent dielectric properties that is widely used in implanted medical devices, such as cardiac assist device and mandrel catheters (32, 33). The parylene layer at the tip of each probe shank was removed to expose the transistor area for sensing. Outlines of individual probes were defined using an additional photolithography step. Wafers were then etched through to release the probes (step 4 in Figure 9.2A). The fabrication process is described in detail in the Materials and Methods.

A 4-inch wafer with 150 probes is shown before the probe release step in Figure 9.2B. The entire wafer was semitransparent after the etching process used to define the probe outlines. A single probe is shown after release in Figure 9.2C. The neuroprobe shanks were characterized using scanning electron microscopy (SEM; Figure 9.2D). Pseudo-colors were assigned to different components, where parylene (dark yellow) is the insulating layer. The Au and Ti source and drain electrodes (yellow) were constructed in an interdigitated design to increase the channel width for higher sensitivity (23). The exposed Au in the interdigitated electrode region was insulated by an alkanethiol self-assembled monolayer, as described in the Materials and Methods. The In_2O_3 (light

blue, thin film without patterning in this fabrication process) was coated onto each 150-μm-thick Si wafer (gray). Each probe had an overall width of 150 μm, and two FETs (60 μm by 80 μm) were separated by 20 μm along the probe length and 10 μm across the probe width.

Solid-state measurements were carried out to test FET performance in a bottom-gate top-contact configuration (Figure 9.2E). Representative transfer and output characteristics are shown in Figure 9.2, F and G, respectively. Each FET measured 80 μm by 60 μm, and the FET channel width/length was 200 μm/5 μm. These miniaturized FETs showed high current on/off ratios (I_{on}/I_{off}) of ~108, comparable to our devices with millimeter dimensions (23).

For biosensing, FET-based neuroprobes were operated in electrolyte solutions via liquid gating. The FETs in electrolyte solutions showed improved transistor characteristics because of the high dielectric constant of physiological solutions (see equation and detailed explanation in the Supplementary Materials) (23). Two FETs were fabricated in a staggered configuration on the tip of each neuroprobe and were gated by a Ag/AgCl reference electrode (Figure 9.3A). A schematic of the liquid-gate transistor operation setup is shown in Figure 9.3B. Here, the electrical double layer formed in the electrolyte solution serves as the gate dielectric. Representative transfer and output characteristics are shown in Figure 9.3, C and D, respectively. The transfer curves of two different devices overlapped with minimal contribution from gate leakage currents (Figure 9.3C).

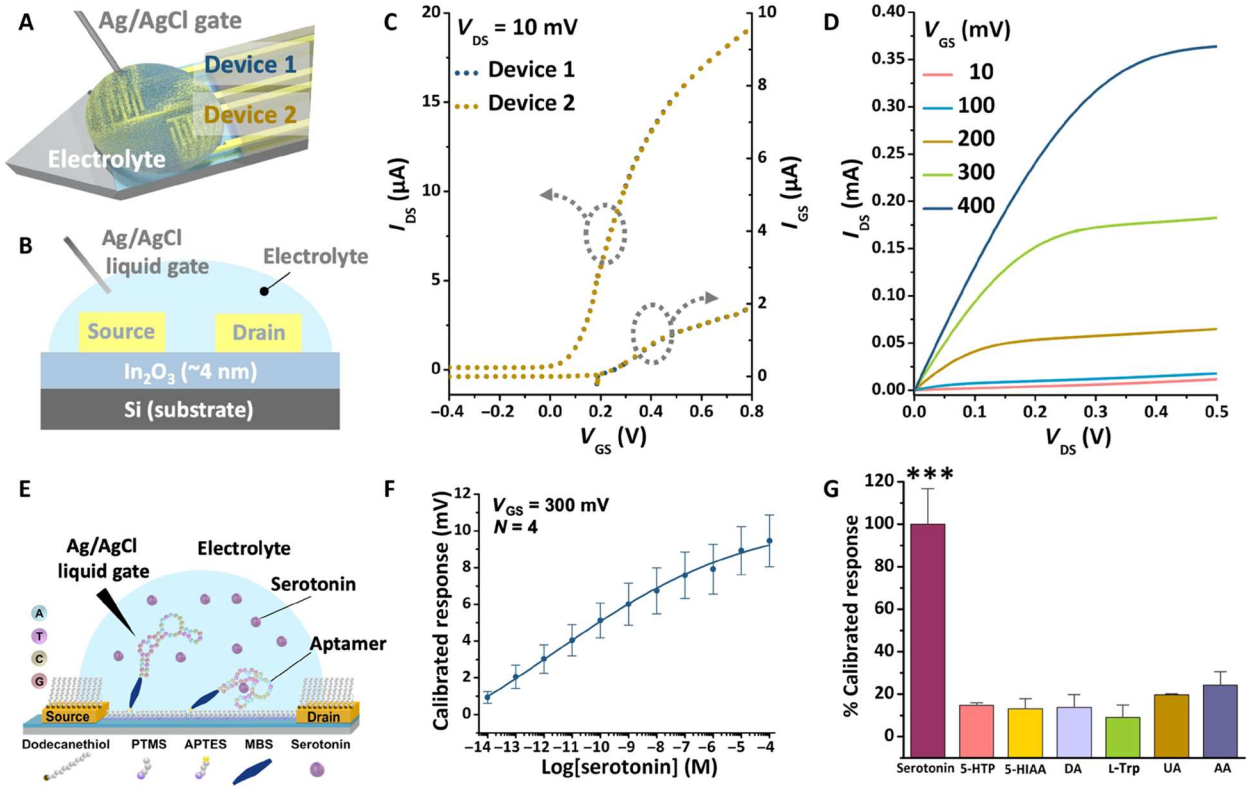

Figure 9.3. Neuroprobe biosensing in vitro. (A and B) Schematic illustrations of the liquid-gate measurement setup [layers not to scale in (B)]. (C) Representative transfer characteristics (IDS-VGS; left) and leakage current (IGS-VGS; right) for two transistors (curves are overlaid) on a single probe in phosphate-buffered saline. (D) Representative transfer characteristics (IDS-VDS) at different gate voltages showing typical transistor behavior with saturation. (E) Schematic illustration showing the surface functionalization for In_2O_3 transistor channels. PTMS, trimethoxy(propyl)silane; APTES, (3-aminopropyl)triethoxysilane; MBS, 3-maleimidobenzoic acid N-hydroxysuccinimide ester. (F) Serotonin aptamer-FET response curve in artificial cerebrospinal fluid (aCSF). Error bars are SEM from N = 4 FETs. (G) Serotonin aptamer-functionalized neuroprobe responses to biologically relevant concentrations of interferents versus serotonin in aCSF (100 nM): 100 μM l-5-hydroxytryptophan (l-5-HTP), 5-hydroxyindoleacetic acid (5-HIAA), dopamine (DA), l-tryptophan (l-Trp), 50 μM uric acid (UA), or 200 μM ascorbic acid (AA). Error bars are standard errors of the means for N = 4 FETs for serotonin and N = 3 FETs for nontarget molecules. ***P < 0.005 versus nontargets.

To construct biosensors, thiol-terminated DNA aptamers were immobilized onto In_2O_3 surfaces using (3-aminopropyl)triethoxysilane and 3-maleimidobenzoic acid N-hydroxysuccinimide ester for linking (Figure 9.3E) (21, 23). In vitro serotonin detection was performed in artificial cerebrospinal fluid (aCSF), which mimics the ionic strength and

composition of the brain extracellular fluid (34). Aptamer-FET neuroprobes detected serotonin over a large concentration range (fM to μM; Figure 9.3F). We used calibrated responses to minimize device-to-device variations [information on calculations is provided in the Supplementary Materials (23, 35)]. The serotonin detection range on neuroprobes with micrometer-scale FETs was similar to that previously reported for FET sensors with mm^2 dimensions because of the quasi–two-dimensional In_2O_3 semiconductor channels used in the design of FETs of both sizes (23).

Neuroprobes were selective in detecting serotonin with respect to serotonin precursors (i.e., tryptophan and l-5-hydroxytryptophan), the major serotonin metabolite 5-hydroxyindoleacetic acid, the monoamine neurotransmitter dopamine, and uric acid and ascorbic acid, all of which coexist in extracellular fluid (Figure 9.3G; see table S1 for statistics). Some of these species are present in brain extracellular fluid at 1000 × greater concentrations than serotonin; all are potential interferents during in vivo sensing (23, 36, 37). The selectivity of aptamer-FET neuroprobes is intrinsic to the aptamers. For other neurochemical sensing platforms, such as fast-scan cyclic voltammetry or enzyme-based neural probes, nonspecific signals generated via the oxidation or reduction of interfering electroactive species or nonspecific H_2O_2 production, respectively, can complicate target-specific and multiplexed neurotransmitter detection (38).

Brain tissue is a complex biological matrix. Neurotransmitters diffuse from release sites through tissue to probe recording sites over at least a couple hundred micrometers. To test the function of neuroprobes in solid matrices that mimic the tortuosity of brain tissue, we used 10 to 15% gelatin in aCSF to mimic the Young's modulus and stiffness (39) and physiological ionic environment of brain tissue. Gelatin was cast in 48-well plates, where each well mimics the size of a mouse brain (~1 cm in diameter). As shown in figure. S1, a hole was templated into each

gelatin mold for the addition of serotonin (100 nM) to simulate neurotransmitter release and diffusion in the brain (Figure 9.4A). This concentration was chosen to represent a physiologically relevant serotonin concentration (34, 36, 40–42).

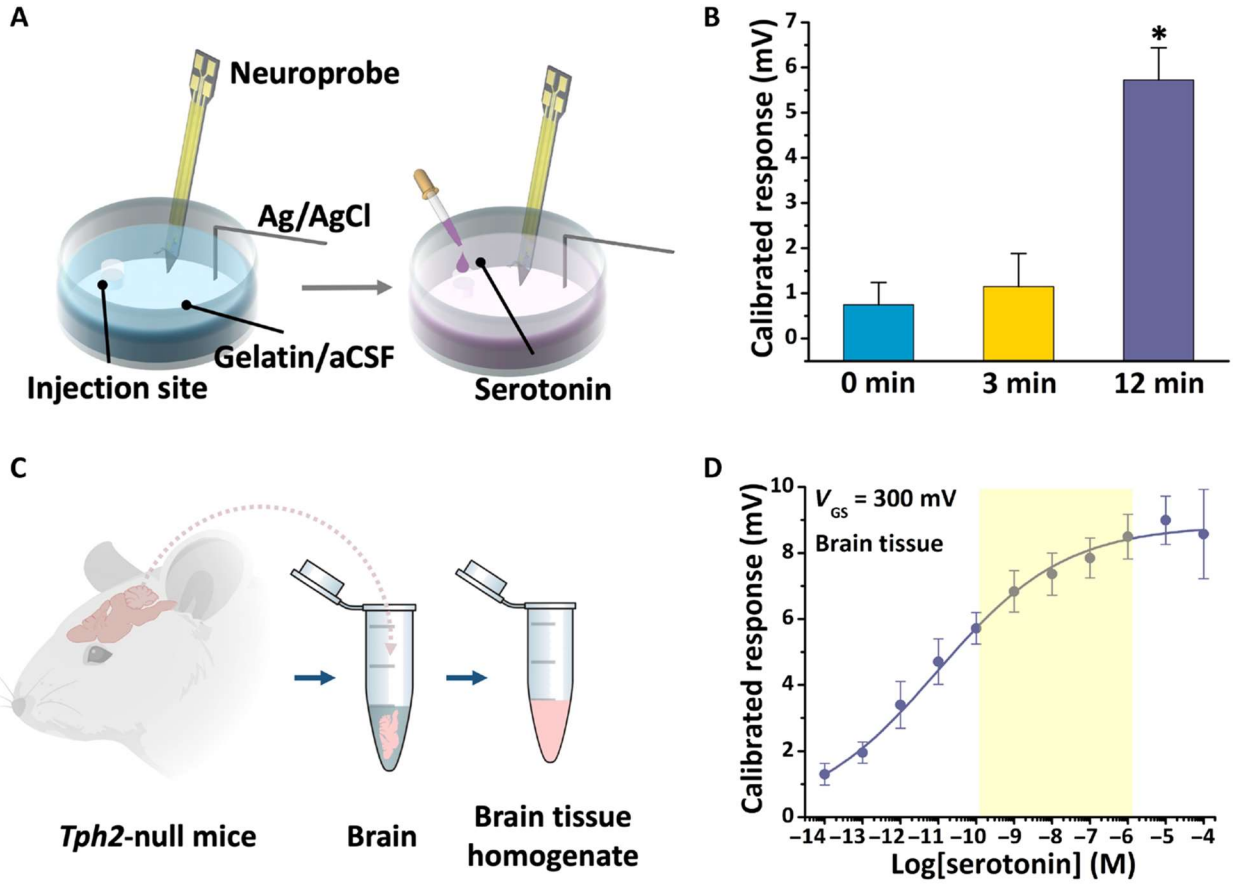

Figure 9.4. In vitro and ex vivo neuroprobe serotonin sensing. (A) Schematic illustrations showing an in vitro experiment in a brain-mimicking solid matrix composed of gelatin in aCSF. (B) Calibrated responses after the addition of 100 nM serotonin over time. Error bars are standard errors of the means for N = 2 individual probes. *P < 0.05 versus 0- and 3-min time points. (C) Schematic illustration of the preparation of a brain tissue homogenate. Brains from *Tph2*-null mice were removed, and tissue was homogenized in aCSF. (D) Serotonin aptamer-FET response curve in brain tissue homogenates. The highlighted region represents serotonin concentrations in the extracellular space in vivo. Error bars are standard errors of the means for N = 3 individual FETs.

Data were collected immediately after the introduction of serotonin, and 3 and 12 min later (Figure 9.4B). There were significant increases in FET responses 12 min after serotonin addition

(see table S1 for statistics), demonstrating that the aptamer-FET neuroprobes detected diffusion-related changes in serotonin levels with respect to time. We previously found that the response times of our aptamer-FET sensors are on the order of seconds (21, 23); the 12-min response time here is due to target diffusion over ~0.2 cm in the gelatin/aCSF matrix from the addition location to the recording site.

We tested neuroprobes in brain tissue ex vivo to assess their ability to operate in a complex biological matrix that more closely approximates the in vivo environment (figure S2). Brain tissue from *Tph2*-null mice lacking expression of the rate-limiting serotonin synthetic enzyme in the central nervous system (CNS) (43) was homogenized in aCSF to provide a tissue environment devoid of endogenous serotonin (Figure 9.4C). As shown in Figure 9.4D, serotonin added exogenously was detected via aptamer-FET neuroprobes over a concentration range similar to that recorded in aCSF (i.e., fM to μM), indicating that biofouling occurring during the measurement period of ~1 hour did not interfere with serotonin detection. The in vivo concentration of extracellular serotonin is highlighted (34, 36, 40–42), showing that the detection range of the aptamer neuroprobes in brain tissue covered the estimated extracellular serotonin concentration range (Figure 9.4D). The sensitivity and selectivity of the aptamer neuroprobes, in addition to the results from the gelatin and brain tissue homogenate experiments, illustrated the potential for in vivo studies.

To evaluate the in vivo capability of the neuroprobes, a sensing experiment was performed using electrical stimulation to release serotonin. Electrical stimulation is widely used in vivo to induce neurotransmitter release in the CNS (44). However, as the detection mechanism of FET-based biosensors relies on aptamer and solution-ion charge redistribution near the semiconductor surface, external electrical stimulation could affect FET signals associated with target capture. To

test for electrical interference, neuroprobes were placed in phosphate-buffered saline (PBS) with stimulating electrodes, as shown in figure S3 (A and B). The IDS-VGS sweeps were collected before and after electrical stimulation (biphasic pulses of 300 A, pulse width of 4 ms, and 30 Hz for 5 s; figure S3C). The FET measurements after stimulation showed negligible differences compared to measurements before stimulation, suggesting little influence of the electrical stimulation on signals measured from the aptamer-FET neuroprobes. The different time scales for neurochemical versus endogenous electrophysiological events likely preclude our sensors, with temporal resolution on the order of seconds, from nonspecifically detecting neurotransmitter-evoked changes in local field potentials (~100 ms).

An in vivo experiment was conducted in a female mouse that constitutively lacked serotonin transporter expression. The serotonin transporter takes up serotonin from the extracellular space. Mice that do not express this transporter have higher basal and stimulated serotonin levels (34, 41). The mouse was acclimated over a number of days of behavior training to being head-fixed (5, 45). A schematic of the experiment is shown in Figure 9.5A. Photographs of the experiment are shown in Figure 9.5B, where a neuroprobe, Ag/AgCl reference electrode, and stimulating electrode are shown implanted into the brain of the mouse. The stimulating electrode was located just above the brain stem serotonin cell bodies. The neuroprobe was implanted into the striatum where serotonin axons project (41). Electrical stimulation of serotonin cell bodies releases serotonin in the striatum (Figure 9.5C). Detailed information is included in the Materials and Methods.

After implantation, we tested device functionality by collecting transfer curves (IDS-VGS) from the FETs. As shown in Figure 9.5D, the transfer curves showed typical FET characteristics. Three overlapping transfer curves were collected immediately before electrical stimulation,

showing that the biosensors were relatively stable when implanted in the brain without observable drift over short times. For in vivo serotonin measurements, prestimulus measurements were made followed by electrical stimulation and determination of serotonin release. Increases in FET-calibrated responses after electrical stimulation were observed, indicating that the neuroprobe having a FET functionalized with a serotonin-specific aptamer detected increases in serotonin after stimulation (Figure 9.5, E and F, and figure S4). Representative continuous calibrated responses are shown in figure S4 for the 1-min period before stimulation (basal levels) and 1 min after stimulation. As summarized in Figure 9.5 (E and F), aptamer-FET biosensors differentiated basal and stimulated serotonin levels, suggesting minimal sensor drift over the measurement period. We previously carried out continuous real-time IDS monitoring under constant voltage bias, where aptamer FETs showed stable signals over 20 min with little drift (21). Here, the temporal resolution is limited by the measurement instrument, which takes ~5 s for each gate voltage sweep. We previously showed ~2-s temporal resolution in real-time IDS measurements (21, 23).

In mice lacking the serotonin transporter, clearance of extracellular serotonin depends on diffusion and uptake by low-affinity transporters (e.g., dopamine, plasma membrane monoamine, or organic cation transporters) (46–48). Thus, the clearance time of extracellular serotonin is prolonged in mice lacking high-affinity serotonin uptake (49, 50). This slower clearance process (figure S4) is consistent with the time course of electrically stimulated serotonin release after pharmacologic inhibition of serotonin transporters determined by fast cyclic square-wave voltammetry (36).

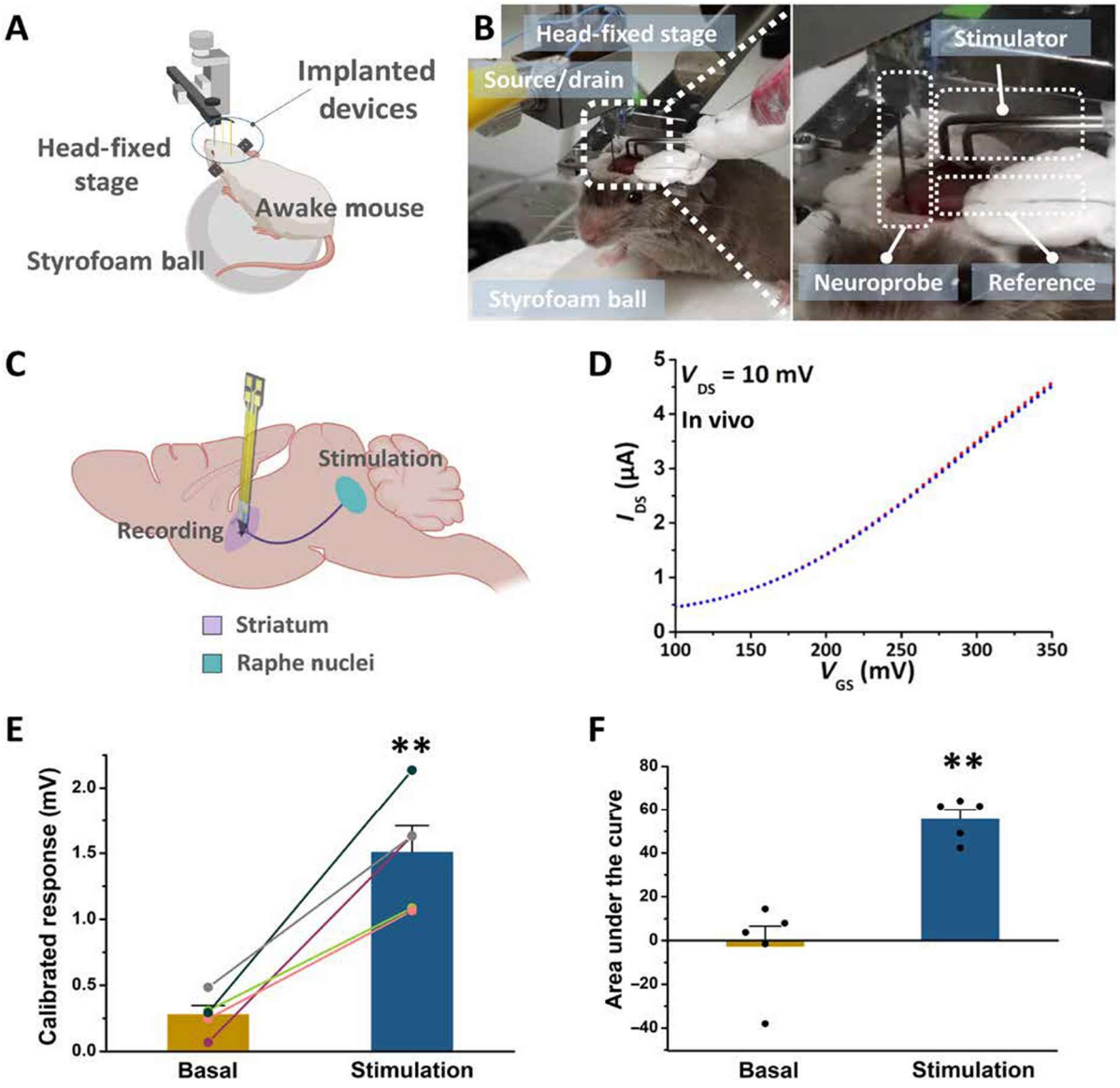

Figure 9.5. In vivo serotonin monitoring using an aptamer-FET neuroprobe. (A) Schematic illustration and (B) photographs of an in vivo experiment, where the neuroprobe, Ag/AgCl reference electrode, and stimulator were implanted into the brain of a head-fixed mouse. (C) Schematic illustration of stimulation and recording sites. The stimulating electrode was implanted into the serotonin cell-body region, and the neuroprobe was implanted into a serotonin terminal region in the striatum. (D) Three consecutive overlapping output sweeps (IDS-VGS) in vivo, where VGS was swept from 100 to 350 mV, while VDS was held at constant 10 mV. (E) Calibrated responses and (F) areas under the curves for in vivo determination of basal and post-electrical stimulation levels from the same mouse, respectively (VGS = 300 mV). Error bars in E. and F. are standard errors of the means. **P < 0.01 versus basal. Photo credit: Kevin M. Cheung, UCLA.

The 150-µm Si probes showed promising in vivo results. Nonetheless, rigid Si-based devices are less desirable for long-term recordings because of the inflammatory responses they evoke (51–53). One strategy to improve the biomaterial interface is to reduce stiffness by fabricating devices with reduced dimensions. The bending stiffness D is defined as

$$D \propto Et^3 \quad (1)$$

where E is the Young's modulus and t is the thickness. Stiffness scales cubically with device thickness (52–54). Hence, we designed second-generation Si neuroprobes with dimensions reduced by two-thirds (i.e., 50-µm thick and 50-µm wide) (Figure 9.6A).

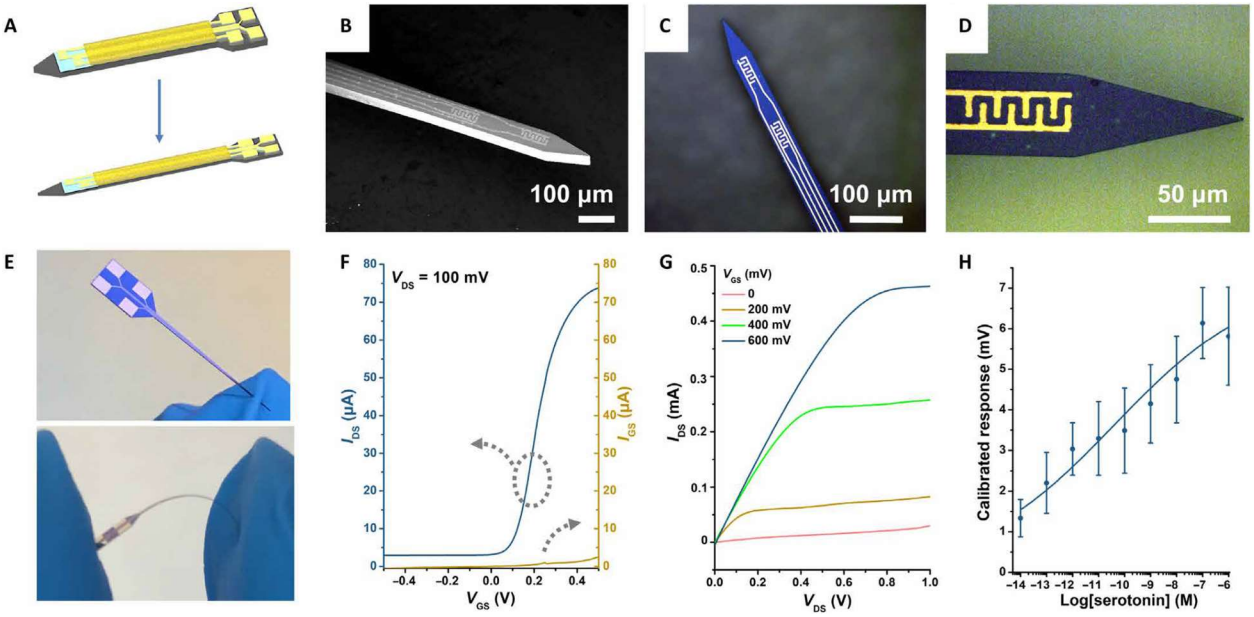

Figure 9.6. Fabrication and characterization of flexible 50-µm neuroprobes. (A) Schematic illustration comparing scaling between a 150-µm-thick and 150-µm-wide probe and a 50-µm-thick and 50-µm-wide probe. (B) SEM image of the shank and tip of a 50-µm neuroprobe showing a two-FET configuration. (C and D) Optical microscope images of 50-m probes. (E) Photographs showing a 50-m neuroprobe, which is stiff enough to penetrate a nitrile glove (top) yet can be easily bent (bottom). (F and G) Representative transfer and output characteristics in aCSF, respectively. (H) Serotonin aptamer-FET response curve in aCSF. Error bars are standard errors of the means for N = 4 individual 30 µm–by–50 µm FETs. Photo credit: Chuanzhen Zhao, UCLA.

The fabrication process for the 50-μm neuroprobes was similar to the fabrication of 150-m probes except that a thinner 50-μm Si wafer was used for the former. The smaller probes are shown in Figure 9.6 (B to E), where two transistors (30 μm by 50 μm each) were patterned on the tip of each probe. The Si probes with reduced size maintained sufficient penetration stiffness yet showed flexibility (Figure 9.6E and movie S1). We previously demonstrated that flexible In_2O_3 FETs are stable even after many bending or crumpling cycles with minimal changes in mobility and device performance (21). The smaller FETs on the 50-μm probes showed typical transistor performance indicated by their transfer and output curves (Figure 9.6, F and G, respectively). We functionalized these smaller FETs with serotonin aptamers. Similar to larger aptamer FETs, the smaller versions showed serotonin sensitivity down to femtomolar concentrations.

9.3 Discussion

We developed implantable aptamer-FET neuroprobes for in vivo neurotransmitter detection. Ultrathin In_2O_3 (~3 to 4 nm) with a high surface-to-volume ratio was prepared using a sol-gel process and used as the channel material in FETs. High-throughput MEMS technologies were used to fabricate 150 neuroprobes per 4-inch Si wafer, where each probe was 150 or 50 μm wide and thick at the shank. Aptamers were coupled to In_2O_3 surfaces to achieve selective detection of serotonin in the micromolar to femtomolar range in physiological environments (i.e., aCSF and brain tissue homogenates). We showed that neuroprobes were functional in vitro in gelatin/aCSF, a material that simulates a tissue matrix, in brain tissue, and under electrical stimulation conditions used to stimulate serotonin release in vivo.

The neuroprobes described represent a general strategy for monitoring neurochemicals in the brain. Previously, we showed that, in addition to serotonin, aptamer FET biosensors can be

used to detect dopamine, glucose, sphingosine-1-phosphate, and phenylalanine. Aptamers for other neurotransmitters have been reported (55, 56), and new, highly selective aptamers are being developed (e.g., norepinephrine, epinephrine, glutamate, -aminobutyric acid, and dynorphin). As we continue to identify and to characterize additional aptamers, we envision that our approach will enable multiplexed monitoring of many different neurotransmitters in the brain with high sensitivity and selectivity, regardless of their electroactivity or redox enzymes available for them. We briefly highlight the advantages of aptamer FET biosensors compared to other currently used neurochemical recording and imaging techniques in the Supplementary Materials (table S2).

Aptamer biosensors can be multiplexed because of the high selectivity of our aptamers and our ability to fabricate FETs at small scales and high densities (30). We recently developed multiplexed sensor arrays to monitor serotonin, dopamine, pH, and temperature simultaneously in real time (21). The capability to monitor multiple neurotransmitters will provide insights into the interplay between signaling pathways in the brain (57). We are developing multimodal neuroprobes with aptamer-FET sensors for neurotransmitter detection and metal electrodes for electrophysiological recordings. Advances in these directions will provide improve knowledge about fundamental brain function and the etiologies of neurological and neuropsychiatric disorders and are anticipated to accelerate discovery and deployment of improved treatment modalities for psychiatric and neurological disorders.

There are challenges remaining with the neuroprobe technology described. For example, while we have achieved temporal resolution on the order of seconds using aptamer-FET sensors (21, 23), subsecond temporal resolution will enable clearer understanding of the dynamic fluxes of neurochemicals and the information encoded therein. This advance requires the development of additional sensing algorithms and instrumentation. Along these lines, we can tune aptamer-target

affinities by altering aptamer stem lengths (23) or aptamer-target kinetics by stem destabilization (58).

For multiplexed neurotransmitter detection, it will be necessary to functionalize individual FETs on the same neuroprobe with different aptamers. Although we have demonstrated duplexing with two aptamers (21), it is challenging to functionalize individual microscale devices that are located close to one another. "Addressable" functionalization strategies include microcontact printing (59). Electroactive linkers have been demonstrated (60) and are under development for the addressable functionalization of small devices (~10 μm apart) with different aptamers. Moreover, we are developing custom hardware and software designed to monitor multiple FETs at the same time to overcome current instrumentation limitations.

While Si neuroprobes are generally suitable for acute experiments (e.g., hours), for chronic recordings, challenges arise because of immunological responses that occur after longer implantation times. The Young's modulus mismatch between implanted devices and brain tissue produces inflammatory responses that interfere with biosensing (51, 61). Here, we report on neuroprobes with reduced dimensions (50 μm) and increased flexibility. Developing neuroprobes based on biocompatible and soft materials is an important ongoing research direction (21, 31).

9.4 Materials and methods

9.4.1 Materials

Prime quality 4-inch Si wafers (boron-doped P-type Si, 0.001 to 0.005 ohm/cm, thickness of 150 or 50 μm) were purchased from Silicon Valley Microelectronics Inc. (Santa Clara, CA, USA). All chemicals were purchased from Sigma-Aldrich Co. (St. Louis, MO), unless otherwise noted below. Oligonucleotides were obtained from Integrated DNA Technologies (Coralville, IA).

SYLGARD 184 for fabricating polydimethylsiloxane (PDMS) wells was from Dow Corning Corporation (Midland, MI). Water was deionized before use (18.2 megohms) via a Milli-Q system (Millipore, Billerica, MA).

9.4.2 Neuroprobe fabrication

Aqueous solutions of 0.1 M indium (III) nitrate hydrate (99.999%) were spin-coated onto Si substrates at 3000 rpm for 30 s. The coated wafers were annealed at 100°C for 10 min and then at 350°C for 4 hours to form continuous In_2O_3 films. A photolithography process was applied to define the source and drain electrodes. Electrodes of 10-nm-thick Ti and overlaying 30-nm-thick Au films were fabricated using a CHA solution electron-beam evaporator (CHA Industries Inc., Fremont, CA) under high vacuum (10−8 torr) at an evaporation rate of 0.1 nm/s. A thin layer of parylene (~1 μm) was coated on probe surfaces using an SCS Parylene C coating system (Specialty Coating System Inc., Indianapolis, IN), defined photolithography, and then etched by oxygen plasma to expose the FETs on the neuroprobe tips. Another photolithographic treatment was performed to define the probe outlines. Deep reactive ion etching with the Bosch process was used to etch through silicon substrates using a Deep Silicon Etcher III (Plasma-Therm, Fremont, CA).

Probes on wafers or post-release were rinsed in ethanol and dried with N_2 to clean their surfaces. After cleaning, (3-aminopropyl) triethoxysilane and trimethoxy(propyl)silane (1:9, v/v) were thermally deposited on In_2O_3 at 40°C for 1 hour and annealed at 60°C for 10 min. Source and drain interdigitated electrodes were insulated with a self-assembled monolayer by immersing into 1 mM ethanolic solutions of 1-dodecanethiol for 1 hour. Probes were immersed in a 1 mM solution of 3-maleimidobenzoic acid N-hydroxysuccinimide ester dissolved in a 1:9 (v/v) mixture of dimethyl sulfoxide and PBS (Gibco, Thermo Fisher Scientific, Waltham, MA) for 30 min. To

immobilize aptamers, probes were immersed in a 1 μM solution of thiolated DNA in PBS overnight. Probes were rinsed with deionized water and dried with N2 before measurements.

9.4.3 In vitro and ex vivo experiments

Here, aCSF was prepared as per the detailed protocol in the supplemental information by Zhao et al. (24). For experiments in aCSF or tissue homogenates, PDMS wells were sealed on top of individual probes (not released from wafers) to hold aCSF and target solutions. The initial solution volume was 40 l. Serotonin was added in 1 l aliquots to produce increasing concentrations. After each addition, the solutions in the wells were gently mixed using a micropipette.

For gelatin experiments, a mixture of 10 to 15% gelatin (lot #H219; Mallinckrodt, St. Louis, MO) in aCSF (w/v) (24) was prepared first. The mixture was microwaved in 10-s increments (to avoid overheating) for ~1 min until the gelatin was completely dissolved. The clear solution was cast in 1-ml aliquots into 48-well plates (lot #CLS3548; Sigma-Aldrich Co., St. Louis, MO). A mold for holes was templated into the gelatin using a 0.125-inch-diameter metal wire (lot #7667A12; McMaster-Carr Supply Co., Atlanta, GA) for the addition of neurotransmitter solutions to simulate neurotransmitter release in the brain. The gelatin solution was kept at 4°C for ~12 hours. Afterward, the metal mold was taken out carefully using tweezers. The Ag/AgCl gate electrodes for this experiment and the in vivo experiment were constructed of 0.010-inch-diameter Ag wire freshly coated with AgCl (A-M Systems, Sequim, WA) by immersing in a bleach solution (Clorox, Oakland, CA) for 5 min. A neuroprobe and a Ag/AgCl reference electrode were each implanted into a single well containing gelatin using tweezers before measurements. A 2-μl aliquot of 50 μM serotonin was added into each templated well containing gelatin for a final concentration of 100 nM serotonin.

For ex vivo experiments, brain tissue lacking serotonin was obtained from *Tph2* knockout mice (39). These mice lack the enzyme (tryptophan hydroxylase 2) needed to synthesize brain serotonin. Most serotonin in the brain is stored in synaptic vesicles. To prepare brain tissue homogenates, cell membranes are disrupted, releasing vesicular serotonin into the homogenates. Hence, the concentration of serotonin in homogenates is much higher than that occurring in vivo in the extracellular space. By using brain tissue from *Tph2*-null mice, we avoided effects of endogenous serotonin in homogenates. Mice were exsanguinated by cardiac perfusion, and brains were cleared of blood containing serotonin synthesized by peripheral tryptophan hydroxylase 1. The brains were then shipped to the University of California, Los Angeles (UCLA) on dry ice from the laboratory of D. Kuhn (Wayne State University, Detroit, MI). Brain tissue was stored at −80°C until use. Brain tissue collection procedures were approved by the Wayne State University Institutional Animal Care and Use Committee.

Brain tissue was homogenized in ice-cold aCSF [1:1 (w/v)] using a VirTis Virsonic 600 ultrasonic cell disruptor (Gardiner, NY) with the microtip set at 4 with 50% duty for 30 to 40 1-s pulses. Commercially available Ag/AgCl reference electrodes (Super Dri-Ref, World Precision Instruments Inc., Sarasota, FL) were placed in the tissue homogenates above the FETs. All FET measurements, including the in vivo measurements described below, were performed using a Keithley 4200A-SCS (Tektronix, Beaverton, OR) semiconductor analyzer. Source-drain current (IDS) transfer curves were obtained by sweeping the gate voltage (VGS) from 100 to 350 mV, while maintaining the drain voltage (VDS) at 10 mV, which took ~5 s for each scan. Calibrated responses were calculated at 300 mV to minimize device-to-device variation, as previously described (23).

9.4.4 In vivo experiments

The Association for Assessment and Accreditation of Laboratory Animal Care International has fully accredited UCLA. All animal care and use met the requirements of the National Institutes of Health Guide for the Care and Use of Laboratory Animals, revised 2011. The UCLA Chancellor's Animal Research Committee (Institutional Animal Care and Use Committee) preapproved all procedures involving animals carried out at UCLA. Mice were generated from a serotonin transporter–deficient lineage on a mixed CD1 × 129S6/SvEv background via heterozygous pairings. Two female serotonin transporter knockout mice (SERT−/−) were studied at 4 to 6 months of age. One mouse was used for a pilot study to determine biosensor and stimulating electrode experimental conditions. A second mouse was used to collect the data in Figure 9.5. Mice were housed in groups of four to five same-sex siblings per cage until head-bar implantation surgery, after which mice were individually housed. The light-dark cycle was set to 12 hours/12 hours with lights on at 0600. All testing was carried out during the light phase. Food and water were available ad libitum with the exception of experimental testing days.

Surgeries were carried out under aseptic conditions with isoflurane anesthesia on the Kopf Model 1900 Stereotaxic Alignment System (Kopf, Tujunga, CA). Beginning on the day of surgery, we administered the nonsteroidal anti-inflammatory drugs carprofen (subcutaneously daily at 5 mg/kg for 3 days) and ibuprofen (0.25 mg/ml in the drinking water for 14 days), in addition to the antibiotic amoxicillin (0.25 mg/ml) in the drinking water for 14 days. Animals underwent a surgical procedure for head-bar implantation. A rectangular head-bar (9 mm by 7 mm by 0.76 mm; 0.6 g, laser-cut from stainless steel at Fab2Order) for head fixation was attached to each side of the skull by C&B-Metabond (Parkell, Edgewood, NY) (14). After surgery, animals recovered for 1 to 3 weeks.

During recovery from head-bar implantation, subjects were trained to acclimate to head fixation by hand for 15 to 30 min per session × 1 to 2 sessions/day for a total 6 to 10 sessions. Afterward, a second surgery to make three craniotomies was carried out 24 to 48 hours ahead of in vivo recordings. A 2.5-mm-wide (medio-lateral) by 1.0-mm-long (anterio-posterior) piece of skull was surgically removed over the brain stem serotonin cell body region (centered at AP −4.48 mm and ML ±0.00 mm from bregma) for the insertion of a stimulating electrode. A 1.5-mm-wide by 1.5-mm-long craniotomy aimed at the right striatum (centered at AP +0.80 mm and ML +0.80 mm from bregma) was made for the insertion of an aptamer-FET neuroprobe. An additional 0.4-mm-diameter hole (centered at AP +2.80 mm and ML −2.00 mm from bregma) was made on the left side of the skull for Ag/AgCl gate electrode implantation.

The dura was left intact over the surgery areas. The craniotomies were sealed with a thin layer of Kwik-Cast and Kwik-Sil (World Precision Instruments, Sarasota, FL). The entire surgery area was then secured with a thin top layer of C&B-Metabond. On the testing day, mice were transferred from their home cages and mounted to a head-fixed stage via their head-bars. Each subject was supported on a Styrofoam ball that served as a treadmill for the subject to engage freely in locomotion.

After a 10-min habituation period, the top layer of C&B-Metabond was carefully removed. The thin layer of Kwik-Cast and Kwik-Sil and the dura above the brain in the craniotomy areas were then removed using ceramic-coated Dumont #5 forceps (Roboz Surgical Instrument Co., Gaithersburg, MD). A Ag/AgCl gate electrode was manually lowered into the designated craniotomy site at 1.5 to 2 mm in depth. An untwisted two-channel tungsten stimulation electrode (Plastics One, Roanoke, VA) was lowered 3.5 mm from the skull level aimed at the serotonin cell

body region using a 10-μm precision manual micromanipulator (Narishige International, Amityville, NY). The stimulation electrode tips were 2.0 mm apart.

After another 10-min habituation period, a train of electrical stimulation pulses (biphasic 300 A × 4 ms at 30 Hz for 5 s) was delivered, which evoked behavioral responses such as freezing, running, shaking, and a notable increase in breathing rate. If no behavioral response was observed, the stimulating electrode was lowered an additional 50 μm per step. Another train of stimulation was delivered with a >5-min interval. This process of locating the stimulating electrode continued until strong stimulation-induced behavioral responses were observed. After positioning, the stimulation electrode (dorso-ventral of −3.5 to −4.5 mm) remained in the same location throughout the experiment.

The source and drain electrodes of the aptamer-FET neuroprobes were connected with wiring using Ag epoxy (Ted Pella, Redding, CA) before functionalization (Figure 9.5B) (25). The FETs were then functionalized with the serotonin aptamer as described above. Source/ drain wires were connected directly to a Keithley 4200A semiconductor analyzer for measurements. An aptamer-FET neuroprobe was lowered to 1.0 mm above the brain surface by hand. A 1-μm precision motorized digital micromanipulator (MP-225; Sutter Instrument, Novato, CA) was then used to lower the probe slowly into the brain. A biphasic, 300-A, 4-ms, and 30-Hz waveform was then applied for 5 s to the stimulating electrode to evoke serotonin release. Sourcedrain current (IDS) transfer curves were obtained by sweeping the gate voltage (VGS) from 100 to 350 mV while maintaining the drain voltage (VDS) at 10 mV. Calibrated responses were calculated at 300 mV to minimize device-to-device variation as previously described (23). Five baseline calibrated responses were collected before each stimulation. Calibrated responses were collected every 5 s over a period of ca. 60 s after each stimulation (figure S4).

At each recording depth, two to four stimulation trains were delivered at 5- to 10-min intervals. The neuroprobe was lowered 50 to 150 μm per step for additional testing. Throughout the experiment, sterile saline was used to keep the exposed skull and brain moist. Sweetened condensed milk diluted with drinking water [1:2 (v/v)] was delivered to the subject every 2 to 3 hours using a dropper. The overall health and behavioral responses to stimulation of the mice were closely monitored throughout the experiment. At the end of the experiment, both electrodes and the neuroprobe were removed. Subjects were euthanized, and the brains were prepared for histological verification of the positions of the stimulation and recording paths/sites.

9.4.5 Data analysis

Data for selectivity testing and gelatin sensing were analyzed by one-way analysis of variance with Dunnett's or Turkey's post hoc tests, respectively. Areas under the curves for stimulation data were calculated by trapezoidal integration of seven stimulated serotonin measurements, which defined each stimulation peak. Baselines for integration were determined by a linear fit of five prestimulus points (basal). Data for in vivo responses were analyzed by two-tailed paired t tests (GraphPad Prism 7.04, San Diego, CA).

9.5 Reference and Notes

1. A. P. Alivisatos, A. M. Andrews, E. S. Boyden, M. Chun, G. M. Church, K. Deisseroth, J. P. Donoghue, S. E. Fraser, J. Lippincott-Schwartz, L. L. Looger, S. Masmanidis, P. L. McEuen, A. V. Nurmikko, H. Park, D. S. Peterka, C. Reid, M. L. Roukes, A. Scherer, M. Schnitzer, T. J. Sejnowski, K. L. Shepard, D. Tsao, G. Turrigiano, P. S. Weiss, C. Xu, R. Yuste, X. Zhuang, Nanotools for neuroscience and brain activity mapping. ACS Nano **7**, 1850–1866 (2013).

2. S. C. Altieri, H. Yang, H. J. O'Brien, H. M. Redwine, D. Senturk, J. G. Hensler, A. M. Andrews, Perinatal vs genetic programming of serotonin states associated with anxiety. Neuropsychopharmacology **40**, 1456–1470 (2015).
3. M. Malvaez, C. Shieh, M. D. Murphy, V. Y. Greenfield, K. M. Wassum, Distinct corticalamygdala projections drive reward value encoding and retrieval. Nat. Neurosci. **22**, 762–769 (2019).
4. N. Dolensek, D. A. Gehrlach, A. S. Klein, N. Gogolla, Facial expressions of emotion states and their neuronal correlates in mice. Science **368**, 89–94 (2020).
5. K. Lee, L. D. Claar, A. Hachisuka, K. I. Bakhurin, J. Nguyen, J. M. Trott, J. L. Gill, S. C. Masmanidis, Temporally restricted dopaminergic control of reward-conditioned movements. Nat. Neurosci. **23**, 209–216 (2020).
6. U. Topalovic, Z. M. Aghajan, D. Villaroman, S. Hiller, L. Christov-Moore, T. J. Wishard, M. Stangl, N. R. Hasulak, C. S. Inman, T. A. Fields, V. R. Rao, D. Eliashiv, I. Fried, N. Suthana, Wireless programmable recording and stimulation of deep brain activity in freely moving humans. Neuron **108**, 322–334.e9 (2020).
7. J. P. Seymour, F. Wu, K. D. Wise, E. Yoon, State-of-the-art MEMS and microsystem tools for brain research. Microsyst. Nanoeng. **3**, 16066 (2017).
8. S. M. Won, E. Song, J. Zhao, J. Li, J. Rivnay, J. A. Rogers, Recent advances in materials, devices, and systems for neural interfaces. Adv. Mater. **30**, e1800534 (2018).
9. G. A. Woods, N. J. Rommelfanger, G. Hong, Bioinspired materials for in vivo bioelectronic neural interfaces. Matter **3**, 1087–1113 (2020).
10. R. Chen, A. Canales, P. Anikeeva, Neural recording and modulation technologies. Nat. Rev. Mater. **2**, 16093 (2017).

11. M. D. Ferro, N. A. Melosh, Electronic and ionic materials for neurointerfaces. Adv. Funct. Mater. **28**, 1704335 (2018).

12. J. Viventi, D. H. Kim, L. Vigeland, E. S. Frechette, J. A. Blanco, Y. S. Kim, A. E. Avrin, V. R. Tiruvadi, S. W. Hwang, A. C. Vanleer, D. F. Wulsin, K. Davis, C. E. Gelber, L. Palmer, J. Van der Spiegel, J. Wu, J. Xiao, Y. Huang, D. Contreras, J. A. Rogers, B. Litt, Flexible, foldable, actively multiplexed, high-density electrode array for mapping brain activity in vivo. Nat. Neurosci. **14**, 1599–1605 (2011).

13. N. Vachicouras, O. Tarabichi, V. V. Kanumuri, C. M. Tringides, J. Macron, F. Fallegger, Y. Thenaisie, L. Epprecht, S. McInturff, A. A. Qureshi, V. Paggi, M. W. Kuklinski, M. C. Brown, D. J. Lee, S. P. Lacour, Microstructured thin-film electrode technology enables proof of concept of scalable, soft auditory brainstem implants. Sci. Transl. Med. **11**, eaax9487 (2019).

14. J. Du, T. J. Blanche, R. R. Harrison, H. A. Lester, S. C. Masmanidis, Multiplexed, high density electrophysiology with nanofabricated neural probes. PLOS ONE **6**, e26204 (2011).

15. G. Rios, E. V. Lubenov, D. Chi, M. L. Roukes, A. G. Siapas, Nanofabricated neural probes for dense 3-D recordings of brain activity. Nano Lett. **16**, 6857–6862 (2016).

16. J. J. Jun, N. A. Steinmetz, J. H. Siegle, D. J. Denman, M. Bauza, B. Barbarits, A. K. Lee, C. A. Anastassiou, A. Andrei, C. Aydin, M. Barbic, T. J. Blanche, V. Bonin, J. Couto, B. Dutta, S. L. Gratiy, D. A. Gutnisky, M. Hausser, B. Karsh, P. Ledochowitsch, C. M. Lopez, C. Mitelut, S. Musa, M. Okun, M. Pachitariu, J. Putzeys, P. D. Rich, C. Rossant, W. L. Sun, K. Svoboda, M. Carandini, K. D. Harris, C. Koch, J. O'Keefe, T. D. Harris, Fully integrated silicon probes for high-density recording of neural activity. Nature **551**, 232–236 (2017).

17. N. Driscoll, A. G. Richardson, K. Maleski, B. Anasori, O. Adewole, P. Lelyukh, L. Escobedo, D. K. Cullen, T. H. Lucas, Y. Gogotsi, F. Vitale, Two-dimensional Ti3C2 MXene for highresolution neural interfaces. ACS Nano **12**, 10419–10429 (2018).

18. Y. Jiang, X. Li, B. Liu, J. Yi, Y. Fang, F. Shi, X. Gao, E. Sudzilovsky, R. Parameswaran, K. Koehler, V. Nair, J. Yue, K. Guo, H.-M. Tsai, G. Freyermuth, R. C. S. Wong, C.-M. Kao, C.-T. Chen, A. W. Nicholls, X. Wu, G. M. G. Shepherd, B. Tian, Rational design of silicon structures for optically controlled multiscale biointerfaces. Nat. Biomed. Eng. **2**, 508–521 (2018).

19. G. Hong, T. M. Fu, M. Qiao, R. D. Viveros, X. Yang, T. Zhou, J. M. Lee, H. G. Park, J. R. Sanes, C. M. Lieber, A method for single-neuron chronic recording from the retina in awake mice. Science **360**, 1447–1451 (2018).

20. J. E. Chung, H. R. Joo, J. L. Fan, D. F. Liu, A. H. Barnett, S. Chen, C. Geaghan-Breiner, M. P. Karlsson, M. Karlsson, K. Y. Lee, H. Liang, J. F. Magland, J. A. Pebbles, A. C. Tooker, L. F. Greengard, V. M. Tolosa, L. M. Frank, High-density, long-lasting, and multi-region electrophysiological recordings using polymer electrode arrays. Neuron **101**, 21–31.e5 (2019).

21. Q. Liu, C. Zhao, M. Chen, Y. Liu, Z. Zhao, F. Wu, Z. Li, P. S. Weiss, A. M. Andrews, C. Zhou, Flexible multiplexed In_2O_3 nanoribbon aptamer-field-effect transistors for biosensing. iScience **23**, 101469 (2020).

22. K. M. Cheung, K. A. Yang, N. Nakatsuka, C. Zhao, M. Ye, M. E. Jung, H. Yang, P. S. Weiss, M. N. Stojanović, A. M. Andrews, Phenylalanine monitoring via aptamer-field-effect transistor sensors. ACS Sens. **4**, 3308–3317 (2019).

23. N. Nakatsuka, K. A. Yang, J. M. Abendroth, K. M. Cheung, X. Xu, H. Yang, C. Zhao, B. Zhu, Y. S. Rim, Y. Yang, P. S. Weiss, M. N. Stojanović, A. M. Andrews, Aptamer-field-effect

transistors overcome Debye length limitations for small-molecule sensing. Science 362, 319–324 (2018).

24. C. Zhao, Q. Liu, K. M. Cheung, W. Liu, Q. Yang, X. Xu, T. Man, P. S. Weiss, C. Zhou, M. Andrews, Narrower nanoribbon biosensors fabricated by chemical lift-off lithography show higher sensitivity. ACS Nano **15**, 904–915 (2021).
25. K. M. Wassum, V. M. Tolosa, J. Wang, E. Walker, H. G. Monbouquette, N. T. Maidment, Silicon wafer-based platinum microelectrode array biosensor for near real-time measurement of glutamate in vivo. Sensors **8**, 5023–5036 (2008).
26. L. C. Moreaux, D. Yatsenko, W. D. Sacher, J. Choi, C. Lee, N. J. Kubat, R. J. Cotton, E. S. Boyden, M. Z. Lin, L. Tian, A. S. Tolias, J. K. S. Poon, K. L. Shepard, M. L. Roukes, Integrated neurophotonics: Toward dense volumetric interrogation of brain circuit activity-at depth and in real time. Neuron **108**, 66–92 (2020).
27. B. Wang, X. Wen, Y. Cao, S. Huang, H. A. Lam, T. L. Liu, P. S. Chung, H. G. Monbouquette, P. Y. Chiou, N. T. Maidment, An implantable multifunctional neural microprobe for simultaneous multi-analyte sensing and chemical delivery. Lab Chip **20**, 1390–1397 (2020).
28. H. Chen, Y. S. Rim, I. C. Wang, C. Li, B. Zhu, M. Sun, M. S. Goorsky, X. He, Y. Yang, Quasi-two-dimensional metal oxide semiconductors based ultrasensitive potentiometric biosensors. ACS Nano **11**, 4710–4718 (2017).
29. N. Aroonyadet, X. Wang, Y. Song, H. Chen, R. J. Cote, M. E. Thompson, R. H. Datar, C. Zhou, Highly scalable, uniform, and sensitive biosensors based on top-down indium oxide nanoribbons and electronic enzyme-linked immunosorbent assay. Nano Lett. **15**, 1943–1951 (2015).

30. J. Kim, Y. S. Rim, H. Chen, H. H. Cao, N. Nakatsuka, H. L. Hinton, C. Zhao, A. M. Andrews, Y. Yang, P. S. Weiss, Fabrication of high-performance ultrathin In_2O_3 film field-effect transistors and biosensors using chemical lift-off lithography. ACS Nano **9**, 4572–4582 (2015).
31. Y. S. Rim, S. H. Bae, H. Chen, J. L. Yang, J. Kim, A. M. Andrews, P. S. Weiss, Y. Yang, H. R. Tseng, Printable ultrathin metal oxide semiconductor-based conformal biosensors. ACS Nano **9**, 12174–12181 (2015).
32. B. J. Kim, J. T. Kuo, S. A. Hara, C. D. Lee, L. Yu, C. A. Gutierrez, T. Q. Hoang, V. Pikov, E. Meng, 3D parylene sheath neural probe for chronic recordings. J. Neural Eng. **10**, 045002 (2013).
33. C. Metallo, R. D. White, B. A. Trimmer, Flexible parylene-based microelectrode arrays for high resolution EMG recordings in freely moving small animals. J. Neurosci. Methods **195**, 176–184 (2011).
34. H. Yang, A. B. Thompson, B. J. McIntosh, S. C. Altieri, A. M. Andrews, Physiologically relevant changes in serotonin resolved by fast microdialysis. ACS Chem. Neurosci. **4**, 790–798 (2013).
35. F. N. Ishikawa, M. Curreli, H. K. Chang, P. C. Chen, R. Zhang, R. J. Cote, M. E. Thompson, C. Zhou, A calibration method for nanowire biosensors to suppress device-to-device variation. ACS Nano **3**, 3969–3976 (2009).
36. H. Shin, Y. Oh, C. Park, Y. Kang, H. U. Cho, C. D. Blaha, K. E. Bennet, M. L. Heien, I. Y. Kim, K. H. Lee, D. P. Jang, Sensitive and selective measurement of serotonin in vivo using fast cyclic square-wave voltammetry. Anal. Chem. **92**, 774–781 (2020).
37. Y. Oh, M. L. Heien, C. Park, Y. M. Kang, J. Kim, S. L. Boschen, H. Shin, H. U. Cho, C. D. Blaha, K. E. Bennet, H. K. Lee, S. J. Jung, I. Y. Kim, K. H. Lee, D. P. Jang, Tracking tonic

dopamine levels in vivo using multiple cyclic square wave voltammetry. Biosens. Bioelectron. **121**, 174–182 (2018).

38. K. Scida, K. W. Plaxco, B. G. Jamieson, High frequency, real-time neurochemical and neuropharmacological measurements in situ in the living body. Transl. Res. **213**, 50–66 (2019).
39. M. A. Kandadai, J. L. Raymond, G. J. Shaw, Comparison of electrical conductivities of various brain phantom gels: Developing a 'brain gel model'. Mater. Sci. Eng. C **32**, 2664–2667 (2012).
40. H. Yang, M. M. Sampson, D. Senturk, A. M. Andrews, Sex- and SERT-mediated differences in stimulated serotonin revealed by fast microdialysis. ACS Chem. Neurosci. **6**, 1487–1501 (2015).
41. T. A. Mathews, D. E. Fedele, F. M. Coppelli, A. M. Avila, D. L. Murphy, A. M. Andrews, Gene dose-dependent alterations in extraneuronal serotonin but not dopamine in mice with reduced serotonin transporter expression. J. Neurosci. Methods **140**, 169–181 (2004).
42. A. Abdalla, C. W. Atcherley, P. Pathirathna, S. Samaranayake, B. Qiang, E. Pena, S. L. Morgan, M. L. Heien, P. Hashemi, In vivo ambient serotonin measurements at carbon-fiber microelectrodes. Anal. Chem. **89**, 9703–9711 (2017).
43. M. Angoa-Perez, M. J. Kane, D. I. Briggs, N. Herrera-Mundo, C. E. Sykes, D. M. Francescutti, D. M. Kuhn, Mice genetically depleted of brain serotonin do not display a depression-like behavioral phenotype. ACS Chem. Neurosci. **5**, 908–919 (2014).
44. N. T. Rodeberg, S. G. Sandberg, J. A. Johnson, P. E. Phillips, R. M. Wightman, Hitchhiker's guide to voltammetry: Acute and chronic electrodes for in vivo fast-scan cyclic voltammetry. ACS Chem. Neurosci. **8**, 221–234 (2017).

45. K. I. Bakhurin, V. Mac, P. Golshani, S. C. Masmanidis, Temporal correlations among functionally specialized striatal neural ensembles in reward-conditioned mice. J. Neurophysiol. **115**, 1521–1532 (2016).

46. F. C. Zhou, K.-P. Lesch, D. L. Murphy, Serotonin uptake into dopamine neurons via dopamine transporters: A compensatory alternative. Brain Res. **942**, 109–119 (2002).

47. M. Zhou, K. Engel, J. Wang, Evidence for significant contribution of a newly identified monoamine transporter (PMAT) to serotonin uptake in the human brain. Biochem. Pharmacol. **73**, 147–154 (2007).

48. L. C. Daws, Unfaithful neurotransmitter transporters: Focus on serotonin uptake and implications for antidepressant efficacy. Pharmacol. Ther. **121**, 89–99 (2009).

49. X. A. Perez, A. M. Andrews, Chronoamperometry to determine differential reductions in uptake in brain synaptosomes from serotonin transporter knockout mice. Anal. Chem. **77**, 818–826 (2005).

50. S. Montanez, W. A. Owens, G. G. Gould, D. L. Murphy, L. C. Daws, Exaggerated effect of fluvoxamine in heterozygote serotonin transporter knockout mice. J. Neurochem. **86**, 210–219 (2003).

51. T. D. Kozai, A. S. Jaquins-Gerstl, A. L. Vazquez, A. C. Michael, X. T. Cui, Brain tissue responses to neural implants impact signal sensitivity and intervention strategies. ACS Chem. Neurosci. **6**, 48–67 (2015).

52. M. Lee, H. J. Shim, C. Choi, D. H. Kim, Soft high-resolution neural interfacing probes: Materials and design approaches. Nano Lett. **19**, 2741–2749 (2019).

53. J. Shi, Y. Fang, Flexible and implantable microelectrodes for chronically stable neural interfaces. Adv. Mater. **31**, e1804895 (2019).

54. J. Rivnay, H. Wang, L. Fenno, K. Deisseroth, G. G. Malliaras, Next-generation probes, particles, and proteins for neural interfacing. Sci. Adv. **3**, e1601649 (2017).

55. J. G. Bruno, M. P. Carrillo, T. Phillips, B. King, Development of DNA aptamers for cytochemical detection of acetylcholine. In Vitro Cell. Dev. Biol. Anim. **44**, 63–72 (2008).

56. T. Mairal Lerga, M. Jauset-Rubio, V. Skouridou, A. S. Bashammakh, M. S. El-Shahawi, A. O. Alyoubi, C. K. O'Sullivan, High affinity aptamer for the detection of the biogenic amine histamine. Anal. Chem. **91**, 7104–7111 (2019).

57. V. Niederkofler, T. E. Asher, S. M. Dymecki, Functional interplay between dopaminergic and serotonergic neuronal systems during development and adulthood. ACS Chem. Neurosci. **6**, 1055–1070 (2015).

58. B. D. Wilson, A. A. Hariri, I. A. P. Thompson, M. Eisenstein, H. T. Soh, Independent control of the thermodynamic and kinetic properties of aptamer switches. Nat. Commun. **10**, 5079 (2019).

59. B. Wang, B. Koo, L. W. Huang, H. G. Monbouquette, Microbiosensor fabrication by polydimethylsiloxane stamping for combined sensing of glucose and choline. Analyst **143**, 5008–5013 (2018).

60. M. Curreli, C. Li, Y. Sun, B. Lei, M. A. Gundersen, M. E. Thompson, C. Zhou, Selective functionalization of In_2O_3 nanowire mat devices for biosensing applications. J. Am. Chem. Soc. **127**, 6922–6923 (2005).

61. Z. J. Du, C. L. Kolarcik, T. D. Y. Kozai, S. D. Luebben, S. A. Sapp, X. S. Zheng, J. A. Nabity, X. T. Cui, Ultrasoft microwire neural electrodes improve chronic tissue integration. Acta Biomater. **53**, 46–58 (2017).

62. M. L. Heien, M. A. Johnson, R. M. Wightman, Resolving neurotransmitters detected by fast-scan cyclic voltammetry. Anal. Chem. 76, 5697–5704 (2004).

63. M. K. Zachek, J. Park, P. Takmakov, R. M. Wightman, G. S. McCarty, Microfabricated FSCV-compatible microelectrode array for real-time monitoring of heterogeneous dopamine release. Analyst **135**, 1556–1563 (2010).

64. S. B. Flagel, J. J. Clark, T. E. Robinson, L. Mayo, A. Czuj, I. Willuhn, C. A. Akers, S. M. Clinton, P. E. Phillips, H. Akil, A selective role for dopamine in stimulus–reward learning. Nature **469**, 53–57 (2011).

65. Y. S. Singh, L. E. Sawarynski, P. D. Dabiri, W. R. Choi, A. M. Andrews, Head-to-head comparisons of carbon fiber microelectrode coatings for sensitive and selective neurotransmitter detection by voltammetry. Anal. Chem. **83**, 6658–6666 (2011).

66. C. Park, Y. Oh, H. Shin, J. Kim, Y. Kang, J. Sim, H. U. Cho, H. K. Lee, S. J. Jung, C. D. Blaha, K. E. Bennet, M. L. Heien, K. H. Lee, I. Y. Kim, D. P. Jang, Fast cyclic square-wave voltammetry to enhance neurotransmitter selectivity and sensitivity. Anal. Chem. **90**, 13348–13355 (2018).

67. B. J. Venton, Q. Cao, Fundamentals of fast-scan cyclic voltammetry for dopamine detection. Analyst **145**, 1158–1168 (2020).

68. K. N. Schultz, R. T. Kennedy, Time-resolved microdialysis for in vivo neurochemical measurements and other applications. Annu. Rev. Anal. Chem. **1**, 627–661 (2008).

69. Y. Liu, J. Zhang, X. Xu, M. K. Zhao, A. M. Andrews, S. G. Weber, Capillary ultrahigh performance liquid chromatography with elevated temperature for sub-one minute separations of basal serotonin in submicroliter brain microdialysate samples. Anal. Chem. **82**, 9611–9616 (2010).

70. O. S. Mabrouk, Q. Li, P. Song, R. T. Kennedy, Microdialysis and mass spectrometric monitoring of dopamine and enkephalins in the globus pallidus reveal reciprocal interactions that regulate movement. J. Neurochem. **118**, 24–33 (2011).

71. R. T. Kennedy, Emerging trends in in vivo neurochemical monitoring by microdialysis. Curr. Opin. Chem. Biol. **17**, 860–867 (2013).

72. J. Zhang, A. Jaquins-Gerstl, K. M. Nesbitt, S. C. Rutan, A. C. Michael, S. G. Weber, In vivo monitoring of serotonin in the striatum of freely moving rats with one minute temporal resolution by online microdialysis-capillary high-performance liquid chromatography at elevated temperature and pressure. Anal. Chem. **85**, 9889–9897 (2013).

73. K. T. Ngo, E. L. Varner, A. C. Michael, S. G. Weber, Monitoring dopamine responses to potassium ion and nomifensine by in vivo microdialysis with online liquid chromatography at one-minute resolution. ACS Chem. Neurosci. **8**, 329–338 (2017).

74. A. Muller, V. Joseph, P. A. Slesinger, D. Kleinfeld, Cell-based reporters reveal in vivo dynamics of dopamine and norepinephrine release in murine cortex. Nat. Methods **11**, 1245–1252 (2014).

75. R. Liang, G. J. Broussard, L. Tian, Imaging chemical neurotransmission with genetically encoded fluorescent sensors. ACS Chem. Neurosci. **6**, 84–93 (2015).

76. K. S. Girven, D. R. Sparta, Probing deep brain circuitry: New advances in in vivo calcium measurement strategies. ACS Chem. Neurosci. **8**, 243–251 (2017).

77. T. Patriarchi, J. R. Cho, K. Merten, M. W. Howe, A. Marley, W. H. Xiong, R. W. Folk, G. J. Broussard, R. Liang, M. J. Jang, H. Zhong, D. Dombeck, M. von Zastrow, A. Nimmerjahn, V. Gradinaru, J. T. Williams, L. Tian, Ultrafast neuronal imaging of dopamine dynamics with designed genetically encoded sensors. Science **360**, eaat4422 (2018).

78. F. Sun, J. Zeng, M. Jing, J. Zhou, J. Feng, S. F. Owen, Y. Luo, F. Li, H. Wang, T. Yamaguchi, Z. Yong, Y. Gao, W. Peng, L. Wang, S. Zhang, J. Du, D. Lin, M. Xu, A. C. Kreitzer, G. Cui, Y. Li, A genetically encoded fluorescent sensor enables rapid and specific detection of dopamine in flies, fish, and mice. Cell **174**, 481–496.e19 (2018).

79. E. K. Unger, J. P. Keller, M. Altermatt, R. Liang, A. Matsui, C. Dong, O. J. Hon, Z. Yao, J. Sun, S. Banala, M. E. Flanigan, D. A. Jaffe, S. Hartanto, J. Carlen, G. O. Mizuno, P. M. Borden, A. V. Shivange, L. P. Cameron, S. Sinning, S. M. Underhill, D. E. Olson, S. G. Amara, D. T. Lang, G. Rudnick, J. S. Marvin, L. D. Lavis, H. A. Lester, V. A. Alvarez, A. J. Fisher, J. A. Prescher, T. L. Kash, V. Yarov-Yarovoy, V. Gradinaru, L. L. Looger, L. Tian, Directed evolution of a selective and sensitive serotonin sensor via machine learning. Cell **183**, 1986–2002.e26 (2020).

80. J. Wan, W. Peng, X. Li, T. Qian, K. Song, J. Zeng, F. Deng, S. Hao, J. Feng, P. Zhang, Y. Zhang, J. Zou, S. Pan, M. Shin, B. J. Venton, J. J. Zhu, M. Jing, M. Xu, Y. Li, A genetically encoded sensor for measuring serotonin dynamics. Nat. Neurosci. **24**, 746–752 (2021).

Chapter 10: Flexible and Implantable Polyimide Aptamer-Field-Effect Transistor Biosensors

Chapter 10 is a manuscript published with the following citation:

Zhao, C., Man, T., Cao, Y., Weiss, P.S., Monbouquette, H.G. and Andrews, A.M., 2022. Flexible and Implantable Polyimide Aptamer-Field-Effect Transistor Biosensors. *ACS sensors*, *7*(12), pp.3644-3653.

ABSTRACT

Monitoring neurochemical signaling across time scales is critical to understanding how brains encode and store information. Flexible (vs stiff) devices have been shown to improve in vivo monitoring, particularly over longer times, by reducing tissue damage and immunological responses. Here, we report our initial steps toward developing flexible and implantable neuroprobes with aptamer-field-effect transistor (FET) biosensors for neurotransmitter monitoring. A high-throughput process was developed to fabricate thin, flexible polyimide probes using microelectromechanical-system (MEMS) technologies, where 150 flexible probes were fabricated on each 4 in. Si wafer. Probes were 150 μm wide and 7 μm thick with two FETs per tip. The bending stiffness was 1.2×10^{-11} $N \cdot m^2$. Semiconductor thin films (3 nm In_2O_3) were functionalized with DNA aptamers for target recognition, which produces aptamer conformational rearrangements detected via changes in FET conductance. Flexible aptamer-FET neuroprobes detected serotonin at femtomolar concentrations in high-ionic strength artificial cerebrospinal fluid. A straightforward implantation process was developed, where microfabricated Si carrier devices assisted with implantation such that flexible neuroprobes detected physiological relevant serotonin in a tissue-hydrogel brain mimic.

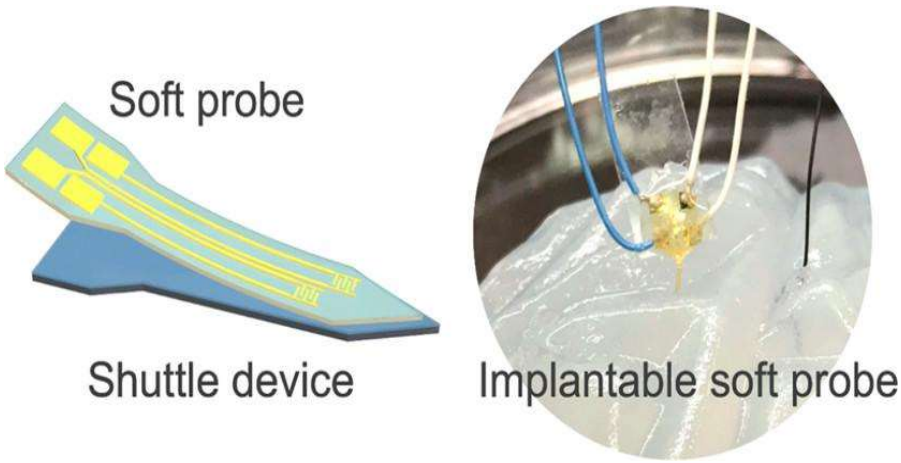

10.1 Introduction

Implantable bioelectronics are powerful tools to monitor neural activity.[1–4] Implanted devices enable new discoveries associated with understanding healthy brain function and the biological basis and treatment mechanisms of neurological and neuropsychiatric disorders.[5–10] Devices for monitoring in vivo electrical signals have been extensively developed enabling chronic recordings lasting over six months with single neuron resolution.[11–20] In addition to electrical signals, chemical communication via neurotransmitters plays a central role in brain information processing. However, existing device technologies for neurochemical recordings are more limited.[5,21–23] A major challenge in neurochemical sensing is the development of biosensors that can detect arrays of neurotransmitters in vivo with high sensitivity and selectivity.

Recently, we developed aptamer-field-effect transistor (FET) biosensors for neurotransmitter detection.[4,23–28] Thin films of biocompatible In_2O_3 (~3 nm) for signal transduction were functionalized with single-stranded DNA (aptamers) for target recognition.[24–26] Upon target capture, negatively charged oligonucleotide backbones undergo conformational changes near FET surfaces resulting in measurable changes in FET conductance and, hence, target-related current. This sensing mechanism is universal since it is independent of the charge or

electrochemical properties of the analytes themselves.[24] We have shown that aptamer-FETs can be used to detect biomarkers, including serotonin, dopamine, glucose, the membrane lipid S-1-P, phenylalanine, and cortisol in complex physiological environments.[24–27] Aptamer-FET biosensors show high selectivity to targets vs structurally similar molecules. Recently, Zhang and co-workers developed graphene-based aptamer-FET biosensors using our aptamers for dopamine and serotonin sensing.[29,30]

To monitor neurotransmitters in vivo, we developed Si-based implantable neuroprobes with miniaturized aptamer-FET biosensors. Probes were either 150 or 50 μm in width and thickness at the tips.[4] The larger neuroprobes were implanted in awake, active mice where they detected electrically stimulated serotonin release with high sensitivity. While our previous study showed results for acute measurements (i.e., hours), challenges remain for stable, chronic in vivo recordings. [31,32]

Conventional implantable electrodes, including the first generation neuroprobes we developed, are typically fabricated using rigid substrates such as metals or Si, which are much stiffer than biological tissues.[33] For example, Si has a Young's modulus of ∼200 GPa, while brain tissue has a Young's modulus of ∼10 kPa. This Young's modulus mismatch of >107 induces immune responses and subsequent glial scar formation. For biosensing applications, immunological responses lead to signal drift due to biofouling.[31,34] Scar formation decreases device recording accuracy and sensitivity over time.[31,34–38] Moreover, the formation of glial scars leads to biosensor failure due to limited access between the sensing surface and the tissue interface.[34]

Recent developments in soft and flexible electronics show the potential for overcoming these limitations.[14,20,22,39–45] Flexible bioelectronics with lower device Young's moduli (i.e.,

increased elasticity) showed reduced immunological responses after brain implantation compared with rigid substrates.[31,34,43,46,47] Flexible devices with the capability to detect neurotransmitters in real time are necessary to understand chemical neurotransmission, particularly via chronic neural recordings.[4,21,30,35] Along these lines, we recently developed a wearable smartwatch for sweat cortisol sensing using flexible polyimide-based aptamer FETs.[28] We also fabricated In_2O_3 nanoribbon aptamer-FET biosensor arrays on flexible poly-(ethylene terephthalate) (PET) for the multiplexed detection of serotonin, dopamine, pH, and temperature in real time.[26] Many flexible substrates (e.g., PET and polyimide) still have Young's moduli (typically on the order of GPa) that are orders of magnitude greater than brain tissue. One promising strategy to reduce the bending stiffness of a material is to reduce its thickness, as bending stiffness decreases cubically with thickness (equation shown in the Supporting Information).[48] Recently, polyimide devices with thicknesses <10 μm have been shown to have optimal bending stiffness and conformal contact with tissue.[20,40,42,49] However, ultrathin devices are difficult to process and handle.[30,40,50] Moreover, due to the low bending stiffness, thin flexible probes suffer from buckling during penetration into tissues, making them challenging to implant.

Here, we report on fabrication and implantation strategies for flexible and implantable polyimide (7 μm) aptamer-FET neuroprobes to monitor the small-molecule neurotransmitter serotonin. We designed a high-throughput process to fabricate polyimide neuroprobes using microelectromechanical-system (MEMS) technologies, which are scalable, high throughput, and compatible with other microfabrication processes.[4] Quasi-2D In_2O_3 FETs were fabricated on the probe tips. With aptamers functionalized on the In_2O_3 surfaces, flexible neuroprobes were used to detect serotonin at femtomolar concentrations in artificial cerebrospinal fluid (aCSF). We used an artificial brain tissue matrix to develop and to test a process to implant flexible probes using a rigid

carrier as a temporary shuttle device with straightforward probe release. Flexible aptamer-FET probes were implanted into a brain-tissue hydrogel mimic and showed high sensitivities to serotonin.

10.2 Experimental Section

10.2.1 Materials

Oligonucleotides (aptamers) were obtained from Integrated DNA Technologies (Coralville, IA). The SYLGARD 184 used to make polydimethylsiloxane (PDMS) wells for recordings was from Dow Corning Corporation (Midland, MI). Deionized water (18.2 MΩ) was dispensed via a Milli-Q system (Millipore, Billerica, MA). Polyimide solution (#PI-2611) was provided by Dupont Teijin Films (Chester, VA). Prime quality 4 in. Si wafers (P/B, thickness 500 and 150 μm) were purchased from Silicon Valley Microelectronics, Inc. (Santa Clara, CA, USA). All other materials were purchased from Sigma-Aldrich Co. (St. Louis, MO) unless otherwise noted.

10.2.2 Neuroprobe Fabrication

Polyimide solutions were spin-coated at 3000 rpm for 30 s onto 500 μm thick Si wafers to form a 7 μm thick film, as reported previously.[28] After coating, substrates were preheated at 90 °C for 90 s and then at 150 °C for 90 s on a hot plate. Afterward, the substrates were transferred to an oven and annealed at 350 °C for 30 min. Aqueous solutions (0.1 M) of indium (III) nitrate hydrate (99.999%) were then spin-coated at 3000 rpm for 30 s onto polyimide-coated Si wafers. After deposition of indium precursors, substrates were heated to 150 °C for 10 min, followed by 3 h of annealing at 350 °C.[23,51] Source and drain electrodes (10 nm Ti and 30 nm Au) were deposited by electron-beam evaporation (CHA Industries, Inc., Fremont, CA) and patterned via standard

photolithography. A second photolithographic process was performed to define the outer perimeter of the probes. Reactive ion etching was used to etch through the polyimide substrates using a plasma etching system (STS-AOE, Plasmatreat, Hayward, CA) with the protection of the photoresist. Probes were released from carrier wafers using tweezers. The source and drain electrodes of the neuroprobes were connected with wiring using Ag epoxy (Ted Pella, Redding, CA).[4]

10.2.3 Implantation of Flexible Neuroprobes

Shuttle devices were fabricated from Si using previously published methods.[4] Briefly, Si substrates (150 μm thick) were coated with photoresist to define probe profiles. Deep reactive ion etching using the Bosch process was used to etch through the unmasked regions of the silicon substrates using a Deep Silicon Etcher III (Plasma-Therm, Fremont, CA). To attach the flexible polyimide probes, Si shuttles were immersed into a physiological buffer solution to form a thin solution film on the Si surfaces. Since probes are destined for eventual brain implantation, we used aCSF as the buffer. Detailed aCSF preparation protocols are described in our previous work.[27] The polyimide probes were then attached to the Si shuttles via capillary forces. Alignment between polyimide probes and Si shuttle devices was achieved using tweezers under an optical microscope (Figure 10.3c).

To mimic the properties of brain tissue for implantation, we used a 0.6% (w/v) agarose hydrogel, which was prepared by mixing agarose powder and aCSF. The mixture was microwaved until the agarose powder was dissolved (∼1 min), poured into a container, and cooled to room temperature. Assembled probes and shuttles were implanted into the brain-mimic hydrogel using tweezers. After implantation for ∼1 min, the Si shuttle devices were removed from the hydrogel leaving the polyimide probes in place (Movie S1).

10.2.4 In Vitro Experiments

To test device biosensing capabilities in vitro, we rinsed the FET probes in ethanol and dried with N_2 immediately before functionalization with thiolated serotonin aptamers. Mixtures of (3-aminopropyl)triethoxysilane and trimethoxy(propyl)silane (1:9, v/v) were thermally deposited on In_2O_3 at 40 °C for 1 h and annealed at 60 °C for 10 min.[4,23,24] Source and drain electrodes were insulated with a self-assembled monolayer of 1-dodecanethiol by immersing in 1 mM ethanolic solutions for 1 h. Probes were then immersed in 1 mM 3-maleimidobenzoic acid Nhydroxysuccinimide ester dissolved in a 1:9 (v/v) mixture of dimethyl sulfoxide and phosphate-buffered saline (PBS, Gibco, Fisher Scientific, Waltham, MA) for 30 min. To immobilize aptamers, probes were immersed in a 1 μM solution of thiolated DNA in PBS overnight. Probes were rinsed with deionized water and dried with N_2 before measurements. In vitro testing was performed by adding different concentrations of serotonin into aCSF in PDMS wells sealed to each device.

10.2.5 Ex Vivo Experiments

Brain tissue lacking serotonin was obtained from *Tph2* knockout mice.[52] Mice were exsanguinated by cardiac perfusion and brains were cleared of blood containing serotonin synthesized by peripheral *Tph1*. The brains were then shipped to UCLA on dry ice from the laboratory of Dr. Donald Kuhn (Wayne State University, Detroit, MI). Brain tissue was stored at −80 °C until use. Brain tissue collection procedures were approved by the Wayne State University Institutional Animal Care and Use Committee.

Brain tissue was homogenized in ice-cold aCSF (1:1 w/v) using a VirTis Virsonic600 ultrasonic cell disruptor (Gardiner, NY) with the microtip set at 4 and a 50% duty cycle for 30−40 pulses-. Homogenized brain tissue solutions were mixed with agarose powder and aCSF to make 0.6% agarose gels. The mixture was microwaved just until the agarose powder dissolved (∼1 min,

melting point of ~65 °C). The solution was poured into a brain mold to mimic brain cortical morphology and immediately cooled. Flexible neuroprobes were implanted into the brain tissue hydrogel using the method described above. A Ag/AgCl gate electrode, constructed from a 0.010-in. diameter Ag wire freshly coated with AgCl (A-M Systems, Sequim, WA) by immersing in a bleach solution (Clorox, Oakland, California) for 5 min, was implanted into the brain tissue hydrogel next to the probe. A 2-μL aliquot of 50 μM serotonin was injected into the hydrogel (~0.2 cm away from the probe tip) for a final serotonin concentration of 100 nM (calculated based on 100 mL aCSF in the hydrogel).

All FET measurements were performed using a Keithley 4200A SCS semiconductor analyzer (Tektronix, Beaverton, OR). Source−drain current (IDS) transfer curves were obtained by sweeping the gate voltage (VGS) from 100 to 350 mV while maintaining the drain voltage (VDS) at 10 mV, which took ~5 s for each scan. Calibrated responses were calculated at 300 mV to minimize device-to-device variation, as previously described.[24,53]

10.2.6 Statistics

Data from FET calibrated responses are reported as means ± standard errors of the means and were analyzed using GraphPad Prism 7.04 (GraphPad Software Inc., San Diego, CA) via one-way analysis of variance followed by Tukey's multiple comparisons post hoc tests with repeated measures.

10.3 Results and Discussion

The process used to fabricate flexible In_2O_3 FET neuroprobes is described in detail in the Experimental Section and illustrated in Figure 10.1 and Figure S1. We leveraged our earlier high-throughput fabrication process for 150 μm and 50 μm Si neuroprobes using MEMS technologies.[4]

Polyimide (~7 μm) and In_2O_3 (~3 nm) films were fabricated sequentially on Si substrates using solution processing, followed by photolithography to define the Au and Ti source and drain electrodes. A layer of parylene can be added to the probe shafts to insulate source/drain interconnects, as we demonstrated previously.[4] Probe outlines were also defined photolithographically. We used In_2O_3 as the semiconductor due to its straightforward sol−gel fabrication. Others have shown that In_2O_3 is more stable than other metal oxides, e.g., indium−gallium−zinc oxide (IGZO), in physiological electrolyte solutions.[23,54] The thickness of In_2O_3 on polyimide (3 nm) was determined by atomic force microscopy, as shown in our previous work.[28]

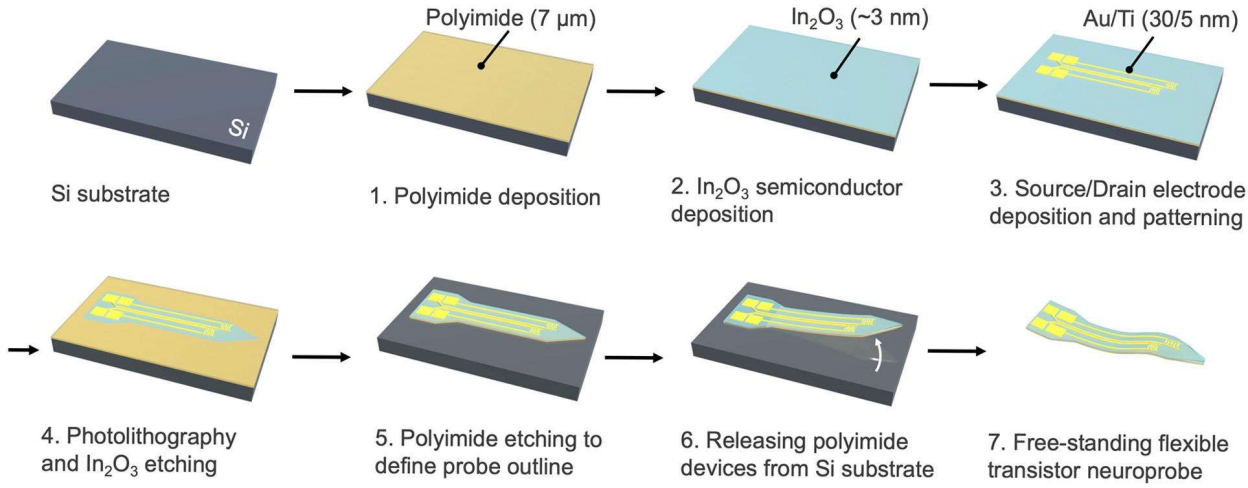

Figure 10.1. Schematic of the flexible neuroprobe fabrication process. A polyimide film was deposited on a Si substrate (1), followed by the deposition of In_2O_3 (2). Source and drain electrodes were patterned by photolithography followed by metal evaporation of Au and Ti (3). To define the outline of the neuroprobe, a second lithography process was used followed by oxygen-plasma etching of In_2O_3 (4) and polyimide (5). Each fabricated polyimide device was released from the Si substrate using tweezers (6) to obtain individual flexible neuroprobes (7).

This fabrication process is high throughput and scalable such that 150 probes were fabricated per 4 in. wafer (Figure 10.2a). Probes were delaminated from Si substrates using

tweezers to produce free-standing devices. A delaminated probe is shown in Figure 10.2b, leaving an outline of the probe on the wafer. The freestanding polyimide probes are flexible and make conformal contact with the convoluted surface of an agarose hydrogel brain model (Figure 10.2c). Each probe was ~7 μm thick and ~150 μm wide with two FETs side-by-side on the tip (Figure 10.2d).

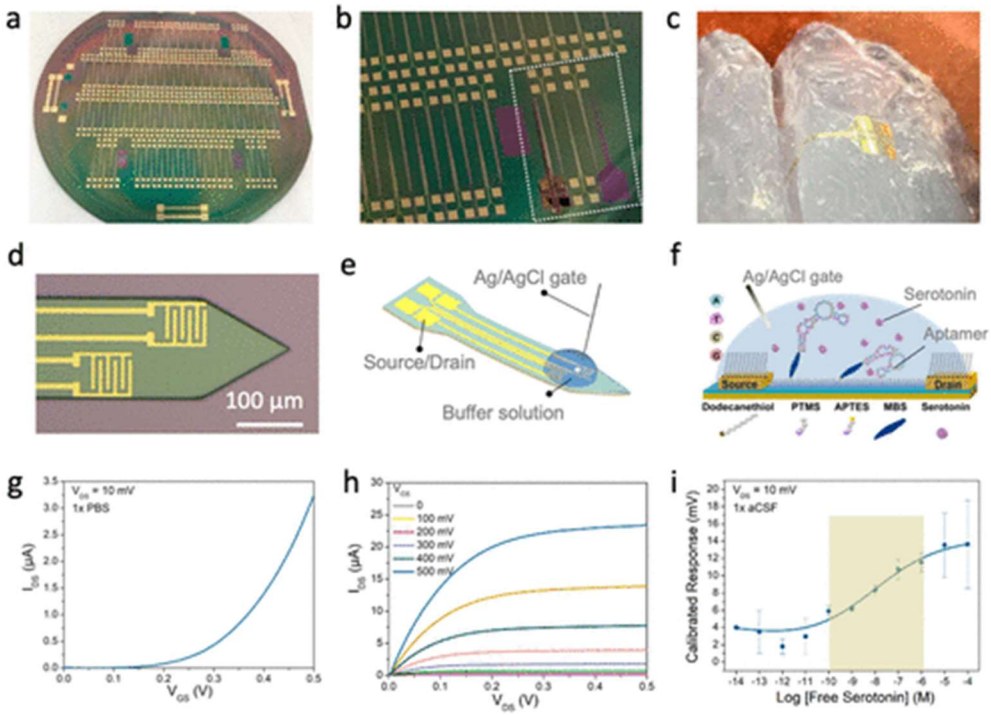

Figure 10.2. Serotonin sensing using aptamer-functionalized flexible neuroprobes. (a) Photograph of 150 flexible probes fabricated on a 4 in. Si wafer. (b) Photograph of released probes on a Si substrate. As highlighted in the white box, the probe on the left has been partially released while the probe on the right has been completely released from the substrate. (c) Photograph of a flexible polyimide probe on a hydrogel matrix, which serves here as a brain mimic, showing the probe flexibility (tip width 150 μm). (d) Optical microscope image showing the tip of one neuroprobe with two field-effect transistors side-by-side. (e) Schematic of the measurement setup of a flexible neuroprobe, where a Ag/AgCl electrode was used to gate the FET through the buffer solution. (f) Schematic of the surface chemistry used to covalently functionalize aptamers onto the In_2O_3 surface. PTMS, trimethoxy(propyl)silane; APTMS, (3-aminopropyl)trimethoxysilane; MBS, 3-maleimidobenzoic acid N-hydroxysuccinimide ester. (g,h) Transfer and output curves, respectively, of a representative FET on a polyimide neuroprobe in phosphate buffered saline. PBS, phosphate buffered saline. (i) Sensing results for serotonin in artificial cerebrospinal fluid, where

the highlighted box shows the physiological range of serotonin in the extracellular space. aCSF, artificial cerebrospinal fluid. Error bars are standard errors of the means of measurements from N = 3 different probes.

The bending stiffness of these polyimide probes is 1.2×10^{-11} N·m^2, which is 7 orders of magnitude lower than that of the smallest optical fibers (230 μm outer diameter polyethylene fibers with silica cores, 1×10^{-5} N·m^2, calculations shown in the Supporting Information).[30,55] The effective bending stiffness of the polyimide probes (bending stiffness per width) is $\sim 8 \times 10^{-8}$ N·m, which is less than that of commonly used soft elastomers, e.g., polydimethylsiloxane (2.2×10^{-7} N· m at 100 μm thickness).[56] Previous histological studies have shown that polyimide devices of similar thickness and bending stiffness induce minimal immune responses.[30,40] Note that the width of the probes and FETs can be scaled down in a straightforward manner to 50 μm using photolithography, as we have previously demonstrated using Si as the device substrate.[4] Polyimide is thermally stable and compatible with most microfabrication processes up to 350 °C. Previously, we showed that the electronic and biosensing performance of In_2O_3 FETs on polyimide remains stable even after 100 bending cycles.[28] This straightforward and universal fabrication strategy opens opportunities to integrate polyimide neuroprobes with other neural recording and modulating modalities on a single flexible platform, e.g., electrophysiology and optical stimulation capabilities.

A Ag/AgCl electrode was used to gate thin-film In_2O_3 FETs on flexible neuroprobes through the buffer solution, where electrical double layers were used as the gate dielectric (Figure 10.2e). Source and drain electrodes were connected to the semiconductor analyzer via copper wiring to apply voltages to the interdigitated electrodes covered by a buffer solution.[4] For serotonin sensing, the In_2O_3 surface was covalently functionalized with serotonin aptamers.[24] The detailed functionalization process is described in the Experimental Section and depicted in Figure 2f. Here,

self-assembled monolayers on the Au source and drain electrodes combined with the electrical double layers in the buffer solution serve as capacitors for insulation.[24,27] Typical transistor performance was observed from the FETs in aCSF, with transfer and output characteristics shown in Figure 10.2g and h, respectively.

Serotonin was introduced to sensors to test responses. We used aCSF to mimic the ionic strength of the extracellular fluid in brain tissue. The FETs on flexible probes responded to serotonin in the pM to μM range covering the physiological range of serotonin in the brain extracellular space,[57−60] as highlighted in yellow in Figure 10.2i. The serotonin aptamer used here was previously demonstrated to be highly selective for serotonin vs interfering molecules (i.e., L-5-hydroxytryptophan, 5-hydroxyindoleacetic acid, dopamine, L-tryptophan, uric acid, and ascorbic acid) when tested on FETs on Si.[4,24] We expect similar selectivity for the flexible polyimide neuroprobes since only the substrate was changed; we used the same aptamer to detect serotonin.

To monitor serotonin in vivo, neuroprobes need to be implanted into different areas of the brain where serotonin cell bodies and axons are found.[57] However, the softness of the polyimide probes leads to bunching during tissue penetration.[3,32] There have been several strategies developed to assist in the implantation of soft probes, including coating probes with a stiffening polymer, rapid freezing, or liquid metal or temperature-adaptive Young's moduli systems.[42,47,50,61−63] However, current implantation strategies typically require reengineering of device architectures or complicated assembly processes. Moreover, since biosensor surfaces are usually functionalized with receptors, e.g., antibodies or aptamers, before the implantation process, implantation strategies should not damage the functionalized layer.

Here, we developed a one-step shuttle-assisted process for flexible neuroprobe implantation using surface tension. As shown in Figure 10.3a, a Si shuttle was fabricated to have the same lateral dimensions as the flexible neuroprobes (150 μm). Fabrication was the same as described in our previous work[4] and in the Experimental Section. The similar shapes of the Si shuttle device and the flexible polyimide neuroprobes minimized tissue damage from the shuttle device during the penetration process. The Si shuttle device was treated with O2 plasma to make it hydrophilic before dipping into the buffer solution (i.e., aCSF). The thin layer of buffer coating the Si shuttle surface was used to affix a flexible neuroprobe via van der Waals forces. The neuroprobe and shuttle were aligned under an optical microscope using tweezers (Figure 10.3b).

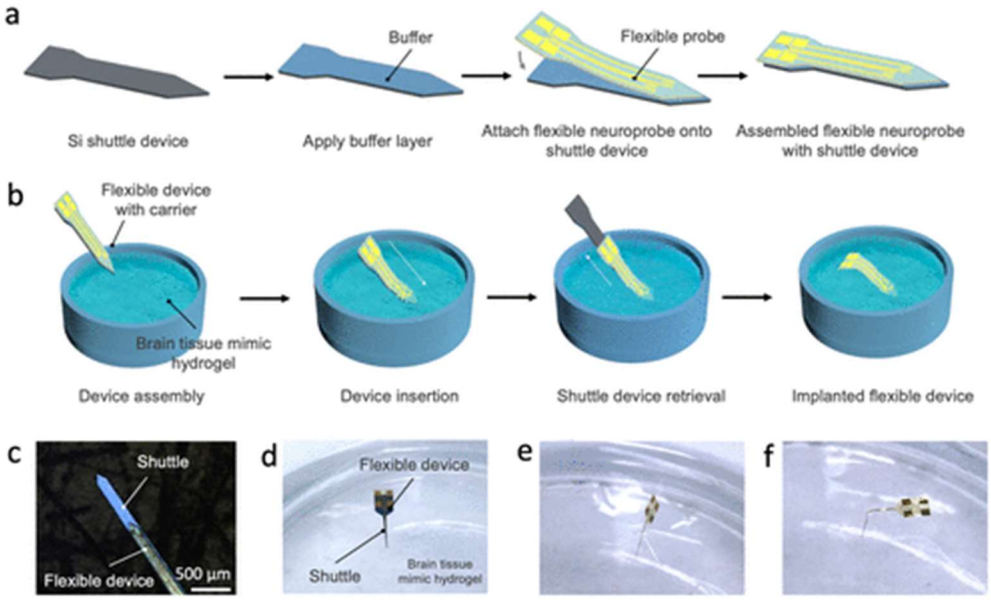

Figure 10.3. Implantation of a flexible neuroprobe into a brain-mimic hydrogel. (a) Schematic illustration of device assembly before implantation. A flexible probe was attached to a Si shuttle via surface tension and aligned under a microscope. (b) Schematic illustration of flexible probe implantation using a Si probe as the shuttle device. The assembled device penetrates the hydrogel without buckling. After insertion, the buffer layer between the flexible probe and the Si shuttle device diffuses between the hydrogel. The edge surface tension is relieved, enabling the flexible probe to be separated from the Si shuttle. The shuttle is removed, leaving the flexible probe implanted in the hydrogel. (c) Optical microscope image of an assembled device, where the

flexible probe is partially aligned to the Si shuttle device. Photographs of (d) an assembled device implanted into the hydrogel, and (e, f) a freestanding flexible probe implanted in the brain-mimic hydrogel.

After assembly, the shuttle+neuroprobe was implanted. To mimic brain tissue, we used a 0.6% agarose hydrogel with aCSF, which closely resembles several critical physical characteristics of brain tissue, including the penetration force.[47,64] After inserting the assembled device into the brain-mimic, the buffer layer between the flexible neuroprobe and shuttle device diffused into the hydrogel, reducing the surface tension holding the two parts together. The shuttle device was then retracted leaving the flexible device in place in the hydrogel (Figure 10.3b−f, Movie S1). During the removal of the shuttle device, we did not observe movement of the flexible probe, as shown in the movie (Movie S1). For future in vivo experiments, it will be necessary to investigate further the accuracy of positioning during the implantation processes.

Sensing in vivo entails detecting specific targets in complex biological matrices containing a wide range of neurotransmitters (nontargets), metabolites and other interferants, and biomacromolecules (biofouling). To investigate the sensing capabilities of the flexible neuroprobes in a biological matrix that more closely approximates an in vivo environment, we used brain tissue from *Tph2*-null mice.[4] These mice do not express the rate-limiting serotonin synthetic enzyme in the central nervous system (CNS), and thus lack endogenous brain serotonin (Figure 10.4a).

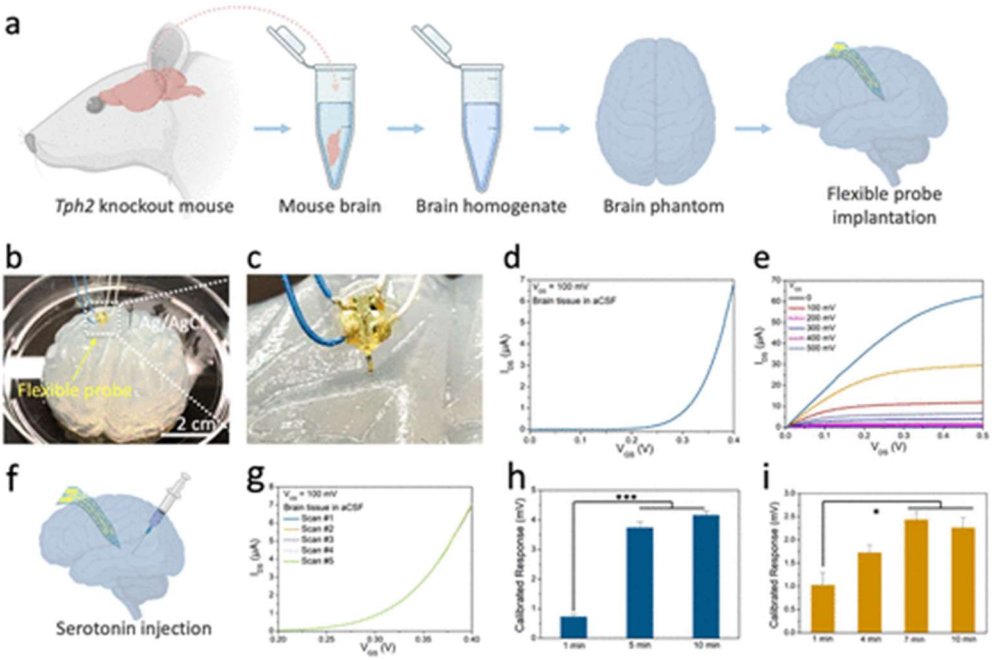

Figure 10.4. Ex vivo sensing of serotonin in a brain phantom. (a) Schematic illustration of brain phantom preparation. Brains from *Tph2* null mice were removed and the tissue was homogenized in artificial cerebrospinal fluid (aCSF). The brain tissue homogenate was then mixed with 0.6% agarose gel in aCSF to make the brain-mimic for flexible probe implantation. (b,c) Photographs of an implanted flexible probe in the brain phantom, where a Ag/AgCl electrode was also implanted to apply a gate voltage. The source and drain electrodes were wired, sealed with epoxy, and connected to external measurement instrumentation. (d) Transfer characteristics of a representative field-effect transistor on a flexible probe after implantation in the brain phantom. (e) Output characteristics of a field-effect transistor on a flexible probe after implantation in the brain phantom. (f) Schematic illustration of serotonin injection using a syringe placed next to an implanted probe. (g) Five consecutive overlapping transfer sweeps of an implanted neuroprobe in the tissue-hydrogel brain-mimic before serotonin injection. (h) Calibrated responses of a representative neuroprobe after exposure to serotonin diffusing to the probe over time (100 nM final concentration). Error bars are standard errors of the means for N = 5 sweeps. ***P < 0.005 for 1 min vs 5 and 10 min. (i) Calibrated responses from a different neuroprobe after exposure to 100 nM serotonin over time. Error bars are standard errors for N = 5 sweeps. *P < 0.05 for 1 min vs 7 and 10 min.

Brain tissue homogenates from *Tph2*-null mice were incorporated into 0.6% agarose hydrogel in aCSF. As such, we produced an ex vivo model that mimicked the ionic strength of the extracellular space and approximated the chemical and physical properties of the in vivo brain environment. Using brain tissue that lacks serotonin prevented swamping the FET sensors with

high concentrations of endogenous intracellular stores of serotonin liberated during tissue homogenization. In vivo, FET sensors would not encounter vesicular serotonin except briefly during implantation.

This type of brain phantom mainly mimics the physical characteristics of the brain (e.g., Young's modulus and penetration force) and ionic strength of the extracellular fluid in the brain.[47,64] The brain tissue in the agarose gel introduces biomolecules found in the in vivo environment. Nonetheless, the preparation process may affect the molecular composition originally present in the brain. Previously, we tested similar biosensors on Si substrates in fresh brain tissue containing endogenous small molecules and macromolecules. In both cases, aptamer-FET sensors showed high target sensitivity and low biofouling.[4,24]

Figure 10.4b, c depicts implantation of a representative flexible neuroprobe into a brain mimic using a Si shuttle, as described above. A Ag/AgCl electrode was then implanted to apply gate voltages through the hydrogel matrix (Figure 10.4b). We characterized the transistor performance of the flexible neuroprobes in this tissue-hydrogel phantom. As shown in Figure 10.4d and e, an implanted neuroprobe showed typical transfer and output characteristics with gate voltage and source−drain voltage modulation.

To simulate neurotransmitter release and diffusion in the brain, we used a syringe to inject 50 μM serotonin into the hydrogel. The injection sites were approximately 2 mm away from the implanted neuroprobes. The final concentration (100 nM) was selected as a physiologically relevant serotonin concentration.[57−60] Data were collected before the introduction of serotonin and at different time intervals after its introduction. As shown in Figure 10.4g, five consecutive transfer curves overlapped with each other in the tissue-hydrogel brainmimic, illustrating that the flexible neuroprobes were stable in the matrix without detectable signal drift prior to injection.

We observed significant increases in the responses of two different neuroprobes as early as 5 min after serotonin addition (see Table S1 for statistics). These data demonstrate that the flexible aptamer-FET neuroprobes detected diffusion-related changes in serotonin levels. We previously found that the response times of our aptamer-FET sensors are on the order of seconds;[26] the 5 min delay in response time here is due to target diffusion over ~2 mm in the hydrogel matrix from the introduction location to the recording site, which is similar to what we observed in a previous study using Si neuroprobes.[4] These findings illustrate that our flexible neuroprobes can be implanted into a solid matrix that mimics the rigidity and chemical composition of brain tissue to monitor physiologically relevant serotonin release.

10.4 Conclusion

We developed flexible and implantable neurochemical probes based on aptamer FET biosensors. A high-throughput fabrication strategy was developed to fabricate In_2O_3 thin film (~3 nm) field-effect transistors on polyimide (7 μM) with up to 150 flexible neuroprobes on a 4 in. Si substrate. Flexible aptamer-FET neuroprobes detected serotonin down to femtomolar concentrations in artificial cerebrospinal fluid. To facilitate the implantation of these flexible devices, we developed a straightforward process where a rigid Si carrier device was used to assist in tissue penetration. To test the functionality of the flexible neuroprobes for future in vivo studies, we developed a brain phantom as an ex vivo model. We used agarose gel to mimic critical physical characteristics of the brain and aCSF to mimic the ionic strength of the brain's extracellular space. Moreover, we combined agarose gel with mouse brain tissue containing interferants and biomacromolecules present in the brain. The brain tissue phantom served as a model to evaluate sensor performance toward in vivo applications for neurochemical sensing. We showed that the

flexible neuroprobes were stable while implanted in the hydrogel matrices with reproducible transistor performance and without short-term biofouling. We were able to detect serotonin injected into the brain tissue phantom suggesting the potential to monitor changes in serotonin levels in vivo.

While soft neuroprobes remain an important goal for tissue like implantable bioelectronics, a longstanding question remains as to how soft and flexible is soft and flexible enough such that immunological responses are minimized. This issue is a grand challenge to the bioelectronics community that needs to be addressed and requires further study. Future histological studies as a function of implantation duration involving flexible vs stiff probes will provide comparative information on immunological responses. Another key question involves the impact of device dimensions. Smaller implanted devices appear to reduce immune responses.[31,32,34] However, understanding how immunological responses change systematically in response to miniaturization is still unclear. Along these lines, we have previously fabricated Si neuroprobes with 50 μm widths and thicknesses to compare with 150 μm neuroprobes in terms of tissue responses. Scaling down the flexible neuroprobes developed in this work can be achieved using a similarly straightforward approach. Further histological studies comparing our devices of different sizes and stiffness are ongoing.

In addition to FETs, aptamers can be coupled with redox reporters for electrochemical sensing. For example, electrochemical aptamer-based (EAB) sensors have been used to track plasma drug concentrations in real-time.[65,66] Recently, a dopamine aptamer was coupled with carbon-fiber microelectrodes noncovalently or using an electrochemical conjugation strategy for dopamine sensing in vivo using cyclic voltammetry.[67,68] We envision that next-generation neuroprobes will need to be soft and multimodal (i.e., sense multiple neurotransmitters and

electrophysiological signals, produce optical or electrical stimulation, and drug delivery all on the same device) and have long-term recording capabilities in vivo. Soft bioelectronics with the capability to detect multiple neurotransmitters simultaneously in real-time are needed to investigate chemical information processing in the brain, particularly in the context of chronic neural recordings during behavior.[21]

10.5 References

1. Seymour, J. P.; Wu, F.; Wise, K. D.; Yoon, E. State-of-the-Art MEMS and Microsystem Tools for Brain Research. Microsyst. Nanoeng. 2017, 3, 16066.
2. Won, S. M.; Song, E.; Zhao, J.; Li, J.; Rivnay, J.; Rogers, J. A. Recent Advances in Materials, Devices, and Systems for Neural Interfaces. Adv. Mater. 2018, 30, No. e1800534.
3. Woods, G. A.; Rommelfanger, N. J.; Hong, G. Bioinspired Materials for in Vivo Bioelectronic Neural Interfaces. Matter 2020, 3, 1087−1113.
4. Zhao, C.; Cheung, K. M.; Huang, I. W.; Yang, H.; Nakatsuka, N.; Liu, W.; Cao, Y.; Man, T.; Weiss, P. S.; Monbouquette, H. G.; Andrews, A. M. Implantable Aptamer-Field-Effect Transistor Neuroprobes for in Vivo Neurotransmitter Monitoring. Sci. Adv. 2021, 7, No. eabj7422.
5. Alivisatos, A. P.; Andrews, A. M.; Boyden, E. S.; Chun, M.; Church, G. M.; Deisseroth, K.; Donoghue, J. P.; Fraser, S. E.; Lippincott-Schwartz, J.; Looger, L. L.; Masmanidis, S.; McEuen, P. L.; Nurmikko, A. V.; Park, H.; Peterka, D. S.; Reid, C.; Roukes, M. L.; Scherer, A.; Schnitzer, M.; Sejnowski, T. J.; et al. Nanotools for Neuroscience and Brain Activity Mapping. ACS Nano 2013, 7, 1850− 1866.

6. Altieri, S. C.; Yang, H.; O'Brien, H. J.; Redwine, H. M.; Senturk, D.; Hensler, J. G.; Andrews, A. M. Perinatal vs Genetic Programming of Serotonin States Associated with Anxiety. Neuropsychopharmacology 2015, 40, 1456−1470.
7. Malvaez, M.; Shieh, C.; Murphy, M. D.; Greenfield, V. Y.; Wassum, K. M. Distinct Cortical-Amygdala Projections Drive Reward Value Encoding and Retrieval. Nat. Neurosci. 2019, 22, 762−769.
8. Dolensek, N.; Gehrlach, D. A.; Klein, A. S.; Gogolla, N. Facial Expressions of Emotion States and Their Neuronal Correlates in Mice. Science 2020, 368, 89−94.
9. Lee, K.; Claar, L. D.; Hachisuka, A.; Bakhurin, K. I.; Nguyen, J.; Trott, J. M.; Gill, J. L.; Masmanidis, S. C. Temporally Restricted Dopaminergic Control of Reward-Conditioned Movements. Nat. Neurosci. 2020, 23, 209−216.
10. Topalovic, U.; Aghajan, Z. M.; Villaroman, D.; Hiller, S.; Christov-Moore, L.; Wishard, T. J.; Stangl, M.; Hasulak, N. R.; Inman, C. S.; Fields, T. A.; Rao, V. R.; Eliashiv, D.; Fried, I.; Suthana, N. Wireless Programmable Recording and Stimulation of Deep Brain Activity in Freely Moving Humans. Neuron 2020, 108, 322−334.
11. Chen, R.; Canales, A.; Anikeeva, P. Neural Recording and Modulation Technologies. Nat. Rev. Mater. 2017, 2, 16093.
12. Ferro, M. D.; Melosh, N. A. Electronic and Ionic Materials for Neurointerfaces. Adv. Funct. Mater. 2018, 28, 1704335.
13. Viventi, J.; Kim, D. H.; Vigeland, L.; Frechette, E. S.; Blanco, J. A.; Kim, Y. S.; Avrin, A. E.; Tiruvadi, V. R.; Hwang, S. W.; Vanleer, A. C.; Wulsin, D. F.; Davis, K.; Gelber, C. E.; Palmer, L.; Van der Spiegel, J.; Wu, J.; Xiao, J.; Huang, Y.; Contreras, D.; Rogers, J. A.; et al. Flexible,

Foldable, Actively Multiplexed, High-Density Electrode Array for Mapping Brain Activity in vivo. Nat. Neurosci. 2011, 14, 1599−1605.

14. Vachicouras, N.; Tarabichi, O.; Kanumuri, V. V.; Tringides, C. M.; Macron, J.; Fallegger, F.; Thenaisie, Y.; Epprecht, L.; McInturff, S.; Qureshi, A. A.; Paggi, V.; Kuklinski, M. W.; Brown, M. C.; Lee, D. J.; Lacour, S. P. Microstructured Thin-Film Electrode Technology Enables Proof of Concept of Scalable, Soft Auditory Brainstem Implants. Sci. Transl. Med. 2019, 11, No. eaax9487.
15. Du, J.; Blanche, T. J.; Harrison, R. R.; Lester, H. A.; Masmanidis, S. C. Multiplexed, High Density Electrophysiology with Nanofabricated Neural Probes. PLoS One 2011, 6, No. e26204.
16. Rios, G.; Lubenov, E. V.; Chi, D.; Roukes, M. L.; Siapas, A. G. Nanofabricated Neural Probes for Dense 3-D Recordings of Brain Activity. Nano Lett. 2016, 16, 6857−6862.
17. Jun, J. J.; Steinmetz, N. A.; Siegle, J. H.; Denman, D. J.; Bauza, M.; Barbarits, B.; Lee, A. K.; Anastassiou, C. A.; Andrei, A.; Aydin, C.; Barbic, M.; Blanche, T. J.; Bonin, V.; Couto, J.; Dutta, B.; Gratiy, S. L.; Gutnisky, D. A.; Hausser, M.; Karsh, B.; Ledochowitsch, P.; et al. Fully Integrated Silicon Probes for High-Density Recording of Neural Activity. Nature 2017, 551, 232−236.
18. Driscoll, N.; Richardson, A. G.; Maleski, K.; Anasori, B.; Adewole, O.; Lelyukh, P.; Escobedo, L.; Cullen, D. K.; Lucas, T. H.; Gogotsi, Y.; Vitale, F. Two-Dimensional Ti3C2 MXene for High-Resolution Neural Interfaces. ACS Nano 2018, 12, 10419−10429.
19. Jiang, Y.; Li, X.; Liu, B.; Yi, J.; Fang, Y.; Shi, F.; Gao, X.; Sudzilovsky, E.; Parameswaran, R.; Koehler, K.; Nair, V.; Yue, J.; Guo, K.; Tsai, H.-M.; Freyermuth, G.; Wong, R. C. S.; Kao, C.-M.; Chen, C.-T.; Nicholls, A. W.; Wu, X.; et al. Rational Design of Silicon Structures for Optically Controlled Multiscale Biointerfaces. Nat. Biomed. Eng. 2018, 2, 508−521.

20. He, F.; Sullender, C. T.; Zhu, H.; Williamson, M. R.; Li, X.; Zhao, Z.; Jones, T. A.; Xie, C.; Dunn, A. K.; Luan, L. Multimodal Mapping of Neural Activity and Cerebral Blood Flow Reveals Long-Lasting Neurovascular Dissociations after Small-Scale Strokes. Sci. Adv. 2020, 6, No. eaba1933.
21. Andrews, A. M. The Brain Initiative: Toward a Chemical Connectome. ACS Chem. Neurosci. 2013, 4, 645.
22. Li, J.; Liu, Y.; Yuan, L.; Zhang, B.; Bishop, E. S.; Wang, K.; Tang, J.; Zheng, Y. Q.; Xu, W.; Niu, S.; Beker, L.; Li, T. L.; Chen, G.; Diyaolu, M.; Thomas, A. L.; Mottini, V.; Tok, J. B.; Dunn, J. C. Y.; Cui, B.; Pasca, S. P.; et al. A Tissue-Like Neurotransmitter Sensor for the Brain and Gut. Nature 2022, 606, 94−101.
23. Kim, J.; Rim, Y. S.; Chen, H.; Cao, H. H.; Nakatsuka, N.; Hinton, H. L.; Zhao, C.; Andrews, A. M.; Yang, Y.; Weiss, P. S. Fabrication of High-Performance Ultrathin In_2O_3 Film Field-Effect Transistors and Biosensors Using Chemical Lift-Off Lithography. ACS Nano 2015, 9, 4572−4582.
24. Nakatsuka, N.; Yang, K. A.; Abendroth, J. M.; Cheung, K. M.; Xu, X.; Yang, H.; Zhao, C.; Zhu, B.; Rim, Y. S.; Yang, Y.; Weiss, P. S.; Stojanovic, M. N.; Andrews, A. M. Aptamer-Field-Effect Transistors Overcome Debye Length Limitations for Small-Molecule Sensing. Science 2018, 362, 319−324.
25. Cheung, K. M.; Yang, K. A.; Nakatsuka, N.; Zhao, C.; Ye, M.; Jung, M. E.; Yang, H.; Weiss, P. S.; Stojanovic, M. N.; Andrews, A. M. Phenylalanine Monitoring via Aptamer-Field-Effect Transistor Sensors. ACS Sens 2019, 4, 3308−3317.

26. Liu, Q.; Zhao, C.; Chen, M.; Liu, Y.; Zhao, Z.; Wu, F.; Li, Z.; Weiss, P. S.; Andrews, A. M.; Zhou, C. Flexible Multiplexed In_2O_3 Nanoribbon Aptamer-Field-Effect Transistors for Biosensing. iScience 2020, 23, 101469.
27. Zhao, C.; Liu, Q.; Cheung, K. M.; Liu, W.; Yang, Q.; Xu, X.; Man, T.; Weiss, P. S.; Zhou, C.; Andrews, A. M. Narrower Nanoribbon Biosensors Fabricated by Chemical Lift-Off Lithography Show Higher Sensitivity. ACS Nano 2021, 15, 904−915.
28. Wang, B.; Zhao, C.; Wang, Z.; Yang, K. A.; Cheng, X.; Liu, W.; Yu, W.; Lin, S.; Zhao, Y.; Cheung, K. M.; Lin, H.; Hojaiji, H.; Weiss, P. S.; Stojanovic, M. N.; Tomiyama, A. J.; Andrews, A. M.; Emaminejad, S. Wearable Aptamer-Field-Effect Transistor Sensing System for Noninvasive Cortisol Monitoring. Sci. Adv. 2022, 8, No. eabk0967.
29. Gao, Z.; Wu, G.; Song, Y.; Li, H.; Zhang, Y.; Schneider, M. J.; Qiang, Y.; Kaszas, J.; Weng, Z.; Sun, H.; Huey, B. D.; Lai, R. Y.; Zhang, Y. Multiplexed Monitoring of Neurochemicals via Electrografting-Enabled Site-Selective Functionalization of Aptamers on Field-Effect Transistors. Anal. Chem. 2022, 94, 8605−8617.
30. Wu, G.; Zhang, N.; Matarasso, A.; Heck, I.; Li, H.; Lu, W.; Phaup, J. G.; Schneider, M. J.; Wu, Y.; Weng, Z.; Sun, H.; Gao, Z.; Zhang, X.; Sandberg, S. G.; Parvin, D.; Seaholm, E.; Islam, S. K.; Wang, X.; Phillips, P. E. M.; Castro, D. C.; et al. Implantable Aptamer-Graphene Microtransistors for Real-Time Monitoring of Neurochemical Release. in Vivo Nano Lett. 2022, 22, 3668−3677.
31. Salatino, J. W.; Ludwig, K. A.; Kozai, T. D. Y.; Purcell, E. K. Glial Responses to Implanted Electrodes in the Brain. Nat. Biomed. Eng. 2017, 1, 862−877.

32. Chen, Y.; Rommelfanger, N. J.; Mahdi, A. I.; Wu, X.; Keene, S. T.; Obaid, A.; Salleo, A.; Wang, H.; Hong, G. How Is FlexibleElectronics Advancing Neuroscience Research? Biomaterials 2021, 268, 120559.
33. Wassum, K. M.; Tolosa, V. M.; Wang, J.; Walker, E.; Monbouquette, H. G.; Maidment, N. T. Silicon Wafer-Based Platinum Microelectrode Array Biosensor for Near Real-Time Measurement of Glutamate in Vivo. Sensors (Basel) 2008, 8, 5023− 5036.
34. Kozai, T. D.; Jaquins-Gerstl, A. S.; Vazquez, A. L.; Michael, A. C.; Cui, X. T. Brain Tissue Responses to Neural Implants Impact Signal Sensitivity and Intervention Strategies. ACS Chem. Neurosci. 2015, 6, 48−67.
35. Du, Z. J.; Kolarcik, C. L.; Kozai, T. D. Y.; Luebben, S. D.; Sapp, S. A.; Zheng, X. S.; Nabity, J. A.; Cui, X. T. Ultrasoft Microwire Neural Electrodes Improve Chronic Tissue Integration. Acta Biomater 2017, 53, 46−58.
36. Schwartz, A. B. Cortical Neural Prosthetics. Annu. Rev. Neurosci. 2004, 27, 487−507.
37. Kozai, T. D. Y.; Vazquez, A. L.; Weaver, C. L.; Kim, S.-G.; Cui, X. T. In vivo Two-Photon Microscopy Reveals Immediate Microglial Reaction to Implantation of Microelectrode through Extension of Processes. J. Neural. Eng. 2012, 9, 066001.
38. Meunier, C. J.; Denison, J. D.; McCarty, G. S.; Sombers, L. A. Interpreting Dynamic Interfacial Changes at Carbon Fiber Microelectrodes Using Electrochemical Impedance Spectroscopy. Langmuir 2020, 36, 4214−4223.
39. Park, Y.; Chung, T. S.; Lee, G.; Rogers, J. A. Materials Chemistry of Neural Interface Technologies and Recent Advances in Three-Dimensional Systems. Chem. Rev. 2022, 122, 5277−5316.

40. Kim, D. H.; Viventi, J.; Amsden, J. J.; Xiao, J.; Vigeland, L.; Kim, Y. S.; Blanco, J. A.; Panilaitis, B.; Frechette, E. S.; Contreras, D.; Kaplan, D. L.; Omenetto, F. G.; Huang, Y.; Hwang, K. C.; Zakin, M. R.; Litt, B.; Rogers, J. A. Dissolvable Films of Silk Fibroin for Ultrathin Conformal Bio-Integrated Electronics. Nat. Mater. 2010, 9, 511−517.
41. Kaltenbrunner, M.; Sekitani, T.; Reeder, J.; Yokota, T.; Kuribara, K.; Tokuhara, T.; Drack, M.; Schwodiauer, R.; Graz, I.; Bauer-Gogonea, S.; Bauer, S.; Someya, T. An Ultra-Lightweight Design for Imperceptible Plastic Electronics. Nature 2013, 499, 458− 463.
42. Luan, L.; Wei, X.; Zhao, Z.; Siegel, J. J.; Potnis, O.; Tuppen, C. A.; Lin, S.; Kazmi, S.; Fowler, R. A.; Holloway, S.; Dunn, A. K.; Chitwood, R. A.; Xie, C. Ultraflexible Nanoelectronic Probes Form Reliable, Glial Scar-Free Neural Integration. Sci. Adv. 2017, 3, No. e1601966.
43. Shi, J.; Fang, Y. Flexible and Implantable Microelectrodes for Chronically Stable Neural Interfaces. Adv. Mater. 2019, 31, No. e1804895.
44. Wang, C.; Qi, B.; Lin, M.; Zhang, Z.; Makihata, M.; Liu, B.; Zhou, S.; Huang, Y. H.; Hu, H.; Gu, Y.; Chen, Y.; Lei, Y.; Lee, T.; Chien, S.; Jang, K. I.; Kistler, E. B.; Xu, S. Continuous Monitoring of Deep-Tissue Haemodynamics with Stretchable Ultrasonic Phased Arrays. Nat. Biomed. Eng. 2021, 5, 749−758.
45. Jiang, Y.; Zhang, Z.; Wang, Y. X.; Li, D.; Coen, C. T.; Hwaun, E.; Chen, G.; Wu, H. C.; Zhong, D.; Niu, S.; Wang, W.; Saberi, A.; Lai, J. C.; Wu, Y.; Wang, Y.; Trotsyuk, A. A.; Loh, K. Y.; Shih, C. C.; Xu, W.; Liang, K.; et al. Topological Supramolecular Network Enabled High-Conductivity, Stretchable Organic Bioelectronics. Science 2022, 375, 1411−1417.
46. Gunasekera, B.; Saxena, T.; Bellamkonda, R.; Karumbaiah, L. Intracortical Recording Interfaces: Current Challenges to Chronic Recording Function. ACS Chem. Neurosci. 2015, 6, 68−83.

47. Wen, X.; Wang, B.; Huang, S.; Liu, T. L.; Lee, M. S.; Chung, P. S.; Chow, Y. T.; Huang, I. W.; Monbouquette, H. G.; Maidment, N. T.; Chiou, P. Y. Flexible, Multifunctional Neural Probe with Liquid Metal Enabled, Ultra-Large Tunable Stiffness for Deep-Brain Chemical Sensing and Agent Delivery. Biosens. Bioelectron. 2019, 131, 37−45.
48. Rogers, J. A.; Lagally, M. G.; Nuzzo, R. G. Synthesis, Assembly and Applications of Semiconductor Nanomembranes. Nature 2011, 477, 45−53.
49. Kim, D. H.; Ahn, J. H.; Choi, W. M.; Kim, H. S.; Kim, T. H.; Song, J.; Huang, Y. Y.; Liu, Z.; Lu, C.; Rogers, J. A. Stretchable and Foldable Silicon Integrated Circuits. Science 2008, 320, 507−511.
50. Cointe, C.; Laborde, A.; Nowak, L. G.; Arvanitis, D. N.; Bourrier, D.; Bergaud, C.; Maziz, A. Scalable Batch Fabrication of Ultrathin Flexible Neural Probes Using a Bioresorbable Silk Layer. Microsyst. Nanoeng. 2022, 8, 21.
51. Chen, H.; Rim, Y. S.; Wang, I. C.; Li, C.; Zhu, B.; Sun, M.; Goorsky, M. S.; He, X.; Yang, Y. Quasi-Two-Dimensional Metal Oxide Semiconductors Based Ultrasensitive Potentiometric Biosensors. ACS Nano 2017, 11, 4710−4718.
52. Angoa-Perez, M.; Kane, M. J.; Briggs, D. I.; Herrera-Mundo, N.; Sykes, C. E.; Francescutti, D. M.; Kuhn, D. M. Mice Genetically Depleted of Brain Serotonin Do Not Display a Depression-Like Behavioral Phenotype. ACS Chem. Neurosci. 2014, 5, 908−919.
53. Ishikawa, F. N.; Curreli, M.; Chang, H. K.; Chen, P. C.; Zhang, R.; Cote, R. J.; Thompson, M. E.; Zhou, C. A Calibration Method for Nanowire Biosensors to Suppress Device-to-Device Variation. ACS Nano 2009, 3, 3969−3976.
54. Aroonyadet, N.; Wang, X.; Song, Y.; Chen, H.; Cote, R. J.; Thompson, M. E.; Datar, R. H.; Zhou, C. Highly Scalable, Uniform, and Sensitive Biosensors Based on Top-Down Indium

Oxide Nanoribbons and Electronic Enzyme-Linked Immunosorbent Assay. Nano Lett. 2015, 15, 1943−1951.

55. Lu, L.; Gutruf, P.; Xia, L.; Bhatti, D. L.; Wang, X.; Vazquez-Guardado, A.; Ning, X.; Shen, X.; Sang, T.; Ma, R.; Pakeltis, G.; Sobczak, G.; Zhang, H.; Seo, D. O.; Xue, M.; Yin, L.; Chanda, D.; Sheng, X.; Bruchas, M. R.; Rogers, J. A. Wireless Optoelectronic Photometers for Monitoring Neuronal Dynamics in the Deep Brain. Proc. Natl. Acad. Sci. U. S. A. 2018, 115, E1374−E1383.
56. Tringides, C. M.; Vachicouras, N.; de Lazaro, I.; Wang, H.; Trouillet, A.; Seo, B. R.; Elosegui-Artola, A.; Fallegger, F.; Shin, Y.; Casiraghi, C.; Kostarelos, K.; Lacour, S. P.; Mooney, D. J. Viscoelastic Surface Electrode Arrays to Interface with Viscoelastic Tissues. Nat. Nanotechnol. 2021, 16, 1019−1029.
57. Mathews, T. A.; Fedele, D. E.; Coppelli, F. M.; Avila, A. M.; Murphy, D. L.; Andrews, A. M. Gene Dose-Dependent Alterations in Extraneuronal Serotonin but Not Dopamine in Mice with Reduced Serotonin Transporter Expression. J. Neurosci. Methods 2004, 140, 169−181.
58. Yang, H.; Thompson, A. B.; McIntosh, B. J.; Altieri, S. C.; Andrews, A. M. Physiologically Relevant Changes in Serotonin Resolved by Fast Microdialysis. ACS Chem. Neurosci. 2013, 4, 790−798.
59. Yang, H.; Sampson, M. M.; Senturk, D.; Andrews, A. M. Sexand SERT-Mediated Differences in Stimulated Serotonin Revealed by Fast Microdialysis. ACS Chem. Neurosci. 2015, 6, 1487−1501.
60. Abdalla, A.; Atcherley, C. W.; Pathirathna, P.; Samaranayake, S.; Qiang, B.; Pena, E.; Morgan, S. L.; Heien, M. L.; Hashemi, P. In Vivo Ambient Serotonin Measurements at Carbon-Fiber Microelectrodes. Anal. Chem. 2017, 89, 9703−9711.

61. Ware, T.; Simon, D.; Liu, C.; Musa, T.; Vasudevan, S.; Sloan, A.; Keefer, E. W.; Rennaker, R. L., 2nd; Voit, W. Thiol-Ene/Acrylate Substrates for Softening Intracortical Electrodes. J. Biomed. Mater. Res. B Appl. Biomater. 2014, 102, 1−11.
62. Ware, T.; Simon, D.; Arreaga-Salas, D. E.; Reeder, J.; Rennaker, R.; Keefer, E. W.; Voit, W. Fabrication of Responsive, Softening Neural Interfaces. Adv. Funct. Mater. 2012, 22, 3470−3479.
63. Tien, L. W.; Wu, F.; Tang-Schomer, M. D.; Yoon, E.; Omenetto, F. G.; Kaplan, D. L. Silk as a Multifunctional Biomaterial Substrate for Reduced Glial Scarring around Brain-Penetrating Electrodes. Adv. Funct. Mater. 2013, 23, 3185−3193.
64. Obaid, A.; Wu, Y.-W.; Hanna, M.; Jáidar, O.; Nix, W.; Ding, J.; Melosh, N. Ultra-Sensitive Measurement of Brain Penetration Mechanics and Blood Vessel Rupture with Microscale Probes. bioRxiv preprint 2020, DOI: 10.1101/2020.1109.1121.306498.
65. Ferguson, B. S.; Hoggarth, D. A.; Maliniak, D.; Ploense, K.; White, R. J.; Woodward, N.; Hsieh, K.; Bonham, A. J.; Eisenstein, M.; Kippin, T. E.; Plaxco, K. W.; Soh, H. T. Real-Time, Aptamer-Based Tracking of Circulating Therapeutic Agents in Living Animals. Sci. Transl. Med. 2013, 5, 213ra165.
66. Dauphin-Ducharme, P.; Yang, K.; Arroyo-Curras, N.; Ploense, K. L.; Zhang, Y.; Gerson, J.; Kurnik, M.; Kippin, T. E.; Stojanovic, M. N.; Plaxco, K. W. Electrochemical Aptamer-Based Sensors for Improved Therapeutic Drug Monitoring and High-Precision, Feedback-Controlled Drug Delivery. ACS Sens. 2019, 4, 2832−2837.
67. Hou, H.; Jin, Y.; Wei, H.; Ji, W.; Xue, Y.; Hu, J.; Zhang, M.; Jiang, Y.; Mao, L. A Generalizable and Noncovalent Strategy for Interfacing Aptamers with a Microelectrode for

the Selective Sensing of Neurotransmitters in Vivo. Angew. Chem., Int. Ed. 2020, 59, 18996−19000.

68. Li, X.; Jin, Y.; Zhu, F.; Liu, R.; Jiang, Y.; Jiang, Y.; Mao, L. Electrochemical Conjugation of Aptamers on a Carbon Fiber Microelectrode Enables Highly Stable and Selective in Vivo Neurosensing. Angew. Chem., Int. Ed. 2022, 61, No. e202208121.

Chapter 11: Recommendations for Future Work

11.1 Integrated NA extraction with the lateral flow assay format

If a diagnostic device is intended for widespread use in a point-of-care (POC) setting, it should be rapid, inexpensive and not reliant on a standard laboratory environment and a trained operator.[1] Currently, with the integration of the hybridization step in the lateral flow assay format, the assay time has been significantly reduced. However, the separate nucleic acid (NA) extraction procedure still relies on rapid commercial NA extraction kits, which require multiple centrifugation procedures for washing and elution. Previous work has indicated that alkaline extraction is a rapid, inexpensive and relatively clean method to isolate circular plasmid DNA or even RNA from bacterial cells. Lysis under alkaline condition followed by simple filtration has been demonstrated to work as an efficient method suitable for *E. coli* detection and still achieved a limit of detection of 100 zM (10^{-19} M) with our device.[2]

Even though for more complex clinical samples, alkaline extraction may not be sufficiently a clean enough extraction procedure to prevent all false positives, with the assistance of lipase, nonionic surfactant and a reducing reagent, there is still a good possibility of a rapid and sample NA extraction scheme. Previous study has demonstrated that a high pH-tolerant lipase could be produced by *Staphylococcus sp*. strain with sustained enzyme activity at pH 12.[3] Common lipase treatment may require ~30 mins treatment time when used to lyse concentrate cell pellets, however the treatment time could be significantly reduced when treating diluted clinical samples. Since our limit of detection can be lower than 10 CFU/mL, lipase treatment is still a potential enhancement for alkaline extraction scheme. Another challenge for RNA extraction is the instability of RNA mainly due to ubiquitous RNase which degrades RNA quickly, especially in human fluids such as

urine.[4] Nonionic surfactant (*e.g.*, Triton X-100, Tween-80 or Tween-20), reducing reagent (*e.g.*, dithiothreitol or DTT), and carrier RNA could be applied with the alkaline solution to enhance the lysing efficiency and stabilize the extracted RNA.[5] In a preliminary investigation, we found that the lipid/phospholipids in urine could lead to false positive results since negatively charged lipid aggregates may result in a nanopore blockage.[2] The nonionic surfactant could prevent the lipid aggregation and help disrupt the normal architecture of the lipid bilayer in the cell lysis step. Dithiothreitol (DTT) is a standard reagent for reducing disulfide bond between and within proteins such as RNase and therefore stabilize the RNA extraction.

In previous work, the hybridization environment is 10 mM sodium chloride, 25 mM Tris-HCl, with pH adjusted to 7, and the testing environment is 10 mM potassium chloride, 5.5 mM 4-(2-hydroxyethyl)-1-piperazineethanesulfonic acid (HEPES), 0.01% Tween-80 with pH adjusted to 7.[6] After the hybridization, the PNA-beads complexes were washed in the testing environment for detection. We have demonstrated that successful detection can also happen in the hybridization environment with nonionic surfactant additives and therefore we saw the potential of unifying all the buffers.[2] In the alkaline extraction, 0.1 M to 1 M sodium hydroxide solution were used to lyse the cell and corresponding Tris-HCl solution was used for neutralization. After neutralization, the solution is also composed of mainly sodium chloride, Tris-HCl and nonionic surfactant. Therefore, there is a potential to integrate NA extraction with the lateral flow assay format. The sample with target pathogen could be lysed in alkaline environment such as sodium hydroxide and then neutralized with Tris-HCL solution. The high salt concentration may affect the hybridization of PNA and target NA, but PNA as an uncharged capture probe may still maintain good hybridization efficiency compared with charged oligonucleotides. If the salt concentration has a large influence on hybridization, a simple desalting column could be included to achieve a similar salt

concentration as the hybridization environment. To further simplify the process, the neutralization agents such as Tris-HCl could be preloaded on the lateral flow chip. After the cell lysis with alkaline extraction, the cell lysate can be directly dropped on the lateral flow chip and the neutralization process will happen immediately as the cell lysate flows across the lateral flow chip driven by capillary force. With integrated hybridization step, the overall assay time can be further reduced without any complex pumps or valves.

11.2 Reduction of bead retention

PNA-bead immobility in the Fusion 5 lateral flow membrane is recognized as one drawback that could influence the limit of detection. As the sample RNA concentration decreases, the number of PNA-beads complexes that hybridize with target NA also decreases and therefore bead retention/and or very slow movement to the detection area under the chip emerged as a problem. Also, cutting of Fusion 5 membrane may also generate glass fiber fragments, and it is hypothesized that the glass fiber fragments is one possible cause of noisy signals. Currently the Fusion 5 lateral flow membrane is used due to its large pore size which should enable PNA-bead movement with the capillary flow and therefore avoid the need for complicated valves and pumps. However, trenches with small enough width could also generate capillary flow that automatically carry the sample and meanwhile avoid the glass fibers. With the assistance of 3D printing techniques, the construction of such cartridge with small trenches is possible. The PNA-beads complex could be preloaded inside the trenches near the proximity of the nanopore. Samples with target NA can be carried to the preloaded beads by the capillary flow and hybridize with the capture probes on PNA-beads complex. Upon hybridization with target NA, the overall negatively charged PNA-beads complex can be driven to the nanopore by an external electric field. The

material of the 3D printed cartridge can be adjusted to prevent NA binding and meanwhile limit bead retention. Further bead retention reduction strategies may include addition of nonionic surfactant, freeze-drying the preloaded PNA-beads complex on the LFA membrane and using a magnetic field to control the movement of magnetic PNA-beads.

11.3 A single device for multiplexing NA detection

One attractive characteristic of the nanopore based sensing platform is the potential for universal application. By changing the capture probe sequence, it can detect different pathogens based on their species-specific signature rRNA sequences. Therefore, it's relatively easy to multiplex for simultaneous detection of various pathogen species. Previous research has indicated that PNA oligonucleotides can routinely be labelled with fluorophores and therefore it provides the possibility to differentiate pathogens for simultaneous detection.[7] A portable fluorescence microscopy platform for fluorescent imaging of nanoparticles on a smart phone has been reported and displayed a great potential for portable optical sensing platform.[8] With help of these techniques, a portable platform for simultaneous pathogen detections based on nanopore technique is theoretically possible.

A prototype of such simultaneous multiplexing NA detection platform is described below. The PNA molecules can be modified with fluorophores to serve as sequence specific capture probes detecting different pathogens based on their signature 16S rRNA sequences. The PNA capture probes will be conjugated with magnetic beads to form neutrally charged PNA-beads complexes. The modified magnetic beads will be preloaded on the 3D printed cartridge with a number of narrow trenches which can generate capillary flow to automatically deliver samples across this cartridge. The PNA-bead complexes should be placed upstream of the nanopore with a

proper distance. Clinical samples lysed in alkaline environment will be dropped on the start side of the 3D printed cartridge and will be driven by capillary force to hybridize with the preloaded PNA-bead complexes. Since the capillary flow may also carry the beads, the magnetic beads should be held still by a strong magnet during the hybridization process. After the hybridization, the magnet should be removed, and the beads hybridized with target NA will be drive to the nanopore under external electric field. A smart phone-based fluorescence microscopy platform can be installed near the nanopore to simultaneously detect multiple signals. The multiplexing of the nanopore based platform serves as a rapid, portable platform for point of care detection screening multiple pathogens simultaneously.

11.4 References

1. Cao, Y.; Zheng, Z.; Monbouquette, H. G. *Curr Opin Biotechnol* **2021,** 71, 145-150.
2. Zheng, Z. (2022). Amplification-Free Detection of 16S rRNA for Next Generation Point-of-Care Diagnostics. UCLA. ProQuest ID: Zheng_ucla_0031D_21248. Merritt ID: ark:/13030/m5cp4cth. Retrieved from https://escholarship.org/uc/item/0q1207sz
3. Cherif, S., Mnif, S., Hadrich, F. et al. A newly high alkaline lipase: an ideal choice for application in detergent formulations. Lipids Health Dis, 2011. 10, 221
4. Sugiyama, R.H., A. Blank, and C.A. Dekker, Multiple ribonucleases of human urine. Biochemistry, 1981. 20(8): p. 2268-74.
5. Rogacs, A., Y. Qu, and J.G. Santiago, Bacterial RNA extraction and purification from whole human blood using isotachophoresis. Anal Chem, 2012. 84(14): p. 5858-63.
6. Koo, B.; Yorita, A. M.; Schmidt, J. J.; Monbouquette, H. G. Lab Chip 2018, 18, (15), 2291-2299.

7. Pellestor, F.; Paulasova, P. *Eur J Hum Genet* **2004,** 12, (9), 694-700.

8. Wei, Q.; Qi, H.; Luo, W.; Tseng, D.; Ki, S. J.; Wan, Z.; Gorocs, Z.; Bentolila, L. A.; Wu, T. T.; Sun, R.; Ozcan, A. *ACS Nano* **2013,** 7, (10), 9147-55.

Appendix A: PNA-beads preparation

1. Wash 1 µL of stock bead solution three times in MES buffer. With each wash, spin down the beads in a microcentrifuge at 14,000 RPM for 15 minutes and remove the supernatant.
2. Resuspend the beads in 600 µL MES buffer. Add 23 mg 1-ethyl-3-(3-dimethylaminopropyl)carbodiimide (EDC) to make 200 mM EDC in MES. Incubate the beads for 15 minutes at 50 °C.
3. Add 11.4 µL aliquoted PNA (100 µM) and incubate for 2 hours at 50 °C.
4. Add 22 mg methoxypolyethylene glycol amine (mPEG-amine). Incubate for one hour at 50 °C.
5. Add 5 µL ethanolamine. Incubate for one hour at 50 °C.
6. Wash beads three times in 0.4x SSC buffer at 14,000 RPM for 15 minutes. Resuspend in 500 µL 0.4x SSC.
7. Remove 100 µL and wash once in potassium chloride buffer for use in Zetasizer.
8. Wash the remaining 400 µL bead solution once in hybridization buffer at 14,000 RPM for 15 minutes. Resuspend in 400 µL hybridization buffer for storage.

Appendix B: Cell culturing and counting

B.1 Culture *E. coli* and *P. putida*

1. Suspend the lyophilized preparations in soy (*E. coli*) and nutrient (*P. putida*) media, respectively, followed by incubation of days. *E. coli* subsequently was cultured in shake flasks at 37 °C and 250 rpm, and *P. putida* at room temperature and 250 rpm.
2. Store the initiated culture at -80 °C to serve later as inocula.
3. Measure 3 mL of soy media for *E. coli* and 3 mL of nutrient media for *P. putida.*
4. Stab a small portion of frozen culture with a pipette and pipette up and down in the culturing media.
5. Culture *E. coli* at 37 °C and 250 rpm, and *P. putida* at room temperature and 250 rpm overnight.

B.2 Rehydrate *C. trachomatis*

1. Tear open pouch at notch and remove vial from pouch and ensure the pellet is at the bottom of the vial before opening.
2. Rehydrate the lyophilized pellet with 1 mL physiological saline solution.
3. Vortex the vial for 10 seconds at full speed to mix.

B.3 Count viable *E. coli*, *P. putida* and *C. trachomatis*

4. Put 1 mL concentrated cells into tube 1.
5. Add 900 μL sterile DI water to tube 2-9.

6. Perform a serial dilution by taking 100 µL concentrated cells, add to tube 2, then take 100 µL of that and add to tube 3 etc.
7. Remove 100 µL from each tube and transfer to Agar plate.
8. Use glass bead to spread the liquid sample evenly on Agar plate.
9. Culture overnight and count the colonies on Agar plate.
10. Multiply the measured CFU by 10 to get the total number of bacteria in the tubes.
11. Culture in tubes 2-9 serve as the stock for future dilution.

B.4 Culture and count *N. gonorrhoeae*

1. Subculture a frozen stock of ATCC strain 43069 onto chocolate agar.
2. Agar plates were incubated at 35C with 5% CO2 for 16-18 hours.
3. Created a 0.5 McFarland of *N. gonorrhoeae*, which represents 1.5 x 10^8 CFUs/ml.
4. Transfer 10 µL of sample above into 9990 uL of 0.85% saline to create 150,000 CFU/mL stock.

Appendix C: Spike sterilized pool human urine with bacterial culture

C.1 *E. coli*, *P. putida* and *C. trachomatis*

1. Transfer 10 µl of the stock (described in Appendix B.3) in 9990 µl human urine to create a final concentration from 10 CFU/mL to 1000 CFU/mL.

C.2 *N. gonorrhoeae*

1. Transfer 10µl of the stock (described in appendix B.4) into 9990 µl of commercial urine to create 150 CFUs/ml.
2. Transfer 666 ul of this into 9.333 mL of urine to create a final 10 CFU/ml

Appendix D: RNA extraction

D.1 Qiagen RNeasy

1. Pipette 1.7 mL of *E. coli* or *P. putida* culture into individual, sterile 2 mL microcentrifuge tubes. Spin down (max speed for 1 min) and remove supernatant. First pour out supernatant, then use a pipette to remove any remaining liquid. Make sure not to disturb cell pellet.
2. Lyse the cells. For each pellet, add 200 µL TE lysozyme + 20 µL proteinase K. Resuspend by pipetting up and down a few times. Vortex for 10 sec. Let incubate at 37 °C for at least 45 minutes. Does not have to be on a shaker. Lysed cells will appear clear/transparent.
3. Prepare RLT buffer. Remove 6 mL RLT buffer, mix with 60 µL b-mercaptoethanol (or, if doing fewer than 8 tubes, however much you need at a ratio of 10 µL b-mercaptoethanol to 1 mL RLT buffer). Add 700 µL of this to each tube. Vortex, then spin down at max speed for 2 min.
4. Remove all supernatant and place into new tubes.
5. Into each tube, add 500 µL 200 proof ethanol. Precipitation may form, but do not centrifuge. Pipette up and down gently.
6. Spin down 700 µL at a time supernatant into column (30 sec at max speed). Discard flow through.
7. Add 700 µL RW1 buffer, let it flow through column (30 sec at max speed). Discard flow through.
8. For new RPE buffer, add 4 volumes ethanol to 1 volume RPE (44 mL to 11 mL to make 55 mL total). Replace collection tube with a new one. Add 500 µL RPE to column, let spin through (30 sec at max speed).

9. Add another 500 µL, let spin through (2 min at max speed).
10. Decant flow through, let spin for another 1 min at max speed.
11. Transfer column to new 1.5 mL tube (with the cap), add 50 µL RNAse free water to elute RNA. Make sure to pipette right into the middle of the membrane. Spin for 1 min at max speed to elute. Add another 50 µL RNAse free water to elute again.
12. Measure RNA concentration and purity with Nanodrop.

D.2 Alkaline Extraction

1. Collect 1 mL culture sample, Spin down (max speed for 1 min) and remove supernatant. First pour out supernatant, then use a pipette to remove any remaining liquid. Make sure not to disturb cell pellet.
2. Add 1000 µL 0.125M NaOH, mix and let rest at room temperature for 1 minute to lyse the cells.
3. Add 1000 µL of 0.25M Tris-HCl (to bring pH to ~8-8.5) and mix for 10 sec to stop the lysis.
4. Transfer lysed sample into 20 mL sterilized plastic syringe with luer lock
5. Attach Whatman Anotop^{TM} 25 mm filter to the luer lock.
6. Finish the filtration by pushing gently on the plunger of the syringe and catch the flowthrough using a 1 mL microcentrifuge tube.
7. Measure RNA concentration and purity with Nanodrop.

D.3 Direct-zol RNA extraction Kit

1. [For pelleted cells] Add 300 µL of TRI Reagent® into pelleted cells and incubate for 5 minutes.
2. [For urine sample] Add 3 mL of the TRI Reagent® into 1mL of urine sample and incubate for 5 minutes.
3. Add an equal volume ethanol (95-100%) to a sample lysed in TRI Reagent® or similar1 and mix thoroughly.
4. Transfer the mixture into a Zymo-Spin™ IC Column2 in a Collection Tube and centrifuge at 14000 rpm for 1 minute
5. Transfer the column into a new collection tube and discard the flow-through.
6. Add 400 µl Direct-zol™ RNA PreWash to the column and centrifuge. Discard the flow-through and repeat this step again.
7. Add 700 µl RNA Wash Buffer to the column and centrifuge for 1 minute to ensure complete removal of the wash buffer. Transfer the column carefully into an RNase-free tube (not included).
8. To elute RNA, add 30 µl of DNase/RNase-Free Water directly to the column matrix and centrifuge.

Appendix E: Kinetically Enhanced Hybridization with prewashed beads

1. Transfer 600 μL of PNA-conjugated beads described in Appendix A in hybridization buffer (10 mM NaCl, 25 mM Tris-HCl, pH 7) to Vivaspin 2 and spin at 2000 rpm for 5 mins, discard filtrate. This step deposits ~2 layers of beads on the filter surface.
2. Transfer RNA prep described in Appendix D to same Vivaspin 2 with filtered beads, spin at 1200 rpm for 10 mins and discard filtrate. Hybridization occurs in this step.
3. Add 600 μL of testing buffer (10 mM KCl, 5.5 mM HEPES, 0.01% Tween-80, pH 7) into same Vivaspin, spin at 1000 rpm for 5 mins and discard filtrate. This step is to wash with the testing buffer.
4. Add 300 μL testing buffer, sonicate for 1 min, reverse spin at 2000 rpm for 2 mins and collect hybridized beads in ~300 μL. Reverse spin removes beads from the filter membrane surface.

Appendix F: Lateral Flow Assay Detection Scheme

F.1 Lateral flow strip assembly

1. Cut Whatman Fusion 5 membrane roll from Cytiva into 2 cm × 2.5 cm strips.
2. Use a paper cutter to cut the Cytiva backing card into 2.5 cm × 8 cm pieces.
3. Cut the Pt-foil into 2 mm × 1 cm small strips and solder a wire on the end to make a Pt-foil electrode.
4. Peel off the film on the backing card and attach a soldered Pt-foil electrode in the middle of the backing card.
5. Attach two Fusion 5 membrane pieces on top of edges of the foil electrode and the backing. A less than 1 mm gap is left between these two Fusion 5 membrane pieces to expose the Pt-foil electrode underneath. We call this assembled card the lateral flow membrane strip, shown in Figure 1.

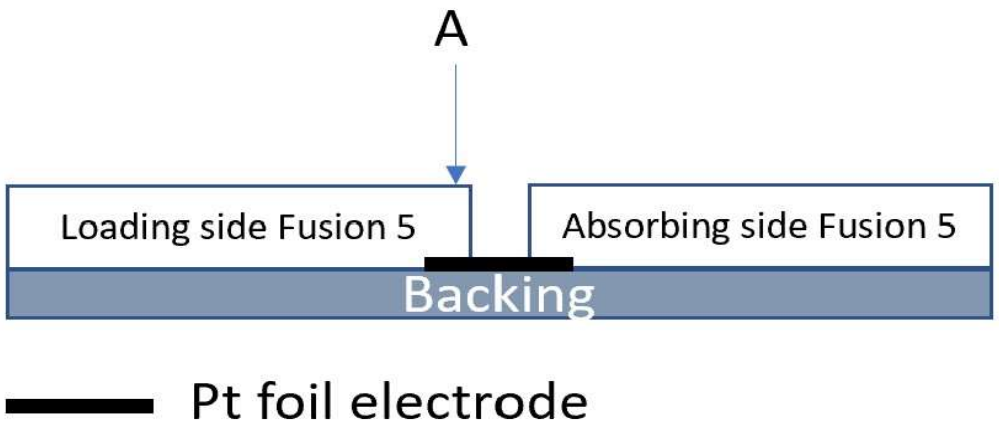

Figure F.1. Lateral flow membrane strip, not to scale. Point A is where PNA-modified beads are loaded and dried (see below).

6. Use sterilized air to blow the lateral flow membrane stripe to remove the free glass fiber fragments or dusts.

7. Mark one side of the chip to be the loading side.
8. Wash PNA/PEG/ethanolamine-modified polystyrene beads with 500 μL hybridization buffer (10 mM NaCl, 25 mM Tris-HCl, pH 7, 0.1% Tween-20).
9. Concentrate the beads by centrifuge filtration at 14,000 RPM for 15 minutes. Remove ~470 μL supernatant and try not to disturb the concentrated beads pellet. Resuspend the beads pellet in the remaining ~30 μL hybridization buffer.
10. Load 10 μL of the concentrated beads next to the gap, shown as point A in Figure 1.
11. Before the beads get dried, apply vibration force to the beads by holding the lateral flow membrane strip to the wall of a bath sonicator. This step helps prevent bead aggregation.
12. Let the beads dry by putting the lateral flow chip in ambient environment for ~30 mins. Cover the lateral flow chip with petri dish to prevent dust contamination.

F.2 Glass chip assembly

1. As shown in Figure 2, we sandwich a glass chip with a ~1 μm - 800 nm diameter "nanopore" (must be smaller than bead diameter used) in the middle with two PDMS O-ring shaped films. Cellophane tape (e.g., Scotch tape) was used to briefly remove the dust on PDMS, and this will ensure good attachment to the glass chip.

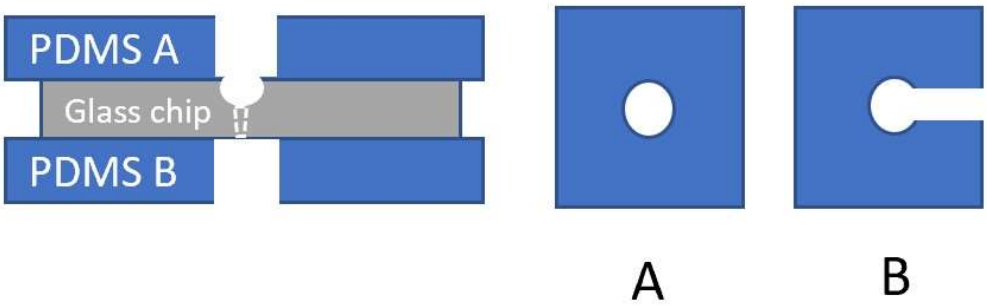

Figure F.2. Glass chip with PDMS films attached, not to scale.

2. The bottom PDMS B film is ~0.3 mm thick and with a circular opening to expose the nanopore. A channel is carved all the way from the edge to the center. This design enables air to escape when the underlying Fusion 5 membrane is wetted (see below) and prevents the formation of bubbles. The top PDMS A has ~1 mm thickness and it also has a circular opening to expose the nanopore. This circular opening acts as a buffer reservoir for the top electrode that is used in detection (see below).

F.3 Whole system assembly

1. Attach the lateral flow membrane strip to the potentiostat by using one Ag/AgCl electrode as both counter and reference electrode, while using the Pt-foil electrode as the working electrode.

2. Put the glass chip assembly on the top of the lateral flow membrane strip. Position the nanopore right on top of the gap in the lateral flow membrane strip.

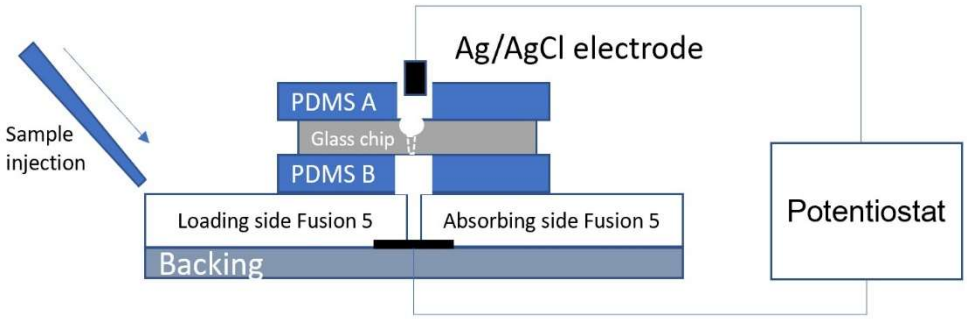

Figure F.**3.** Detection system, not to scale.

3. Put a droplet ~50 µL of hybridization buffer in the opening of the top PDMS A of the glass chip assembly.
4. Gently lower the Ag/AgCl electrode mentioned above into the top buffer reservoir in PDMS A also mentioned above to establish an electrical connection through the pore in the glass chip.

F.4 Detection

1. Deposit ~400 µL of our testing sample onto the loading side of the Fusion 5 membrane. Due to capillary flow, the liquid sample will flow over the beads so that the target RNA or DNA in the sample will hybridize with the PNA probe on our modified beads. The beads move more slowly in the Fusion 5 membrane than the fluid but at least some get carried into the gap below the pore in the glass chip. Fluid will pass through the gap and to the absorbing side of the Fusion 5 membrane. Fluid also will fill the opening in PDMS B

below the glass chip, and air will escape through the channel in PDMS B so that bubbles formation can be prevented.

2. During this process, the power to the potentiostats is turned on and data is collected using EC-lab software on a computer. A constant voltage of 1.5 V is applied.
3. A stable baseline current will appear. For a positive test, after ~200-900 s, a sustained drop in the current will occur due to the PNA-beads with hybridized target nucleic acid blocking the nanopore, and we take this as our detection signal. For a negative test, there is just a stable baseline current, no drops are observed.

Appendix G: Microprobe Fabrication

G.1 Material

Silicon wafers were ordered from Silicon Valley Microelectronics (Santa Clara, CA) with the following parameters: 100 mm diameter, p-type boron doped, orientation <1 0 0>, 150 μm thickness. All microfabrication was conducted in the UCLA Nanofabrication Laboratory (NanoLab).

G.2 Microfabrication Process Traveler

Process	Step	Name	Description	Remarks
I. Field oxide formation process				
	1	Label	Label wafer on the back unpolished side	Use diamond pen
Cleaning Steps	2	Piranha bath	Remove organic contaminants: H_2SO_4:H_2O_2 = 17:1 T=70°C; time=10 min	Use wafer carrier Refresh solution with 250mL H2O2 if hasn't been used that day
	3	Rinse	Time = 2min	Use rinse cycle in PFC hood
	4	HF bath	Remove native oxide: 5s in HF:DI=1:10 or 1s in BOE	Caution very corrosive
	5	Rinse	Time = 2 mins, afterwards N_2 blow dry	Gentle water stream Don't use spin dryer (wafers will break)
Furnace	6	Oxide furnace	Thermally grow 1μm SiO_2 Wet recipe (WET1100.001) T=1100°C, time=2.5hr	Keep everything clean (gloves/mask on) • High temperature (use caution) • Use quartz boat. Load wafers ASAP Measure the SiO_2 thickness center/top/bottom/left/right, average it
	7	Nanospec	Measure SiO_2 thickness	Measure center/top/bottom/left/right,

			(Silicon dioxide on silicon)	average it and compare with step #6
Cleaning Steps	8	Piranha bath	Remove organic contaminants: H_2SO_4:H_2O_2 = 17:1 T=70°C; time=10min	Use wafer carrier • Refresh solution with 250mL H_2O_2 if hasn't been used that day
	9	Rinse	Time = 2 mins	Use rinse cycle in PFC Hood, need to train PFC sink
II. Electrode sites, channels, and bonding pads formation				
	10	Dehydration bake	T=150°C Time ≥ 5 min	Drive off moisture, and improve PR adhesion. Before the dehydration bake, use acetone clean the previously stored wafers and use DI water to rinse first.
Lithography I	11	HDMS coat	Improve PR adhesion Time ≥ 5 min	HMDS: hexamethyldisilazane • Toxic (operate underneath hood) • Do not place wafer in the middle of metal container. • Handle dips down and will break wafer when putting cover on. Check the HDMS inside make sure it's saturated
	12	Photoresist spin coat	PR: AZ5214-EIR Thickness: ~1.6μm 1000 RPM Ramp = 1000 Time = 20sec	Clean wafer chuck with acetone • Make sure PR covers at least 2/3 of the wafer surface prior to spin volume is about 1.5 volume of the dropper To programming the parameters: Press step button + number button (1-9) to select the step to program. Select speed/ramp to set the speed = 1000 rpm Ramp = 1000 Select step terminate button to set the time to be 20 sec

				Load the wafer and press vacuum button to turn on the vacuum. After covering wafer with PR, step on the start button on the ground using your foot. Press vacuum button to turn off vacuum and collect wafer.
	13	Soft bake	T=100°C Time = 1 min. (critical) Place at the center of hotplate	Make sure wafer is flat on hotplate
	14	Exposure	Karl Suss alignment: Soft contact Expose for 9.5 sec (when power = 8 mW/cm^2)	If power varies, use this formula to correct exposure time: t (sec) = 18 × (8 / actual power in mW/cm^2)
	15	Development	Remove exposed PR DIW:AZ400K=5:1 Developer ~19 sec.	Swishing back and forth Cover the beaker with aluminum foil
	16	Microscope	Inspection	Make sure wafer is fully developed. DO NOT hardbake after this step (for better liftoff results) If the line is very thick, that usually means overdevelop
	17	Remove ~100Å PR	Tegal (~2 mins) Or Technics	Remove 100A PR for the whole wafer to prevent metal from being washed off during lift-off. Better to inspect again.
Metal Deposition	18	Metal deposition	Old CHA (evaporated metal deposition) Cr/Pt = 200 Å/1000Å Deposition rate: 1 Å/sec	• Deposit metal within 3 days after Lithography I • Total deposition time: ~3hrs
	19	Lift-off	Sonicate in acetone (in 2L beaker)	• Use 3 beakers of acetone in series to clean each wafer. • Keep wafers wet by rinsing with acetone • Rinse with DIW and dry with N_2

	20	Microscope	Inspection	Check for broken leads, chipped sites
III. Insulation layer deposition				
Oxide/Nitride Deposition	21	PECVD oxide	STS PECVD: 7500 Å Recipe: HFSIOST Time: ~30min	• Sonicate with acetone and blow dry wafer with N_2 prior to placing in machine • Check deposition rate first (~10 min), then measure the thickness
	22	Nanospec	Measure SiO_2 thickness (Silicon dioxide on silicon) Goal: 7500 Å	Use measured value subtracts field oxide thickness to calculate deposited thickness
	23	PECVD nitride	STS PECVD: 7500 Å Recipe: HFSINST Time: ~50min	
	24	Nanospec	Nanospec Measure Si3N4 thickness (silicon nitride on silicon dioxide) Goal: 7500 Å	For previous oxide thickness, type in average from step #22
IV. Open electrodes/soldering pads				
Lithography II	25	Dehydration bake	T=150°C Time ≥ 5 min	Drive off moisture
	26	HDMS coat	Improve PR adhesion Time ≥ 5 min	
	27	Photoresist spin coat	PR: AZ5214-EIR Thickness: ~1.6µm 2500 RPM Ramp = 1000 Time = 30sec	• Clean wafer chuck with acetone • Make sure PR covers at least 2/3 of the wafer surface prior to spin To program the spin coating please see step 12.
	28	Soft bake	T=100°C, time = 1 min. (critical) Place at the center of hotplate	Make sure wafer is flat on hotplate
	29	Exposure	Karl Suss alignment: Soft contact, expose for 18 sec (when power = 8 mW/cm^2)	If power varies, use this formula to correct exposure time: t (sec) = 18× (8 / actual power in mW/cm^2) Make sure four alignment marks are all matched

	30	Development	Remove exposed PR DIW:AZ400K = 5:1 ~19 sec.	Swishing back and forth
	31	Microscope	Inspection	Make sure wafer is fully developed.
	32	Hard bake	T = 150°C, 5min. Place at center of hotplate	• Do not post bake before inspection • Let cool before storing
Nitride/Oxide Etch	33	Si wafer carrier	Apply moist cooling grease on 500μm Si wafer carrier Bake more than 3min @ 80°C on hotplate	• Use q-tips to apply grease in circles over entire surface of carrier wafer • Make sure wafer backside is clean of grease • Stick wafer onto carrier wafer tightly by placing onto wafer and rotating until flats are aligned Use Kimwipe absorbed with acetone to remove the photoresist along the edge of the wafer, otherwise the PR may get burnt and stick on the sucker.
	34	Nitride and oxide etch	AOE (recipe: OXIDAPIC) Etch time: ~4 min. (this etch time may be longer or shorter depending on the status of the AOE)	• Remove 1.5 μm of nitride and oxide insulation layer • Do not run the etching more than 2 min for each time Perform O_2 clean first with thick dummy wafer
	35	Inspection	Voltmeter or Nanospec	• Voltmeter: check if resistance between test metal electrodes is zero. • Nanospec: check if thickness of oxide ≤field oxide thickness (oxide thickness<10,000A)
Cleaning Steps	36	PR strip	Matrix stripper (Matrix Asher 105) "3 min strip" recipe	Make sure to keep wafer stuck to carrier wafer until after this step
	37	Release carrier	Slide wafer off carefully	Clean wafer backside and carrier wafer with acetone
V. Define probe outline				

Lithography III	38	Dehydration bake	T=150°C Time ≥ 5 min	Drive off moisture
	39	Photoresist spin coat	PR: AZ4620 Thickness: ~7μm 3000RPM, Ramp: 1000, Time: 30sec	• Clean chuck with acetone • Make sure PR covers at least 2/3 of wafer surface To program the spin coating please see step 12.
	40	Soft bake (prebake)	T=100°C, 1'30". (critical) Place at center of hotplate	Make sure wafer is flat on hotplate
	41	Exposure	Karl Suss alignment: Soft contact, exposure time: 18 sec (power: 8mW/cm^2). After the exposure relax the wafer in ambient temperature for 5 mins.	If power varies, use this formula to correct exposure time: t (sec) = 18× (8/actual power in mW/cm^2)
	42	Development	Remove exposed PR DIW:AZ400K = 4:1 4-10 mins. Depending on the situation higher ratio like 3:1 or 2:1 could be used	For post development, rinse with DI water for 2 min. Blow dry with N_2
	43	Microscope	Inspection	Make sure wafer is fully developed
	44	Hard bake	120°C for 5 mins	
Si Wafer Etch-Through	45	Si wafer carrier	Apply moist cooling grease on 500μm thick Si carrier wafer Bake 3 min. @ 75°C	• Use q-tips to apply grease in circles over entire surface of carrier wafer • Make sure wafer backside is clean of grease • Stick wafer onto carrier wafer tightly by placing onto wafer and rotating until flats are aligned
	46	Nitride/oxide etch	AOE (recipe: OXIDAPIC) Etch time: ~7-8 min. (This etch time may be	• Remove all nitride and oxide from exposed areas • Do not run the etching

			longer or shorter depending on the status of the AOE)	more than 2 mins for each time
	47	Si etch through	FDRIE (deep reactive ion etch): Recipe FN-DY ~20 min. total etch time (this etch time may be longer or shorter depending on the status of the FDRIE)	• Do not run DRIE for more than 5 minutes at a time (could overheat the wafer) • O_2 plasma clean for 30 min BEFORE use
	48	Inspection	Microscope	Do not release wafer from carrier until etch through of silicon is confirmed. Should be able to see cooling grease through the outlines for silicon etch through. Also use nanospec to check the gap between probes, should be less than 100 Å
Stripping PR	49	Release carrier	Slide wafer off carefully	Clean carrier with acetone
	50	PR strip	PR stripper sink (ALEG 355) T=75°C, at least 30 min.	Rinse with DI water for 2 min. after Blow dry with N_2

Appendix H: Preparation of Glutamate and Choline Sensors

H.1 Materials

L-Glutamate oxidase (EC 1.4.3.11) obtained from US Biological, Choline oxidase from Anthrobacter globiformis (Sigma), m-Phenylenediamine (PPD) obtained from Sigma, Nafion (5 wt. % in lower aliphatic alcohols and water, contains 15-20% water) obtained from Sigma, chitosan (From crab shells, minimum 85% deacetylated), Bovine serum albumin (BSA) as lyophilized powder obtained from Sigma, Glutaraldehyde solution, 25% in water (Sigma), D-(+)-glucose, L-ascorbic acid, and dopamine hydrochloride were obtained from Sigma. Sodium phosphate buffer (PBS) was composed of 50 mM sodium phosphate (dibasic) and 100 mM sodium chloride (pH 7.4). Deionized water was generated using a Millipore Milli-Q Water System and was used for preparation of all solutions.

H.2 Procedure

H.2.1 Probe Assembly

1. Detach each probe off of wafer (press on corner w/ fine forceps) and check for broken leads, chipped site and poor insulation layer under microscope.
2. Cut 4 insulated Pt wires per probe and strip one end ~1 cm, another end ~2 mm.
3. Solder (@ 510 °C) wires on soldering pads of the microprobe. Apply rosin soldering flux on the Pt electrode and apply Pt wires on the rosin soldering flux then use solder tip with melted lead drop to touch the Pt wires.

4. Sonicate the soldered microprobe in isopropyl alcohol for approximately 2 minutes. Rinse with DI water and blow dry with gas. Repeat this step with another cleaner isopropyl alcohol again.
5. Insulate the soldered part with epoxy on the back/front side of microprobe. Repeat this step until no wire or solder is exposed. Wait for about 20 mins.
6. Label probe with tape

H.2.2. Acid clean

A clean scan in 0.1 M H_2SO_4 (diluted with DI water; Cyclic voltammetry: -0.2 V to 1.5 V, 50 mV/s, 5 cycles) was done to remove any surface impurities.

H.2.3 Bare sensor test

1. Make a 10 mM H_2O_2 (diluted with DI) dilution solution.
2. A bare sensor test in 10 mL PBS (0.7 V vs Ag/AgCl) was done to check sensor response to 20 μM H_2O_2 (inject 20 μL of 10 mM H_2O_2). Good sensors should give an increase in current of ~2 nA.

H.2.4 PPD deposition and Nafion coating

1. Prepare 5 mM PPD in 1X PBS (5.4 mg PPD powder + 10 mL 1X PBS) in 15 mL falcon tube. Sonicate vortex and sonicate for complete mixing.
2. Electrodeposit PPD: Apply 0.85 V vs Ag/AgCl until charge, Q (nA*h) reaches 0.21.
3. The pH of the chitosan solution (0.04% m/v) was adjusted to pH = 3 using hydrochloric acid (HCl) to dissolve the chitosan flakes. After filtering with a 0.2 μm syringe filter, the pH was adjusted to 5 using sodium hydroxide (NaOH) solution (0.5 M). A constant

potential of -0.7 V *vs.* Ag/AgCl was applied at the PPD-coated Pt electrode surface for 2 min while immersed in the chitosan solution to electrodeposit a chitosan film.

4. Dip-coat in 2% Nafion and bake the sensor at 115 °C for 20 minutes.

H.2.5 Enzyme immobilization with micro contact printing

1. One 2 µL aliquot of GluOx (0.25 U/µL; 3 mg/ml diluted with DI) was mixed with 1-4 µL BSA solution (10 mg/mL diluted with DI) depends on the status of GlutOx; Or one 4 µL aliquot of ChOx (0.5 U/µL; 20 mg/ml diluted with DI) was mixed with either 1 µL PMPC-g-PAH polymer (20 mg/ml) or 2 µL BSA solution (60 mg/mL diluted with DI).
2. A droplet (~3 µL) of the prepared enzyme ink was deposited on the PDMS micro-stamp and with the micro-stamp located on the center of the droplet.
3. Pre-align the micro-stamp with the target Pt electrode under microscope.
4. Monitor under the microscope and wait ~20 mins to see the edge of the ink droplet shrink to a similar size of the micro-stamp but still maintain wettability with high viscosity. Perform the stamping by raising the microscope stage to make gentle contact with the PDMS micro-stamp.
5. The microprobe was exposed to vapor from 5% glutaraldehyde (GAH) solution at room temperature for 1 min.
6. Sensor stored at 4 °C at least overnight.